2019-10-01

Preparation and Detailed X-Ray Photoelectron Spectroscopy and Spectroscopic EllipsometryAnalysis of Ultrathin Protective Coatings

Brian Ivins Johnson
Brigham Young University

BYU ScholarsArchive Citation

Johnson, Brian Ivins, "Preparation and Detailed X-Ray Photoelectron Spectroscopy and Spectroscopic EllipsometryAnalysis of Ultrathin Protective Coatings" (2019). *Theses and Dissertations*. 8119.
https://scholarsarchive.byu.edu/etd/8119

Preparation and Detailed X-Ray Photoelectron Spectroscopy and Spectroscopic Ellipsometry Analysis of Ultrathin Protective Coatings

Brian Ivins Johnson

A dissertation submitted to the faculty of
Brigham Young University
in partial fulfillment of the requirements for the degree of

Doctor of Philosophy

Matthew Richard Linford, Chair
David D. Allred
Roger G. Harrison
Kara J. Stowers

Department of Chemistry and Biochemistry

Brigham Young University

ABSTRACT

Preparation and Detailed X-Ray Photoelectron Spectroscopy and Spectroscopic Ellipsometry Analysis of Ultrathin Protective Coatings

Brian Ivins Johnson
Department of Chemistry and Biochemistry, BYU
Doctor of Philosophy

Ultra-thin films (UTFs) are important in many applications, seen in the semiconductor industry, in chromatography, in sensing, in microfluidics, in aerospace, and in robotics. They also protect materials from corrosion, change surface energies, limit water intrusion into materials, allow material self-cleaning and self-healing, provide scratch resistance, and impart other specific chemical properties. In many cases, UTFs drastically alter surface properties and therefore their applications. It is imperative that proper and consistent characterization be performed on coatings to confirm and understand their desired properties.

In Chapter two, Al oxidation under MgF_2 protective layers is studied using real time X-ray photoelectron spectroscopy (XPS), and spectroscopic ellipsometry (SE). These tools allowed me to monitor Al oxidation for both short (hours) and long (months) periods of time. XPS revealed the chemical changes that took place in these materials as a function of time, and these changes were verified with SE. These studies help increase an understanding of aluminum changes under MgF_2 protective layers.

The third chapter demonstrates ab initio calculations guided X-ray photoelectron spectroscopy (XPS) analysis of surfaces functionalized with fluorinated silanes. This study addresses deficiencies in the literature where CF_2:CF_3 ratios from experimental XPS data do not match theoretical CF_2:CF_3 ratios. In a systematic approach, I developed semi-empirical models directed both by ab initio calculations and adjustable, empirical parameters. These models were effective in describing the raw data and exceeded fitting methods used in literature.

In Chapter four, SiO_2 UTFs with variable thicknesses deposited on Eagle XG® glass substrates are characterized. Challenges associated with this work consisted of similar optical functions of the film and substrate as well as backside reflections from the substrate. These obstacles were met using a multi-sample analysis (MSA), a variable angle spectroscopic ellipsometric approach, and mechanical abrasion/roughening of the substrate backside. With these approaches, I developed a model that precisely fit the data collected from all the samples and gave the correct optical function of the material along with thickness values for each film.

Surface characterization represents a commitment of resources. It takes time to make measurements, and it takes time to analyze and understand the results. As presented in this work, I increase understanding of ultra-thin films at interfaces using both a multi-tool approach as well as using multiple analytical methods on data collected from each tool.

Keywords: Spectroscopic ellipsometry, XPS, Aluminum oxide, Silicon dioxide, Real-time analysis, Perfluorocarbon analyses, Ultra-Thin Film Analysis

ACKNOWLEDGEMENTS

Graduate school has been a life changing event for me. In the last 5 years, I had the opportunity to cross paths with many wonderful people who contributed to my success. My advisor Dr. Matthew Linford has gone out of his way to ensure my family and I were taken care of. He also imparted a plethora of knowledge and challenged my intellect. But most important, he mentored me in my communication skills. I know these skills will be more important in my career and future more than all the technical knowledge that he imparted to me. Dr. David Allred also played a significant role in my development here at school. His constant positiveness about my projects and willingness to mentor me in my NASA projects helped to keep me going when it seemed impossible to complete my program. I will always owe my success to both Dr. Linford and Dr. Allred for their patience and guidance during my time here.

In my work, I enlisted the help of many others, each gifted in their own respective fields. Though there are many who helped me on my path to graduation, I specifically want to acknowledge the help of Tahereh Gholian Avval. Without her constant positive support, work, and words, I would not have been as successful as I was in my work here. Tahereh’s constant willingness to put aside her own work and help me in research areas where I was not proficient encouraged me to continue and ultimately complete my program here. I also want to express my thanks to my undergraduates Grant Hodges, Karen Membreño, and Victoria Carver who all contributed their time and talents to help with the success of my work.

I also want to take time to thank Anubhav Diwan and the staff at Moxtek. Their willingness to fund my projects contributed in large amounts to my success here. In addition, other supporting groups such as Utah NASA Space Grant Consortium, Surface Vacuum Society, American Vacuum

Society, and all of the other groups and consortiums that funded me for trips as well as allowed me to present my data at their conferences.

My lab mates both past and present consisted of a diverse group of people with impressive talents. I have learned much more than science from my lab mates. Their willingness to share cultures, stories, and religions from their countries enriched my life. It also opened my eyes to a beauty and diversity from around the world that I never really knew existed. I will forever be grateful for this generosity afforded by them.

For much of my knowledge in SE and ToFSIMS, I want to thank Hao Wang as well as Cody Cushman. Both of these former graduate students were excellent mentors and they helped me gain both confidence and aptitude in many of the sampling techniques in our lab. As well, Cody went out of his way to get to know me and was a good friend. The out of school activities that Cody invited me and my kids to were a refreshing break for me as well as my kids. I also want to thank Bhupinder Singh for making me feel so welcome and included when I first came to the lab, his constant up-beat personality was a strength to me.

I want to thank Janet Fanoimoana who helped me to realize that BYU was the right place for me to be. I will always be grateful for her caring help that made me to know that everything was going to be ok. In addition, I need to thank all of the support staff in the chemistry office. Without their dedication to my success, I would not have been able to complete this work.

To my family who sacrificed much of my time so that I could complete my degree-I give GREAT thanks. My Family's constant support and optimism in me proved to be a major driving force in my progress here. Their quirks always put a smile in my face and lightened up my day. Brianna, Johnathan, Sael, Melissa, and Matthew are all the lights of my life and make my world go around.

I want to give a special thanks to my greatest fan. My lovely wife Saely. Her constant, unconditional support and passion for my success has been the main driving force behind my work. Without her undying support, all of the truly important work (the work at home) would not have been done. Saely's commitment to the kids and their wellbeing in the face of many great adversities has inspired me and been the one force that allowed me to complete my work here. It was her dedication to our family (and me) that contributed the most to my success at school.

Finally, to my Heavenly Father who has blessed me with my intellect, my trials, and with the incredible support system of people that I have previously mentioned. Without His support, none of my success would be possible. I hope that I can stay strong and return at least some of the graciousness afforded to my success here by my Heavenly Father as well as everyone around me.

TABLE OF CONTENTS

LIST OF ABBREVIATIONS

AFM ——— Atomic force microscopy

ALD ——— Atomic layer deposition

BASF ——— Badische Anilin und Soda-Fabrik

BE ——— Binding energy

bcc ——— Body-centered cubic

BEMA ——— Bruggeman effective medium approximation

fcc ——— Face-centered cubic

FTIR ——— Fourier transform infrared spectroscopy

GLP ——— Gaussian-Lorentzian product functions

GLS ——— Gaussian-Lorentzian sum functions

IR ——— Infrared

KE ——— Kinetic energy

K-K ——— Kramers-Kronig

LPCVD ——— Low pressure chemical vapor deposition

MSE ——— Mean square error

MEMS ——— Micro electrical mechanical systems

MSA ——— Multi-sample analysis

NEMS ——— Nano electrical mechanical systems

NAP-XPS ——— Near ambient pressure X-ray photoelectron spectroscopy

PECVD ——— Plasma enhanced chemical vapor deposition

PTFE ——— Polytetrafluoroethylene

SEM ——— Scanning electron microscope

SE ——— Spectroscopic ellipsometry

Tof-SIMS ——— Time-of-flight secondary ion mass spectrometry

TEM ——— Transmission electron microscope

UTF ——— Ultrathin films

UV ——— Ultraviolet

VASE ———— Variable angle spectroscopic ellipsometry

WCA ———— Water contact angle goniometry

XRD ———— X-ray diffraction

XES ———— X-ray emission spectroscopy

XPS ———— X-ray photoelectron spectroscopy

LIST OF FIGURES

LIST OF TABLES

CHAPTER 1: Introduction

1.1 Focus of the Work

This work describes the preparation and characterization of three ultra-thin, protective layers. The first of these studies focuses on the analysis of aluminum surfaces protected by ultra-thin films (UTFs) of MgF_2. The second centers on the deposition and characterization of protective films of hydrophobic fluorosilanes. The third is on the SE analysis of sputtered SiO_2, by which the optical properties of this material are elucidated.

Because of its unique properties and numerous applications,[1-3] aluminum is extremely important, both as a bulk material and as a thin film. Aluminum is generally considered to be an easy metal to work with. It has a relatively low melting point, it is ductile yet strong enough to be used in structural applications, it is lightweight, it can be alloyed, and it is unmatched in its ability to reflect light over a wide energy range including into the deep UV.[1-4] Accordingly, aluminum is the best-suited reflective coating/material for astronomical observation.[4-6] A drawback to aluminum is that its surface oxidizes quickly in the air.[6-8] And although a small amount of oxide is not a limitation for most of aluminum's applications, aluminum oxide, even when only a few nanometers thick, absorbs short wavelength light, which significantly limits aluminum's ability to act as a space mirror and collect light over the widest possible wavelength range.[4, 6, 8-10] A general strategy employed to overcome this deficiency, while preserving aluminum's desired optical properties, is to coat it with a wide band gap material.[11-16] Wide band-gap materials such as MgF_2 and other inorganic fluorides have been studied and used for decades to protect aluminum reflectors, including those in the Hubble space telescope.[4, 10, 12-14] Thus, the overall goal of depositing thin films of fluoride salts on aluminum mirrors is to create robust layers that will limit and even prevent aluminum oxidation prior to launch while allowing adequate reflection at shorter wavelengths.[4, 6, 11, 14] However, despite the high optical transparency enjoyed by many inorganic fluorides, even 3 nm of MgF_2 can start to impede the passage of deep UV light, while still not being thick enough to act as an adequate oxidation barrier for aluminum. Accordingly, a number of studies have focused on developing robust, transparent passivation layers for aluminum using different deposition schemes and materials.[6, 14] Work centered around gaining a better understanding of how aluminum can be passivated and oxidizes and reacts with its environment is of utmost importance in further optimizing this metal for important applications in astronomical data collection. Indeed, aluminum is currently being proposed as the primary reflector for future space missions such as the LVOIR project, which will be the flagship NASA space observatory for the 2020s and 2030s.

Modification of surfaces with low free energy materials, including perfluorocarbons, and the concomitant analysis of these materials, plays an important role in many areas of society, including in self-cleaning surfaces, superhydrophobic surfaces, low adhesion surfaces, corrosion resistance, and micro/nano electrical mechanical systems (NEMS/MEMS).[17-24] Hydrophobic treatments/coatings are even applied to concrete,[25] as well as to some materials to increase their biocompatibility.[26-28] There have been many reports of the deposition and subsequent analysis of perfluorocarbon-containing coatings. One of the well-known reagents for making such surface modifications is with silanes with moderately long to long fluorinated chains of the form: –$CH_2CH_2(CF_2)_nCF_3$, where n is usually small – less than 10.[19-22] SE is a useful method for characterizing such ultrathin films. However, as many UTFs are less than 5 nm thick, it is not possible to simultaneously determine both their optical functions and thicknesses with SE.[29] Nevertheless, in many cases, the optical function is not of primary importance for these materials because of the increasingly limited dependence of the film thickness on optical function for very thin films.[29, 30] Thus, while SE can confirm fluorosilane film deposition, it does not provide a significant amount of chemical information about them. In contrast, XPS C 1s narrow scans provide important, direct chemical information about fluorosilane films because the different types of carbon atoms in the silane adsorbate yield fairly well separated XPS signals, i.e., the CF_2 and CF_3 signals are well separated from the hydrocarbon envelope and moderately well separated from each other.[31-35] Nevertheless, there is some complexity in the analysis of the C 1s fluorocarbon envelope. Indeed, as I show in Chapter 3, conventional approaches to fitting the CF_2/CF_3 C 1s envelope do not yield the theoretical $CF_2:CF_3$ ratio. Indeed, ab initio calculations suggest that the two CF_2 groups closest to the CH_2 groups in $-CH_2CH_2\underline{C}F_2\underline{C}F_2(CF_2)_nCF_3$ chains have noticeably different chemical environments than the other CF_2 groups in the chain, which ultimately should manifest itself as different chemically shifted C 1s signals.[23, 36-38] However, given the inherent widths of these signals and their overlapping nature, it would be difficult to elucidate their positions using traditional, empirical peak fitting approaches. Thus, there is an opportunity to gain a greater understanding of these important materials by using first principles calculations of fluorinated silane adsorbates to guide subsequent narrow scan peak fitting.[39-42]

Silicon dioxide is extremely important, both as a bulk material and in thin film form. Accordingly, it has been extensively studied and characterized.[43-52] SiO_2 has numerous applications, including in energy storage, microelectronics, semiconductor devices, multilayer optical coatings, microelectromechanical systems (MEMS), and as a substrate for thin films and coatings.[53-57] The surface of SiO_2 can be modified using a variety of reagents, especially silanes,[58-61] which allows its surface to be tailored for specific applications, including enhanced adhesion, superhydrophobicity (if the surface has the proper roughness), self-cleaning, chemical sensing, and chemical separations.[62-65] There are a variety of methods for depositing SiO_2, including plasma enhanced chemical vapor deposition (PECVD),[66, 67] low pressure chemical vapor deposition (LPCVD),[68] e-beam evaporation,[69] atomic layer deposition (ALD),[70-73] sol-gel deposition,[74, 75] and sputtering.[76-78] SiO_2 films are also routinely prepared on silicon wafers via thermal oxidation.[79-81] Although each of these methods deposits (or grows) silicon dioxide, the optical and mechanical properties of these films vary depending on the deposition method used. For any optical modeling, it is useful to have a good approximation of the optical functions of the materials being probed.

Not all thin films on substrates are trivial to analyze. For example, when thin films such as SiO_2 have about the same optical properties as their substrates, e.g., a glass, optical analyses are more challenging.[82] An important way of providing additional information in an optical analysis is through a multi-sample analysis (MSA), which is an analysis of a series of similar materials. That is, MSAs can break correlation between parameters in a model and even allow additional parameters to be introduced into a model in a meaningful fashion. An MSA may consist of an analysis of a series of nominally identical films with different thicknesses on the same substrate. Additional ways of adding more information into these models can be by acquiring data at multiple angles and/or by depositing the film in question on different substrates.[29, 30, 82, 83] An additional, important consideration in the SE analysis of thin films on transparent substrates is backside reflections from the substrates because this reflected light is incoherent with the light reflected from the front face of the material. That is, incoherent light contributes nothing to an analysis – it can only limit its accuracy/confound it.[84] Thus, it is advantageous to find ways to remove backside reflections from transparent substrates. In summary, it is important to use methods that can analyze transparent films on transparent substrates that include removal of backside reflections.[84]

Understanding the compositions of UTF surfaces and how they interact with their environments is key to being able to control their desired properties and improve results. Therefore, numerous papers and research projects have been devoted to characterizing UTF surfaces.[19-24, 85] Many of these studies illustrate the value of a multi-technique/multi-instrument approach to surface and material analysis.[19-24, 45] Some of the more commonly used methods for UTF surface characterization include Fourier transform infrared spectroscopy (FTIR), water contact angle goniometry (WCA), atomic force microscopy (AFM), scanning electron microscopy (SEM), time-of-flight secondary ion mass spectrometry (ToF-SIMS), spectroscopic ellipsometry (SE), and X-ray photoelectron spectrometry (XPS).[20, 36] Less common/more exotic methods such as low energy ion scattering[86] and the advanced methods available at synchrotrons are also of value here.[87-89] Though each of these techniques independently provides valuable and unique information, in general, no single instrument or method can provide a comprehensive characterization of a material.[45] As the importance of UTFs grows, the demands on their advanced characterization will also increase. Accordingly, there is an increasing need for advanced and novel approaches to film characterization based on current instrumentation, first principles calculations and modeling, and newer, cutting edge instrumentation and data analysis methods.

1.2 Approach

In my work at BYU, I primarily used SE and XPS to characterize my UTFs. These are powerful techniques that can provide a great deal of information about thin film structure, thickness, morphology, and chemistry.

For my first study, Chapter 2, I used XPS and SE to follow the chemical and optical changes in MgF_2 – protected aluminum as it oxidized. Because of the importance of aluminum and aluminum oxide, there have been many studies on these materials using various experimental and theoretical methods that include XPS and SE.[9, 11, 44, 90-92] In my work, the rate of Al oxidation was monitored from the time it was coated in situ with MgF_2 and exposed to the air. Here, I used XPS narrow scans of the Mg 2s and Al 2p regions along with computations based on Hill's work[93-95] to determine the MgF_2 UTF thicknesses on evaporated aluminum thin films. I showed that thicker MgF_2 layers reduce Al oxidation in an exponential fashion. I also analyzed freshly prepared MgF_2/Al stacks by in situ SE over the course of 4 h and the results were analyzed in an MSA. Optical constants of extremely thin metal films can vary greatly depending on thickness, morphology, and deposition conditions. Accordingly, when a relatively simple model with only two parameters (the thicknesses of the aluminum and aluminum oxide layers) was applied to the in situ SE data, some of the thicknesses of the Al_2O_3 films were unphysical – they were negative.[96] Thus, a second, more satisfactory model was developed in which the optical function of Al was allowed to vary, along with the thicknesses of the Al and Al_2O_3 layers.[96] As expected, this model indicated that thicker MgF_2 films led to slower oxidation of the underlying aluminum. Thus, XPS and SE can be used together to follow aluminum oxidation under MgF_2 layers of varying thickness. In spite of the importance of protecting aluminum mirrors, I am not aware of any other systematic XPS and SE analysis of MgF_2 - protected aluminum mirrors. My studies increase our understanding of how Al is oxidized under protective layers. With this increased knowledge, the development of robust, transparent passivation layers for Al can be further optimized to create superior astronomical reflectors for data collection.

In my analysis of perfluorocarbon UTFs, Chapter 3, I developed a series of increasingly sophisticated models for understanding perfluorocarbon silane adsorption onto surfaces. In my first model, I used two unconstrained peaks to model the CF_2/CF_3 envelope (one for CF_2 and the other for CF_3). Here, the fits were good, but the slope of the plot of the $CF_2:CF_3$ ratio from the fits vs. the theoretical CF_2:CF_3 ratio, m_{CF_2/CF_3}, was lower than the expected value of unity. To aid in this fitting, I then determined the expected peak widths of the $–CF_2–$ and $–CF_3$ moieties from pure/model compounds. Based on these peak widths, I developed two empirical models. These attempts yielded either a good fit or a good m_{CF_2/CF_3} value, but not both. To further understand this problem, I then performed ab initio calculations of the silane adsorbates. These predicted that the CF_2 groups in the chains of CF_2 moieties would have different XPS binding energies, especially those at the ends of the chains, i.e., $–CH_2\underline{C}F_2CF_2$… and $–CH_2CF_2\underline{C}F_2$… A model based entirely on these calculations was then considered. It included a fit component of equal area and width for each type of CF_2 or CF_3 carbon in the silane and positioned these peaks at the relative energies dictated by the calculations. Of course, this model gave an ideal value of unity to m_{CF_2/CF_3}. However, the peak fits were only moderately good. Finally, two semi-empirical models were considered. They were guided by the first principles calculations, but they also had some adjustable parameters. These models are arguably the best that were developed in this study. Because of the importance of fluorinated materials and XPS, I believe that these results will be relevant to the surface and materials community.

For the analysis of the sputtered SiO_2 presented in Chapter 4, SE was used to characterize reactively sputtered SiO_2 films on Eagle XG® glass with nominal thicknesses of 20, 40, and 60 nm.[82] The uncoated backsides of two sets of samples were mechanically roughened: one set with a rotary hand-held tool and the another with a sandblasting tool. This was done to suppress unwanted (incoherent) reflections.[97, 98] It also allowed these two methods for roughening the surfaces to be compared. SE measurements were obtained in reflection mode from 196 – 1688 nm in 1° increments from 55° to 60°. The samples were evaluated via an MSA, wherein data from samples with different film thicknesses were fit simultaneously.[29] The optical constants of the sputtered SiO_2 films were taken to be the same for all the samples, as were those of the substrates. In particular, the refractive index of the SiO_2 was modeled using a Sellmeier model, as dictated by two poles. These poles are unbroadened oscillators that are positioned outside of the wavelength region of interest. They have an impact on the refractive index, but not the extinction coefficient, of a material. The Sellmeier model is appropriate for materials that are transparent over the entire wavelength range considered. Accordingly, no oscillators were included to model absorbing features. The goodness of the modeling was indicated by the mean square error (MSE) of the fit. The final models also included a Bruggeman effective medium approximation (BEMA) roughness layer, which consisted of 50% volume fractions of SiO_2 and void.[99] In one model I considered, the thickness of this roughness layer was set to the value obtained by atomic force microscopy (AFM). Data from nine samples (three of each thickness) were simultaneously fit with the models. We also considered an interface layer between the sputtered film and the substrate, but it did not significantly improve the fit, so it was omitted, i.e., I maintained as much simplicity as possible in the model. This study yielded precise optical constants for reactively sputtered thin films of SiO_2 on a transparent substrate, which showed that with an MSA and proper sample preparation a difficult thin film analysis can be performed with accuracy.

This work focuses on the application of two important surface analytical methods to the analysis of three protective thin films. For completeness, one of these films was an organic material (an organosilane) and the other two were inorganic ($MgF_2/Al/Al_2O_3$ and SiO_2).

1.3 Background

This section focuses on the significance of surface chemistry and surface analysis. It also explains the importance of my work in the surface analytical arena. It starts by explaining the technological relevance of surface chemistry, followed by a description of the surfaces I used in my studies, as well as the significance they play in industry, academia, and every-day life.

1.3.1 Technological Significance of Surface Chemistry

Surfaces can be defined as the boundaries between bulk materials and their associated environments.[100] Assuming 0.7 nm as the dimensions of a unit cell, e.g., simple cubic, face centered cubic (fcc), or body centered cubic (bcc) structures, simple calculations suggest ca. 10^{21} atoms/cm^3, but only ca. 10^{14} atoms/cm^2 at a surface of the material. Because surface atoms are not surrounded by other atoms, as they would be in the bulk, surface atoms exhibit different chemical reactivity.[101, 102] A prime example of a material that exhibits differences between surface and bulk reactivity is gold, which has a surface reactivity that is noticeably greater than the bulk reactivity.[102, 103] Some of the products and technology that are driven by surface chemistry include catalysts, fuels, semiconductors, biomedical technology, solar cells, batteries, and reflective and protective coatings.[100, 104]

Surface chemistry has a rich history. In the late 1880s, a German chemical company, the Badische Anilin und Soda-Fabrik (BASF), used the so-called "contact process" with a heterogenous catalyst to convert sulfur dioxide to sulfur trioxide.[102, 105, 106] As heterogenous catalysts then progressed into the 20th century, their sophistication increased. From zeolites to platinum nano-clusters and bimetallic cluster catalysts used in the petroleum industry for cracking and purifying gasoline products, heterogenous catalysts have afforded engineers accelerated reactions and improved yields.[100, 105, 107-113] Proceeding into the 21st century, surface modification technology has advanced to allow optimization of catalytic selectivity.[100, 114, 115] However, to facilitate increased selectivity at the molecular level, surface chemistry processes have needed to be monitored in real-time. By such in situ monitoring, the influence of surface chemistry on reactions has been better understood.[100, 116]

As this catalytic revolution moved forward so did the technology to modify surfaces. Scientists such as Langmuir, Hinshelwood, Emmett, and Brunauer worked to understand adsorption and surface reactivity kinetics.[105, 117-119] Langmuir, an early pioneer in surface chemistry derived the Langmuir isotherm, which describes the chemisorption of a gas on a surface as a function of pressure.[105, 120] In 1913, while addressing a sporadic problem with abnormally high thermionic emissions from some tungsten light filaments, Langmuir was able to theoretically ascertain that the enhanced emissions were from the desorption of a monolayer of thorium on the filament surface (originating from thorium oxide added to tungsten filaments in order to improve filament performance at high temperatures).[120] From here, Langmuir's work expanded into more sophisticated experiments conducted by researchers like Clausing.[120] With the tools and understanding they developed, the semiconductor industry was born. In 1947, the first point-contact germanium transistor was born out of research on catalytic reactions and the electronic surface states of germanium.[100, 121] Additional advances in thin film properties and deposition then came out of work on epitaxial film growth, nanoscale engineering, surface etching, vapor phase depositions, etc.[100, 122-124] It has been through research centered on building an increased understanding of previous work that advances in thin films have been more fully realized.

An early area of UTF analysis that garnered interest is metallic films and their reactions with species in their environments.[100, 125-127] Knowing that most metallic surfaces are quite reactive, researchers endeavored to understand catalytic processes on them by performing surface kinetic studies under various reaction conditions.[128] Using these types of in situ studies, researchers were able to understand complex principles such as how surface morphology and atomic arrangements play a role in reaction kinetics.[128, 129] With these pioneering examples and tools, the power of in situ molecular-level studies on metallic surfaces in controlled environments was more fully realized. Another area of interest regarding metallic surface reactions involves metal oxidation. In general, the reactive properties of metallic surfaces that make them effective catalysts also makes them susceptible to oxidation. Thus, for multiple reasons, the chemical changes associated with metals after oxidation are of great interest. Moreover, oxidation is different for the various metals. For example, while oxidation leads to the passivation of stainless steel,[100] it causes complete corrosion of iron. For some metals, an oxide is beneficial,[100] and even preferred, as in the case of passivation/anti-corrosion and when the oxide has catalytic properties. However, the oxidation of some metals can be detrimental to its desired function – aluminum loses its reflectivity at short wavelengths when it is oxidized.[4, 6-10, 130, 131] Clearly, the interactions of adsorbates, including oxygen, with metals and metal oxides, are complex and important.

Not only do reactive, metallic films attract the attention of researchers, but inert films are also of great interest in many thin film studies.[19-24] One important class of inert films is comprised of hydrophobic and superhydrophobic surfaces, where these low-adhesion/low-friction materials have low surface energies and are quite unreactive. These features are useful for applications in micro/nano electrical mechanical systems (NEMS/MEMS), self-cleaning surfaces, and low adhesion surfaces.[17, 19, 132] One method used for adding hydrophobic functionality to surfaces is to coat them with thin hydrocarbon and/or fluorocarbon layers.[18, 20, 85, 132] Understanding these materials is crucial when depositing them on a desired surface. For example, undesirable results stemming either from unwanted adhesion or inadequate adhesion can lead to MEM failure, from too much adhesion, or medical failures when adhesion is inadequate.[28, 133, 134] Clearly, when a surface is modified, certain surface changes are expected, and if a coating is placed on a surface but it is unable to either remain on the surface or impart the desired functionality, the surface is rendered useless. Accordingly, a wide range of functions and properties have been researched for superhydrophobic coatings. Some examples of these properties include photo reactivity, transparency, biocompatibility, and tunable hydrophobic/hydrophilic properties.[28, 135-137] Fundamental studies will increase our understanding and potential benefits of hydrophobic/inert coatings.[104]

As mentioned above, oxide films are present on most metals. They are also present on most semiconductor surfaces.[104] In general, metal and semiconductor oxides have vastly different chemical properties than unoxidized metals or semiconductors.[104] One area where oxides have had an impact in surface chemistry is in semiconductors where improved control of oxide levels has improved memory devices.[138] Another area of research where oxides play crucial roles includes biofilm studies where, for example, Pd adsorption on biofilms was adversely affected when Mn oxide films were not present.[139] Not only can oxides provide anchors for metal adsorptions, they also play a key role in the functionalization of silicon surfaces (through silica) with silane coupling agents.[104, 140, 141] Surface modification with silanes has proved important for a variety of industries,[104, 138-140, 142] where the successful functionalization of oxide surfaces, e.g., silica,[104, 140, 141] with organosilanes was described as far back as the 1950s. Thus, a deeper understanding of oxides and silanes is directly relevant to modern technology.

The history of surface chemistry is rich. Indeed, an increased understanding of surface chemistry has allowed technology to thrive exponentially. It is through understanding the mechanics of surface chemistry that science has been able to understand the intricacies of surface dynamics. In the work presented here, both inorganic and organic UTF’s were analyzed, integrating multiple analytical techniques and data analysis methods not previously studied at the depth to which I have endeavored. It is the goal of this work to continue bridging the gap of the science of surface chemistry to practical applications through a heightened understanding of inter/intra molecular interactions from integrated analytical techniques.

1.3.1.1 Aluminum

Aluminum compounds have a rich history stemming from as early as 1550 BCE where aluminum salts were used for medicinal purposes,[143-145] to ancient Rome where naturally doped alumina was used as decorative jewelry in the form of sapphires and rubies.[143, 146-148] However, aluminum metal, unlike other metals such as gold, silver, or copper alluded mankind in its fully reduced form until the early 19th century.[143] Although aluminum metal comprises approximately 8% of the earth's crust by weight, it was not postulated until 1807 by Sir Humphry Davy, nor was it isolated until 1825 by the Danish Chemist Hans Christian Ørsted.[143, 149-155] Furthermore, it was not until 1858 that Henri Deville first commercialized aluminum production.[143, 156] Aluminum has filled many structural as well as technological voids worldwide. Indeed, from its industrial origins in 1900 up to 1971, approximately 250 million tons of it were manufactured, and from 1972 to 2017 the amount of aluminum metal manufactured was about 1 billion tons.[143] The explosion of aluminum usage worldwide is seen in items such as soda cans, cars, and many other applications requiring lightweight, inexpensive macro-scaffolds.[143]

As noted above, aluminum is a plentiful, inexpensive metal with a myriad of applications.[1-3] And though the general history of aluminum usage centers around its structural properties, as well as its ability to alloy well with other metals, these properties are not the only ones that have been studied.[157-162] Aluminum is the best suited reflective coating for space mirrors because of its unmatched ability to reflect over a wide energy (wavelength) range, including into the deep UV.[4, 6] The first optical studies of aluminum go back as far as Quinke in 1874 with subsequent research showing reflectivity as high as 84% down to a wavelength of 297.6 nm.[162] However, deeper optical analyses of aluminum were only possible when it was discovered that the metal could be sputtered onto surfaces.[162, 163] Accordingly, in the early parts of the 20th century scientists such as Mott, Heines, Segall, and Ehrenreich, among many others, extensively studied aluminum's properties, including its Fermi surface, its deHass van-Alphen effects, and optical transitions in it.[158, 162, 164] Through these studies, a more complete understanding of the optical properties of aluminum was gained.[162] However, like most metals, aluminum is prone to oxidation. Along these lines, it was observed that aluminum's oxide layer adhered well to its surface and that it passivated the remaining metallic aluminum.[162] It was also found that as long as the aluminum oxide thickness was less that the wavelength of incident light, the electric waves of the incident and reflected light nearly cancel each other in the oxide layer, thus making any coupling between the oxide and metal negligible.[162] This property makes the oxide transparent at longer wavelengths (IR region). In addition, the band-gap here adversely affects the optical transparency and it is reduced at shorter wavelengths (UV regions), with a 50% decrease of reflectivity at 126 nm for an oxide layer of only 1.76 nm.[162]

The interest of the aforementioned studies were spurred by aluminum's extraordinary and broad reflectivity that make it the best candidate for advanced space mirrors that operate deep into the UV. However, in order to collect data at the shorter wavelengths, optically transparent films needed to be developed to prevent Al oxidation. Thin coatings of Y_2O_3 and HfO_2 have proven successful for protecting aluminum mirrors at high angles of incidence, where SiO_2 passivation coatings reduced reflectance.[162] Other thin films that have been researched for oxidation reduction are LiF and MgF_2 coatings. These particular coatings are a standard in preserving reflectance at down to 100 nm and have been used in astronomical reflectors such as the Hubble Telescope.[4, 6, 11, 12, 14, 162]

By monitoring the Al oxidation rate as a function of MgF_2 thickness as presented in my research, optical engineers can further optimize aluminum reflectors to maintain a maximum bandwidth for reflection. Moreover, the data collected from this study will act as a baseline for future aluminum oxidation rate research with other thin fluorine-based films (AlF_3, LiF) used on aluminum to make dielectric mirrors. These mirrors are of great importance as they will be able to reflect down into the Lyman UV range (91-103 nm). In addition, the techniques developed in my research will dovetail into future research that will contrast the effectiveness of oxidation protection between the multiple thin-films used for dielectric mirrors and the thick MgF_2 films currently used to protect aluminum. Ultimately, with this information, the already wide range of reflectance of aluminum can be further optimized for the reflectors in space telescopes.

1.3.1.2 Hydrophobic Surfaces and Morphology

A hydrophobic surface is defined as a surface with a water contact angle greater than 90° but less than 150°.[165-167] Superhydrophobicity is just as it sounds, a step above hydrophobicity – it shows a water contact angle of 150° or greater.[165-167] These surfaces are of great importance in today's world where their uses are widespread. Indeed, they are seen in applications ranging from self-cleaning surfaces to MEMs and biocompatible devices.[17, 19, 132] Hydrophobicity can be imparted to a surface either through morphological means, chemical means, or both.[168-171] Superhydrophobicity is often referred to as the lotus effect. It is a self-cleaning property that is usually achieved through morphological means, which has its roots in the Nelumbo or lotus flower.[169, 172-174] The lotus effect, as well as other natural hydrophobic coatings, have inspired researchers for generations.[166, 168, 169, 173] Spawned by such observations in nature, early researchers (Wenzel and Cassie) investigated hydrophobic phenomena for the textile and clothing industries using water contact angle analyses to assess waxes and wax-like materials for waterproofing commercial lightweight fabrics.[168, 170] However, in the decades following Wenzel and Cassie's work, research on the subject did not advance very quickly, and significant interest in hydrophobic studies did not start again until the 1990s with studies on polytetrafluoroethylene (PTFE), alkyl silanes, and perfluoroalkyl silanes.[169, 171, 175, 176] Nevertheless, despite little recorded advancement between the early works in this field and the hydrophobic research of the 90s, hydrophobic surface research eventually experienced a strong resurgence, thus illustrating the importance of these modified surfaces.[171, 174]

Many of the chemicals used for hydrophobic surface modification contain alkyl and fluoroalkyl carbon moieties. However, when it comes to superhydrophobicity, fluorocarbons have an advantage.[19, 177, 178] Fluorocarbon surface modification research initially stemmed from hydrocarbon research.[174] Indeed, because fluorine has a much larger atomic radius, the number of fluorine atoms per unit volume in a fluorocarbon is quite a bit less than that of hydrogen atoms in a hydrocarbon chain, thus lowering the overall surface mass density.[177] In addition, because of the size of the fluorine atoms a sheath envelopes the carbon chain backbone, which physically protects the chain from chemical attack and imparts a lower surface energy.[178] The low surface energy of fluorinated coatings and fluorocarbon moieties imparts chemical inertness, thermal stability, and lubricative properties to materials protected by fluorinated coatings.[178] An excellent example of this is the application of hydrophobic and superhydrophobic perfluorinated thin films to MEMS devices where robust, low surface energy SAMS are desired.[18, 24, 179]

Thin film perfluorocarbon coatings also play an important role in the optics industry.[180-184] In optics it is important that any protective layer be inert, able to withstand adverse weather conditions, have a low index of refraction, not be flammable, and be able to repel liquids, either aqueous or oil based.[181, 183, 184] As described above, perfluorocarbon thin films possess these characteristics which makes them of keen interest in optics.[180-184] And not only are these UTF's transparent and inert, but with their high water contact angles, water easily flows off the surfaces and removes external contaminants, which gives them self-cleaning properties.[166] The combination of these effects makes perfluorinated UTF coatings attractive to optical applications where surfaces need to be optically clean both at the micro and macro levels. As presented here, the importance of hydrophobic and superhydrophobic surfaces as well as the amount of research and characterization spent on them shows how important these films are in both industry and academia.

In the work I present here, I address the challenges of matching theoretical to experimental CF_2:CF_3 ratios in XPS analyses of fluorocarbon thin films. In particular, I was able to create a predictive analytical model that closely returns the theoretical CF_2:CF_3 ratio. This was accomplished using four UTF's comprised of different perfluorocarbon length chains deposited on a flat surface, which yielded high quality empirical fits. In the past, predictive models of this type have only been able to achieve CF_2:CF_3 ratios as high as 1:0.84. With my work, I was able to increase the predictive power of XPS CF_2:CF_3 data analyses using ab initio calculations combined with empirical methods for XPS peak fitting. In summary, this project not only focused on obtaining the right ratio, it looked at the strength of combining multiple analytical approaches to facilitate accurate and precise data analysis.

1.3.1.3 Silicon/Silicon Dioxide

Silicon dioxide (and silicon) are extremely important inorganic thin film materials. As such, they have been extensively studied and characterized in various states.[43-52] Indeed, they have numerous applications, including in energy storage, microelectronics, semiconductor devices, multilayer optical coatings, and microelectromechanical systems (MEMS).[54, 56, 69, 185, 186] Because the surface of SiO_2 can be modified using a variety of reagents, including silanes,[58-61] it can be tailored for specific applications, such as enhanced adhesion, superhydrophobicity (if the surface is appropriately rough), self-cleaning, chemical sensing, and chemical separations.[62-65] This makes SiO_2 (silica) an indispensable material in technology. Silica can be deposited through a variety of methods, including plasma enhanced chemical vapor deposition (PECVD),[66, 67] low pressure chemical vapor deposition (LPCVD),[187] e-beam evaporation,[69] atomic layer deposition (ALD),[70-72, 188] sol-gel deposition,[189, 190] and sputtering.[72, 76-78] SiO_2 films are also routinely prepared on silicon wafers via thermal oxidation.[79, 80, 191] And while each of these methods deposits silicon dioxide, the optical and mechanical properties of these films may vary somewhat depending on the deposition method used. For example, in one study,[192] presumably undertaken at 632.8 nm, the refractive index for reactively sputtered SiO_2 on glass varied from 1.453 – 1.460. In another, which was performed at 632.8 nm,[193] PECVD of SiO_2 resulted in a refractive index of 1.461 – 1.489. Variations in film properties may also result from inhomogeneities in material density, morphology, and stoichiometry as a function of depth and/or lateral position on a surface.[194] Stress can play a role in distorting the amorphous network, which can change the optical properties of the film and/or substrate, sometimes inducing birefringence. Impurities in the sputter target and/or from the chamber may influence the optical properties of the films as well. Other factors that influence thin film properties include deposition temperature, deposition rate, the chemical environment during deposition, and the energy with which deposited particles impinge on a substrate. Because of these variations, it is important to have optical constants specific to a deposition method for characterization of similar films and/or as a starting point for modeling.

In this study, SE was used to characterize reactively sputtered SiO_2 films with nominal thicknesses of 20, 40 and 60 nm deposited using a proprietary method on Eagle XG® glass substrates. This analysis presented a unique challenge in that both substrate and thin films were transparent. However, by employing a multi-sample analysis (MSA) of our variable angle spectroscopic ellipsometry (VASE) data, I was able to determine the optical constants from 196 – 1688 nm, and some accompanying physical characterization, of sputtered 20 – 60 nm SiO_2 films.

1.3.2 UTF Surface Analysis

A clear picture of how surfaces interact with each other and with their surroundings is essential for understanding how we can modify them for a desired task. To create this knowledge, techniques and instruments have been developed that can analyze materials at the molecular level.[100] Some of these specialized tools and techniques include scanning electron microscopy (SEM) and transmission electron microscopy (TEM), which are capable of resolving features smaller than the wavelengths of visible light to provide structure, crystallinity, size, and shapes of objects of interest.[100] X-ray diffraction (XRD) is used to determine crystallographic orientations of atoms in crystals and has the ability to give physical and chemical properties of materials.[195] Time-of-flight secondary ion mass spectrometry (ToF-SIMS) can provide the elemental and molecular compositions of the top 2 – 5 nm of surfaces.[196] Other useful surface analytical methods include X-ray photoelectron spectroscopy (XPS), spectroscopic ellipsometry (SE), X-ray emission spectroscopy (XES), and near ambient pressure XPS (NAP-XPS).[100, 197-200] Each of these techniques was specifically developed to probe surfaces and serve as workhorses for research as well as quality control in both academic and industrial settings.[100] These techniques have the power to probe either a few nanometers into a material and/or a few nanometers laterally on a surface.[100] These capabilities allow researchers to understand surface processes at the molecular level. It is reasonable to expect that the importance of these techniques will grow in the future.[100]

1.4 Spectroscopic Ellipsometry[201]

SE is a generally a non-destructive method used for obtaining data about surfaces and materials, e.g., their thickness, surface roughness, composition, crystallinity, and refractive index. SE is quick and can operate in most environments, including under vacuum and at ambient conditions. In an SE analysis, a light source with known polarization is simply directed onto a surface of interest, and the light reflected back is analyzed for changes in both intensity and polarization. From these changes a plethora of information can be determined about a surface.

1.4.1 Theory

The theory of SE is based on the measurement of polarization changes in light that take place when it is reflected off of or transmitted through a surface. In particular, in SE, a polarized beam of light is directed onto a surface. This light source can be viewed as consisting of two perpendicular components: a "p" polarized component with an electric field that is perpendicular to the plane of incidence, and an "s" polarized component with an electric field that is parallel to the plane of incidence. Ellipsometry then measures the polarization and amplitude changes that take place when this light is reflected off of or transmitted through a surface via psi (Ψ) and delta (Δ) in ***Equation 1***, which is the fundamental equation of ellipsometry.

$$\textbf{(1)} \qquad \rho = \frac{\tilde{r}_p}{\tilde{r}_s} = tan\Psi e^{-i\Delta}$$

Ultimately, by measuring the polarization state of the light that reflects off of a surface, we can determine many of its properties, including film thicknesses, film and substrate optical constants, surface roughness, interfacial mixing, material composition, degree of material crystallinity, material anisotropy, and film uniformity. A simple representation of an ellipsometer is depicted in Figure 1-1.

Ellipsometry centers around how light interacts with matter, specifically with surfaces. Light is a transverse, electromagnetic wave that consists of an electric field perpendicular to a magnetic field. Some of light's important characteristics are its energy (seen as its color or frequency), intensity (a measure of its electric field strength), and finally its polarization, i.e., the shape of its electric field. ***Equation 2*** defines a beam of light traveling in the z-direction with electric field components in the x and y directions.

$$\textbf{(2)} \qquad \vec{E} = \vec{E}_x + \vec{E}_y = \hat{x}E_{x0}e^{i\delta_x} + \hat{y}E_{y0}e^{i\delta_y}$$

When the electric field components of all the light in a beam are in the same direction, the light is said to be linearly polarized. Circularly polarized light consisted of light with equal amplitudes in the x and y directions, but where the phases of these waves are 90° apart. More generally, elliptically polarized light has arbitrary amplitudes and phases in the x and y directions.

Equation 3 shows how the beam of light in ***Equation 2*** can be represented as a vector called the Jones vector.

$$\textbf{(3)} \qquad \begin{bmatrix} E_x \\ E_y \end{bmatrix} = \begin{bmatrix} E_{x0}e^{i\delta_x} \\ E_{y0}e^{i\delta_y} \end{bmatrix}$$

The Jones vector system works only when the light is completely polarized when it reflects from the surface of a sample. Here, interactions/reflections of this polarized light on the surface are represented by a matrix acting on the incoming beam (E_x^{in} and E_y^{in}) and transforming it into an exiting beam with different polarizations (E_x^{out} and E_y^{out}), as shown in ***Equation 4*,** the Jones matrix. Optical elements that change the polarization state of light can be quantified/described using different Jones matrices.

$$(4)\qquad \begin{bmatrix} E_x^{out} \\ E_y^{out} \end{bmatrix} = \begin{bmatrix} j_{xx} & j_{xy} \\ j_{yx} & j_{yy} \end{bmatrix} \begin{bmatrix} E_x^{in} \\ E_y^{in} \end{bmatrix}$$

To fully describe light in SE, including when it is depolarized, the Stokes vector is employed (***Equation 5***). This vector consists of 4 intensity values that can completely describe the polarization state of any light beam.

$$(5)\qquad \vec{S} = \begin{bmatrix} S_0 \\ S_1 \\ S_2 \\ S_3 \end{bmatrix} = \begin{bmatrix} E_{ox}^2 + E_{oy}^2 \\ E_{ox}^2 - E_{oy}^2 \\ 2E_{ox}E_{oy}cos\delta \\ 2E_{ox}E_{oy}sin\delta \end{bmatrix}$$

The interaction of light with a surface is then defined through a Mueller matrix (***Equation 6***).

$$(6)\qquad \begin{bmatrix} S_{0\,out} \\ S_{1\,out} \\ S_{2\,out} \\ S_{3\,out} \end{bmatrix} = \begin{bmatrix} m_{11}m_{12}m_{13}m_{14} \\ m_{21}m_{22}m_{23}m_{24} \\ m_{31}m_{32}m_{33}m_{34} \\ m_{41}m_{42}m_{43}m_{44} \end{bmatrix} \bullet \begin{bmatrix} S_{0\,in} \\ S_{1\,in} \\ S_{2\,in} \\ S_{3\,in} \end{bmatrix}$$

That is, the Mueller matrix represents the optical properties of the matter with which the light interacts. The index of refraction, n, of a material defines the speed of light in that material, and the extinction coefficient, k, defines the degree to which the material absorbs the light. The optical constants of a material are a function of the wavelength of light, λ, and as such, are represented as n(λ) and k(λ) to show this dependence. The optical constants of a material are often represented together as a complex number, the complex refractive index **(*Equation 7*)**, which is mathematically related to the complex dielectric function **(*Equation 8*)**.

$$(7)\qquad \tilde{n} = n - ik$$

$$(8)\qquad \tilde{\varepsilon} = \varepsilon_1 - i\varepsilon_2 = \tilde{n}^2$$

It is important to note that the optical constants, n and k, of a material are dependent on each other and as such, cannot be varied independently. The mathematical relationship between n an k is the Kramers-Kronig relationship. Optical constants that obey this equation are fully physically viable/meaningful. In the parlance of ellipsometry, they are said to be “K-K consistent”. A pictorial depiction of the Kramers-Kronig relationship is given in Figure1-2. This figure shows that if there is absorption in a material, i.e., if k or ε_2 shows a peak, there is a corresponding change in n or ε_1. Absorptions result when dipoles in a material interact with an electromagnetic wave, i.e., light. Moreover, these interactions occur at different frequencies. For example, infrared light may excite vibrations in materials, ultraviolet and visible light may excite electrons to higher energy orbitals, and free electrons in metals may interact directly with light.

When light enters a medium with a different index of refraction, its velocity changes but its frequency stays the same. As a result, its wavelength must change, which causes light to refract. A change in refractive index also results in light being reflected from a material. For light impinging on a plane at an oblique angle of incidence, the angle of incidence, θ_i, is equal to the angle of reflection, θ_r. Snell’s law (***Equation 9***) describes the refraction of light as it passes from one medium (1) into a different medium (2).

$$\textbf{(9)} \qquad \tilde{n}_1 sin\emptyset_1 = \tilde{n}_2 sin\emptyset_2$$

The polarized light used for SE is divided into two components, as shown in Figure 1-3. The s component is parallel to the surface of a sample, and the p component is perpendicular to the same surface. More specifically, the p component lies in the ‘plane of incidence’ of the sample, which is defined by the incoming and reflected light beams and the surface normal. Thus, the Jones matrix formulation for SE is written as Equation 10:

$$\textbf{(10)} \qquad \begin{bmatrix} E_p^{out} \\ E_s^{out} \end{bmatrix} = \begin{bmatrix} j_{pp} & j_{ps} \\ j_{sp} & j_{ss} \end{bmatrix} \begin{bmatrix} E_p^{in} \\ E_s^{in} \end{bmatrix}$$

The Fresnel equations (*Equations 11 - 14*) provide a detailed description of the interaction of light with a material, e.g., its reflection, r, and transmission, t, as a function of its polarization state (s or p).

(11) $$\tilde{r}_p = \frac{E_{rp}}{E_{ip}} = \frac{n_t \cos\theta_i - n_i \cos\theta_t}{n_t \cos\theta_i + n_i \cos\theta_t}$$

(12) $$\tilde{r}_s = \frac{E_{rs}}{E_{is}} = \frac{n_i \cos\theta_i - n_t \cos\theta_t}{n_i \cos\theta_i + n_t \cos\theta_t}$$

(13) $$\tilde{t}_p = \frac{E_{tp}}{E_{ip}} = \frac{2 n_i \cos\theta_i}{n_t \cos\theta_i + n_i \cos\theta_t}$$

(14) $$\tilde{t}_s = \frac{E_{ts}}{E_{is}} = \frac{2 n_i \cos\theta_i}{n_i \cos\theta_i + n_t \cos\theta_t}$$

The Fresnel coefficients ($\tilde{r}_p$, $\tilde{r}_s$, $\tilde{t}_s$, and $\tilde{t}_p$) are solutions to Maxwell's equations at a boundary between two materials and they describe the reflection and refraction of polarized light. As seen here, the Fresnel coefficients depend on n(λ) and k(λ) for a material. In ellipsometry, the ratio of the complex Fresnel coefficients is measured, which describes the change in polarization state of the reflected light. As shown in Figure 1-4, in these equations, Δ is the phase change of the components of the light, and Ψ is a measure of the ratio of amplitudes.

For data collection in SE, Ψ and Δ are measured and analyzed; and from the Ψ and Δ components, the optical constants n(λ) and k(λ), and thicknesses of materials can be quantified. Nevertheless, in thin film measurements there are also multiple reflections and accordingly there is no simple relationship between Ψ/Δ, n and k, and thickness. This results in an 'inverse' problem with SE, meaning that in order to determine thicknesses and optical properties of materials, regression models must be created to best match/fit experimentally determined Ψ and Δ values. Despite this limitation, data collection with SE has an inherent advantage because it measures a ratio of two values to obtain Ψ and Δ. Thus, results are not affected by diffuse scattering caused by dust, rough surfaces, or pinholes, and results are not affected by fluctuating or low light levels, except to the degree that they influence the signal-to-noise ratio of the data. Thus SE measurements are more accurate and reproducible, no reference is needed, and the whole light beam does not have to be collected. Additionally, because SE measures two quantities at each wavelength (Ψ and Δ), two unknowns can be determined per wavelength. Spectroscopic ellipsometry is performed at multiple wavelengths, which increases the number of data points that can be collected. Furthermore, because the data consists of Ψ and Δ as a function of wavelength, the number of data points collected at one time is large. Finally, the data can be collected from a sample at multiple angles of incidence, which further increases the amount of data available for material analyses.

1.4.2 Data Analysis

While SE data collection often only takes a few minutes, its proper analysis/work-up may take hours, days, or more. Figure 1-5 shows the general strategy for modeling SE data. After collecting the data, one creates a model. The model needs to represent the appropriate materials, layers, roughness values, etc. of the surface/material being measured. That is, each of the layers needs an approximate thickness, along with a set of accompanying optical constants. Layers can be fully or partially transparent. In general, instrument software packages contain files with the optical constants of different materials, which are useful starting points for these data analyses. Optical constants of materials are also found in the scientific literature and databases. After a stack is created/modeled, the instrument software generates Ψ(λ) and Δ(λ) values, and these are compared to the experimental values. Finally, parameters in the model are varied to minimize the difference between the modeled and experimental Ψ(λ) and Δ(λ) values. This process is repeated iteratively as shown in the general strategy for fitting in Figure 1-5.

As alluded to above, SE fitting often requires the determination of the optical constants of the materials being analyzed. This is often done by using dispersion models, which are parameterized functions that model optical constants in either an empirical or K-K consistent way. This is a standard approach that has a variety of advantages. It allows better flexibility in data fitting – one is not restricted to literature optical constants. In addition, these models are often based on a small number of parameters and are, therefore, insensitive to small amounts of noise. The Cauchy and Sellmeier dispersion models, which are given in *Equations 15* and *16*, respectively, are widely used to model transparent materials.

$$\textbf{(15)} \quad \boldsymbol{n = A + \frac{B}{\lambda^2} + \frac{C}{\lambda^4}}$$

$$\textbf{(16)} \quad \boldsymbol{n^2 = 1 + \frac{A_1\lambda^2}{\lambda^2 - {\lambda_1}^2} + \frac{A_2\lambda^2}{\lambda^2 - {\lambda_2}^2}}$$

Transparent materials have what is called a Brewster angle. This is the angle at which none of the p-polarized light is reflected from the sample (it is all transmitted) so the value of Ψ becomes zero here. In general, analytical measurements are more sensitive when there are large changes in a signal as opposed to smaller ones. Accordingly, it is advantageous to collect data near the Brewster angle of materials. Figure 1-6 shows a plot of the reflectance of the p- and s-polarized light from a material as a function of the angle of incidence of the light. Note where the reflectance of the p-polarized light goes to zero in this plot. The shaded area around this point is generally good for data collection. For absorbing films and substrates, many different oscillators/dispersion models such as the Gaussian, Lorentzian, Tauc-Lorentz, Cody-Lorentz, and Drude models are used to model the data. Another basic model that can be used as a starting point (or the end point) for modeling the optical properties of materials is the B-spline.

Because of the many different types of materials that can be deposited as thin films, and the many different ways/formats this can be done, other analytical methods have been developed that can aid in SE data analysis. One of these is referred to as a multi-sample analysis (MSA). In an MSA, data from multiple, similar samples are analyzed together. For example, an MSA may consist of an analysis of multiple measurements from different thicknesses of the same film on the same substrate or alternatively from the same film, perhaps with the same thickness in each case, on different substrates. With this technique, a model that is more representative of a set of samples can be derived and the parameters driving that model are optimized. MSAs have the advantage of reducing fit parameter correlation and even allowing additional parameters to be considered in a model – an MSA often yields a more robust model than the analysis of a single sample. Real time (in situ) analyses of a film deposition or of a sample that changes with time can also generate the data sets for MSAs. For example, one might follow/monitor the growth of a film in an atomic layer deposition process, or one may observe the oxidation of a metal film as a function of time. These processes will change the thicknesses of layers and/or the optical constants of the materials themselves.

Many thin film samples contain multiple layers (stacks). One strategy for studying these films by SE is to deposit the different films in the stack separately as single films on a substrate. The individual layers are then analyzed to determine their optical constants. The optical constants from the single layers are then used to model the individual layers in multilayer stacks. An advantage of this approach is that it reduces the number of parameters needed to model the final material because a large number of fit parameters in a model can result in fit parameter correlation.

This method is represented in Figure 1-7. In a second strategy, the first layer in the stack is deposited and measured by SE, after which its optical constants and thickness are determined and fixed. The second layer is then deposited over the first, and its optical properties/thickness are similarly determined and fixed. This approach is then continued for additional layers in the stack, as represented in Figure 1-8. Using these techniques as well as the general iterative analytical model presented in Figure 1-5, SE models ranging from very simple to advanced can be created to fit collected data.

It is important to have criteria and/or figures of merit for evaluating the quality of a fit. While not quantitative, a visual evaluation of a fit (the so-called 'chi-by-eye' method) can be a very important starting point for understanding a model. That is, it is common to begin by trying to determine the general quality of a fit by eye, looking for any significant discrepancies between the results of the model and the experimental data. Quantitative measures of the quality of a fit are also very important. In SE, the mean squared error (MSE) is often used for this purpose. It is based on the difference between the experimentally determined and modeled values of $\Psi(\lambda)$ and $\Delta(\lambda)$. If a fit is poor, as determined by visual inspection or the MSE value, additional parameters or layers may need to be added to a model and/or it may need to be entirely revised. When this exercise is completed, the model parameters are evaluated for correlation. This can be performed with a uniqueness plot, in which the MSE for a model is repeatedly determined for one of the parameters in the model as it is varied. If there is fit parameter correlation, i.e., the MSE stays about the same over the specified range, the model is not unique, and another modeling scheme should be considered.

In the end, SE analysis can provide reliable and valuable data for film thicknesses, roughness, and optical constants, as well as other surface and material properties that are not as relevant to this work. However, it is important to recognize that SE is rarely able to provide a complete understanding of a surface or a material by itself. The combination of SE with other analytical techniques, i.e., a multi-instrument analysis of a material, is an important and more advanced approach for understanding the structures and properties of surfaces. I will now discuss another analytical technique that can be combined with SE to give significantly more information about surfaces.

1.5 XPS

X-ray photoelectron spectroscopy (XPS) is a surface analytical technique that is based on the photoelectric effect. In XPS, the kinetic energies (KEs) of the core electrons ejected from a sample by X-rays of a known energy are measured. Using the energies of the X-ray source, the KEs of the photoelectrons, and the work function of the instrument, binding energies (BEs) are calculated for the photoelectrons, which determine the elements present at a surface. That is, BE values are unique and reproducible (to within a few eV) for each element. The chemical composition, e.g., whether an atom is oxidized or attached to another more electropositive or electronegative atom, causes changes in the BE of a sample. These changes are referred to as 'chemical shifts'. Chemical shifts can be extremely important for understanding materials. XPS is very surface sensitive. It probes about 5 – 10 nm into materials. XPS is also quantitative. For these reasons, XPS has become one of the most widely used techniques to analyze surface chemical composition.

1.5.1 Theory

When an X-ray with an energy greater than the binding energy of a core electron for a certain element is directed onto a surface with that element, that core electron can be ejected. This process is referred to as photoemission and the ejected electron is referred to as a photoelectron. After ejection, the photoelectron is guided by an electrostatic lens system into a hemispherical analyzer, which consists of two concentric, biased hemispheres (Figure 1-9).[202] The lenses retard the photoelectrons to a focused energy value ($\boldsymbol{E_i}$), and toggle the entry slit bias energy ($\boldsymbol{V_i}$) such that they enter the hemispherical analyzer with a constant energy referred to as the pass energy ($\boldsymbol{PE}$). The relationship between these values is given in Equation 1:

(17) $\boldsymbol{E_i - eV_i = PE}$ [202]

During data collection for spectral analysis, the operator sets a specific range of interest for probing. Here, V_i, the inner hemispherical ring voltage (V_{in}), and the outer hemispherical ring voltage (V_{out}) are varied to ensure that the electrons being collected travel along the equipotential plane (R_o) to the exit slit for analysis at the detector. However, the relationship of the R_o plane to V_i, V_{in}, and V_{out} does not only depend on the bias voltages applied, but on the inner and outer radii of the hemispherical rings as well. The relationship of the PE to each of these components for the hemispherical analyzer is shown in Equation 18:

(18) $\boldsymbol{(V_{out} - V_{in}) = \frac{PE}{e}\left(\frac{R_{out}}{R_{in}} - \frac{R_{in}}{R_{out}}\right)}$ [202]

where R_{in} and R_{out} are the inner and outer radii of the analyzer respectively, (V_{out}-V_{in}) is the potential difference between the two hemispheres, and $\boldsymbol{\frac{PE}{e}}$ is the KE of the electrons of interest. Thus, XPS data collection is driven by mathematical relationships between the analyzer dimensions, voltages applied, and core electron KEs. However, the mathematical relationships do not stop here. When the photoelectron is ejected from a sample, the BE is not directly measured, instead, the KE of the ejected core electron is measured as presented above. The key equation that explains this phenomenon is:

$$\textbf{(19)}\quad \mathbf{E_{X\text{-}ray} = h\nu = BE_{sample} + KE_{spec} + \Phi_{spec}}$$

Here, $E_{X\text{-}ray}$ (or hν) is the energy of the incident X-ray, which is very often an Al K_α X-ray in conventional standalone instruments, BE_{sample} is the binding energy of the sample, Φ_{spec} is the work function of the spectrometer, and KE_{spec} is the kinetic energy of the electron of interest as measured at the spectrometer (detector). Though this overall equation does not show the KE of the photoelectron as it leaves the sample, nor the work function, Φ, of the sample, it is theoretically correct – this will be discussed below.[203]

It is useful to understand the band theory of materials when performing XPS. When atoms come together to form solids, their orbitals overlap to create bands of orbitals/energy levels. Obviously, the valence electrons of the atoms in a solid will interact to form bands to a greater extent than the core electrons.[203] The formation of semiconductors and insulators results in a filled valence band and an empty conduction band that are separated by a gap with gap energy E_g. Obviously, different materials will have different band gaps. Insulators have large band gaps, which is why, for example, quartz is transparent. Semiconductors have smaller band gaps. There is often sufficient energy available at room temperature to promote a few of their electrons across their gaps. Metals do not have band gaps, $E_g = 0$, which explains their higher electrical and thermal conductivity and also opacity. These differences are illustrated in Figure 1-10.[203] The Fermi (E_F) level of a solid resides between its conduction and valence bands. It is the energy at which there is a 50% probability of finding an electron. In the case of a metal, the Fermi level will be at the top of the valence band. More precisely, the Fermi level will be at the energy of the highest occupied orbital at 0 K. The Fermi level is important in XPS because, in the case of conducting samples, it is the reference point for the work functions of the sample and spectrometer (their Fermi levels align if they are in electrical contact), and also the reference point for the BEs of the photoelectrons measured by the technique. As noted, the energy required to remove an electron from a metal to the vacuum level (E_{vac}) is called the work function of the metal (Φ_{metal}), which can be written $E_{vac} - E_F = \Phi_{metal}$.[203] This relationship is valid for other types of materials as well. Equation 20 summarizes the relationship between the KE of the photoelectron when it leaves the sample sample, the sample's work function, and the BE of the photoelectron:

(20) $\mathbf{E_{X\text{-}ray} = h\nu = BE_{sample} + KE_{sample} + \Phi_{sample}}$[203]

Although this expression looks very similar to the fundamental equation for XPS given in Equation 19 above, it is different in that the KE of the photoelectron at the sample as well as the work function of the sample are present in it. Thus, to determine the KE of the photoelectron at the sample, its work function would also need to be known. It would be impractical for XPS analysis to be required to know the work functions of all samples one might analyze, and, of course, one cannot assume that the work function of a sample will be the same as the work function of the spectrometer. That is, as shown in Figure 1-11, KE_{sample} and KE_{spec} are not generally equal. Note that the E_F values of the sample and the spectrometer are the same in Figure 1-11 (the Fermi levels align), which, again, takes place when the samples are conducting and in electrical contact with the spectrometer.[204] Therefore, by conservation of energy, Equation 21 is obtained:

(21) $\mathbf{KE_{sample} + \Phi_{sample} = KE_{spec} + \Phi_{spec}}$

Thus, to avoid having to know the work function for each sample, the work function of the spectrometer is determined in XPS, which then allows the binding energies of the elements to be determined from the kinetic energies of the photoelectrons measured at the spectrometer (see Equation 22). The work function of the spectrometer is usually about 4 eV.[203]

$$\mathbf{(22)}\ \ \mathbf{BE_{sample} = h\nu - KE_{spec} - \Phi_{spec}}^{203}$$

As noted, these derivations and proofs are valid for conducting samples that are in electrical contact with the spectrometer. However, not all materials are conductive. To measure/analyze insulators by XPS, it is common to use one of the peaks in the spectrum as a standard to which the other peaks are referenced. For example, there are many examples in the Literature of the use of the C 1s signal from adventitious carbon as a reference, where its position is often taken as 285.0 or 284.6 eV.[203] There are, however, some concerns about the validity of this widely applied approach.[202] In addition, insulators generally require the use of an electron "flood" gun to replace the electrons that are ejected by the X-rays during sample illumination. If a flood gun is not used, a positive charge will develop on the sample. Initially, this will cause a shift in the apparent binding energies of the sample, which will ultimately result in signal distortion.

Using the basic principles outlined here, XPS data can be collected in an accurate and reliable fashion from many different types of samples.

1.5.2 Data Analysis

The data collected in XPS narrow scans is very often rich with quantitative chemical information provided by the peak areas and peak shifts of the components in the fits.[13, 33, 34] Accordingly, important decisions that guide research projects, and that can even have significant financial implications, depend on the results from XPS data analyses, i.e., accurate peak fitting is of great importance in XPS.[34, 205] When analyzing XPS data, some basic rules apply: (1) Set an appropriate baseline, (2) Use proper peak shapes to approximate the chemical components of the collected data, (3) Properly constrain the peaks, e.g., FWHM values and area ratios, using information about the sample, including the information given by quantum mechanics (4) Consider data from other techniques (or other XPS analyses) when fitting the spectra, and (5) Minimize the number of fit parameters.[206]

From quantum mechanics, Lorentzians are expected to be the line shapes for XPS signals. However, the peaks that are observed in XPS spectra very often have a significant degree of Gaussian character – in most cases, pure Lorentzians are *not* observed. There are multiple reasons for this. One is that the X-rays will not be perfectly monochromatic – there will be some spread in the energies of the incident X-rays, which will broaden the signals. Another is that the photoelectrons must travel through the spectrometer and are therefore affected by the fields and slits in it, which adds additional broadening to the signal. And finally, sample heterogeneity causes broadening – the line shapes for many polymers and glasses are mostly Gaussian.[34] Ultimately, many of the processes that lead to peak broadening are mathematically consistent with the natural (Lorentzian) line shape being convolved with a Gaussian signal.

A variety of functions (line shapes) are used to model XPS signals. These include pure Lorentzian line shapes, pure Gaussian line shapes, and combinations of Gaussian and Lorentzian functions, where there are different ways that a Gaussian and a Lorentzian can be combined into line shapes that are relevant to XPS. These include the Gaussian-Lorentzian sum function (GLS), the Gaussian-Lorentzian product function (GLP), and the Voigt function, which is the convolution of a Gaussian and a Lorentzian function. Different software packages may offer additional line shapes. Because there are a variety of choices for line shapes in peak fitting, it is important to understand them in some detail to know how they affect a fit.[34] First, the Voigt function is arguably the most accurate shape for much XPS peak fitting because it is the convolution of a Gaussian and a Lorentzian function. However, in the past convolutions were computationally expensive, which created interest in simpler functions, e.g., the GLS and GLP, that might adequately represent the line shapes in XPS. Interestingly, while convolutions can now be done with relative ease on modern computers, the GLS and GLP functions continue to be relevant in XPS data analysis.

The pure Gaussian, G, and pure Lorentzian, L, functions are listed in Equations 23 and 24.

$$\textbf{(23)}\qquad \boldsymbol{G(x;F,E,h) = h * exp\left[-4\ ln2\ \frac{(x-E)^2}{F^2}\right]}$$

$$\textbf{(24)}\qquad \boldsymbol{L(x;F,E,h) = \left[\frac{h}{1+4\frac{(x-E)^2}{F^2}}\right]}$$

Here, h is the height of the function, E is the center positions of the functions, and F is the function width. When contrasting the shapes of the Lorentzian and Gaussian functions, two main differences are apparent: the sharpness of the peaks (the Lorentzian is sharper) and the extent to which the functions extend out (the Lorentzian extends further – it has 'wings'). These differences are illustrated in Figure 1-13.

The GLP and GLS functions are given in Equations 25 and 26, respectively.

$$\textbf{(25)}\qquad \boldsymbol{GLP(x;F,E,m,h) = h \times exp\left[-4\ ln2(1-m)\ \frac{(x-E)^2}{F^2}\right] \times \left[\frac{1}{1+4m\frac{(x-E)^2}{F^2}}\right]}$$

$$\textbf{(26)}\qquad \boldsymbol{GLS(x;F,E,m,h) = h \times (1-m)exp\left[-4\ ln2\ \frac{(x-E)^2}{F^2}\right] + \left[\frac{h \times m}{1+4\frac{(x-E)^2}{F^2}}\right]}$$

Here, all of the variables are the same as in Equations 23 and 24, except for the addition of the mixing parameter m, which varies from 0 to 1 and provides the degree of Lorentzian character in the function, i.e., in each case, m = 0 corresponds to a pure Gaussian and m = 1 corresponds to a pure Lorentzian. Figures 1-13 and 1-14 show GLS and GLP functions with different amounts of Lorentzian character (different values of m). These plots reveal that as m increases, the shape of the GLS moves proportionally towards the Lorentzian line shape, while the m value must be quite high for the GLP to have a Lorentzian shape. That is, the GLP is more compact than the GLS because it is the product of a Gaussian, which goes to zero quickly, and the more extended

Lorentzian function. Both the GLS and GLP have been used in the Literature for fitting XPS spectra, and there has been some discussion/debate about them.[13, 34, 207] Ultimately, it appears that while the GLS function more closely approximates the Voigt function,[207] both functions are of value in XPS peak fitting. In practice, the GLS and GLP are often handled in a somewhat empirical fashion – it is often a good idea to try to fit the data with both kinds of functions, and the function that better fits the data is selected.

Proper constraints on synthetic peaks are important when fitting XPS spectra. One of these is FWHM values. When analyzing a narrow scan with multiple components in different oxidation states, the FWHM values will often be quite similar. An exception here would be when there are metal and oxide signals together, e.g., Al and Al_2O_3 (the signals from the metal will generally be narrower). Unfortunately, peak widths are not always well constrained in fits in the literature.[206] Another important constraint that must be accounted for in XPS peak fitting is spin-orbit splitting. This constraint only applied to peaks from p, d, and f orbitals, not s orbitals. That is, signals from s orbitals always appear as single peaks, but signals from p, d, and f orbitals always come in pairs. The ratio of these peaks is fixed, i.e., there are $2j+1$ electrons are in each state, where the quantum number $j = |l \pm s|$. For example, if the Al 2p signal is analyzed, one will see two peaks: the $2p_{3/2}$ and $2p_{1/2}$ states, that will come in a 2:1 ratio as given by $2*(3/2) + 1 = 4$ and $2*(1/2) + 1 = 2$. There are also many examples in the literature of researchers failing to properly account for spin-orbit splitting.[206]

It is important to have statistical measures for determining the quality of a fit.[34, 206, 208] These may include the chi squared value, the Abbe criterion, and the standard deviation of the residuals to the fit. If possible, it is useful to show the residuals to a fit. Other tools for determining the quality of a fit may include uniqueness plots and various chemometric methods.[34, 207, 209, 210] In the end, it is the goal of the XPS practitioner to develop accurate, reproducible, and quantitative models that can be evaluated statistically.

To fit an XPS narrow scan, a baseline is first applied to the data followed by a set of peaks that approximate the oxidation/chemical states of the material being fit.[33, 34] When placing peaks, proper peak constraints (FWHM, area ratios, etc.) are set as previously discussed.[206] Next, the synthetic peak shapes are chosen and optimized to fit the experimental data. Finally, a goodness-of-fit figure of merit is applied to assess how well the peak model follows the experimental data.[206] These steps are repeated in an iterative fashion, if necessary, to ensure a meaningful analysis. Ultimately, if the operator follows the rules for XPS peak fitting that are outlined here, the technique should prove to be a powerful tool for surface analysis.

1.6 Conclusion

Ultrathin films are key components in many modern technologies. Thus, advances in their synthesis/deposition and control of their growth is paramount to bring our technology to even higher levels. These reasons are an important motivation for continued research in this area.

Metallic surfaces are generally quite reactive with their environments, usually resulting in thin oxide films. For some metals, the presence of an oxide layer is beneficial, and even desirable. However, for the case of aluminum mirrors for space applications, this is not true. Aluminum reflects over an unmatched wavelength range that makes it a highly desirable material for space reflectors, but oxidation limits its full reflective capability, especially at very short wavelengths. Aluminum oxidation can be retarded by depositing transparent MgF_2 protective layers on it. However, aluminum, in general, still oxidizes slowly, even when protected, and MgF_2 coatings that are too thick attenuate the light that the Al might reflect. In my work, I monitored the real-time oxidation of aluminum beneath protective MgF_2 layers. Through this work, an increased understanding of how MgF_2 films retard Al oxidation was obtained, thereby providing information to help optimize and protect future space mirrors.

Inert thin films play a key role in many technical applications such as NEMS/MEMS and in self-cleaning materials. In particular, perfluorocarbon thin-films have gained much interest because of their low-adhesion/low-friction properties. In a number of recent studies, quantitative XPS analyses have not generally matched the theoretical CF_2:CF_3 ratios that would be expected from fluorocarbon adsorbates. In my work, I developed a semi-empirical model for fitting the fluorocarbon portion of C 1s XPS narrow scans by combining information from ab initio calculations with standard practices found in the Literature. My approach gives quite good results. I believe that this approach will prove useful for other researchers.

Silicon dioxide (SiO_2) is an important inorganic thin film with numerous technological applications that include energy storage, surface functionalization, and semiconductors. Because of the great importance of SiO_2, many methods have been used to deposit it in thin film form on a wide variety of substrates, including Eagle XG® glass (EXG). In this dissertation, I show the determination of the optical constants of SiO_2 thin films sputtered on EXG. However, because EXG and SiO_2 have very similar optical constants, a rigorous process of data collection and analysis had to be employed. This process included using variable angle analyses techniques, multi-sample techniques, and proper sample preparation. By following this advanced sampling and analysis scheme, high-quality optical constants from transparent thin-films on a transparent substrate were successfully determined and reported.

An understanding of thin films is of great importance for our modern technology. My work provides novel insights and processes for improving thin film analysis and synthesis.

1.7 Figures

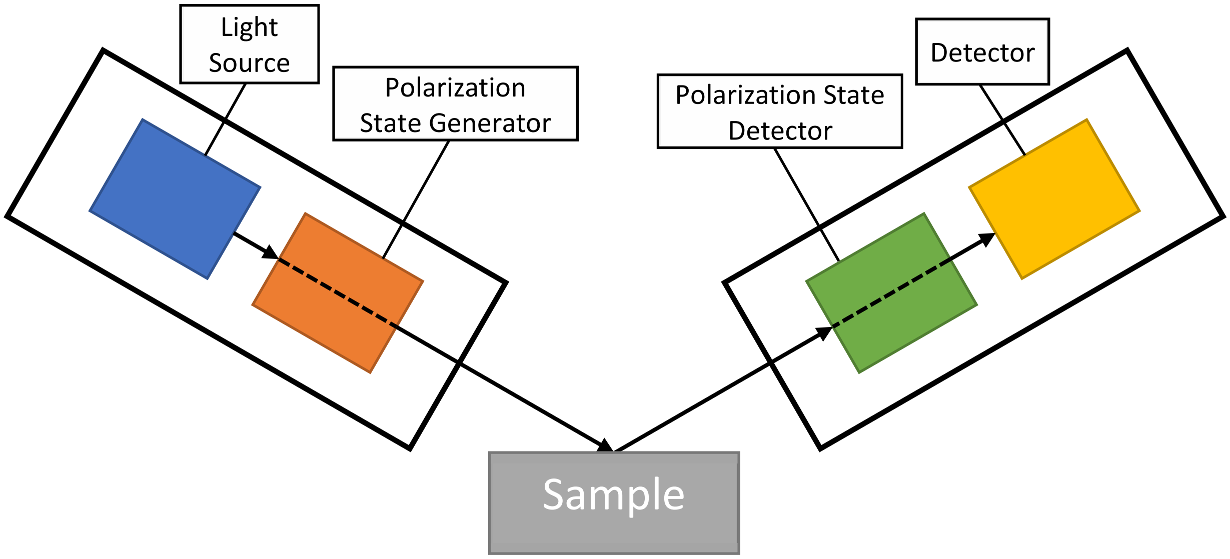

Figure 1-1 Simplified model of an ellipsometer.

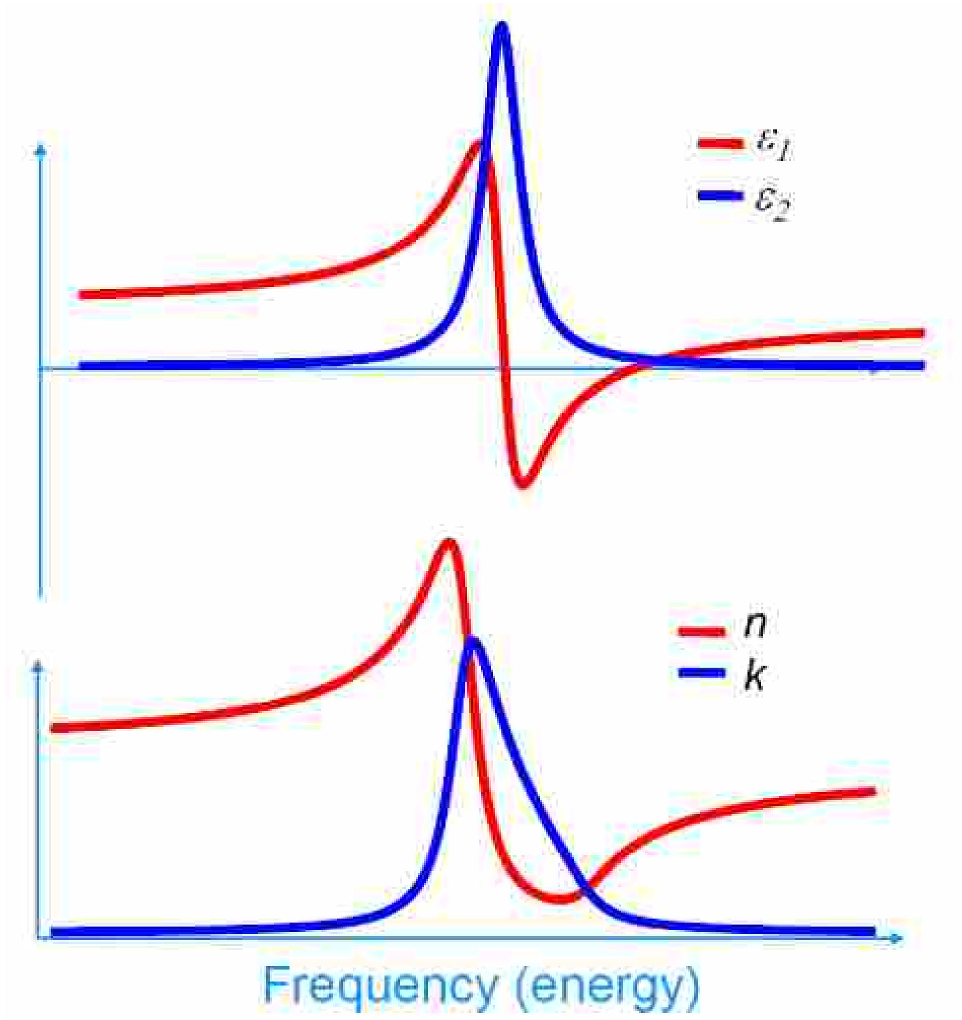

Figure 1-2 Pictorial representation of the Kramers-Kronig relationship. Used with permission from J.A. Woollam Company

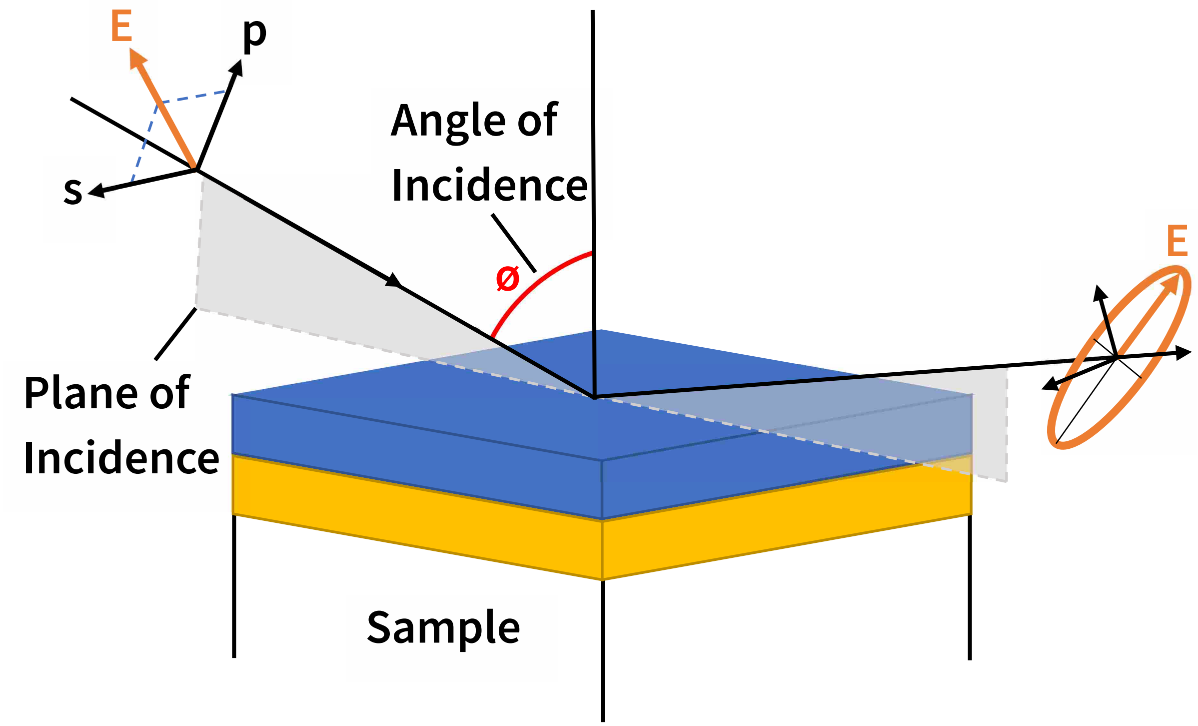

Figure 1-3 Representation of p and s polarized light in the SE experiment. Adapted from Thompkins and Hilfiker Spectroscopic Ellipsometry: Practical Application to Thin Film Characterization[211]

$$\frac{\tilde{r}_p}{\tilde{r}_s} = tan\Psi e^{-i\Delta} = \rho$$

$$\tilde{r}_p = \frac{n_t \cos\theta_i - n_i \cos\theta_t}{n_t \cos\theta_i + n_i \cos\theta_t}$$

$$\tilde{r}_s = \frac{n_i \cos\theta_i - n_t \cos\theta_t}{n_i \cos\theta_i + n_t \cos\theta_t}$$

$$\rho = \frac{\left(\frac{n_t \cos\theta_i - n_i \cos\theta_t}{n_t \cos\theta_i + n_i \cos\theta_t}\right)}{\left(\frac{n_i \cos\theta_i - n_t \cos\theta_t}{n_i \cos\theta_i + n_t \cos\theta_t}\right)}$$

Figure 1-4 Relationship between Fresnel coefficients and Ψ and Δ in SE.

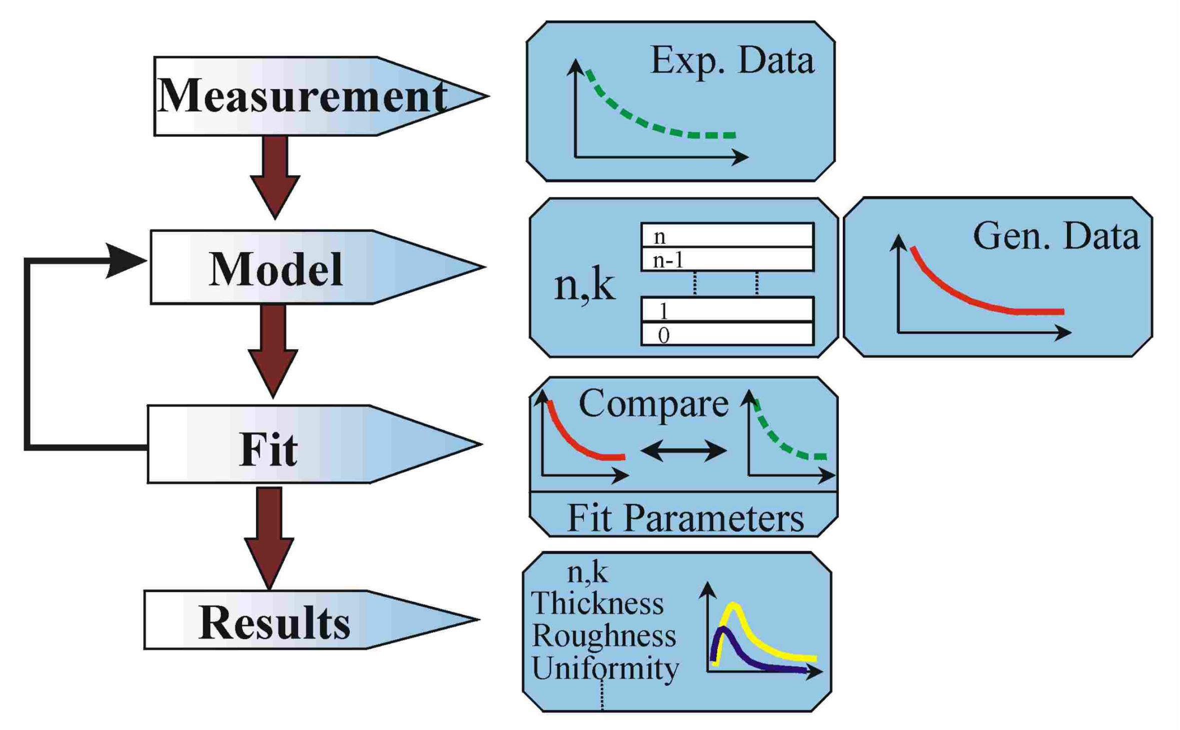

Figure 1-5 General approach to modeling SE data. Used with permission from J.A. Woollam Company

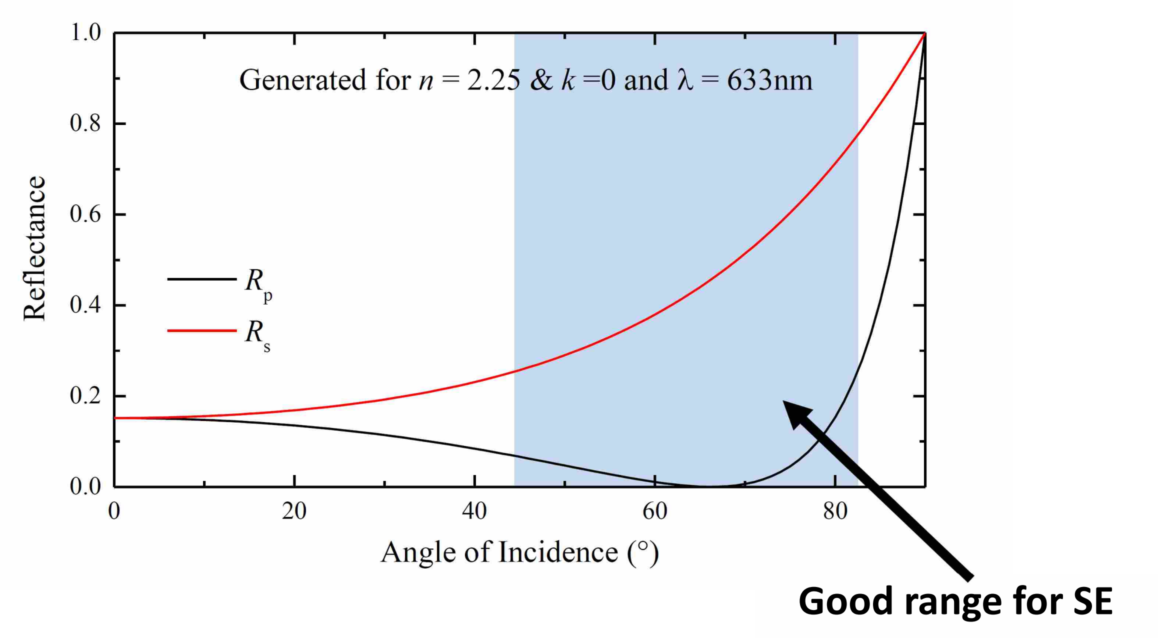

Good range for SE

Figure 1-6 Brewster Angle used for SE Range Selection. Used with permission from J.A. Woollam Company

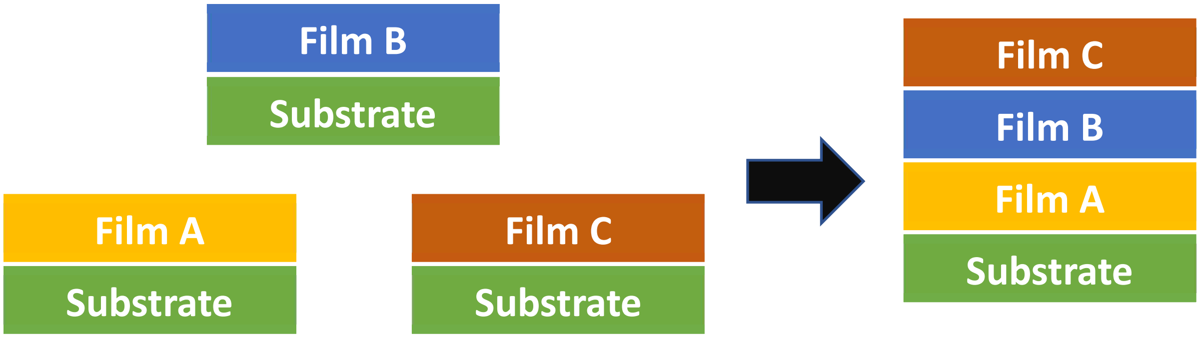

Figure 1-7 General strategy for analyzing multilayer structures, which is to first determine the optical properties of the individual components/layers in them. Adapted from Thompkins and Hilfiker Spectroscopic Ellipsometry: Practical Application to Thin Film Characterization[211]

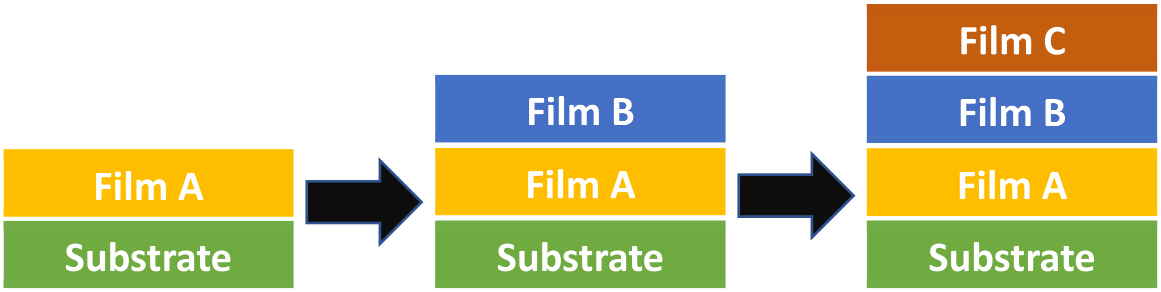

Figure 1-8 General strategy for analyzing multilayer structures, which is to first determine the optical properties of the first layer, then the second layer after its deposition, and so forth. Adapted from Thompkins and Hilfiker Spectroscopic Ellipsometry: Practical Application to Thin Film Characterization[211]

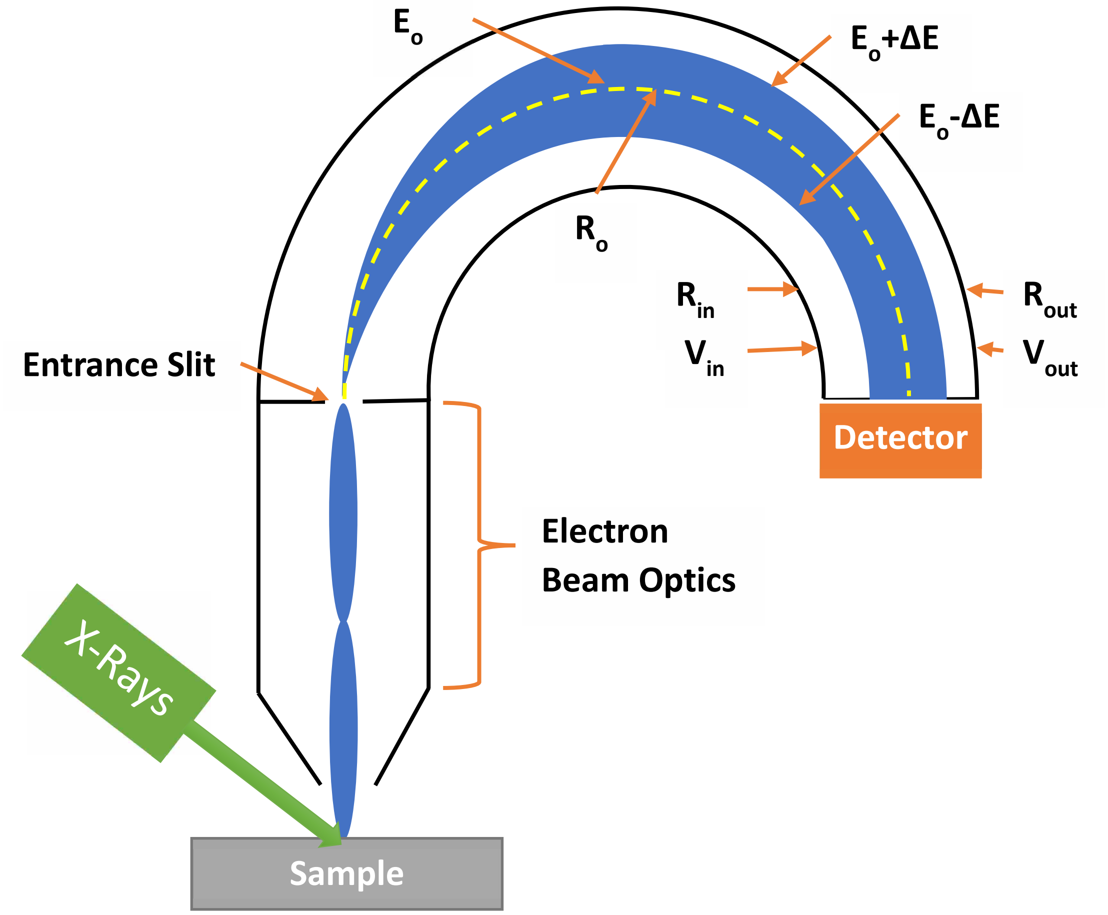

Figure 1-9 Representation of hemispherical analyzer

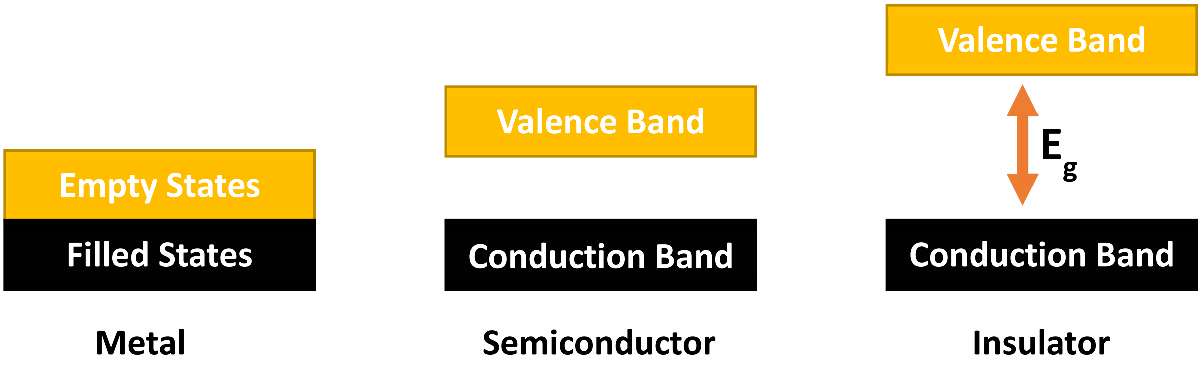

Figure 1-10 Simplified depiction of the band structure of a metal, a semiconductor, and an insulator.

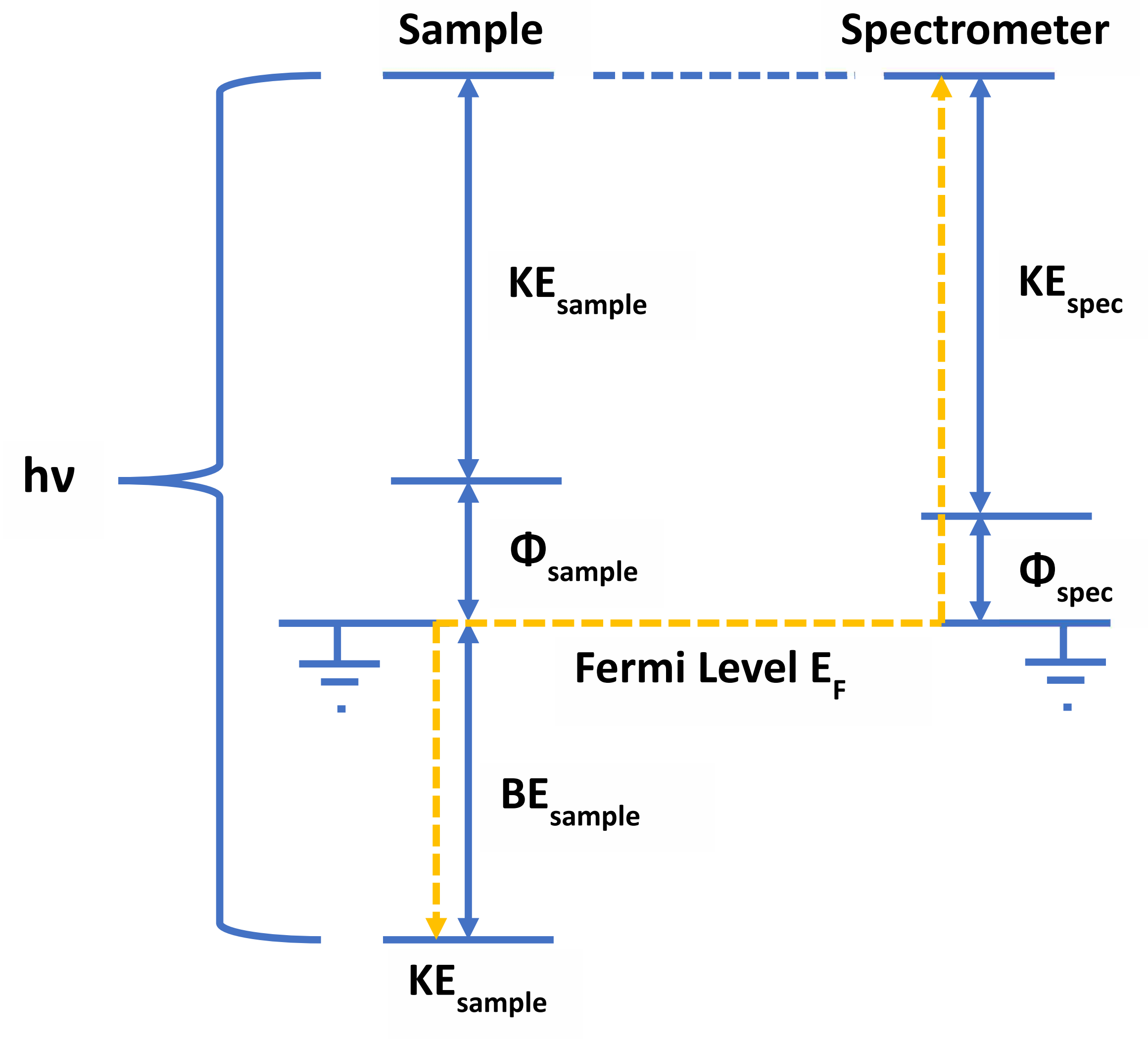

Figure 1-11 Energy level diagram showing a sample and a spectrometer in electrical contact with each other with both grounded and their Fermi levels aligned. The respective sample and spectrometer work functions, Φsample and Φspec, are also shown. In addition, the kinetic energy of a free photoelectron for the sample, KEsample, and the kinetic energy of the photoelectron as measured by the spectrometer, KEspec are shown. The energy of the incident X-ray (hv), is shown to be equal to BEsample + Φsample + KEsample. This diagram is not drawn to scale.

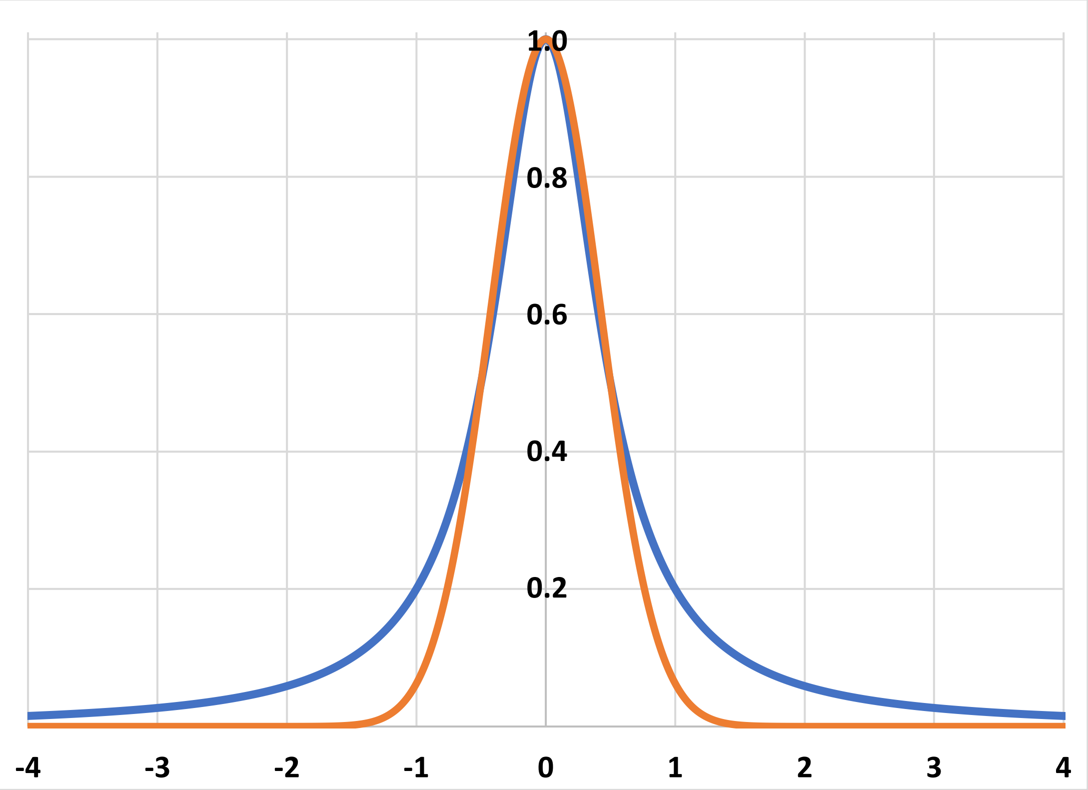

Figure 1-12 ▬ Gaussian function from Eq. (23) with parameters h = 1, E = 0, and F = 1. ▬ Lorentzian from Eq. (24) with parameters h = 1, E = 0, and F = 1.

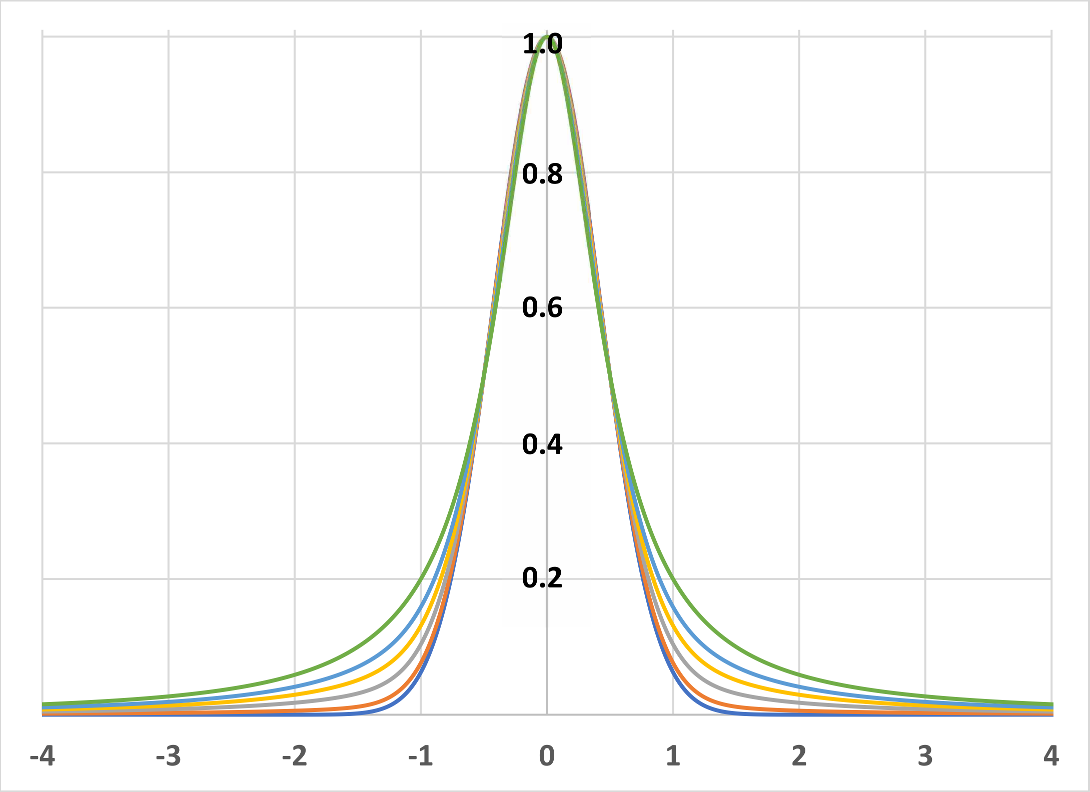

Figure 1-13 Graph of the GLS function (Eq. (26)) with parameters h = 1, E = 0, and F = 1 for (from bottom to top) m = 0, 0.1, 0.3, 0.5, 0.7, and 1.

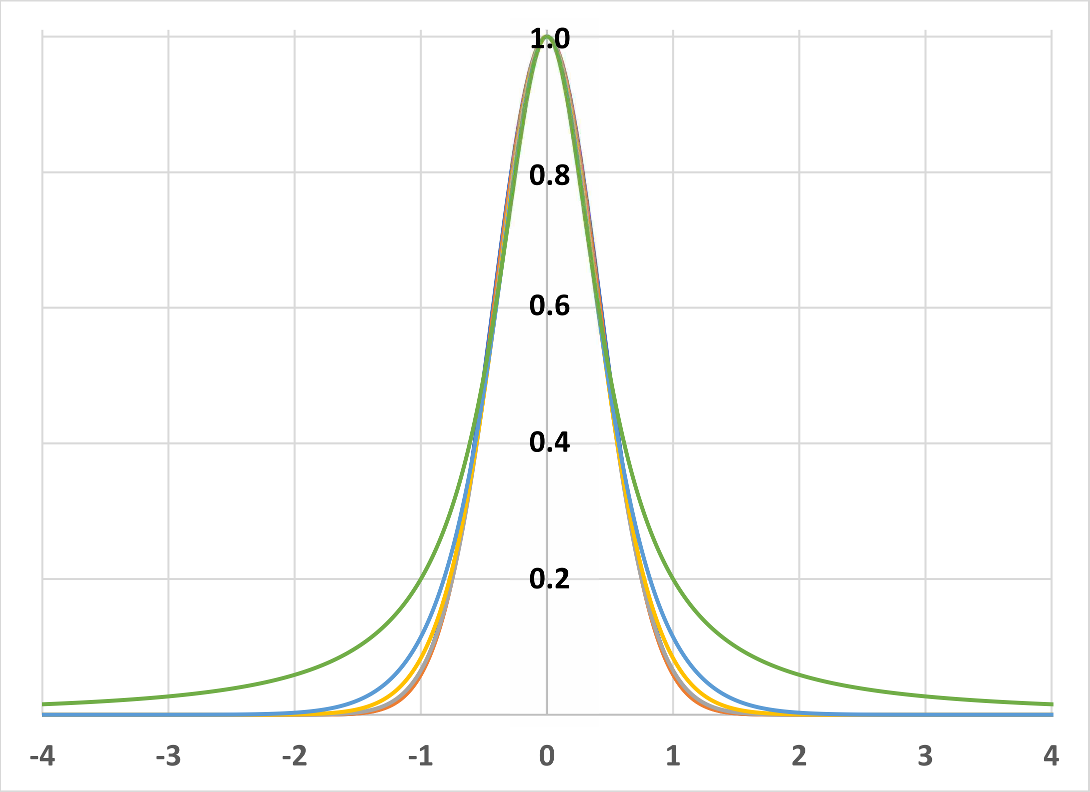

Figure 1-14 Graph of the GLP function (Eq. (25)) with parameters h = 1, E = 0, and F = 1 for (from bottom to top) m = 0, 0.1, 0.3, 0.5, 0.7, and 1.

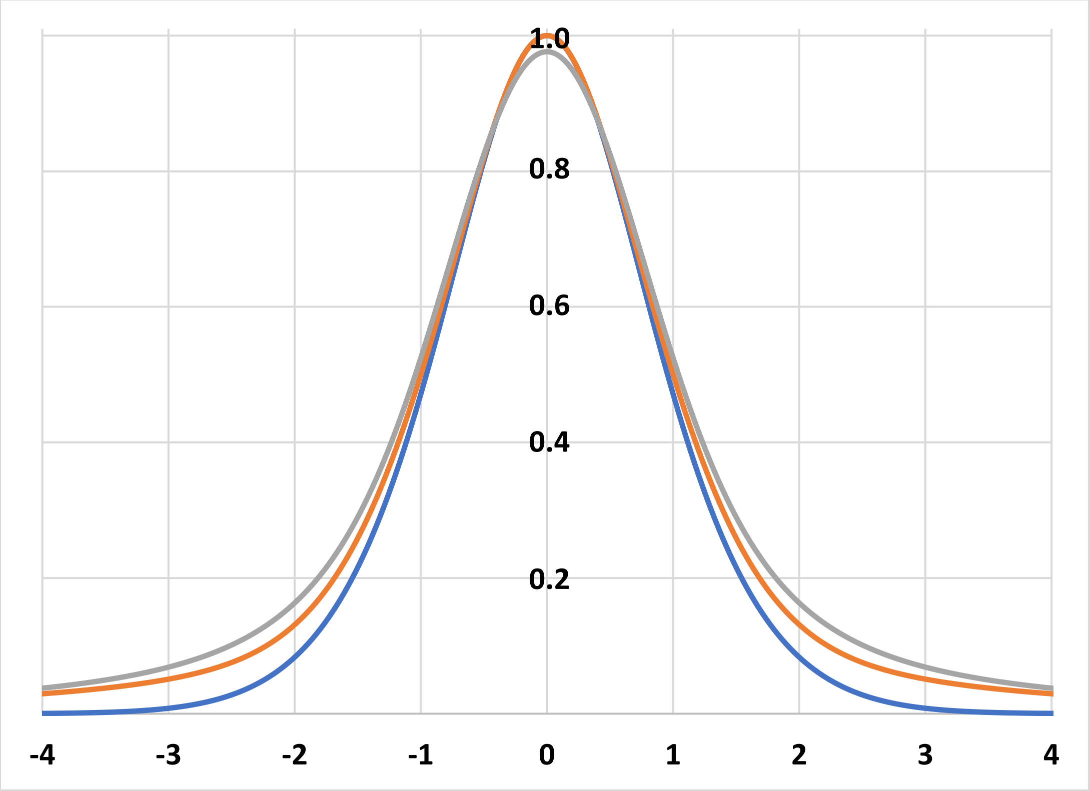

Figure 1-15 Graphs of the GLS function with m = 0.5 (orange line), the GLP function with m = 0.5 (blue line), and the Voigt function (gray line). All three functions have widths of 2 and are centered at the origin. The Voigt function represented here is the convolution of a Gaussian function with a width of 1.3 and a Lorentzian function with the same width. A figure similar to this one previously appeared in paper by Hesse and coworkers.[210]

1.8 References

1. Bertram, M.; Martchek, K. J.; Rombach, G., Material flow analysis in the aluminum industry. *Journal of Industrial Ecology* **2009,** *13* (5), 650-654.

2. Das, S.; Yin, W., Trends in the global aluminum fabrication industry. **2007,** *59* (2), 83-87.

3. Skillingberg, M.; Green, J., Aluminum applications in the rail industry. *LIGHT METAL AGE-CHICAGO-* **2007,** *65* (5), 8.

4. Hass, G.; Tousey, R., Reflecting coatings for the extreme ultraviolet. **1959,** *49* (6), 593-602.

5. Hass, G., Filmed surfaces for reflecting optics. **1955,** *45* (11), 945-952.

6. Bridou, F.; Cuniot-Ponsard, M.; Desvignes, J.-M.; Maksimovic, I.; Lemaire, P. In *VUV mirrors for the (80-120 nm) spectral range*, Advances in Optical Thin Films, International Society for Optics and Photonics: 2004; pp 627-637.

7. Trost, J.; Brune, H.; Wintterlin, J.; Behm, R.; Ertl, G., Interaction of oxygen with Al (111) at elevated temperatures. *The Journal of chemical physics* **1998,** *108* (4), 1740-1747.

8. Brune, H.; Wintterlin, J.; Behm, R.; Ertl, G., Surface migration of ''hot''adatoms in the course of dissociative chemisorption of oxygen on Al (111). *Physical review letters* **1992,** *68* (5), 624.

9. Zhukovskii, Y. F.; Jacobs, P.; Causá, M., On the mechanism of the interaction between oxygen and close-packed single-crystal aluminum surfaces. *Journal of Physics and Chemistry of Solids* **2003,** *64* (8), 1317-1331.

10. Do, T.; McIntyre, N.; Harshman, R.; Lundy, M.; Splinter, S., Application of parallel factor analysis and x-ray photoelectron spectroscopy to the initial stages in oxidation of aluminium. I. The Al 2p photoelectron line. **1999,** *27* (7), 618-628.

11. Fernández-Perea, M.; Larruquert, J. I.; Aznárez, J. A.; Pons, A.; Méndez, J. A., Vacuum ultraviolet coatings of Al protected with MgF 2 prepared both by ion-beam sputtering and by evaporation. **2007,** *46* (22), 4871-4878.

12. Wilbrandt, S.; Stenzel, O.; Nakamura, H.; Wulff-Molder, D.; Duparré, A.; Kaiser, N., Protected and enhanced aluminum mirrors for the VUV. *Applied optics* **2014,** *53* (4), A125-A130.

13. Sherwood, P. M., Curve fitting in surface analysis and the effect of background inclusion in the fitting process. *Journal of Vacuum Science & Technology A: Vacuum, Surfaces, and Films* **1996,** *14* (3), 1424-1432.

14. De Marcos, L. V. R.; Larruquert, J. I.; Méndez, J. A.; Gutiérrez-Luna, N.; Espinosa-Yáñez, L.; Honrado-Benítez, C.; Chavero-Royán, J.; Perea-Abarca, B., Optimization of MgF 2-deposition temperature for far UV Al mirrors. **2018,** *26* (7), 9363-9372.

15. Fateh, B.; Brooks, G. A.; Rhamdhani, M.; Taylor, J.; Davis, J.; Lowe, M., Study of Early Stage Interaction of Oxygen with Al; Methods, Challenges and Difficulties. In *Light Metals 2011*, Springer: 2011; pp 725-730.

16. Lousada, C. M.; Korzhavyi, P. A., First stages of oxide growth on Al (1 1 0) and core-level shifts from density functional theory calculations. *Applied Surface Science* **2018,** *441*, 174-186.

17. Mayer, T. M.; de Boer, M. P.; Shinn, N. D.; Clews, P. J.; Michalske, T. A., Chemical vapor deposition of fluoroalkylsilane monolayer films for adhesion control in microelectromechanical systems. *Journal of Vacuum Science & Technology B: Microelectronics and Nanometer Structures Processing, Measurement, and Phenomena* **2000,** *18* (5), 2433-2440.

18. Ashurst, W. R.; Carraro, C.; Maboudian, R.; Frey, W., Wafer level anti-stiction coatings for MEMS. *Sensors and Actuators A: Physical* **2003,** *104* (3), 213-221.

19. Touhara, H.; Okino, F., Property control of carbon materials by fluorination. *Carbon* **2000,** *38* (2), 241-267.

20. Gnanappa, A. K.; O'Murchu, C.; Slattery, O.; Peters, F.; O'Hara, T.; Aszalós-Kiss, B.; Tofail, S. A., Improved aging performance of vapor phase deposited hydrophobic self-assembled monolayers. *Applied Surface Science* **2011,** *257* (9), 4331-4338.

21. Ferraria, A. M.; da Silva, J. D. L.; do Rego, A. M. B., XPS studies of directly fluorinated HDPE: problems and solutions. *Polymer* **2003,** *44* (23), 7241-7249.

22. Zhang, F.-Y.; Advani, S. G.; Prasad, A. K.; Boggs, M. E.; Sullivan, S. P.; Beebe Jr, T. P., Quantitative characterization of catalyst layer degradation in PEM fuel cells by X-ray photoelectron spectroscopy. *Electrochimica Acta* **2009,** *54* (16), 4025-4030.

23. Pujari, S. P.; Spruijt, E.; Cohen Stuart, M. A.; van Rijn, C. J.; Paulusse, J. M.; Zuilhof, H., Ultralow adhesion and friction of fluoro-hydro alkyne-derived self-assembled monolayers on H-terminated Si (111). *Langmuir* **2012,** *28* (51), 17690-17700.

24. de Boer, M. P.; Knapp, J. A.; Michalske, T. A.; Srinivasan, U.; Maboudian, R., Adhesion hysteresis of silane coated microcantilevers. *Acta Materialia* **2000,** *48* (18-19), 4531-4541.

25. De Vries, J.; Polder, R., Hydrophobic treatment of concrete. *Construction and Building Materials* **1997,** *11* (4), 259-265.

26. Li, Y.; Ren, S., *Building decorative materials*. Elsevier: 2011.

27. Teare, D.; Spanos, C.; Ridley, P.; Kinmond, E.; Roucoules, V.; Badyal, J.; Brewer, S.; Coulson, S.; Willis, C., Pulsed plasma deposition of super-hydrophobic nanospheres. *Chemistry of materials* **2002,** *14* (11), 4566-4571.

28. Busscher, H.; Stokroos, I.; Golverdingen, J.; Shakenraad, J., Adhesion and spreading of human fibroblasts on superhydrophobic FEP-Teflon. *Cells and Materials* **1991,** *1* (3), 5.

29. Hilfiker, J. N.; Singh, N.; Tiwald, T.; Convey, D.; Smith, S. M.; Baker, J. H.; Tompkins, H. G., Survey of methods to characterize thin absorbing films with spectroscopic ellipsometry. *Thin Solid Films* **2008,** *516* (22), 7979-7989.

30. Woollam, J. A.; Johs, B. D.; Herzinger, C. M.; Hilfiker, J. N.; Synowicki, R. A.; Bungay, C. L. In *Overview of variable-angle spectroscopic ellipsometry (VASE): I. Basic theory and typical applications*, Optical Metrology: A Critical Review, International Society for Optics and Photonics: 1999; p 1029402.

31. Fulghum, J. E., Recent developments in high energy and spatial resolution analysis of polymers by XPS. *Journal of electron spectroscopy and related phenomena* **1999,** *100* (1-3), 331-355.

32. Tougaard, S., Improved XPS analysis by visual inspection of the survey spectrum. *Surface and Interface Analysis* **2018,** *50* (6), 657-666.

33. Gupta, V.; Ganegoda, H.; Engelhard, M. H.; Terry, J.; Linford, M. R., Assigning oxidation states to organic compounds via predictions from X-ray photoelectron spectroscopy: a discussion of approaches and recommended improvements. *Journal of Chemical Education* **2013,** *91* (2), 232-238.

34. Jain, V.; Biesinger, M. C.; Linford, M. R., The Gaussian-Lorentzian Sum, Product, and Convolution (Voigt) functions in the context of peak fitting X-ray photoelectron spectroscopy (XPS) narrow scans. *Applied Surface Science* **2018,** *447*, 548-553.

35. Jain, V.; Wheeler, J. J.; Ess, D. H.; Linford, M. R., Poly(γ-Benzyl L-Glutamate) (PBLG), by Near-Ambient Pressure XPS. *Surface Science Spectra* **2019,** *Submitted.*

36. Wu, L.; Cai, L.; Liu, A.; Wang, W.; Yuan, Y.; Li, Z., Self-assembled monolayers of perfluoroalkylsilane on plasma-hydroxylated silicon substrates. *Applied Surface Science* **2015,** *349*, 683-694.

37. Hozumi, A.; Ushiyama, K.; Sugimura, H.; Takai, O., Fluoroalkylsilane monolayers formed by chemical vapor surface modification on hydroxylated oxide surfaces. *Langmuir* **1999,** *15* (22), 7600-7604.

38. Han, L. M.; Timmons, R. B.; Lee, W. W., Pulsed plasma polymerization of an aromatic perfluorocarbon monomer: Formation of low dielectric constant, high thermal stability films. *Journal of Vacuum Science & Technology B: Microelectronics and Nanometer Structures Processing, Measurement, and Phenomena* **2000,** *18* (2), 799-804.

39. Giesbers, M.; Marcelis, A. T.; Zuilhof, H., Simulation of XPS C1s spectra of organic monolayers by quantum chemical methods. *Langmuir* **2013,** *29* (15), 4782-4788.

40. Hehre, W. J., Ab initio molecular orbital theory. *Accounts of Chemical Research* **1976,** *9* (11), 399-406.

41. Yang, X.; Rees, R. J.; Conway, W.; Puxty, G.; Yang, Q.; Winkler, D. A., Computational modeling and simulation of CO2 capture by aqueous amines. *Chemical reviews* **2017,** *117* (14), 9524-9593.

42. Tardio, S.; Cumpson, P. J., Practical estimation of XPS binding energies using widely available quantum chemistry software. *Surface and Interface Analysis* **2018,** *50* (1), 5-12.

43. Kitamura, R.; Pilon, L.; Jonasz, M., Optical constants of silica glass from extreme ultraviolet to far infrared at near room temperature. *Applied Optics* **2007,** *46* (33), 8118-8133.

44. Kanyal, S. S.; Jensen, D. S.; Zhu, Z.; Linford, M. R., Silicon (100)/SiO_2 by ToF-SIMS. *Surface Science Spectra* **2015,** *22* (2), 1-6.

45. Jensen, D. S.; Kanyal, S. S.; Madaan, N.; Hancock, J. M.; Dadson, A. E.; Vail, M. A.; Vanfleet, R.; Shutthanandan, V.; Zhu, Z.; Engelhard, M. H., Multi-instrument characterization of the surfaces and materials in microfabricated, carbon nanotube-templated thin layer chromatography plates. An analogy to 'The Blind Men and the Elephant'. *Surface and Interface Analysis* **2013,** *45* (8), 1273-1282.

46. Tan, G. L.; Lemon, M. F.; French, R. H., Optical properties and London dispersion forces of amorphous silica determined by vacuum ultraviolet spectroscopy and spectroscopic ellipsometry. *Journal of the American Ceramic Society* **2003,** *86* (11), 1885-1892.

47. Herzinger, C.; Johs, B.; McGahan, W.; Woollam, J.; Paulson, W., Ellipsometric determination of optical constants for silicon and thermally grown silicon dioxide via a multi-sample, multi-wavelength, multi-angle investigation. *Journal of Applied Physics* **1998,** *83* (6), 3323-3336.

48. Jensen, D. S.; Kanyal, S. S.; Madaan, N.; Vail, M. A.; Dadson, A. E.; Engelhard, M. H.; Linford, M. R., Silicon (100)/SiO_2 by XPS. *Surface Science Spectra* **2013,** *20* (1), 36-42.

49. Lee, M. V.; Guo, D.; Linford, M. R.; Zuilhof, H., Molecular Modeling of Alkyl Monolayers on the Si (100)− 2× 1 Surface. *Langmuir* **2004,** *20* (21), 9108-9113.

50. Linford, M. R.; Fenter, P.; Eisenberger, P. M.; Chidsey, C. E., Alkyl monolayers on silicon prepared from 1-alkenes and hydrogen-terminated silicon. *Journal of the American Chemical Society* **1995,** *117* (11), 3145-3155.

51. Singh, B.; Diwan, A.; Jain, V.; Herrera-Gomez, A.; Terry, J.; Linford, M. R., Uniqueness plots: A simple graphical tool for identifying poor peak fits in X-ray photoelectron spectroscopy. *Appl. Surf. Sci.* **2016,** *387*, 155-162.

52. Yang, L.; Lua, Y.-Y.; Lee, M. V.; Linford, M. R., Chemomechanical functionalization and patterning of silicon. *Accounts of Chemical Research* **2005,** *38* (12), 933-942.

53. Liao, S.; Zong, X.; Seger, B.; Pedersen, T.; Yao, T.; Ding, C.; Shi, J.; Chen, J.; Li, C., Integrating a dual-silicon photoelectrochemical cell into a redox flow battery for unassisted photocharging. *Nature communications* **2016,** *7*.

54. Faggin, F., The MOS silicon gate technology and the first microprocessors. *Nuovo Cimento Rivista Serie* **2015,** *38*, 575-621.

55. Sadigov, A.; Ahmadov, F.; Ahmadov, G.; Ariffin, A.; Khorev, S.; Sadygov, Z.; Suleymanov, S.; Zerrouk, F.; Madatov, R., A new detector concept for silicon photomultipliers. *Nuclear Instruments and Methods in Physics Research Section A: Accelerators, Spectrometers, Detectors and Associated Equipment* **2015**.

56. Sinha, G.; Yadav, R. K., Optimization of multilayer antireflection coating for visible spectrum on silicon substrate for solar cell application. *Journal of Optical Technology* **2015,** *82* (12), 827-830.

57. Wang, W.; Chen, J. P.; Zivkovic, A. S.; Tanguy, Q. A. A.; Xie, H. K., A Compact Fourier Transform Spectrometer on a Silicon Optical Bench With an Electrothermal MEMS Mirror. *J. Microelectromech. Syst.* **2016,** *25* (2), 347-355.

58. Johnson, B. I.; Cushman, C. V.; Lunt, B. M.; Kaykhaii, M.; Linford, M. R., An Introduction to Silanes, their Chemical Vapor Deposition onto Si/SiO_2, and Characterization of the Resulting Monolayers. *Vacuum Technology & Coating* **2016**.

59. Quast, A. D.; Zhang, F.; Linford, M. R.; Patterson, J. E., Back-Surface Gold Mirrors for Vibrationally Resonant Sum-Frequency (VR-SFG) Spectroscopy Using 3-Mercaptopropyltrimethoxysilane as an Adhesion Promoter. *Applied Spectroscopy* **2011,** *65* (6), 634-641.

60. Husseini, G. A.; Peacock, J.; Sathyapalan, A.; Zilch, L. W.; Asplund, M. C.; Sevy, E. T.; Linford, M. R., Alkyl monolayers on silica surfaces prepared using neat, heated dimethylmonochlorosilanes with low vapor pressures. *Langmuir* **2003,** *19* (12), 5169-5171.

61. Lee, M. V.; Nelson, K. A.; Hutchins, L.; Becerril, H. A.; Cosby, S. T.; Blood, J. C.; Wheeler, D. R.; Davis, R. C.; Woolley, A. T.; Harb, J. N., Nanografting of silanes on silicon dioxide with applications to DNA localization and copper electroless deposition. *Chemistry of Materials* **2007,** *19* (21), 5052-5054.

62. Ali, A. M.; Harraz, F. A.; Ismail, A. A.; Al-Sayari, S. A.; Algarni, H.; Al-Sehemi, A. G., Synthesis of amorphous ZnO-SiO_2 nanocomposite with enhanced chemical sensing properties. *Thin Solid Films* **2016,** *605*, 277-282.

63. Steinegger, P.; Asai, M.; Dressler, R.; Eichler, R.; Kaneya, Y.; Mitsuka, A.; Nagame, Y.; Piguet, D.; Sato, T. K.; Schadel, M.; Takeda, S.; Toyoshima, A.; Tsukada, K.; Turler, A.; Vascon, A., Vacuum Chromatography of TI on SiO_2 at the Single-Atom Level. *J. Phys. Chem. C* **2016,** *120* (13), 7122-7132.

64. Zhao, Y.; Xu, Z.; Wang, X.; Lin, T., Photoreactive azido-containing silica nanoparticle/polycation multilayers: durable superhydrophobic coating on cotton fabrics. *Langmuir* **2012,** *28* (15), 6328-6335.

65. Yi-Qin, J.; Yu-Gang, J.; Hua-Song, L.; Li-Shuan, W.; Dan-Dan, L.; Cheng-Hui, J.; Rong-Wei, F.; De-Ying, C., Optical Constants of SiO_2 Films Deposited on Si Substrates. *Chinese Physics Letters* **2014,** *31* (4), 046401.

66. Jung, H.; Kim, W.-H.; Oh, I.-K.; Lee, C.-W.; Lansalot-Matras, C.; Lee, S. J.; Myoung, J.-M.; Kim, H., Growth characteristics and electrical properties of SiO_2 thin films prepared using

plasma-enhanced atomic layer deposition and chemical vapor deposition with an aminosilane precursor. *Journal of Materials Science* **2016,** *51* (11), 5082-5091.

67. Amirzada, M. R.; Tatzel, A.; Viereck, V.; Hillmer, H., Surface roughness analysis of SiO_2 for PECVD, PVD and IBD on different substrates. *Appl. Nanosci.* **2016,** *6* (2), 215-222.

68. Son, J.; Efremov, A.; Chun, I.; Yeom, G. Y.; Kwon, K. H., On the LPCVD-Formed SiO2 Etching Mechanism in CF4/Ar/O-2 Inductively Coupled Plasmas: Effects of Gas Mixing Ratios and Gas Pressure. *Plasma Chem. Plasma Process.* **2014,** *34* (2), 239-257.

69. Wang, C.; Cho, S. J.; Kim, N. Y., Comparison of SiO_2-based double passivation scheme by e-beam evaporation and PECVD for surface passivation and gate oxide in AlGaN/GaN HEMTs. *Microelectron. Eng.* **2013,** *109*, 24-27.

70. Fang, G.; Xu, L.; Ma, J.; Li, A., Theoretical Understanding of the Reaction Mechanism of SiO_2 Atomic Layer Deposition. *Chemistry of Materials* **2016,** *28* (5), 1247-1255.

71. Choi, H.; Uhm, H. S.; Kwon, G. C.; Cho, B.; Yoo, J., Plasma Enhanced Atomic Layer Deposition of SiO_2 Using Space-Divided Plasma System. *Sci. Adv. Mater.* **2016,** *8* (4), 872-877.

72. Jung, H.; Kim, W. H.; Oh, I. K.; Lee, C. W.; Lansalot-Matras, C.; Lee, S. J.; Myoung, J. M.; Lee, H. B. R.; Kim, H., Growth characteristics and electrical properties of SiO2 thin films prepared using plasma-enhanced atomic layer deposition and chemical vapor deposition with an aminosilane precursor. *Journal of Materials Science* **2016,** *51* (11), 5082-5091.

73. Pfeiffer, K.; Shestaeva, S.; Bingel, A.; Munzert, P.; Ghazaryan, L.; van Helvoirt, C.; Kessels, W. M.; Sanli, U. T.; Grévent, C.; Schütz, G., Comparative study of ALD SiO 2 thin films for optical applications. *Optical Materials Express* **2016,** *6* (2), 660-670.

74. Kesmez, Ö.; Çamurlu, H. E.; Burunkaya, E.; Arpaç, E., Sol–gel preparation and characterization of anti-reflective and self-cleaning SiO 2–TiO 2 double-layer nanometric films. *Solar Energy Materials and Solar Cells* **2009,** *93* (10), 1833-1839.

75. Hinczewski, D. S.; Hinczewski, M.; Tepehan, F.; Tepehan, G., Optical filters from SiO 2 and TiO 2 multi-layers using sol–gel spin coating method. *Solar Energy Materials and Solar Cells* **2005,** *87* (1), 181-196.

76. Fu, S. W.; Chen, H. J.; Wu, H. T.; Shih, C. F., Effect of SiO_2 layers on electroluminescence from Si nanocrystal/SiO_2 superlattices prepared using argon ion beam assisted sputtering. *Vacuum* **2016,** *126*, 59-62.

77. Kim, J. K.; Jeong, S. H.; Oh, S. A.; Moon, S. J.; Imura, K.; Okada, T.; Noguchi, T.; Yun, E. J.; Bae, B. S., Electrical Characteristics of a-IGZO TFTs With SiO_2 Gate Insulator Prepared by RF Sputtering. *J. Disp. Technol.* **2016,** *12* (3), 5.

78. Ikuno, T.; Ogawa, S.; Suzuki, N.; Ito, T.; Sugimoto, N.; Takeda, Y.; Motohiro, T.; Higuchi, K., Resonant tunneling properties of SiO_2/polycrystalline Si/SiO_2 multilayers fabricated by radio-frequency magnetron sputtering. *Journal of Applied Physics* **2015,** *118* (10), 5.

79. Nagata, K.; Ogura, A.; Hirosawa, I.; Suwa, T.; Teramoto, A.; Hattori, T.; Ohmi, T., Structural Analyses of Thin SiO_2 Films Formed by Thermal Oxidation of Atomically Flat Si Surface by Using Synchrotron Radiation X-Ray Characterization. *ECS J. Solid State Sci. Technol.* **2015,** *4* (8), N96-N98.

80. Kageshima, H.; Uematsu, M.; Shiraishi, K., Theory of thermal Si oxide growth rate taking into account interfacial Si emission effects. *Microelectron. Eng.* **2001,** *59* (1-4), 301-309.

81. Tatsumura, K.; Watanabe, T.; Yamasaki, D.; Shimura, T.; Umeno, M.; Ohdomari, I., Large-scale atomistic modeling of thermally grown SiO(2) on Si(111) substrate. *Japanese Journal of Applied Physics Part 1-Regular Papers Brief Communications & Review Papers* **2004,** *43* (2), 492-497.

82. Johnson, B. I.; Cushman, C. V.; Rowley, J.; Lunt, B. M.; Smith, N. J.; Martin, A.; Linford, M. R., Optical constants of SiO2 from 196 to 1688 nm (0.735–6.33 eV) from 20, 40, and 60 nm films of reactively sputtered SiO2 on Eagle XG® glass by spectroscopic ellipsometry. *Surface Science Spectra* **2017,** *24* (2), 026002.

83. Cushman, C. V.; Johnson, B. I.; Martin, A. C.; Lunt, B. M.; Smith, N. J.; Linford, M. R., Eagle XG® glass: Optical constants from 196 to 1688 nm (0.735-6.33 eV) by spectroscopic ellipsometry. *Surface Science Spectra* **2017,** *24* (2), 026001(1)-026001(8).

84. Johnson, B. I.; Hodges, G.; Cushman, C.; Banerjee, J.; Smith, N. J.; Linford, M. R., Appropriate Backside Roughening is Key for Good Spectroscopic Ellipsometry Analysis of Transparent Materials. *Vac Technol Coating* February, 2018, pp 26-30.

85. Diwan, A.; Jensen, D. S.; Gupta, V.; Johnson, B. I.; Evans, D.; Telford, C.; Linford, M. R., Superhydrophobic Surfaces with Very Low Hysteresis Prepared by Aggregation of Silica Nanoparticles During In Situ Urea-Formaldehyde Polymerization. *Journal of nanoscience and nanotechnology* **2015,** *15* (12), 10022-10036.

86. Cushman, C. V.; Brüner, P.; Zakel, J.; Major, G. H.; Lunt, B. M.; Smith, N. J.; Grehl, T.; Linford, M. R., Low energy ion scattering (LEIS). A practical introduction to its theory, instrumentation, and applications. *Analytical Methods* **2016,** *8* (17), 3419-3439.

87. Clarke, S. M.; Friščić, T.; Jones, W.; Mandal, A.; Sun, C.; Parker, J. E., Observation of a two-dimensional halogen-bonded cocrystal at sub-monolayer coverage using synchrotron X-ray diffraction. *Chemical Communications* **2011,** *47* (9), 2526-2528.

88. Sunde, M.; Serpell, L. C.; Bartlam, M.; Fraser, P. E.; Pepys, M. B.; Blake, C. C., Common core structure of amyloid fibrils by synchrotron X-ray diffraction. *Journal of molecular biology* **1997,** *273* (3), 729-739.

89. Lee, M. V.; Lee, J. R.; Brehmer, D. E.; Linford, M. R.; Willey, T. M., Unanticipated C☐ C Bonds in Covalent Monolayers on Silicon Revealed by NEXAFS. *Langmuir* **2009,** *26* (3), 1512-1515.

90. Do, T.; Splinter, S.; Chen, C.; McIntyre, N., The oxidation kinetics of Mg and Al surfaces studied by AES and XPS. **1997,** *387* (1-3), 192-198.

91. Lazić, I.; Thijsse, B. J., An improved molecular dynamics potential for the Al–O system. *Computational Materials Science* **2012,** *53* (1), 483-492.

92. Madaan, N.; Kanyal, S. S.; Jensen, D. S.; Vail, M. A.; Dadson, A. E.; Engelhard, M. H.; Samha, H.; Linford, M. R., Al2O3 e-Beam Evaporated onto Silicon (100)/SiO2, by XPS. *Surface Science Spectra* **2013,** *20* (1), 43-48.

93. Cumpson, P. J., The Thickogram: a method for easy film thickness measurement in XPS. **2000,** *29* (6), 403-406.

94. Iwai, H.; Hammond, J. S.; Tanuma, S., Recent status of thin film analyses by XPS. *Journal of Surface Analysis* **2009,** *15* (3), 264-270.

95. Hill, J.; Royce, D.; Fadley, C.; Wagner, L.; Grunthaner, F., Properties of oxidized silicon as determined by angular-dependent X-ray photoelectron spectroscopy. *Chemical Physics Letters* **1976,** *44* (2), 225-231.

96. Johnson, B. I.; Gholian Avval, T.; Hodges, G.; Membreno, K.; Allred, D. D.; Linford, M. R. In *Real-Time Monitoring of Aluminum Oxidation Through Wide*

Band Gap MgF2 Layers for Protection of Space Mirrors, 2019 25th Annual Fellowship Symposium, Brigham Young University, Utah NASA Space Grant Consortium: Brigham Young University, 2019.

97. Synowicki, R., Suppression of backside reflections from transparent substrates. *Physica Status Solidi (c)* **2008,** *5* (5), 1085-1088.

98. Tompkins, H.; Tiwald, T. In *Spectroscopic Ellipsometry Analysis of Optical Coatings on Transparent Substrates*, Proceedings of the Annual Technical Conference-Society of Vacuum Coaters, 2007; p 354.

99. Benzarti, Z.; Khelifi, M.; Halidou, I.; El Jani, B., Study of Surface and Interface Roughness of GaN-Based Films Using Spectral Reflectance Measurements. *Journal of Electronic Materials* **2015,** *44* (10), 3243-3252.

100. Somorjai, G. A.; Li, Y., Impact of surface chemistry. *Proceedings of the National Academy of Sciences* **2011,** *108* (3), 917-924.

101. Somorjai, G. A.; Li, Y., *Introduction to surface chemistry and catalysis*. John Wiley & Sons: 2010.

102. Ertl, G., *Reactions at solid surfaces*. John Wiley & Sons: 2010; Vol. 14.

103. Haruta, M., New generation of gold catalysts: nanoporous foams and tubes—is unsupported gold catalytically active? *ChemPhysChem* **2007,** *8* (13), 1911-1913.

104. Yates, J. T.; Campbell, C. T., Surface chemistry: Key to control and advance myriad technologies. *Proceedings of the National Academy of Sciences* **2011,** *108* (3), 911-916.

105. Sinfelt, J. H., Role of surface science in catalysis. *Surface Science* **2002,** *500* (1-3), 923-946.

106. Maxted, E. B., Catalysis and its industrial applications. **1933**.

107. Kluksdahl, H. E., Reforming a sulfur-free naphtha with a platinum-rhenium catalyst. Google Patents: 1968.

108. Sutton, E.; Greenwood, A.; Adams, F., New processing concept. Continuous Platforming.[Platforming plant of 20,000 bbl/day]. *Oil Gas J.;(United States)* **1972,** *70* (21).

109. Sinfelt, J.; Cusumano, J., Bimetallic catalysts. *Exxon monograph. Wiley, New* **1983,** *44*.

110. Sinfelt, J. H., Bimetallic catalysts. *Scientific American* **1985,** *253* (3), 90-101.

111. Sinfelt, J., Supported "bimetallic cluster" catalysts. *Journal of Catalysis* **1973,** *29* (2), 308-315.

112. Sinfelt, J. H., Catalysis by alloys and bimetallic clusters. *Accounts of Chemical Research* **1977,** *10* (1), 15-20.

113. Sinfelt, J. H., Structure of bimetallic clusters. *ACCOUNTS of chemical research* **1987,** *20* (4), 134-139.

114. Anastas, P. T.; Kirchhoff, M. M.; Williamson, T. C., Catalysis as a foundational pillar of green chemistry. *Applied Catalysis A: General* **2001,** *221* (1-2), 3-13.

115. Anastas, P. T.; Kirchhoff, M. M., Origins, current status, and future challenges of green chemistry. *Accounts of chemical research* **2002,** *35* (9), 686-694.

116. Somorjai, G. A.; Park, J. Y., Cover Picture: Molecular Factors of Catalytic Selectivity (Angew. Chem. Int. Ed. 48/2008). *Angewandte Chemie International Edition* **2008,** *47* (48), 9161-9161.

117. Langmuir, I., The constitution and fundamental properties of solids and liquids. Part I. Solids. *Journal of the American chemical society* **1916,** *38* (11), 2221-2295.

118. Hinshelwood, C. N., Kinetics of chemical change. **1940**.

119. Emmett, P.; Brunauer, S., The adsorption of nitrogen by iron synthetic ammonia catalysts. *Journal of the American Chemical Society* **1934,** *56* (1), 35-41.

120. Suits, C. G.; Martin, M. J., Irving Langmuir (1881–1957) A Biographical Memoir. *National Academy of Sciences Biographical Memoir* **1974**, 214.

121. Brattain, W. H., Surface properties of semiconductors. *Science* **1957,** *126* (3265), 151-153.

122. Li, J. L.; Liu, X. Y., Architecture of supramolecular soft functional materials: From understanding to micro-/nanoscale engineering. *Advanced functional materials* **2010,** *20* (19), 3196-3216.

123. Goodby, J. W., The nanoscale engineering of nematic liquid crystals for displays. *Liquid Crystals* **2011,** *38* (11-12), 1363-1387.

124. Chen, G.; Yan, L.; Luo, H.; Guo, S., Nanoscale Engineering of Heterostructured Anode Materials for Boosting Lithium-Ion Storage. *Advanced Materials* **2016,** *28* (35), 7580-7602.

125. Banares, M.; Wachs, I., Molecular structures of supported metal oxide catalysts under different environments. *Journal of Raman Spectroscopy* **2002,** *33* (5), 359-380.

126. Over, H.; Seitsonen, A., Oxidation of metal surfaces. *Science* **2002,** *297* (5589), 2003-2005.

127. Davies, S. H.; Morgan, J. J., Manganese (II) oxidation kinetics on metal oxide surfaces. *Journal of Colloid and Interface Science* **1989,** *129* (1), 63-77.

128. Blakely, D.; Kozak, E.; Sexton, B.; Somorjai, G., New instrumentation and techniques to monitor chemical surface reactions on single crystals over a wide pressure range (10− 8–105 Torr) in the same apparatus. *Journal of Vacuum Science and Technology* **1976,** *13* (5), 1091-1096.

129. Strongin, D., The importance of C7 sites and surface roughness in the ammonia synthesis reaction over iron. **1986**.

130. Pena, D. A.; Uphade, B. S.; Smirniotis, P. G., TiO2-supported metal oxide catalysts for low-temperature selective catalytic reduction of NO with NH3: I. Evaluation and characterization of first row transition metals. *Journal of catalysis* **2004,** *221* (2), 421-431.

131. Jiang, H.; Ma, J.; Li, C., Mesoporous carbon incorporated metal oxide nanomaterials as supercapacitor electrodes. *Advanced materials* **2012,** *24* (30), 4197-4202.

132. Liu, S.; Liu, X.; Latthe, S. S.; Gao, L.; An, S.; Yoon, S. S.; Liu, B.; Xing, R., Self-cleaning transparent superhydrophobic coatings through simple sol–gel processing of fluoroalkylsilane. *Applied Surface Science* **2015,** *351*, 897-903.

133. Van Meerbeek, B.; De Munck, J.; Yoshida, Y.; Inoue, S.; Vargas, M.; Vijay, P.; Van Landuyt, K.; Lambrechts, P.; Vanherle, G., Adhesion to enamel and dentin: current status and future challenges. *OPERATIVE DENTISTRY-UNIVERSITY OF WASHINGTON-* **2003,** *28* (3), 215-235.

134. Maboudian, R.; Ashurst, W. R.; Carraro, C., Tribological challenges in micromechanical systems. *Tribology letters* **2002,** *12* (2), 95-100.

135. Tadanaga, K.; Kitamuro, K.; Matsuda, A.; Minami, T., Formation of superhydrophobic alumina coating films with high transparency on polymer substrates by the sol-gel method. *Journal of sol-gel science and technology* **2003,** *26* (1-3), 705-708.

136. Shi, F.; Niu, J.; Liu, J.; Liu, F.; Wang, Z.; Feng, X. Q.; Zhang, X., Towards understanding why a superhydrophobic coating is needed by water striders. *Advanced Materials* **2007,** *19* (17), 2257-2261.

137. Bayer, I.; Tiwari, M.; Megaridis, C., Biocompatible poly (vinylidene fluoride)/cyanoacrylate composite coatings with tunable hydrophobicity and bonding strength. *Applied Physics Letters* **2008,** *93* (17), 173902.

138. McGovern, W. R.; Anariba, F.; McCreery, R. L., Importance of oxides in carbon/molecule/metal molecular junctions with titanium and copper top contacts. *Journal of The Electrochemical Society* **2005,** *152* (5), E176-E183.

139. Dong, D.; Nelson, Y. M.; Lion, L. W.; Shuler, M. L.; Ghiorse, W. C., Adsorption of Pb and Cd onto metal oxides and organic material in natural surface coatings as determined by

selective extractions: new evidence for the importance of Mn and Fe oxides. *Water Research* **2000,** *34* (2), 427-436.

140. Osterholtz, F.; Pohl, E., Kinetics of the hydrolysis and condensation of organofunctional alkoxysilanes: a review. *Journal of Adhesion Science and Technology* **1992,** *6* (1), 127-149.

141. Ingall, M. D.; Honeyman, C. H.; Mercure, J. V.; Bianconi, P. A.; Kunz, R. R., Surface functionalization and imaging using monolayers and surface-grafted polymer layers. *Journal of the American Chemical Society* **1999,** *121* (15), 3607-3613.

142. Pan, Q.; Li, L.; Shaikhutdinov, S.; Freund, H.-J., Planar model system of the Phillips (Cr/SiO2) catalyst based on a well-defined thin silicate film. *Journal of catalysis* **2018,** *357*, 12-19.

143. Ashkenazi, D., How aluminum changed the world: A metallurgical revolution through technological and cultural perspectives. *Technological Forecasting and Social Change* **2019,** *143*, 101-113.

144. Rabinovich, D., The allure of aluminium. *Nature chemistry* **2013,** *5* (1), 76.

145. Gomes, C.; Hernandez, R.; Sequeira, M.; Silva, J., Characterization of clays used for medicinal purposes in the Archipelago of Cape Verde. *Geochimica Brasiliensis* **2012,** *23* (3), 315-331.

146. Butini, E.; Butini, F.; Angle, M.; Cerino, P.; De Angelis, A.; Tomei, N.; Altamura, F., Archaeometric and gemmological analyses of a Roman imperial gold-and-sapphire jewel from Colonna (Rome, Italy). *Measurement* **2018,** *128*, 160-169.

147. Bengtsson Melin, P., For love, healing and protection: notes on Medieval finger rings with sapphires and other gemstones in Swedish collections. **2014**.

148. Fuglesang, S. H., Viking and medieval amulets in Scandinavia. **1989**.

149. Christie, T.; Brathwaite, B.; Thompson, B., Mineral commodity report 1-aluminium. *New Zealand mining* **1993,** *12*, 20-23.

150. Eskin, D. G., *Physical metallurgy of direct chill casting of aluminum alloys*. CRC press: 2008.

151. Habashi, F., From the SelectedWorks of Fathi Habashi. **2018**.

152. Habashi, F., Aluminum, Physical and Chemical Properties. *Encyclopedia of Metalloproteins* **2013**, 57-58.

153. Habashi, F., The Story of Aluminum. *Metal* **2016,** *70*, 343-350.

154. Kumar, V.; Milewski, L., Charles Martin Hall and the great aluminum revolution. *Journal of Chemical Education* **1987,** *64* (8), 690.

155. Osborn, E. L., From bauxite to cooking pots: Aluminum, chemistry, and West African artisanal production. *History of Science* **2016,** *54* (4), 425-442.

156. Schatzberg, E., Symbolic culture and technological change: The cultural history of aluminum as an industrial material. *Enterprise & Society* **2003,** *4* (2), 226-271.

157. Rakić, A. D., Algorithm for the determination of intrinsic optical constants of metal films: application to aluminum. *Applied optics* **1995,** *34* (22), 4755-4767.

158. Ehrenreich, H.; Philipp, H.; Segall, B., Optical properties of aluminum. *Physical Review* **1963,** *132* (5), 1918.

159. Philipp, H.; Ehrenreich, H., Optical Constants in the X-Ray Range. *Journal of Applied Physics* **1964,** *35* (5), 1416-1419.

160. Hagemann, H.-J.; Gudat, W.; Kunz, C., Optical constants from the far infrared to the x-ray region: Mg, Al, Cu, Ag, Au, Bi, C, and Al 2 O 3. *JOSA* **1975,** *65* (6), 742-744.

161. Shiles, E.; Sasaki, T.; Inokuti, M.; Smith, D., Self-consistency and sum-rule tests in the Kramers-Kronig analysis of optical data: applications to aluminum. *Physical Review B* **1980,** *22* (4), 1612.
162. Smith, D.; Shiles, E.; Inokuti, M., The optical properties of metallic aluminum. In *Handbook of optical constants of solids*, Elsevier: 1997; pp 369-406.
163. Crookes, W., II. On electrical evaporation. *Proceedings of the Royal Society of London* **1892,** *50* (302-307), 88-105.
164. Segall, B., Fermi Surface of Aluminum. *Physical Review* **1963,** *131* (1), 121.
165. Boscher, N. D.; Vaché, V.; Carminati, P.; Grysan, P.; Choquet, P., A simple and scalable approach towards the preparation of superhydrophobic surfaces–importance of the surface roughness skewness. *Journal of Materials Chemistry A* **2014,** *2* (16), 5744-5750.
166. Ganesh, V. A.; Raut, H. K.; Nair, A. S.; Ramakrishna, S., A review on self-cleaning coatings. *Journal of Materials Chemistry* **2011,** *21* (41), 16304-16322.
167. Feng, X.; Jiang, L., Design and creation of superwetting/antiwetting surfaces. *Advanced Materials* **2006,** *18* (23), 3063-3078.
168. Cassie, A.; Baxter, S., Large contact angles of plant and animal surfaces. *Nature* **1945,** *155* (3923), 21.
169. Gao, L.; McCarthy, T. J., "Artificial lotus leaf" prepared using a 1945 patent and a commercial textile. *Langmuir* **2006,** *22* (14), 5998-6000.
170. Wenzel, R. N., Resistance of solid surfaces to wetting by water. *Industrial & Engineering Chemistry* **1936,** *28* (8), 988-994.
171. Chen, W.; Fadeev, A. Y.; Hsieh, M. C.; Öner, D.; Youngblood, J.; McCarthy, T. J., Ultrahydrophobic and ultralyophobic surfaces: some comments and examples. *Langmuir* **1999,** *15* (10), 3395-3399.
172. Cassie, A., Contact angles. *Discussions of the Faraday society* **1948,** *3*, 11-16.
173. Bormashenko, E.; Gendelman, O.; Whyman, G., Superhydrophobicity of lotus leaves versus birds wings: different physical mechanisms leading to similar phenomena. *Langmuir* **2012,** *28* (42), 14992-14997.
174. Gao, L.; McCarthy, T. J., A perfectly hydrophobic surface (θA/θR= 180/180). *Journal of the American Chemical Society* **2006,** *128* (28), 9052-9053.
175. Tadanaga, K.; Katata, N.; Minami, T., Super-water-repellent Al2O3 coating films with high transparency. *Journal of the American ceramic society* **1997,** *80* (4), 1040-1042.
176. Shibuichi, S.; Onda, T.; Satoh, N.; Tsujii, K., Super water-repellent surfaces resulting from fractal structure. *The Journal of Physical Chemistry* **1996,** *100* (50), 19512-19517.
177. Sauer, B.; Dee, G., Polymer Surfaces: Thermodynamics. **2001**.
178. Pruitt, L.; Elmaghrum, S., Fluorocarbon polymers in biomedical engineering. **2017**.
179. Kim, S. H.; Asay, D. B.; Dugger, M. T., Nanotribology and MEMS. *Nano today* **2007,** *2* (5), 22-29.
180. Wang, J.; Song, X.; Shen, J.; Yang, G.; Huang, H., Fluorocarbon thin film with superhydrophobic property prepared by pyrolysis of hexafluoropropylene oxide. *Applied Surface Science* **2012,** *258* (24), 9782-9785.
181. Vitale, A.; Bongiovanni, R.; Ameduri, B., Fluorinated oligomers and polymers in photopolymerization. *Chemical reviews* **2015,** *115* (16), 8835-8866.
182. Motamedi, M.; Warkiani, M. E.; Taylor, R. A., Transparent surfaces inspired by nature. *Advanced Optical Materials* **2018,** *6* (14), 1800091.

183. Martinu, L.; Poitras, D., Plasma deposition of optical films and coatings: A review. *Journal of Vacuum Science & Technology A: Vacuum, Surfaces, and Films* **2000,** *18* (6), 2619-2645.

184. Kim, E.; Cho, S. Y.; Yeu, D.-M.; Shin, S.-Y., Low optical loss perfluorinated methacrylates for a single-mode polymer waveguide. *Chemistry of materials* **2005,** *17* (5), 962-966.

185. Sadigov, A.; Ahmadov, F.; Ahmadov, G.; Ariffin, A.; Khorev, S.; Sadygov, Z.; Suleymanov, S.; Zerrouk, F.; Madatov, R., A new detector concept for silicon photomultipliers. *Nuclear Instruments and Methods in Physics Research Section A: Accelerators, Spectrometers, Detectors and Associated Equipment* **2016,** *824*, 135-136.

186. Liao, S.; Zong, X.; Seger, B.; Pedersen, T.; Yao, T.; Ding, C.; Shi, J.; Chen, J.; Li, C., Integrating a dual-silicon photoelectrochemical cell into a redox flow battery for unassisted photocharging. *Nature Communications* **2016,** *7*, 11474.

187. Son, J.; Efremov, A.; Chun, I.; Yeom, G. Y.; Kwon, K. H., On the LPCVD-Formed SiO_2 Etching Mechanism in $CF_4/Ar/O_2$ Inductively Coupled Plasmas: Effects of Gas Mixing Ratios and Gas Pressure. *Plasma Chem. Plasma Process.* **2014,** *34* (2), 239-257.

188. Pfeiffer, K.; Shestaeva, S.; Bingel, A.; Munzert, P.; Ghazaryan, L.; van Helvoirt, C.; Kessels, W. M.; Sanli, U. T.; Grévent, C.; Schütz, G., Comparative study of ALD SiO_2 thin films for optical applications. *Optical Materials Express* **2016,** *6* (2), 660-670.

189. Kesmez, Ö.; Çamurlu, H. E.; Burunkaya, E.; Arpaç, E., Sol–gel preparation and characterization of anti-reflective and self-cleaning SiO_2–TiO_2 double-layer nanometric films. *Solar Energy Materials and Solar Cells* **2009,** *93* (10), 1833-1839.

190. Hinczewski, D. S.; Hinczewski, M.; Tepehan, F.; Tepehan, G., Optical filters from SiO_2 and TiO_2 multi-layers using sol–gel spin coating method. *Solar Energy Materials and Solar Cells* **2005,** *87* (1), 181-196.

191. Tatsumura, K.; Watanabe, T.; Yamasaki, D.; Shimura, T.; Umeno, M.; Ohdomari, I., Large-scale atomistic modeling of thermally grown SiO_2 on Si(111) substrate. *Japanese Journal of Applied Physics Part 1-Regular Papers Brief Communications & Review Papers* **2004,** *43* (2), 492-497.

192. Wu, W.-F.; Chiou, B.-S., Optical and mechanical properties of reactively sputtered silicon dioxide films. *Semiconductor Science and Technology* **1996,** *11* (9), 1317.

193. Jeong, S.-H.; Kim, J.-K.; Kim, B.-S.; Shim, S.-H.; Lee, B.-T., Characterization of SiO_2 and TiO_2 films prepared using rf magnetron sputtering and their application to anti-reflection coating. *Vacuum* **2004,** *76* (4), 507-515.

194. Groner, M.; Fabreguette, F.; Elam, J.; George, S., Low-temperature Al_2O_3 atomic layer deposition. *Chemistry of Materials* **2004,** *16* (4), 639-645.

195. Sima, F.; Ristoscu, C.; Duta, L.; Gallet, O.; Anselme, K.; Mihailescu, I., Laser thin films deposition and characterization for biomedical applications. In *Laser Surface Modification of Biomaterials*, Elsevier: 2016; pp 77-125.

196. Cushman, C. V.; Zakel, J.; Sturgell, B. S.; Major, G. I.; Lunt, B. M.; Brüner, P.; Grehl, T.; Smith, N. J.; Linford, M. R., Time-of-flight secondary ion mass spectrometry of wet and dry chemically treated display glass surfaces. *Journal of the American Ceramic Society* **2017,** *100* (10), 4770-4784.

197. Johnson, B. I.; Avval, T. G.; Hodges, G.; Membreno, K.; Carver, V.; Allred, D. D.; Linford, M. R., Oxidation of Aluminum Protected by Wide Band Gap MgF2 Layers as Followed by X-ray Photoelectron Spectroscopy. In *TechCon 2019 62nd Annual SVC Technical Conference*, Long Beach Convention Center, Ca, 2019.

198. Avval, T. G.; Chatterjee, S.; Bahr, S.; Dietrich, P.; Meyer, M.; Thißen, A.; Linford, M. R., Carbon dioxide gas, CO2 (g), by near-ambient pressure XPS. *Surface Science Spectra* **2019,** *26* (1), 014022.
199. Avval, T. G.; Chatterjee, S.; Hodges, G. T.; Bahr, S.; Dietrich, P.; Meyer, M.; Thißen, A.; Linford, M. R., Oxygen gas, O2 (g), by near-ambient pressure XPS. *Surface Science Spectra* **2019,** *26* (1), 014021.
200. Avval, T. G.; Cushman, C. V.; Bahr, S.; Dietrich, P.; Meyer, M.; Thißen, A.; Linford, M. R., Dimethyl sulfoxide by near-ambient pressure XPS. *Surface Science Spectra* **2019,** *26* (1), 014020.
201. Johnson, B. I.; Hilfiker, J.; Linford, M., Some Fundamentals of Spectroscopic Ellipsometry. *Vacuum Technology & Coating* **2019**.
202. Greczynski, G.; Hultman, L., X-ray photoelectron spectroscopy: towards reliable binding energy referencing. *Progress in Materials Science* **2019**, 100591.
203. Linford, M. R., Understanding One of the Governing Equations of XPS and Highlights from a Recent Paper by Akagawa and Fujiwara. *Vacuum Technology & Coating March* **2014**, 31-37.
204. Girault, H. H., *Analytical and physical electrochemistry*. EPFL press: 2004.
205. Crist, B. V., Advanced peak-fitting of monochromatic XPS spectra. *Journal of Surface Analysis* **1998,** *4* (3), 428-434.
206. Singh, B.; Hesse, R.; Linford, M. R., Good practices for XPS (and other types of) peak fitting. *Vac Technol Coating* **2015,** *12*, 25-31.
207. Hesse, R.; Streubel, P.; Szargan, R., Product or sum: Comparative tests of Voigt, and product or sum of Gaussian and Lorentzian functions in the fitting of synthetic Voigt-based X-ray photoelectron spectra. *Surface and Interface Analysis: An International Journal devoted to the development and application of techniques for the analysis of surfaces, interfaces and thin films* **2007,** *39* (5), 381-391.
208. Singh, B.; Herrera-Gomez, A.; Terry, J.; Linford, M. R., Good Practices for XPS Peak Fitting, II. *Vacuum Technology & Coating* **2016**.
209. Hesse, R.; Chassé, T.; Streubel, P.; Szargan, Error estimation in peak-shape analysis of XPS core-level spectra using UNIFIT 2003: how significant are the results of peak fits? *Surface and Interface Analysis: An International Journal devoted to the development and application of techniques for the analysis of surfaces, interfaces and thin films* **2004,** *36* (10), 1373-1383.
210. Hesse, R.; Chassé, T.; Szargan, R., Peak shape analysis of core level photoelectron spectra using UNIFIT for WINDOWS. *Fresenius' journal of analytical chemistry* **1999,** *365* (1-3), 48-54.
211. Tompkins, H. G.; Hilfiker, J. N., *Spectroscopic Ellipsometry: Practical Application to Thin Film Characterization*. Momentum Press: 2015.

CHAPTER 2: Illuminating the Oxidation of Aluminum Thin Films Protected by Ultrathin MgF_2 Layers Using Spectroscopic Ellipsometry and X-Ray Photoelectron Spectroscopy

2.1 Statement of Attribution

Paper Submitted to OSA Continuum in October 2019 Brian I. Johnson,[1,4] Tahereh G. Avval,[1] R.S. Turley,[2,3] Matthew R. Linford,[1] and David D. Allred[2*]

[1]Department of Chemistry and Biochemistry, Brigham Young University, C100 BNSN, Provo, Utah 84602, USA

[2] Department of Physics and Astronomy, Brigham Young University, N265 ESC, Provo, Utah 84602, USA

2.2 Abstract

Combined X-ray photoelectron spectroscopy (XPS) and spectroscopic ellipsometric (SE) studies concur on the time-dependent aluminum oxide thickness in evaporated MgF_2 over Al bilayers. Dynamic SE can track second-by-second oxide growth for the first postdeposition hours. Oxide growth is computed from relative XPS peak areas as corrected for electron attenuation through the MgF_2 overlayer. An empirical formula fits time-dependent data for aluminum surfaces protected by MgF_2 as a function of MgF_2 layer thickness: aluminum-oxide thickness= k*log(t)+b. The prefactor, k, depends only on MgF_2 thickness, decreasing monotonically with increasing MgF_2 thickness. This method of employing SE should be extendable to study other metal/overlayer combinations.

2.3 Introduction

Aluminum is the only material that can provide broad-band IR-optical-UV and far ultraviolet (FUV) reflectance. Unfortunately, aluminum begins oxidizing immediately upon air exposure. Even under high-vacuum conditions oxidation[1-8] and loss of vacuum ultraviolet (VUV) reflectance are observed.[9]

The aluminum oxide which forms, though only 3.5-5 nm thick, effectively blocks aluminum's high reflectance above about 9 eV (<140 nm), which is the point at which sapphire's absorption constant rises above 0.01/nm.[10] To circumvent oxidation, wide-bandgap, dielectric (low-atomic-number metal fluoride) thin films are deposited on the aluminum film before it is exposed to air.[4, 11-15] MgF_2 and LiF thin barrier layers have been used for decades to protect aluminum reflectors, particularly for VUV applications including space telescopes. Space telescopes place large demands on reflective coatings. Hubble's far UV performance was due to its MgF2 on Al mirror coatings. Concept plans for two potential NASA missions of the 2030's -the Large UV-Optical-IR Surveyor (LUVOIR) and the Habitable Exoplanet Imaging Mission (HabEx)- call for substantial reflectance down to 100 nm.[16-18] Recent efforts to achieve this goal have focused on depositing the fluorides on heated substrates,[11] using barriers containing LiF,[19] employing atomic layer deposition (ALD),[17, 20-22] and using capping layers including AlF_3.[12, 19] This has allowed aluminum's region of high reflectance to be expanded to somewhat shorter wavelengths.

In addition to optical performance, there are significant environmental requirements. Coatings must survive years of storage prior to launch. This environment may not be optimal for survival during portions of this time. This is particularly an issue for LiF which is hygroscopic and for thinner overcoats. Lifetime tests show that some processes produce layers that should survive some exposure to humid environments.[19] However, these are macroscopic tests. The question of the nature of the degradation on the atomic level has not been addressed. Fundamental knowledge of atomic-scale changes could provide technologists insights in identifying problems and allowing problems to be corrected early. This could also help formulate accelerated lifetime tests and give confidence that the final coatings will survive to launch and beyond.

In spite of the importance of barrier-layer protected mirrors, tools that can easily detect and quantify the time-dependent *oxidation* of aluminum *under* protective fluoride barrier layers have been late in coming. Here we show that variable-angle, spectroscopic ellipsometry (VASE) can be such a tool and present a systematic study of MgF_2-protected Al mirrors as an example of its use. VASE is known to be useful in obtaining the thicknesses and optical constants of ultrathin metal films.[23] Recently this technique was expanded to observing the thickness of ultrathin aluminum under a fluoride barrier decrease with time.[24-26] The concomitant appearance and growth of a dielectric layer on top of the aluminum under the fluoride layer was also noted. While this was inferred to be aluminum oxide, it took an XPS study on the same series of MgF_2 layers on Al to show definitively that the dielectric material which ellipsometry measures to be increasing in aging samples is oxide.[27, 28] This study also indicates that the oxidation is uniform across the sample. That is, the data does not support the hypothesis that the oxidation is primarily from pinholes. We also show that, while the Cabrera –Mott approach can fit the oxide thickness derived from XPS, that thickness is fit better by a simpler expression. Oxide thickness increases linearly with the logarithm of time. The slopes of the equation for the time-dependent thickness decrease with increasing fluoride thickness as anticipated. This approach potentially might be useful to project mirror lifetimes. The films studied here were deposited at room temperature. However, the technique described here is amenable to samples deposited at elevated temperatures or via ALD and should be adaptable to studying other barriers such as LiF and other mirror metals such as silver.

2.4 Experimental

2.4.1 Sample Deposition

Except as specifically described below, all aluminum and MgF_2 films were deposited without substrate heating in a Denton DV-502A thermal evaporator. Details are described elsewhere.[24, 25, 27] The sample substrates were cleaved from Si (100) wafers. In studying aluminum films, the wafer utilized was purchased with a nominal 300 nm of CVD Si_3N_4. The CVD Si_3N_4 dielectric layer on the substrate is referred to as the interference layer (IL) and aids in the quantification of the oxide growth via ellipsometry.[24] The Al was deposited at a rate of 3.5 nm/sec on to achieve a thickness of 150 Å. The MgF_2 was then immediately deposited (time between depositions was less than 60 seconds) on the Al film at a rate of ca. 0.3nm/sec. The time for both depositions was 35 to 45 s. The time between the end of the evaporation of the aluminum film and the beginning of the evaporation of the overcoat was minimized to avoid oxide build up on the freshly evaporated Al and was usually less than 60 seconds. Past work has shown that high rates are conducive for producing the purest (highly reflective) aluminum layers. The high rates limit the incorporation of oxygen into the film. A quartz crystal monitor (QCM) was employed to close the shutter between the source and the substrate when the programed thickness was reached.

Our goal was not the replication of state-of-the-art, protected, front-surface aluminum mirrors in every detail. Rather, we aimed at producing materials and structures that facilitated study via SE and XPS but were otherwise as similar as possible to the relevant aspects of the best mirrors. Ours were test samples for addressing scientific/technological questions, such as, "What is the rate of oxidation of aluminum coatings protected by a certain thickness of barrier?" And it is known that heating the substrate as the fluoride is deposited enhances optical properties, can the same be said for barrier-layer properties. We hypothesize that small amounts of oxygen incorporation are not likely to change oxidation rates significantly, though this should be investigated. Likewise, it was hypothesized that aluminum thickness would not affect aluminum oxidation rate. Thus, the behavior of our ultrathin aluminum coatings should be useful in understanding state-of-art aluminum mirrors.

2.4.2 Characterization

Ellipsometric data was acquired using a J.A. Woollam M-2000D, variable-angle, spectroscopic ellipsometer (J.A. Woollam Company, Lincoln, ME, USA) over the wavelength range of 190-1688 nm. Time-dependent SE measurements were obtained for various samples using the 'in situ' mode of the instrument. The ellipsometer acquired delta and psi data at 75° every 2.3 s for a period of 4 h. Data were subsequently modeled using the CompleteEASE® SE instrument analysis software. The model in Figure 2-1 shows the types of Al +MgF_2 stacks prepared and studied. The optical constants for all layers except #2 (CVD Si_3N_4) and #4 (Al) were modeled with the optical constants in the CompleteEASE® data base. The substrate was Si-JAW. For layers 1 and 3 SiO2-JAW (silicon native oxide) was used. Layer 5 used Al_2O_3 (parametric model), and Layer 6 used MgF_2 (a Sellmeier model of the ordinary-ray refractive indices of MgF_2). The substrate and layers 1-3 come as a unit. It is impossible to know the thickness of the oxide under the Si_3N_4. We set it to 1.4 nm, which is a typical thickness for native oxide on Si wafers. With SE we learned that the native oxide on top of our CVD Si_3N_4 is about 2 nm. This is from measuring wafer pieces after etching in buffered HF to remove only the oxide layer. The optical constants for

‘Layer 2 CVD Si_3N_4’ were obtained by measuring a number of CVD nitride-coated substrates prior to deposition.[24] We found that the optical constants of CVD silicon nitride could be parameterized successfully as a Tauc-Lorentz oscillator plus a Gaussian oscillator located near the band edge. Measurement were made on each specific sample prior to the deposition of the aluminum and the fluoride. The Si_3N_4 thickness was then fit. On occasion, the thickness of this layer was sometimes fit to decrease the MSE of the substrate fit. The typical change in thickness was less than 1%, which is well within the tolerance of thickness uniformity across the wafer the substrates were taken from. These parameters were then held fixed during the analysis of the delta and psi data to determine the Al (Layer 4) and Al_2O_3 (Layer 5) thicknesses.

The optical constants for the aluminum film were obtained from multisample analyses as described in results. Interference enhancement, as the technique is known, has been found to increase significantly the sensitivity to the absorber optical properties and thickness.[23] The purpose of a thick dielectric layer between the aluminum layer and the Si substrate is to enhance the information content of multiple-angle measurements.[24] Spectroscopic ellipsometry and transmitted or reflected intensity was shown, for example, to produce a unique result for the Cr films on fused silica substrates.[23] It should be noted that the Al in the films suitable for these ellipsometric studies are a factor of 3-4 times too thin for standard telescope mirrors.

XPS was performed with a Surface Science SSX-100 instrument (maintained by Service Physics, Bend, OR, USA) with a hemispherical analyzer. The instrument employs monochromatic Al Kα X-rays. Survey scans were collected with an X-ray spot size of 800 x 800 μm^2 with a resolution of 4, nominal pass energy of 150 eV, 6 passes/scans, and a step size of 1 eV. High resolution scans were collected over the Al 2s region, centered at a binding energy of 120 eV, with an energy window of 40 eV and a step size of 0.0625 eV. The number of scans ranged between 15 and 35, and the spot size was 800 x 800 μm^2 with a resolution of 3 (nominal pass energy of 100 eV). Area ratios were calculated using the CasaXPS modeling software (Casa Software Ltd., Version 2.3.18PR1.0).

2.4.3 MgF_2 Thickness Standard Preparation

MgF_2 thickness standards for XPS analysis allow the thickness of MgF_2 on Al films to be measured via XPS. To prepare the standards, MgF_2 films of seven different thicknesses on Si were deposited unheated (that is, about 300K) substrates. These were approximately 25 x 25 mm silicon pieces cleaved from a single-side polished 150 mm diameter epi silicon wafer. The samples were cleaned by a low-pressure air plasma (Herrick model PDC-32G). The native oxide thickness on each sample was then measured via ellipsometry prior to MgF_2 deposition. The native oxide thickness was about 1.5 nm. After the fluoride deposition, the thicknesses of the MgF_2 layers were measured via SE at an angle of 75°. The ellipsometric data was modeled using the optical models in the instrument software for MgF_2 (MgF_2 (Sellmeier-ordinary ray)) to obtain the fluoride thickness, while Si and SiO_2 used Si_JAW and SIO2_JAW, respectively. An additional set of five MgF_2 standards of varying thicknesses were prepared on heated substrates (ca. 500K) by the processes described above except the substrate heating. Differences in the attenuation coefficient of the two sets showed the importance of substrate heating for maximum density; as will be discussed below.

After deposition, the standards were analyzed with XPS to assess the attenuation length of the MgF_2. This included narrow scans of the Mg 2s and Al 2p features. It should be noted that the thickest MgF_2 in the films suitable for these XPS studies are a factor of 3-4 times thinner for standard protected mirrors due to analysis depth limitations of XPS. (On the other hand, for ellipsometry the fluoride layer can be arbitrarily thick.)

2.5. Results and Discussion

2.5.1 Determination of Fluoride Thickness

Ellipsometric measurements depend on reflecting light of a known polarization from a surface and measuring changes in that polarization. Spectroscopic ellipsometry utilizes a suite of colors, in our case, >700 individual wavelengths. Through the creation of parametric models of layers and adjustment of the parameters in them, ellipsometric measurements can be used to determine a variety of material properties including film thicknesses, surface roughness, and optical constants of materials. In the case of multi-angle measurements this can yield as many as 10000 individual values of Δ and Ψ used fit with a model possessing far fewer adjustable parameters. This can remarkably constrain layer thickness estimates. Parameterization also decreases the correlation between constants while maintaining smooth, continuous, and, if desired, Kramers–Kronig consistent optical properties for the absorbing material.

However, due to the potential presence of two dielectric layers- the MgF_2 overlayer and any aluminum oxide- above the aluminum in the Al+MgF_2 bilayer (see Figure 2-1), the individual thicknesses of the MgF_2 overlayer and the oxide could not be determined with precision using spectroscopic ellipsometry alone. This is unless the thickness of one of the layers were known at a given time and it is known that the fluoride overlayer itself does not change thickness and index with time. While the thickness monitor provided thickness control of the magnesium fluoride deposited, an independent measurement of the thickness and stability of the deposited MgF_2 layer was desired and this measurement was XPS.

In this analysis, we employed an equation from Cumpson, which is based on Hill's equation.[29, 30] It is as follows:

$$\ln\left(\frac{I_o/s_o}{I_s/s_s}\right)-\left[\left(\frac{E_o}{E_s}\right)^{0.75}-\frac{1}{2}\right]\frac{d}{\lambda_o\cos(\theta)}-\ln 2=\ln\sinh\left(\frac{d}{2\lambda_o\cos(\theta)}\right) \qquad (1)$$

Here, I_o and s_o are the intensity and sensitivity factor respectively of the Mg 2s photoelectrons in the top layer of the MgF_2 standards (here, the MgF_2 film), and I_s and s_s are the intensity and sensitivity factor of the Si 2p electrons from the substrate (here, the Si/SiO_2 layer), and the take-off angle (cos θ in Equation 1) of our XPS system is 35°.

Finally, the attenuation coefficient, λ_o, for MgF_2 needs to be known. This was the purpose of the MgF_2-films-on-silicon standards described in section 2.2. SE could be used to determine their thickness (here, d in Equation 1). This is possible because there was no aluminum or aluminum oxide to confound the identification of the magnesium fluoride layer's thickness. Then the samples were measured via XPS and Equation 1 was solved iteratively to determine the attenuation coefficient, λ_o, for MgF_2. Peak areas (I_o and I_s here) and binding energies (E_o and E_s for Mg 2s and Si/SiO_2 2p photoelectrons, respectively) were calculated. This resulted in four different values of λ_o for the samples deposited on unheated substrates. These are: (1.6 nm MgF_2, λ_o: 6.1 nm), (2.1 nm MgF_2, λ_o: 5.3 nm), (3.3 nm MgF_2, λ_o: 4.6 nm), and (5.1 nm MgF_2, λ_o: 4.2 nm) and are plotted in Figure 2-2.

Note that the value of the attenuation coefficient decreased as MgF_2 thickness increased. This can be understood if the thinner fluoride layers were porous or rough. Porous films logically would have larger attenuation lengths since the vacuum portion of the films do not absorb electrons. The ellipsometer would measure greater film thickness than allowed by the MgF_2 contained in the film if it were fully dense. How does one account for the index of a porous layer not being noticeably smaller than that of the fluoride? Ellipsometric measurements are made in air. Under these conditions, small pores fill with water by capillary action even in conditions of low humidity. Water has an index not much smaller than that of magnesium fluoride so the combination of fluoride and water is a layer that resembles magnesium fluoride. (The water will leave in the vacuum of the XPS and thus will not be detected by that technique.)

It is well known that the initial layers of dielectrics are frequently porous when deposited on the substrates at ambient temperatures. The films become denser as the film thickness increases, but bulk densities are often not achieved without adding energy during deposition. Substrate heating is thought to produce denser films at all thicknesses by increasing the surface mobility of adatoms. While ion bombardment works well for oxides, fluoride films are damaged by this technique.

To achieve higher density films, the five fluoride films of different thicknesses deposited at about 500 K were subjected XPS analysis. The attenuation length of these films does not vary with thickness as seen in Figure 2-2 (bottom set of points marked by triangles). The average value of λ_o was 3.79 ± 0.21 nm for the heated MgF_2 films.

This value of the attenuation length, 3.79 nm, was then used in equation 1 to determine the thickness of the various MgF_2 layers deposited on aluminum. Here, Al 2p electrons coming from the aluminum film were used to compute Al/Al_2O_3 ratio. E_o and E_s are the binding energies of Mg 2s and Al 2p photoelectrons respectively and λ_o is the attenuation coefficient of the aforementioned Mg 2s photoelectrons. These thicknesses were within 5% of the value programmed into the QCM used to control the deposition thicknesses in the evaporator. Thus, overall, this approach accounted for any run-to-run variation in the deposition of the MgF_2.

2.5.2 SE Analysis of the Oxidation of MgF_2 Under Aluminum

To study the oxidation of MgF_2 under aluminum, as described in section 2.1 Al (nominal thickness of ca. 15 nm), followed by MgF_2 (various thicknesses) were deposited onto fully characterized $Si/SiO_2/Si_3N_4/SiO_2$ substrates. These $Si/SiO_2/Si_3N_4/SiO_2/Al/MgF_2$ stacks were then removed from the evaporation chamber. Once in air "the clock started" for the sample's aging. As quickly as possible – usually 5-6 minutes, each sample was moved to the ellipsometer, and a four-hour run was commenced that repeatedly collected SE data from the sample at 75°. Some of the samples were then analyzed by XPS to determine the thicknesses of its MgF_2 and oxide layers. The delta and phi ellipsometric data was then analyzed to obtain the time-dependent thickness of the oxide for each four-hour set of SE data.

A preliminary question was answered quickly. Could some of the changes observed be due to changes in the fluoride overlayer? Of the commonly used fluoride overcoats for aluminum, magnesium fluoride is the most stable. An ellipsometric study of 15nm MgF_2 on Si films showed no changes for samples stored in laboratory air over a period of a day. Thus, calculations proceeded attributing all changes in SE data to the appearance of an aluminum oxide film on the Al. (Prior work had shown that the SE data was not compatible with the interpretation that the oxide is forming below the Al.)

Two models of Al optical constants were considered to determine the aluminum and aluminum oxide thicknesses for the Al+MgF_2 stacks. Both approaches used the previous SE characterizations of the individual $Si/SiO_2/Si_3N_4/SiO_2$ substrates applied to each different stack modeled. In the first approach, the same Al optical constants were used for *all* samples. This is Model 1. These Al constants had been obtained from an MSA involving most of the samples, as detailed elsewhere.[26] This approach had a significant problem but was not unfruitful. The problem was this: the fits to SE for most samples generated oxide thicknesses less than zero. The MSE is shown in the second column (labeled Model 1) of Table 2-1.

Table 2-1 Mean Square Error for fitting aluminum and aluminum oxide for Model 1 and 2. Model 1 uses the same Al optical constants for all samples. For model 2 they are optimized individually for each sample

MgF_2 Thickness	**Model 1 MSE**	**Model 2 MSE**
0.000 nm	1.20	0.32
1.45 nm	0.75	0.41
1.73 nm	15.49	1.39
1.96 nm	3.28	2.93
2.59 nm	300.00	7.62
2.99 nm	1.23	0.37
3.81 nm	0.75	0.32
4.20 nm	16.96	3.52
4.97 nm	0.83	0.25
5.00 nm	33.69	5.81
Negative Al_2O_3 thicknesses	6 of 9	2 of 10
Unfittable Samples	1	0

Negative oxide thicknesses are not physical. On the other hand, fitting the optical constants for the aluminum in each individual stack individually resulted in more reasonable fits for the oxide thickness and yielded significantly lower MSE values. This is the 3rd column in Table 2-1, labeled Model 2.

Interestingly, in spite of the fact that Model 1 yielded apparent negative Al_2O_3 thicknesses for a significant fraction of the samples, the trends, with increasing time, in apparent Al_2O_3 and Al thicknesses for all samples that could be fit, were not unreasonable. The apparent Al_2O_3 thicknesses was observed to increase with time accompanied by a decrease in the Al thicknesses. To visualize these trends, thickness data were plotted against log of time (Figure 2-3).

Using log of time allowed data taken over many orders of magnitude to be plotted on the same graph. When this was done it was noted that the data of the Al_2O_3 thicknesses vs. time for the different samples lay on approximately straight lines. That is, they could be reasonably fit to equation of the form:

$$d_{Al_2O_3} = k \ln t + b \qquad (2)$$

where d_{Al2O3} is the thickness of the Al_2O_3 film, t is time, k is the slope, representing a characteristic slowing of oxidation, and b is thickness of the oxide at 1unit of time.

The negative thicknesses for Al_2O_3 produced by Model 1 Al constants are unphysical. It is reasonable to hypothesize that this is due to the requirement that the same optical constants for Al be applied to *all* samples regardless to differences in deposition conditions. In the case of dielectric thin films this often a good assumption. However, as previously noted, optical constants for extremely thin metal films cannot be expected to be constant.[23, 26, 31, 32] Since the photon energy in the SE characterization are significantly less than aluminum's plasma edge of 15 eV, anything that affects the number, or scattering behavior, of free electrons could markedly change a Al film's optical constants.[33] In fact, the oscillatory motion of free electrons in an ultrathin aluminum film in a photon's electromagnetic field could be impeded both by the film's top and bottom surfaces[34] and the presence of numerous grain boundaries[35] arising from the extremely small grain size characteristic of ultrathin films deposited at a small fraction of their melting temperature. (The general effect on microstructure of thickness and deposition temperature is treated by a number of authors.[36, 37]) Nguyen et al used spectroscopic ellipsometry to comprehensively study the effect of Al thickness on optical constants, observing that for thicknesses >6nm, "the interband relaxation time increases with thickness, providing evidence that grain-boundary scattering is the dominant mechanism controlling the optical properties in the bulk film stage."[35] The smaller MSE values for Model 2 (see Table 2-1) suggests that fitting the Al optical constants in each sample separately is justified, lending support the hypothesis that the Al optical constants vary between the samples. Two additional indications that this approach is an improved representation of our materials are the facts that all of the samples could be fit with Model 2, and that only two of the ten samples used showed any negative Al_2O_3 thicknesses.

Plots of Al_2O_3 thickness vs. the log of time were also found to be quite linear for the second approach as well as the first and were fit with Equation 2. The slopes (that is, the k values) in equation 2 arising from the application of the two Al models are plotted in Figure 2-4 as a function of the MgF_2 overlayer thickness in each of ten samples. It is clear that k decreases as the thickness of the MgF_2 overlayer increases, which is the expected behavior for a barrier layer.

It is significant that the two curves nearly overlap. That is, these results suggest that while the absolute thicknesses of oxides using the first model might be incorrect, the *changes with time are meaningful*, and, furthermore, that the values of k determined here, and the fact that they decrease with increasing MgF_2 thickness, are not artifacts of either approach.

2.5.3 X-ray Photoelectron Spectroscopic Analysis

The thickness of the MgF_2 layer on Al could not be modeled unequivocally using SE due potential correlation with the developing aluminum oxide layer, as noted previously. Therefore, to measure the thickness of the MgF_2 layer, XPS itself was used in conjunction with SE. XPS is a surface sensitive technique that probes ca. 10 nm into a surface. It can monitor elemental compositions and oxidation states of materials as well. XPS data are modeled using curve fitting techniques that account for differences in composition. This peak fitting is important because XPS line widths and chemical shifts due to changes in oxidation states are of comparable size.[30] To study the oxidation rates of Al as a function of MgF_2 thickness, as discussed in section 2.1, seven Al +MgF_2 samples were prepared. All samples were analyzed at the Al 2s binding energy (BE) position of 118 eV. While the intensities of the Al 2p region were very similar, the Al 2s region was selected as spin-orbit splitting, such as seen in Al 2p peak analysis, does not need to be considered.

Figure 2-5 shows that the Al surface below the MgF_2 oxidizes to Al_2O_3 over time. The extent of oxidation can be measured by plotting the Al_2O_3/Al ratios over time. Photoelectrons do not come out with the same energy but are broadened to a Lorentzian shape by the exponential decay probability for the core hole. The spectrum is further broadened to have a more Gaussian shape by phonon interactions and disorder. In fitting the Al 2s peak, two types of synthetic line shapes were considered: Gaussian-Lorentzian product (GLP) functions, and Gaussian-Lorentzian sum (GLS) functions.[38] Because they fit the data better than the GLP functions, GLS were employed here. These partition the peak into Gaussian and into Lorentzian components. It has been observed that the Al peak from pure Al is most Lorentzian than Al in Al_2O_3.[38, 39] This is attributed both to the oxide's greater disorder and to phonon broadening.[40-42]

The best fit percentage of the peak shape that is due to Lorentzian in a given sample is found by minimizing the standard deviation of the residuals (STDEVRes) over all of the samples analyzed. In the bare Al samples the Lorentzian values for the Al_2O_3 peaks were best fit with 20% Lorentzian character, thus yielding GLS values of 50 and 20 for Al and Al_2O_3 respectively. In the samples with a MgF_2 protective layer, GLS values of 50 and 0 for Al and Al_2O_3, respectively fit the data best. The decreased Lorentzian peak character from the bare to the protected oxide layers indicate increased disorder in the XPS oxide spectra[40] under the MgF_2 overlayer.

Using these parameters, we determined the areas under the Al_2O_3 and Al peaks and the full width half maximum (FWHM) of seven samples, two bare and five with MgF_2 overlayers. These results are recorded in Table 2-2. Our data showed the average FWHM for the Al to be 1.75 ± 0.07 eV for both bare and coated samples. On the other hand, the Al_2O_3 2s peaks for the bare and coated samples averaged 2.45 ± 0.1 eV and 2.92 ± 0.13 eV, respectively. The oxide FWHM values fell within range of literature γ-Al_2O_3 and Al values.[41-44] In addition, binding energy (BE) differences between Al_2O_3 and Al peaks were 2.57 ± 0.12 eV averaged over all samples. It may that the differences in the FWHM are attributable to differences between the MgF_2 over layer and the native oxide that forms.

Table 2-2 Average FWHM values, peak energy (BE) differences, and ratios of FWHM values for the Al and Al_2O_3 fit components in the Al 2s narrow scans considered in this study

MgF_2 Thickness (nm)	Average FWHM Al 2s Peak	Average FWHM Al_2O_3 2s Peak	Average BE Difference Al-Al_2O_3 2s Peaks	Average FWHM Ratio Al_2O_3 /Al 2s Peaks
0	1.79 ± 0.08	2.51 ± 0.11	2.39 ± 0.03	1.40 ± 0.03
0	1.76 ± 0.03	2.40 ± 0.05	2.36 ± 0.06	1.41 ± 0.09
1.73	1.76 ± 0.14	2.96 ± 0.14	2.49 ± 0.10	1.68 ± 0.09
1.92	1.68 ± 0.06	2.82 ± 0.08	2.59 ± 0.08	1.68 ± 0.08
1.96	1.74 ± 0.04	2.99 ± 0.08	2.46 ± 0.04	1.72 ± 0.06
2.25	1.71 ± 0.04	3.15 ± 0.22	2.75 ± 0.24	1.84 ± 0.16
4.23	1.83 ± 0.04	2.69 ± 0.10	2.48 ± 0.06	1.48 ± 0.04
Average	**1.75 ± 0.07**	**2.79 ± 0.12**	**2.50 ± 0.11**	**1.60 ± 0.09**

The consistency of the statistics in Table 2-2 also increased our confidence in the validity of our data. Using these standards, we were able to quantify aluminum oxidation changes over time. As such, we can show the graphical representation of changes in the aluminum oxidation starting from immediate removal from the evaporator chamber and extending to 8 months. In Figure 2-6, Al_2O_3/Al ratios are graphed as functions of the log of time. It can be observed that plotting the data points as a function of the log of time shows points fall, more or less, on a straight line. Empirically, then, oxidation followed a logarithmic model over an extended time-period of observation. That the rate of oxidation decreases with time is not surprising since as the oxide film thickness grows, it creates a protective boundary that greatly reduces atmospheric oxygen or water access to the aluminum metal surface.[24] As shown, the rates were empirically fit using regression analysis to the general equation using the Al_2O_3 to Al ratios shown in Equation 3:

$$Al_2O_3 / Al = k \ln t + b \tag{3}$$

Here, k is the slope. Table 2-3 gives changes in oxidation prefactors as a function of the MgF_2 thicknesses.

Table 2-3 Oxidation rate prefactors from different MF2 thicknesses

MgF_2 Thickness (nm)	Prefactor of Slope Oxidation
0	0.100
0	0.103
1.73	0.061
1.92	0.041
1.96	0.043
2.25	0.032
4.23	0.021

2.5.4 Aluminum Oxidation Models Under Protective Layers

Understanding the mechanism behind thin-film oxidation is a century-old problem.[44] While applying protective or barrier overcoats to isolate a surface from the environment is a common approach to slow degradation, the study of the kinetics of the oxidation *under that barrier* is much less common. The exceptions arise when the overlayer is ultrathin as is the case of graphene on Cu.[45, 46] Even in these cases, however, appeals to classic oxidation theory are rare. Here is the problem. Rather than a two-layer model (an oxide on a metal substrate) a trilayer (barrier/oxide/metal) model must be invoked. The difficulty is not just that there are more interfaces. In our case, the barrier is structurally and chemically quite different from the oxide forming below it. The formation of Mott potentials and mechanisms of mass and charge transport can be expected to change, transitioning between the growing oxide and the magnesium fluoride overcoat.

Nevertheless, the fact that oxide thicknesses on a log-of-time plot fall on straight lines whose slopes depend on the MgF_2 thickness suggests that consideration of classical oxidation models may yield insight. The fact the slopes decrease with increasing fluoride thicknesses suggests that the limiting factor to oxidation is the MgF_2 layer. Perhaps it limits diffusion of an oxygen containing species through it to the MgF_2-oxide interface, but what of the logarithmic behavior?

The oxidation of many metals at low temperatures, after the initial nucleation and lateral consolidation of oxide, is said to be logarithmic, either direct or inverse. The Cabrera-Mott (CM) model predicts a form of inverse logarithmic. Replotting some of the oxide thickness data according to the CM model allows a comparison to be made. In the CM model, charged surface-oxygen species and metal ions generate a (Mott) potential that drives oxidation. If the CM model is applicable, the placement of the thickness data on the graph will produce straight lines. This is done in figure 2-7. Here the plot is done according to the form corrected by Ghez.[47] It can be seen in this figure that, while there is rough agreement with the Cabrera Mott model, the agreement is worse than for a direct logarithmic plot. In Table 2-4 furthermore, the goodness-of-fit (R^2) values of direct logarithmic and indirect are recorded for several samples. The middle column is for CM and the right column for direct logarithmic. In all but one case the R^2 value for direct logarithmic is significantly closer to 1.0. 1.0 would be a perfect fit. Note that two of the plots are for bare Al, and in agreement with other researchers[4, 48-50] we find that oxidation of bare aluminum is fit well by the log of time approach. Note that Grimblot and Eldridge[50] say that CM works as well as direct logarithmic.

While failure of data to be fit well by the CM model cannot be interpreted as implying CM model is not applicable,[51] it is profitable to look for those models which predict direct logarithmic dependence. An early model proposed by Mott posited electron tunneling through the oxide as rate determining. For this case, a direct logarithmic expression for the growth of oxide films identical to equations two and three. Fehlner also observed on page 204,[52] that direct logarithmic kinetics are observed for group I and II elements. Magnesium is a group II element, but there is no reason why one would expect its fluoride to block oxygen or water passage like its oxide does?

Table 2-4 R^2 Values for XPS Fits

MgF_2 Thickness	Cabrera-Mott	Empirical Fit
0.00	0.9395	0.9908
0.00	0.9184	0.9857
1.73	0.9635	0.9913
1.92	0.9204	0.9856
1.96	0.8736	0.9495
2.25	0.9545	0.9535
4.23	0.9785	0.9905

2.6 Conclusion

Ellipsometric studies show changes in aluminum films under ultrathin films of magnesium or aluminum fluoride that can be interpreted as oxidation of the aluminum forming an oxide layer on top. XPS measurements in this study confirmed that, in the case of MgF_2 films with thicknesses between 0-6 nm, these changes are due to the slow oxidation of the underlying aluminum film. This is seen both in the increase of the signal from oxygen and in the chemical shift in the Al 2s electron emission peak toward higher binding energy as the surface of the metal oxidizes to Al^{+3}. The extent of oxide growth can be modeled from the relative area of each peak once they are corrected for the attenuation through MgF_2 layer. We discussed the figure of merit used to choose the fraction of Lorentzian or Gaussian character for fitting the area of Al in the Al_2O_3 and Al peaks, and with this standard we showed that amount of oxidation increases with the logarithmic of time, by plotting the Al_2O_3/Al ratios.

Both XPS and SE allow the growth of the aluminum oxide to be tracked and quantified. Based on graphs of oxidation as a function of time, we produce an empirical formula: oxide thickness= k*log(t) +b, which fits the measured time-dependent aluminum oxide thickness on aluminum surfaces protected by MgF_2. k is a factor that depends on MgF_2 thickness, and decreases with increasing MgF_2 thickness. Values for k for various thicknesses are presented. These differ only slightly between SE and XPS data. This study also contributes to the use of SE and XPS as analytical techniques generally. In their differing attenuation depths, temperature deposited ultrathin films and indicates that porosity decreases with increasing thickness. We also show that for each SE sample, that because the optical constants of ultrathin metals films depend strongly on deposition conditions and their thickness, the optical constants for Al, as well as the Al and Al_2O_3 thicknesses, they need to be individually fit. Similarly, as another first, we show how dynamic SE data track oxide growth over a period of several hours after the evaporated Al + MgF_2 bilayer is first exposed to the air. In dynamic SE, measurements are made every few seconds.

The SE and techniques developed and presented here may be generally applicable for films protected by thicker fluoride layers and/or enhanced fluorides. Enhanced means films deposited at elevated temperature. These techniques may allow for extrapolation of barrier-layer effectiveness for room-temperature deposited MgF_2 on Al to thicker fluoride films and point the way to producing survey methods for identifying which films might qualify for further study. However, it should be noted that the Al in the films suitable for these ellipsometric studies are a factor of 3-4 times too thin for standard telescope mirrors.

2.7 Figures

Figure 2-1 Representation of the optical stacks prepared and analyzed in this work. The bottom layers up through Layer 3 represent the Si/Si_3N_4 substrate. Layers 4 and 6 represent the Al and Mg deposited on the substrate. Layer 5 represents the oxidized Al that forms on the Al layer

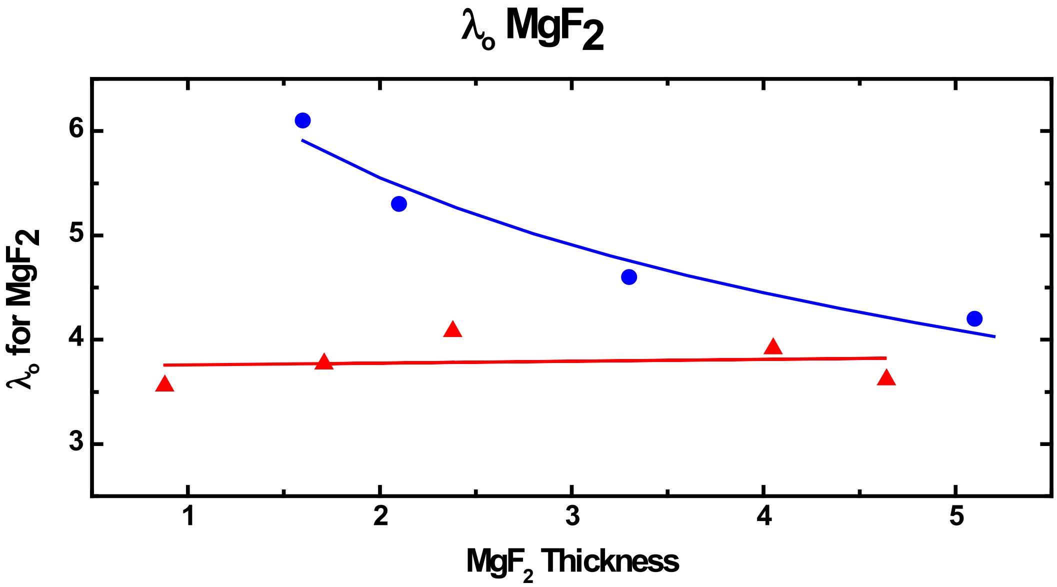

Figure 2-2 Measured (apparent) XPS electron attenuation length as a function of MgF_2 thickness as determined by SE. Top curve joins points for samples deposited on room-temperature substrate. Bottom curve joins points for samples deposited at about 500 K.

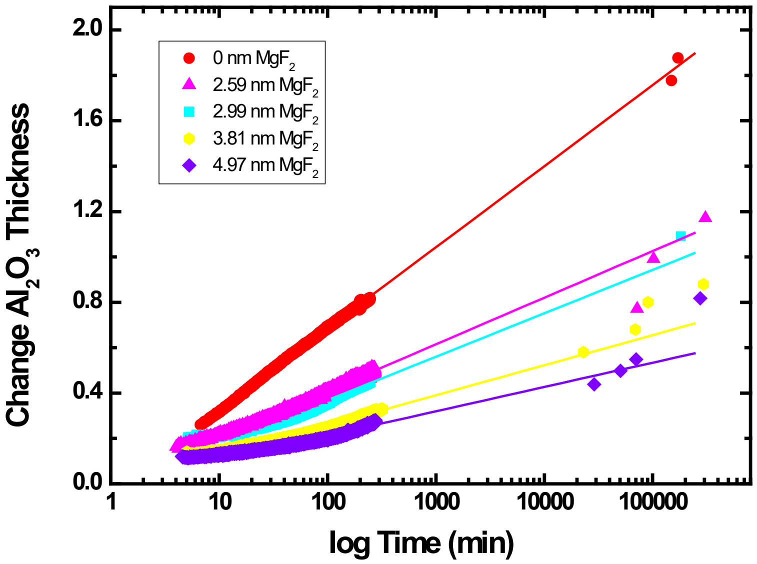

Figure 2-3 Changes in aluminum oxide thickness as a function of time in minutes for films with five different magnesium fluoride thicknesses. From top to bottom these are zero, 2.59, 2.99, 3.81, and 4.97 nm.

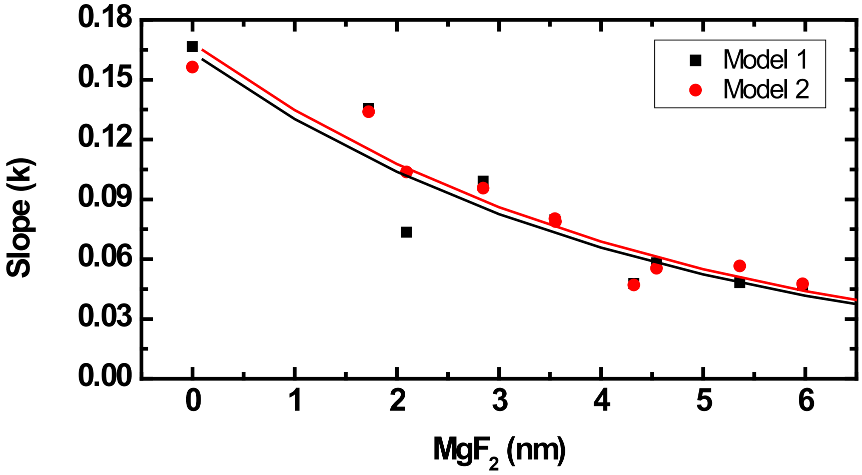

Figure 2-4 Values of k determined from Equation 2 from data generated from Models 1 (squares and lower curve) and 2 (circles and lower curve) employed in this study.

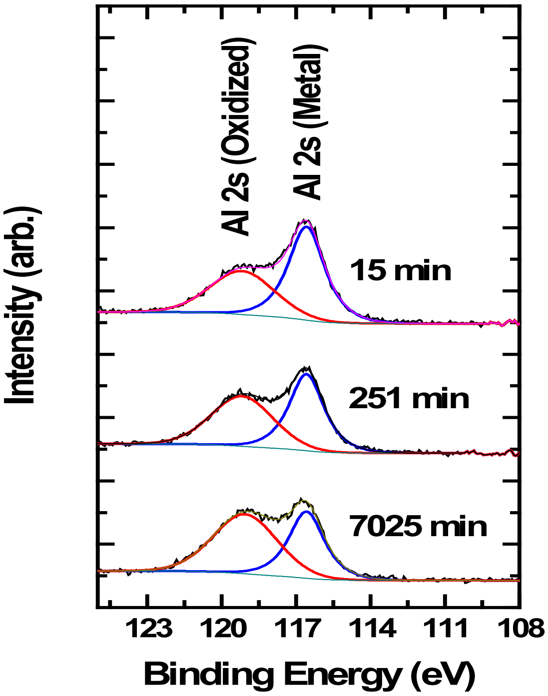

Figure 2-5 XPS spectra (aluminum x-rays) as binding energies for the aluminum 2S peak. Left-hand curve corresponds to oxidized aluminum. The right-hand curve corresponds to an oxidized aluminum. The top curve is from a sample that was placed in the XPS shortly after it was evaporated. The bottom curve showing considerably more oxidation was made after 725 minutes.

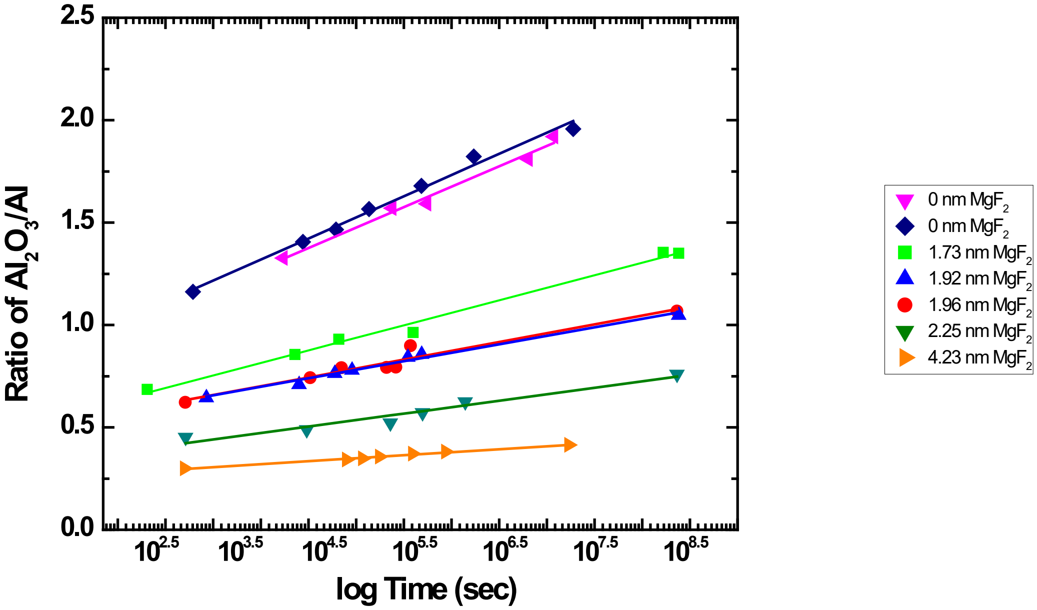

Figure 2-6 Extent of aluminum oxidation as measured by XPS. The ratio of the area of the Al peak in aluminum oxide divided by the area of the aluminum peak from unoxidized aluminum as a function of time on a log graph.

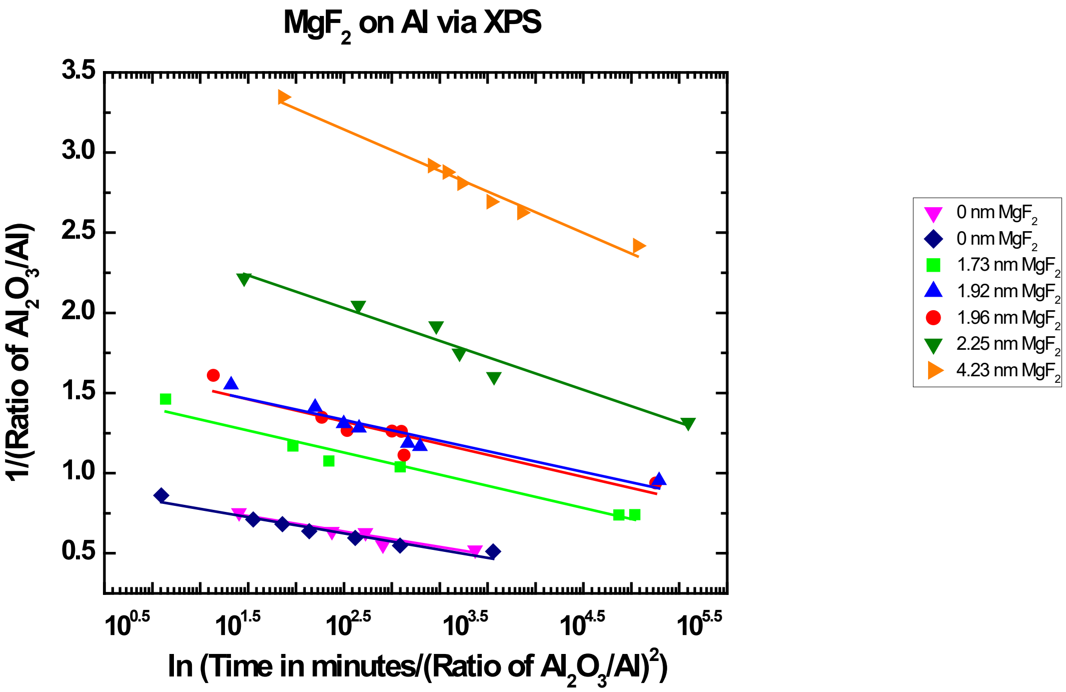

Fig. 2-7. Bare aluminum films and under various thickness of MgF$_2$ overlayers. Cabrera-Mott type plot. 1/thickness vs log (time/ thickness^2)

2.8 Acknowledgements

We thankfully acknowledge John E. Ellsworth, Department of Physics and Astronomy, Brigham Young University for his help with vacuum systems and BYU’s College of Physical and Mathematical Sciences for student support.

We would also like to gratefully acknowledge the Utah NASA Space Grant Consortium under a NASA award- #NNX15AI24H to Utah Space Grant Consortium for funding a portion of Brian Johnson’s research time and for supporting the project generally.

2.9 References

1. Brune, H.; Wintterlin, J.; Trost, J.; Ertl, G.; Wiechers, J.; Behm, R., Interaction of oxygen with Al (111) studied by scanning tunneling microscopy. *The Journal of chemical physics* **1993,** *99* (3), 2128-2148.

2. Wintterlin, J.; Brune, H.; Höfer, H.; Behm, R., Atomic scale characterization of oxygen adsorbates on Al (111) by scanning tunneling microscopy. *Applied Physics A* **1988,** *47* (1), 99-102.

3. Batra, I. P.; Kleinman, L., Chemisorption of oxygen on aluminum surfaces. *Journal of electron spectroscopy and related phenomena* **1984,** *33* (3), 175-241.

4. Fateh, B.; Brooks, G.; Rhamdhani, M.; Taylor, J.; Davis, J.; Lowe, M., Study of Early Stage Interaction of Oxygen with Al; Methods, Challenges and Difficulties. In *Light Metals 2011*, Springer: 2011; pp 725-730.

5. Kotenev, V., Combining ellipsometry and electron microscopy for identifying the initial stages of aluminum oxidation II. Ellipsometry. *Protection of metals* **2000,** *36* (5), 409-418.

6. Khan, J.; Makowiecki, D., Investigation of room-temperature oxidation of aluminum thin films by scanning high-energy electron diffraction. *Surface Science* **1978,** *77*, L155-L161.

7. Do, T.; McIntyre, N., Pressure effects on aluminium oxidation kinetics using X-ray photoelectron spectroscopy and parallel factor analysis. *Surface science* **1999,** *440* (3), 438-450.

8. Krueger, W. H.; Pollack, S., The initial oxidation of aluminum thin films at room temperature. *Surface Science* **1972,** *30* (2), 263-279.

9. Hass, G.; Hunter, W.; Tousey, R., Reflectance of evaporated aluminum in the vacuum ultraviolet. *JOSA* **1956,** *46* (12), 1009-1012.

10. Palik, F. G. a., Aluminum Oxide (Al2O3). In *The Handbook of Optical Constants II*, Academic Press: 1991; Vol. II, pp 761–775.

11. De Marcos, L. V. R.; Larruquert, J. I.; Méndez, J. A.; Gutiérrez-Luna, N.; Espinosa-Yáñez, L.; Honrado-Benítez, C.; Chavero-Royán, J.; Perea-Abarca, B., Optimization of MgF 2-deposition temperature for far UV Al mirrors. *Optics express* **2018,** *26* (7), 9363-9372.

12. Wilbrandt, S.; Stenzel, O.; Nakamura, H.; Wulff-Molder, D.; Duparré, A.; Kaiser, N., Protected and enhanced aluminum mirrors for the VUV. *Applied optics* **2014,** *53* (4), A125-A130.

13. Hunter, W.; Osantowski, J.; Hass, G., Reflectance of aluminum overcoated with MgF 2 and LiF in the wavelength region from 1600 Å to 300 Å at various angles of incidence. *Applied optics* **1971,** *10* (3), 540-544.

14. Cox, J.; Hass, G.; Waylonis, J., Further studies on LiF-overcoated aluminum mirrors with highest reflectance in the vacuum ultraviolet. *Applied optics* **1968,** *7* (8), 1535-1540.

15. Bridou, F.; Cuniot-Ponsard, M.; Desvignes, J.-M.; Maksimovic, I.; Lemaire, P. In *VUV mirrors for the (80-120 nm) spectral range*, Advances in Optical Thin Films, International Society for Optics and Photonics: 2004; pp 627-636.

16. Bolcar, M. R.; Balasubramanian, K.; Crooke, J.; Feinberg, L.; Quijada, M.; Rauscher, B. J.; Redding, D.; Rioux, N.; Shaklan, S.; Stahl, H. P., Technology gap assessment for a future large-aperture ultraviolet-optical-infrared space telescope. *Journal of Astronomical Telescopes, Instruments, and Systems* **2016,** *2* (4), 041209.

17. Balasubramanian, K.; Hennessy, J.; Raouf, N.; Nikzad, S.; Ayala, M.; Shaklan, S.; Scowen, P.; Del Hoyo, J.; Quijada, M. In *Coatings for UVOIR telescope mirrors*, UV/Optical/IR Space Telescopes and Instruments: Innovative Technologies and Concepts VII, International Society for Optics and Photonics: 2015; p 96020I.

18. Hennessy, J. J.; Balasubramanian, K.; Moore, C. S.; Jewell, A. D.; Nikzad, S.; France, K. C.; Quijada, M. A., Performance and prospects of far ultraviolet aluminum mirrors protected by atomic layer deposition. *Journal of Astronomical Telescopes, Instruments, and Systems* **2016,** *2* (4), 041206.
19. Fleming, B.; Quijada, M.; Hennessy, J.; Egan, A.; Del Hoyo, J.; Hicks, B. A.; Wiley, J.; Kruczek, N.; Erickson, N.; France, K., Advanced environmentally resistant lithium fluoride mirror coatings for the next generation of broadband space observatories. *Applied Optics* **2017,** *56* (36), 9941-9950.
20. Moore, C. S.; Hennessy, J.; Jewell, A. D.; Nikzad, S.; France, K. In *Recent developments and results of new ultraviolet reflective mirror coatings*, Space Telescopes and Instrumentation 2014: Ultraviolet to Gamma Ray, International Society for Optics and Photonics: 2014; p 91444H.
21. Hennessy, J.; Moore, C. S.; Balasubramanian, K.; Jewell, A. D.; Carter, C.; France, K.; Nikzad, S. In *Atomic layer deposition and etching methods for far ultraviolet aluminum mirrors*, Astronomical Optics: Design, Manufacture, and Test of Space and Ground Systems, International Society for Optics and Photonics: 2017; p 1040119.
22. Hennessy, J.; Moore, C. S.; Balasubramanian, K.; Jewell, A. D.; France, K.; Nikzad, S., Enhanced atomic layer etching of native aluminum oxide for ultraviolet optical applications. *Journal of Vacuum Science & Technology A: Vacuum, Surfaces, and Films* **2017,** *35* (4), 041512.
23. Hilfiker, J. N.; Singh, N.; Tiwald, T.; Convey, D.; Smith, S. M.; Baker, J. H.; Tompkins, H. G., Survey of methods to characterize thin absorbing films with spectroscopic ellipsometry. *Thin Solid Films* **2008,** *516* (22), 7979-7989.
24. Allred, D. D.; Turley, R. S.; Thomas, S. M.; Willett, S. G.; Greenburg, M. J.; Perry, S. B. In *Adding EUV reflectance to aluminum-coated mirrors for space-based observation*, UV/Optical/IR Space Telescopes and Instruments: Innovative Technologies and Concepts VIII, International Society for Optics and Photonics: 2017; p 103980Y.
25. Miles, M. In *Evaporated Aluminum Fluoride as a Barrier Layer to Retard Oxidation of Aluminum Mirrors,*, Brigham Young University, Brigham Young University, 2017.
26. Johnson, B. I.; Avval, T. G.; Hodges, G. T.; Carver, V.; Membreno, K.; Allred, D. D.; Linford, M. R. In *Using ellipsometry and x-ray photoelectron spectroscopy for real-time monitoring of the oxidation of aluminum mirrors protected by ultrathin MgF2 layers*, Astronomical Optics: Design, Manufacture, and Test of Space and Ground Systems II, International Society for Optics and Photonics: 2019; p 111160O.
27. Johnson, B. I.; Avval, T. G.; Hodges, G.; Membreno, K.; Carver, V.; Allred, D. D.; Linford, M. R., Oxidation of Aluminum Protected by Wide Band Gap MgF2 Layers as Followed by X-ray Photoelectron Spectroscopy. In *TechCon 2019 62nd Annual SVC Technical Conference*, Long Beach Convention Center, Ca, 2019.
28. Johnson, B. I.; Avval, T. G.; Hodges, G.; Membreno, K.; Allred, D. D.; Linford, M. R., Real-Time Monitoring of Aluminum Oxidation Through Wide Band Gap MgF2 Layers for Protection of Space Mirrors. In *25th Annual Fellowship Symposium*, Brigham Young University, 2019.
29. Cumpson, P. J.; Seah, M. P., Elastic scattering corrections in AES and XPS. II. Estimating attenuation lengths and conditions required for their valid use in overlayer/substrate experiments. *Surface and Interface Analysis: An International Journal devoted to the development and application of techniques for the analysis of surfaces, interfaces and thin films* **1997,** *25* (6), 430-446.

30. Cumpson, P. J., The Thickogram: a method for easy film thickness measurement in XPS. *Surface and Interface Analysis: An International Journal devoted to the development and application of techniques for the analysis of surfaces, interfaces and thin films* **2000,** *29* (6), 403-406.

31. Baba, K.; Shiraishi, K.; Obi, K.; Kataoka, T.; Kawakami, S., Optical properties of very thin metal films for laminated polarizers. *Applied optics* **1988,** *27* (12), 2554-2560.

32. Tompkins, H. G.; Tasic, S.; Baker, J.; Convey, D., Spectroscopic ellipsometry measurements of thin metal films. *Surface and Interface Analysis: An International Journal devoted to the development and application of techniques for the analysis of surfaces, interfaces and thin films* **2000,** *29* (3), 179-187.

33. Fox, M., Optical properties of solids. Oxford University Press (Oxford, 2001): 1970.

34. Smith, D.; Shiles, E.; Inokuti, M.; Palik, E., Handbook of optical constants of solids. *Handbook of Optical Constants of Solids* **1985,** *1*, 369-406.

35. Nguyen, H. V.; An, I.; Collins, R., Evolution of the optical functions of thin-film aluminum: A real-time spectroscopic ellipsometry study. *Physical Review B* **1993,** *47* (7), 3947.

36. Movchan, B.; Demchishin, A., STRUCTURE AND PROPERTIES OF THICK CONDENSATES OF NICKEL, TITANIUM, TUNGSTEN, ALUMINUM OXIDES, AND ZIRCONIUM DIOXIDE IN VACUUM. *Fiz. Metal. Metalloved. 28: 653-60 (Oct 1969).* **1969**.

37. Ohring, M., *Materials science of thin films*. Elsevier: 2001.

38. Jain, V.; Biesinger, M. C.; Linford, M. R., The Gaussian-Lorentzian Sum, Product, and Convolution (Voigt) functions in the context of peak fitting X-ray photoelectron spectroscopy (XPS) narrow scans. *Applied Surface Science* **2018,** *447*, 548-553.

39. Shah, D.; Patel, D. I.; Roychowdhury, T.; Rayner, G. B.; O'Toole, N.; Baer, D. R.; Linford, M. R., Tutorial on interpreting x-ray photoelectron spectroscopy survey spectra: Questions and answers on spectra from the atomic layer deposition of Al2O3 on silicon. *Journal of Vacuum Science & Technology B, Nanotechnology and Microelectronics: Materials, Processing, Measurement, and Phenomena* **2018,** *36* (6), 062902.

40. Sherwood, P. M., Curve fitting in surface analysis and the effect of background inclusion in the fitting process. *Journal of Vacuum Science & Technology A: Vacuum, Surfaces, and Films* **1996,** *14* (3), 1424-1432.

41. Rotole, J. A.; Sherwood, P. M., Gamma-alumina (γ-Al2O3) by XPS. *Surface Science Spectra* **1998,** *5* (1), 18-24.

42. Rotole, J. A.; Sherwood, P. M., Corrundum (α-Al2O3) by XPS. *Surface Science Spectra* **1998,** *5* (1), 11-17.

43. Wyatt, D. M.; Gray, R. C.; Carver, J. C.; Hercules, D. M.; Masters, L. W., Studies of Polymeric Bond Failure on Aluminum Surfaces by X-ray Photoelectron Spectroscopy (ESCA). *Applied Spectroscopy* **1974,** *28* (5), 439-445.

44. Strohmeier, B. R., Gamma-Alumina (γ-Al2O3) by XPS. *Surface Science Spectra* **1994,** *3* (2), 135-140.

45. Chen, S.; Brown, L.; Levendorf, M.; Cai, W.; Ju, S.-Y.; Edgeworth, J.; Li, X.; Magnuson, C. W.; Velamakanni, A.; Piner, R. D., Oxidation resistance of graphene-coated Cu and Cu/Ni alloy. *ACS nano* **2011,** *5* (2), 1321-1327.

46. Galbiati, M.; Stoot, A. C.; Mackenzie, D.; Bøggild, P.; Camilli, L., Real-time oxide evolution of copper protected by graphene and boron nitride barriers. *Scientific reports* **2017,** *7*, 39770.

47. Ghez, R., On the Mott-Cabrera oxidation rate equation and the inverse-logarithmic law. *The Journal of Chemical Physics* **1973,** *58* (5), 1838-1843.

48. Martin, M.; Fromm, E., Kinetics of aluminium film oxidation measured by a modified quartz crystal microbalance. *Thin Solid Films* **1993,** *236* (1-2), 199-203.

49. Martin, M.; Mader, W.; Fromm, E., Oxidation of iron, aluminium and titanium films in the temperature range 50–200° C. *Thin Solid Films* **1994,** *250* (1-2), 61-66.

50. Grimblot, J.; Eldridge, J. M., II. Oxidation of Al Films. *Journal of the Electrochemical Society* **1982,** *129* (10), 2369-2372.

51. Young, D.; Dignam, M., Metal oxidation—II. Kinetics in the thin and very thin film regions under conditions of electron equilibrium. *Journal of Physics and Chemistry of Solids* **1973,** *34* (7), 1235-1250.

52. Fehlner, F. P., Low temperature oxidation, the role of vitreous oxides. **1986**.

CHAPTER 3: Semi-Empirical Peak Fitting Guided by Ab Initio Calculations of X-Ray Photoelectron Spectroscopy Narrow Scans of Chemisorbed, Fluorinated Silanes

3.1 Statement of Attribution

Paper submitted to Surface and Interface Analysis October 2019-Brian I. Johnson, Tahereh G. Avval, Joshua John Wheeler, Hans Anderson, Kara J. Stowers, Daniel H. Ess, Matthew R. Linford* Department of Chemistry and Biochemistry, Brigham Young University, C100 BNSN, Provo, Utah 84602

3.2 Abstract

Here we address the issue of finding correct CF_2/CF_3 area ratios from X-ray photoelectron spectroscopy (XPS) C 1s narrow scans of materials containing $–CH_2CH_2(CF_2)_nCF_3$, n = 0, 1, 2, …, moieties. For this work, we modified silicon wafers with four different fluorosilanes. The smallest had a trifluoropropyl (n = 0) moiety, followed by nonafluorohexyl (n = 3), tridecafluoro (n = 5), and finally heptadecafluoro (n = 7) moieties. Monolayer deposition of the fluorosilanes was confirmed by spectroscopic ellipsometry (SE), wetting, and XPS. Analysis of the trifluoropropyl (n = 0) surface and a sample of polytetrafluoroethylene provided pure component XPS spectra for $–CF_3$ and $–(CF_2)_n–$ moieties, respectively. Initial XPS C 1s peak fitting, which was not entirely adequate, followed Literature precedent. Additional insight into the fluorosilane adsorbates and C 1s fits was provided by density functional theory (DFT). By combining DFT results with empirical analyses, we obtained more accurate CF_2/CF_3 area ratios while maintaining high quality fits. Overall, six different fitting approaches with increasing complexity and/or input from theory were considered.

3.3 Introduction

A useful method for adding hydrophobic functionality to many materials is to coat them with a thin film containing hydrocarbon and/or fluorocarbon moieties, e.g., polymers or small molecules containing the $–CH_2CH_2(CF_2)_nCF_3$ group.[1-4] Such low free energy surfaces (hydrophobic and superhydrophobic)[2, 5-9] generally exhibit low friction and adhesion and have important applications in, for example, micro/nano electrical mechanical systems (NEMS/MEMS) and self-cleaning surfaces.[4, 7, 10] Commonly used methods for characterizing these materials, which has often been through multi-technique/multi-instrument analyses,[11] include X-ray photoelectron spectrometry (XPS), water contact angle goniometry (WCA), Fourier transform infrared spectroscopy (FTIR), atomic force microscopy (AFM), scanning electron microscopy (SEM), spectroscopic ellipsometry (SE), and time-of-flight secondary ion mass spectrometry (ToF-SIMS).[1, 12] Less common/more exotic methods such as low energy ion scattering (LEIS), and the gamut of advanced methods available at synchrotrons have also been of value here.[13-16] Each of these techniques provides unique information.

XPS is the most widely employed method for chemically analyzing surfaces, and its use has grown rapidly over the past few decades.[17-19] XPS owes its success to the fact that it can quantitatively provide: (i) surface concentrations through integration of peaks in survey and narrow scans, (ii) oxidation state information about the elements in a material (often) through peak fitting, and (iii) surface morphologies through analysis of inelastic backgrounds.[18, 20-22] However, XPS data work-up is often nontrivial. Issues that should be addressed in XPS peak fitting include determining the correct baseline, the functional form of the synthetic peaks, the binding energy (BE) assignments of the fit components, their FWHM values, and their peak area ratios. Good XPS data analysis relies on operator skill/experience, prior knowledge of the sample, information from other characterization techniques, an understanding of one's instrument, and literature precedent.[17, 22, 23]

Peak fitting and model building are central to the scientific enterprise. However, when building a model, there is a tension between including enough parameters to make it a reasonable representation of the underlying physics and chemistry, but not so many that fit parameter correlation[24] or over fitting of the data (fitting the noise) occurs – an overly large number of fit parameters in a model can easily cause the values assigned to them to become physically meaningless. Thus, model/fit validity can often be improved by reducing the number of fit parameters and/or by better defining or constraining them. Fits with too many parameters can often be identified with uniqueness plots or Monte Carlo analyses.[24, 25] An additional approach for improving XPS models, i.e., peak fitting, is to obtain additional information about the adsorbed species and/or surface via ab initio (quantum) calculations.[26] These first principles calculations typically provide predictions of the number of oxidation states/fit components in a peak envelope and their positions (binding energies, BEs).[27, 28]

Tardio and Cumpson[29] and Zuilhof et al.[26] recently noted that core electron BEs can be simply approximated as the ionization energy (E) from the associated core level electron (Eq. 1).

(1) $BE = -E$

Recent studies have used ab initio and density functional theory (DFT) methods to guide XPS (and near ambient pressure XPS, NAP-XPS) peak fitting to substantiate experimental data, predict energy shifts, interpret spectra, and study surface states.[26, 29, 30, 27, 31-34] Rather than calculating the complete BE, a commonly used approximation has been to use a Koopman's theorem-based approach.[26] Here, the BE is approximated as the negative of the orbital energy via Hartree-Fock

(HF) calculations, where the orbital relaxation (R) and electron correlation (ΔC) terms are neglected (note that they are not in Eq. 1). While an approximation, this approach is well suited for C 1s XPS data from organic materials.[26] This method is computationally efficient, and C 1s XPS data can be predicted with 0.3 eV accuracy.[26] Therefore, a Koopman's theorem-based approach was used in this study.

In this work, we developed a series of increasingly sophisticated models (Models (a) – (f) (see Table 3-1)) for understanding perfluorocarbon silane adsorption onto surfaces.

Table 3-1 Descriptions of the models considered in this study.

Model	Number of CF_2 peaks	FWHM Value Constraints	Area Constraints	Input from Ab Initio Calc.
(a)	1	None	None	No
(b)	1	Set to value from standards	None	No
(c)	1	Set to value from standards	Set to theoretical values	No
(d)	One for each CF_2 moiety	Set to value from standards	All peak areas set equal	All peaks constrained to ab initio positions
(e)	3	Set to value from standards	2 CF_2 peak areas set equal to the CF_3 peak area, the other CF_2 area floated	Constraints on the three CF_2 BEs
(f)	One for each CF_2 moiety	Set to value from standards	All peak areas set equal	All CF_2 BEs Constrained Relative to Each Other

These models fitted the CF_2/CF_3 region of the spectra we analyzed. The hydrocarbon regions at lower binding energies, which showed evidence for adventitious carbon, were not considered in this analysis. In our first model, Model (a), the CF_2/CF_3 envelope was described using two unconstrained peaks: one for the CF_2 moieties and the other for the CF_3 groups, i.e., one peak to describe all the CF_2 moieties. The resulting fits were good, but the slope of the linear fit to the CF_2/CF_3 ratios from the models vs. the theoretical CF_2/CF_3 ratios, m_{CF_2/CF_3}, was lower than the expected value of unity. To aid in this fitting, we next determined experimental peak widths of the $–CF_2–$ and $–CF_3$ groups using pure/model compounds. Based on these peak widths, we developed two empirical models. The first of these, Model (b), consisted of two peaks (one for the –CF_2– moieties), where the FWHM values for these peaks were set to the value obtained from the standards. Unfortunately, m_{CF_2/CF_3} was further from its theoretical value here than it was in Model (a). In Model (c), one peak described the –CF_2– moieties, the FWHM values were set to the values obtained from the standards, and the peak areas were set to their theoretical values. Unfortunately, the standard deviation of the residuals (STDRes) of this fit was high. Models (d), (e), and (f) rely on input from ab initio calculations. In Model (d), every CF_2 group in each molecule (and the CF_3 group) was represented by a separate peak. These peaks had equal areas and their relative positions were obtained from the ab initio calculations. The STDRes values of this fit was also high. In Model (e), the CF_2 envelope was fitted with three peaks: one for each of the two CF_2 groups that were closest to the CH_2CH_2 moiety in the silanes (these peaks had the same area as the CF_3 peak), and another peak to represent the remaining CF_2 groups (its area was not constrained). The STDRes values for these fits were low. This is arguably the best model we developed. In the final model, Model (f), a fit component was included for every fluorinated carbon in the silane (as in Model (d)). However, the positions of the CF_3 and group of CF_2 peaks were allowed to move independently of each other (the CF_2 peak positions were constrained based on the ab initio calculations relative to each other). This fit was also of high quality. However, this fit required knowledge of the structure of the adsorbates. Because of the importance of fluorinated materials and XPS we believe that these results will be relevant to the surface and materials community.

3.4 Experimental

3.4.1 Instrumentation

XPS was performed with a Service Science SSX-100 instrument (maintained by Service Physics, Bend, OR, USA) that employed monochromatic Al Kα X-rays, a hemispherical analyzer, and a take-off angle of 35°. Survey scans were obtained with an X-ray spot size of 800 x 800 μm^2 with a resolution of 4 (nominal pass energy of 150 eV), with 5 passes, and a step size of 1 eV. High resolution scans were collected over the C 1s regions centered at a BE of 290 eV with an energy window of 30 eV and a step size of 0.0625 eV. The number of scans was 35, and the spot size was 800 x 800 μm^2 with a resolution of 3 (nominal pass energy of 100 eV). Charge compensation was not employed during this data acquisition. Area ratios were calculated, and peak fitting performed, using the CasaXPS modelling software (Casa Software Ltd., Version 2.3.18PR1.0), where the quality of the fits was determined based on the STDRes values of a given fit. SE was performed with a variable angle spectroscopic ellipsometer (M-2000D, J.A. Woollam, Lincoln, ME, USA, wavelength range: ca. 190-1688 nm). Data were acquired at 75° and subsequently modelled using the CompleteEASE software from the J.A. Woollam Company. Native oxide – terminated silicon and also fluorosilane films on native oxide – terminated silicon were modeled in the same way, i.e., as films of silicon dioxide on silicon using the optical functions for SiO_2 and Si provided in the instrument software (SiO2_JAW and Si_JAW, respectively). This approach is reasonable because of the weak dependence of film thickness on material optical functions for very thin films.[30] The thickness of each fluorosilane film was taken as the difference between the thicknesses of the 'SiO_2' layers measured before and after the fluorosilane deposition. Water Contact Angle (WCA) Goniometry was performed with a Ramé-Hart (Netcong, NJ) contact angle goniometer (Model 100–00) fitted with a manual syringe.

3.4.2 Deposition of Fluorosilanes

3.4.2.1 Reagents

(3,3,3-Trifluoropropyl)tricholorsilane, $CF_3(CH_2)_2SiCl_3$, (3,3,4,4,5,5,6,6,6-nonafluorohexyl)trichlorosilane, $CF_3(CF_2)_3(CH_2)_2SiCl_3$, (tridecafluoro-1,1,2,2-tetrahydrooctyl)tricholorsilane, $CF_3(CF_2)_5(CH_2)_2SiCl_3$, and (heptadecafluoro-1,1,2,2-tetrahydrodecyl)tricholorsilane, $CF_3(CF_2)_7(CH_2)_2SiCl_3$, were used as received from Gelest (Morrisville, PA), see Figure 3-1. Millipore Mili-Q 18 MΩ-cm distilled water was used to measure the static (θ_s), advancing (θ_a), and receding (θ_r) WCAs. Isooctane (2,2,4-trimethylpentane) was used as received from Alfa Aesar/Fisher Scientific (Houston, TX). Sulfuric acid and 30% hydrogen peroxide were obtained from Fisher Chemical (Houston TX) and used as received.

3.4.2.2 Silicon cleaning

Native-oxide terminated pieces of silicon were rinsed with isopropyl alcohol, dried with a jet of nitrogen, rinsed with methanol, dried again with nitrogen, and then cleaned in piranha solution (7:3 H_2SO_4(conc.)/H_2O_2(conc.)) for 2 h at ca. 90 °C. The surfaces were then rinsed with high purity water and stored/immersed for ca. 30 min in high purity water before they were used. *Piranha solution is extremely dangerous. It reacts violently with many organic materials. It should be handled with great care and disposed of in accord with institutional and governmental regulations.*

3.4.2.3 Fluorosilane deposition

Clean, dry pieces of silicon were immersed in 10 mM solutions of a trichlorofluorosilane in isooctane for 10 min. All depositions were performed under a blanket of an inert gas (N_2). Each deposition was repeated in triplicate.[31]

2.2.4. Analysis of polytetrafluoroethylene by XPS.

A piece of polytetrafluoroethylene was purchased from the BYU Chemistry Department stock room, cleaned with Millipore Mili-Q 18 MΩ-cm distilled water, and blown dry with nitrogen. It was then mounted onto a piece of silicon using double-sided conductive carbon tape, and analyzed by XPS with a fine nickel mesh 0.5 – 1 mm over its surface to help compensate for charging. The instrument flood gun was set at 5 eV during data acquisition, and the BEs of the spectra were corrected to the F 1s signal.

3.4.3 Computational Methodology

Quantum chemical calculations were performed using the Gaussian 09 software.[32] HF/6-31G* geometry optimizations and frequency evaluations were performed on the perflourocarbon silane models with n = 0, 3, 5, and 7 in $–CH_2CH_2(CF_2)_nCF_3$ carbon chains. Energies were also evaluated with HF/6-31+G* (which gave nearly identical results to the HF/6-31G*) as well as the M06-2X/6-31G*, and B3LYP/6-31G* which gave nearly identical results to each other. Relative BE differences between different carbon atoms and peak splitting were calculated using core 1s Kohn-Sham and HF orbital energies.[26, 29]

3.5 Results and Discussion

3.5.1 SE and WCAs of Fluorosilane-Modified Surfaces

In this study, we deposited four fluorosilanes ($CF_3(CH_2)_2SiCl_3$, $CF_3(CF_2)_3(CH_2)_2SiCl_3$, $CF_3(CF_2)_5(CH_2)_2SiCl_3$, and $CF_3(CF_2)_7(CH_2)_2SiCl_3$) onto silicon wafers from isooctane solutions. These adsorbates can be described by their $–CH_2CH_2(CF_2)_nCF_3$ moieties with n = 0, 3, 5, and 7, respectively. The characterization of the resulting surfaces involved multiple instruments[11] as well as theoretical and semi-empirical modeling. After preparation, these surfaces were pristine; they had no visible defects. Spectroscopic ellipsometry, SE,[33-35] showed 1 – 2 nm increases in film thickness after the depositions, where the longest adsorbate ($CF_3(CF_2)_7(CH_2)_2SiCl_3$) appeared to produce the thickest film (see Figure 3-2). Note that while the fluorosilane adsorbates used in this study are capable of polymerizing, the rather thin films that were obtained from them suggest approximately monolayer quantities of material. Water contact angle (WCA) goniometry is another rapid and convenient method for probing surfaces.[36, 37] As expected, clean, bare silicon showed very low WCAs (<10°), which suggests that most of the adventitious hydrocarbon on it had been removed. After the fluorosilane depositions, the wetting properties of these surfaces changed dramatically – the advancing water contact angles, $\theta_a(H_2O)$, rose to ca. 90° for the three-carbon adsorbate and then up to ca. 120° for the longer chain adsorbates (see Figure 3-2). This increase in hydrophobicity with increasing number of carbons in the fluoroalkylsilane adsorbate is consistent with literature results.[38] As additionally indicated in Figure 3-2, the contact angle hysteresis, $\theta_a(H_2O) - \theta_r(H_2O)$, decreased as the number of carbons in the adsorbate increased.

3.5.2 Initial XPS Analysis

XPS survey and accompanying narrow scans were collected from the fluorosilane modified surfaces prepared in this study. The survey spectra[39] of all of the surfaces were quite similar – they contained O Auger, F Auger, F 1s, O 1s, C 1s, Si 2s, and Si 2p signals (see Figure 3-3). The split C 1s signal in Figure 3 is consistent with different chemical states for carbon. In the C 1s narrow scans (see Figure 3-4), there were two obvious features that correlated with the structures of the silane adsorbates. The first is the increase in intensity of the CF_2/CF_3 peaks (the portion of the peak envelope above ca. 289 eV, which we will refer to as the CF_2/CF_3 C 1s envelope) compared to the hydrocarbon region of the spectrum (the portion of the peak envelope below ca. 289 eV) with increasing number of fluorinated carbons in the adsorbate. The second is the increase in the CF_2 signal (at ca. 291.5 eV) relative to the CF_3 signal (at ca. 293.8 eV) with increasing fluorocarbon chain length.[5, 12, 40, 41] In Figure 3-4, the goodness of each fit is indicated by the STDRes value and the residuals to the fits.

3.5.3 C 1s Narrow Scan Analysis

3.5.3.1 Unconstrained model

Our first C1s narrow scan analysis (Model (a), see Table 3-1) was performed using two peaks to model the CF_2 and CF_3 signals in which these two fit components were unrestrained, i.e., their positions and FWHM values floated. The resulting fits were quite good (Figure 3-4a) with STDRes values of 0.90 ± 0.04 (average and standard deviation from six different narrow scans). However, the slope of the plot of the CF_2/CF_3 ratio from the fits vs. the theoretical CF_2/CF_3 ratio, m_{CF_2/CF_3}, was lower than the expected value of unity: 0.71 ± 0.05, and the y-intercept was too high (see Table 3-2). Note that in this and all subsequent fits, the hydrocarbon portion of the C 1s envelopes were fit with two or three unconstrained peaks – only purpose of these peaks was to match the hydrocarbon envelope – they do not have any theoretical significance.

Table 3-2 Results from fits to straight lines (y = mx + b) of the CF_2/CF_3 ratios obtained from our peak fitting vs. the theoretical CF_2/CF_3 ratios. When the CF_2/CF_3 ratios were constrained to their theoretical values, $m_{CF_2/CF_3} = 1$ and the y-intercept is zero.

Model*	Slope (m_{CF_2/CF_3})	y-intercept	R^2
(a)	0.71 ± 0.05	0.14 ± 0.22	0.9913
(b)	0.65 ± 0.05	0.18 ± 0.25	0.9860
(c)	1.000	0.000	1.000
(d)	1.000	0.000	1.000
(e)	0.91 ± 0.01	-0.03 ± 0.04	0.9998
(f)	1.000	0.000	1.000

*As depicted in Figure 3-4.

Finally, with regards to these fits and those discussed below, different synthetic peaks (Gaussian-Lorentzian sum, GLS, and product functions, GLP) with different degrees of Lorentzian character were considered.[22] [5, 42-46] The GLP functions did not describe the peak envelopes as well as the GLS functions. Best fits were generally obtained with SGL peaks with 20 – 30% Lorentzian character. Accordingly, all the peak fitting in this study was performed with SGL peaks with 25% Lorentzian character.

3.5.3.2 Determination of pure component peak widths

The width/FWHM value of a synthetic peak component plays an important role in XPS peak fitting. Because there is no $–CF_2–$ signal to overlap with it, the $CF_3(CH_2)_2SiCl_3$ thin film shows an isolated peak for the $–CF_3$ moiety. It had a width of 1.76 ± 0 eV (data from two different samples). PTFE was used as a pure material to determine/estimate the width of its $–CF_2–$ peak, which was 1.785 ± 0.5 eV (data from two different samples). Based on these results, we used a FWHM value of 1.77 eV for all the fit components (synthetic peaks) in this study. This value is in reasonable agreement with the FWHM value of 1.60 eV used by Ewen and co-workers in their XPS analysis of poly(perfluoroalkyl methacrylate) films,[47] and the FWHM values of 1.79, 1.61, and 1.78 eV used by Sakai and co-workers for their CF, CF_2, and CF_3 fit components, respectively, in their XPS analysis of fluorinated, plasma enhanced chemical vapor deposition films.[45]

3.5.3.3 Two-peak models with constrained peak widths

The next two attempts to model the fluorocarbon portion of the C 1s envelopes of surfaces modified with $CF_3(CF_2)_3(CH_2)_2SiCl_3$, $CF_3(CF_2)_5(CH_2)_2SiCl_3$, and $CF_3(CF_2)_7(CH_2)_2SiCl_3$ were with two fit components that were again assumed to correspond to $–CF_2–$ and $–CF_3$ moieties. The first of these attempts (see Figure 3-4b and Model (b) in Table 3-1) gave these peaks equal FWHM values of 1.77 eV (see Section 3.3.1), which were otherwise unconstrained in position and area. This approach yielded good fits to the C 1s envelopes with STDRes values of 0.95 ± 0, 1.23 ± 0.04, and 1.25 ± 0.01, for the adsorbates with n = 3, 5, and 7 in $–CH_2CH_2(CF_2)_nCF_3$, respectively. However, m_{CF_2/CF_3} was again lower than expected: 0.65 ± 0.05, and the y-intercept was too high (see Figure 3-5 and Table 3-2).

In the second attempt with two synthetic fit components (see Figure 3-4c and Model (c) in Table 3-1), the area ratios of the $–CF_2–$ and $–CF_3$ fit components were set to their theoretical values so that only their positions were allowed to vary. The resulting STDRes values rose to 1.41 ± 0.04, 1.85 ± 0.05, and 2.10 ± 0.09, respectively. That is, the first of these empirical models offers a good fit, but a low value of m_{CF_2/CF_3}, while the second model offers a perfect value of m_{CF_2/CF_3}, by constraint, but a lower quality fit. It was a goal of this study to obtain both good $–CF_2–$ to $–CF_3$ ratios (m_{CF_2/CF_3} values) and good fits.

3.5.3.4 Calculations

To gain insight into the fitting of our CF_2/CF_3 C 1s envelopes, we performed DFT calculations on the three longer-chain silanes (n = 0, 3, 5, and 7 in $–CH_2CH_2(CF_2)_nCF_3$). (Figure 3-6) Table 3-3 shows the resulting C 1s binding energies relative to the CF_3 C 1s binding energies in the molecules. These values are the negative values of the ab initio 1s orbital energies.

Table 3-3 Relative C 1s binding energies (top) obtained from ab initio calculations of $CF_3(CF_2)_3(CH_2)_2SiCl_3$ (6 carbons), $CF_3(CF_2)_5(CH_2)_2SiCl_3$ (8 carbons) and $CF_3(CF_2)_7(CH_2)_2SiCl_3$ (10 carbons) referenced to the CF_3 C 1s binding energy in each molecule (set at 0 eV), and differences between the binding energies of adjacent carbon atoms (bottom). The CF_3 C 1s binding energies from the calculations were 314.24, 314.23, and 314.32 eV, respectively.

Carbons	**CH_2(1)**	**CH_2(2)**	**CF_2(1)**	**CF_2(2)**	**CF_2(3)**	**CF_2(4)**	**CF_2(5)**	**CF_2(6)**	**CF_2(end)**	**CF_3**
6	-8.13	-7.80	-2.67	-2.12	N/A	N/A	N/A	N/A	-1.91	0.00
8	-8.73	-7.80	-2.85	-2.20	-1.90	-1.78	N/A	N/A	-1.76	0.00
10	-8.75	-7.89	-2.93	-2.29	-1.98	-1.82	-1.73	-1.69	-1.75	0.00
Differences between adjacent carbons										
6	-0.33	-5.12	-0.56	-0.21	N/A	N/A	N/A	N/A	-1.91	0.00
8	-0.93	-4.95	-0.64	-0.30	-0.12	-0.02	N/A	N/A	-1.76	0.00
10	-0.86	-4.96	-0.65	-0.31	-0.15	-0.09	-0.05	0.06	-1.75	0.00

They reveal that the binding energies of the CF_2 carbons are not constant in these adsorbates. Indeed, the spread in C 1s CF_2 binding energies (highest CF_2 binding energy minus lowest CF_2 binding energy) for the n = 3, 5, and 7 adsorbates is 0.76, 1.09, and 1.18 eV, respectively. These results suggest that the two-peak fits considered in Section 3.3.2 are oversimplifications and that an exploration of more complex models is justified. Table 3-3 lists the differences between the C 1s ab initio BEs of the adjacent carbons in the three adsorbates. These values show that the C 1s BEs of the first two CF_2 groups after the CH_2 group, i.e., $–CH_2\underline{C}F_2CF_2\ldots$ and $–CH_2CF_2\underline{C}F_2\ldots$, are the most different among the CF_2 groups, which otherwise have quite similar binding energies.

We used these calculations to predict the CF_2/CF_3 C 1s envelopes of our silane adsorbates (Model (d) in Table 3-1). This was done by creating a synthetic fit component for each CF_2 and CF_3 entity in a given adsorbate and fixing the relative positions of these peaks to those obtained in the first principle calculations. These peaks were constrained (i) to have the same widths, where this single width was an adjustable parameter in the fits, and (ii) to shift in BE as a group, i.e., the entire group of peaks could move to obtain the best fit, but their relative positions were constrained to the values obtained from the ab initio calculations. Figure 3-4d shows that the resulting fits for the n = 3, 5, and 7 adsorbates were only moderately good, i.e., they showed STDRes values of 1.48 ± 0.17, 1.84 ± 0.01, and 2.19 ± 0.11, respectively. We previously reported the use of DFT calculations to predict an XPS narrow scans.[48] Like the fits here, these previous results were only moderately successful.

While HF/6-31G* ab initio calculations provided insight into our XPS narrow scans, they were unable to fully predict the experimental fluorocarbon envelopes. Accordingly, to improve these results, we performed the same calculations with additional levels of theory (HF/6-31+G**, M06-2X DFT, and B3LYP/6-31G*). Unfortunately, the results from these methods were nearly identical to our original results. For example, for all of these methods, the BE differences between the CF_3 and CF_2 carbons were too small.

3.5.3.5 Semiempirical Model with Input from the DFT Calculations

The results from the previous section suggested that while our ab initio calculations may not be able to fully predict our C 1s narrow scans, they do provide some valuable insight into them. Accordingly, we considered two semiempirical methods for fitting our fluorocarbon C 1s envelopes.

In our first semiempirical fit (Model (e) in Table 3-1), we modeled the CF_2 region with three synthetic peaks that had relative positions predicted by theory, i.e., for each adsorbate their positions were fixed to those of the lowest energy CF_2 peak ($–CH_2\underline{C}F_2CF_2…$), the next lowest energy CF_2 peak ($–CH_2CF_2\underline{C}F_2…$), and the average BE of the remaining CF_2 peaks. The two lower energy CF_2 peaks and the CF_3 peak were constrained to have the same areas. However, the area of the highest energy CF_2 peak was allowed to float. The resulting fits for the 6, 8, and 10 carbon adsorbates showed quite good STDRes values of 0.86 ± 0.01, 1.10 ± 0.08, and 1.49 ± 0.03, respectively (Figure 3-4e), its m_{CF_2/CF_3} value was 0.91 ± 0.01, and its y-intercept is quite close to zero (see Figure 3-5 and Table 3-2). This approach, which has an R^2 value of 0.9998, is arguably the best model considered here.

Our second semiempirical fit (Model (f) in Table 3-1) was quite similar to the fit based solely on the ab initio calculations (Model (d) in Table 3-1). Here, we created separate synthetic peaks of equal area and width for each CF_2 carbon in each adsorbate with relative positions dictated by the ab initio calculations (see Figure 3-4f). A peak with the same area and width was also used to account for the CF_3 signal in the CF_2/CF_3 C 1s envelopes. However, the position of the CF_3 fit component was allowed to vary relative to the CF_2 synthetic peaks – the positions of the CF_2 peaks were decoupled from the position of the CF_3 peak. The only other fit parameter in this model was the peak areas of the peaks, which were the same. By definition, this fit offers an ideal m_{CF_2/CF_3} value of unity. In addition, it results in quite low STDRes values of 1.05 ± 0.02, 1.21 ± 0.02, and 1.52 ± 0.02 for the n = 0, 3, 5, and 7 (in $–CH_2CH_2(CF_2)_nCF_3$) adsorbates.

3.5.3.6 Comparison to Literature Results

In addition to the results from this study, Figure 3-5 shows CF_2/CF_3 ratios obtained from previously reported XPS analysis of materials containing $–CH_2CH_2(CF_2)_nCF_3$, n = 0, 1, 2, …, moieties. Unfortunately, these prior results are a little difficult to compare to ours because the previous authors did not report the synthetic peak shape they used in their fitting, and Tsibouklis et al. were the only ones that reported a FWHM value (1.60 eV) for their fit components. Keeping that uncertainty in mind, we can, however, conclude that Tsibouklis et al. (open green diamonds in Figure 3-5) did a rather good job of obtaining good CF_2/CF_3 ratios from their data. The ratios obtained by Zuo et al. (open, light blue, down triangles in Figure 3-5) were also fairly close to the theoretical ratios. However, their results seemed to diverge from the expected values with an increasing number of CF_2 units. Hozumi et al. reported only two values (open, orange pentagons in Figure 3-5), which differed to a fairly significant extent from the theoretical ratios.

3.6 Conclusion

In this work, we have studied the CF_2/CF_3 C 1s envelopes of four fluorosilane adsorbates: $CF_3(CH_2)_2SiCl_3$, $CF_3(CF_2)_3(CH_2)_2SiCl_3$, $CF_3(CF_2)_5(CH_2)_2SiCl_3$, and $CF_3(CF_2)_7(CH_2)_2SiCl_3$. Starting with a completely unconstrained model, we built increasing complex and/or informed models that yielded better fits, i.e., lower STDRes values, m_{CF_2/CF_3} values closer to unity, y-intercepts approaching 0, and R^2 values approaching 1. Our best fits were semiempirical models that drew on conventional approaches for XPS narrow scan analysis and ab initio calculations.

3.7 Figures

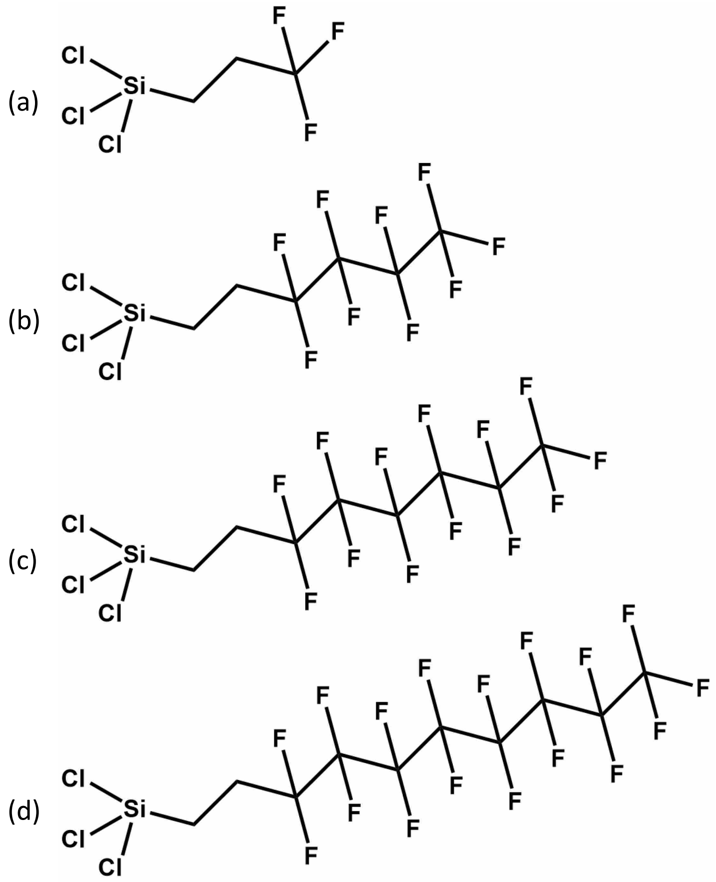

Figure 3-1 Trichlorosilanes used to make standards (a) (3,3,3-trifluoropropyl)tricholorsilane (b) 3,3,4,4,5,5,6,6,6-Nonafluorohexyltrichlorosilane (c) (Tridecafluoro-1,1,2,2-tetrahydrooctyl)tricholorsilane (d) (Heptadecafluoro-1,1,2,2tetrahydrodecyl)tricholorsilane

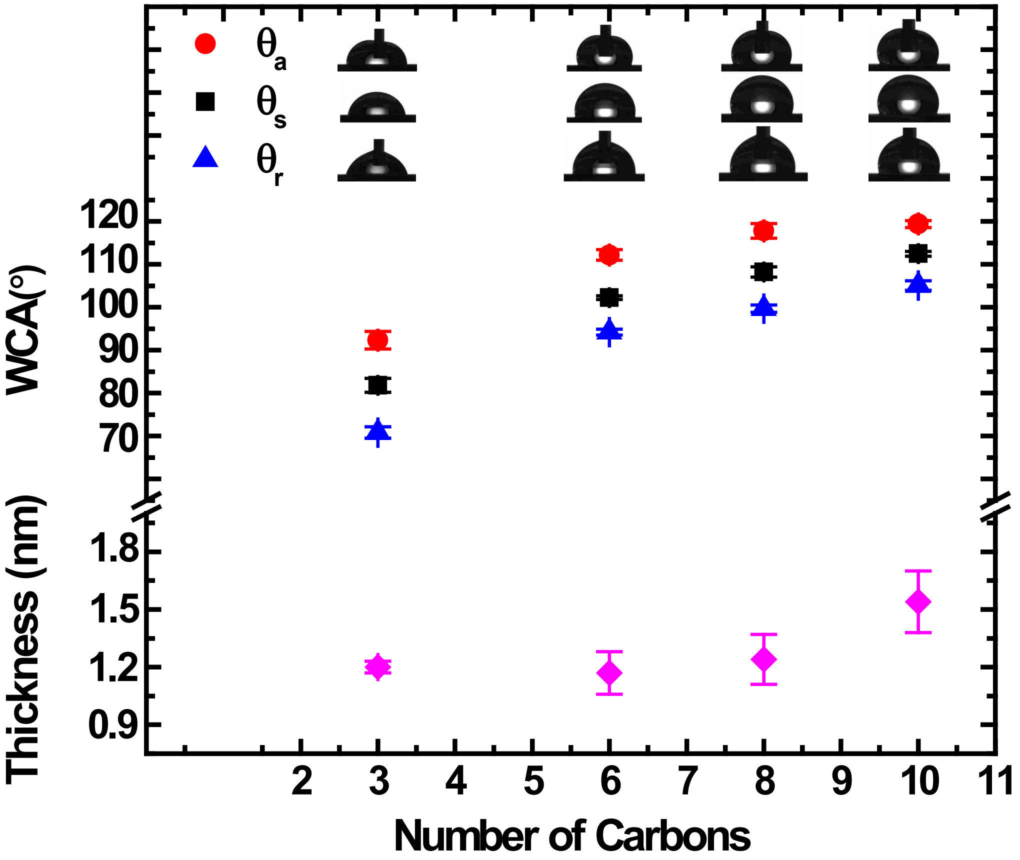

Figure 3-2 Top. Advancing, static, and receding water contact angles (θ_a, θ_s, and θ_r, respectively) of films of $CF_3(CH_2)_2SiCl_3$ (3 carbons), $CF_3(CF_2)_3(CH_2)_2SiCl_3$ (6 carbons), $CF_3(CF_2)_5(CH_2)_2SiCl_3$ (8 carbons), and $CF_3(CF_2)_7(CH_2)_2SiCl_3$ (10 carbons), and pictures of representative droplets. The errors in these measurements are approximately the sizes of the symbols in the plot. Bottom. Ellipsometric thickness measurements.

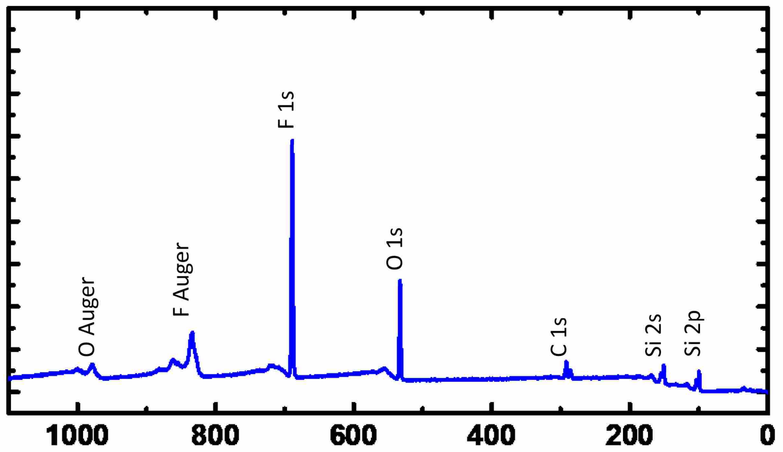

Figure 3-3 Representative XPS survey scan of a piece of silicon modified with $CF_3(CF_2)_5(CH_2)_2SiCl_3$.

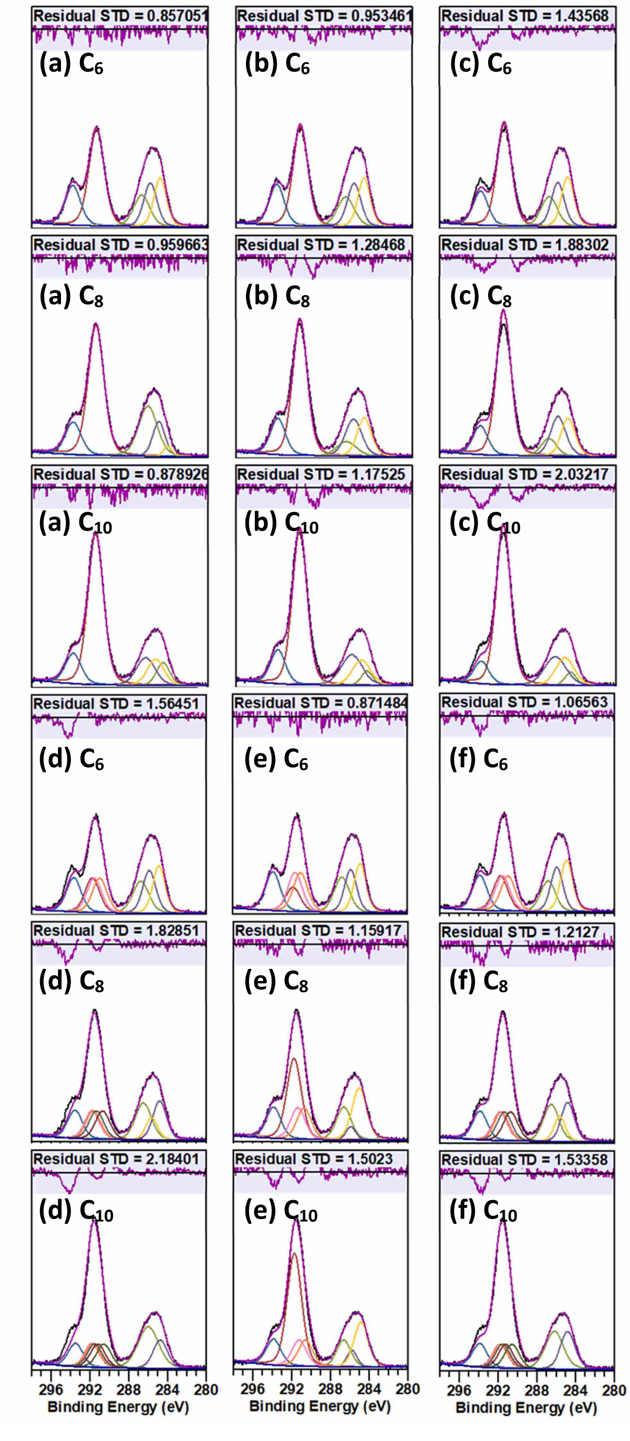

Figure 3-4 Results of peak fitting in this work. (a) Simple two-peak model with no constraints. (b) Simple two-peak model with FWHM values fixed and equal. (c) Simple two-peak model with FWHM values and areas fixed. (d) Fit based entirely on ab initio calculations, i.e., constrained BE values, and FWHM values fixed. (e) Semi-empirical model with three CF_2 components with BE values constrained by the ab initio calculations. (f) Semi-empirical model with all CF_2 peaks constrained by ab initio calculations and all FWHM values constrained, but CF_2 peaks able to float independent of the CF_3 fit component.

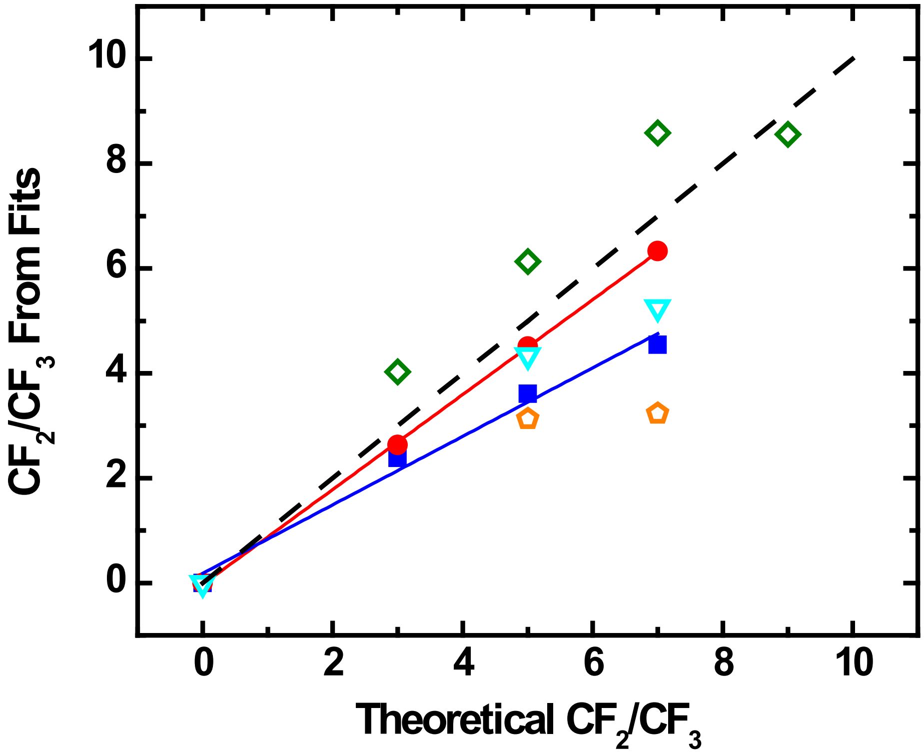

Figure 3-5 Plot of the CF_2/CF_3 ratio from two of the fits in this work: the simple two-peak model with FWHM values fixed (solid, blue squares), and first semi-empirical model (solid, red circles) vs. the theoretical CF_2/CF_3 ratio. Also shown are results from Tsibouklis et al. (open, green diamonds),[52] Zuo et al. (open, light blue, down triangles),[43] and Hozumi et al. (open, orange pentagons).[45]

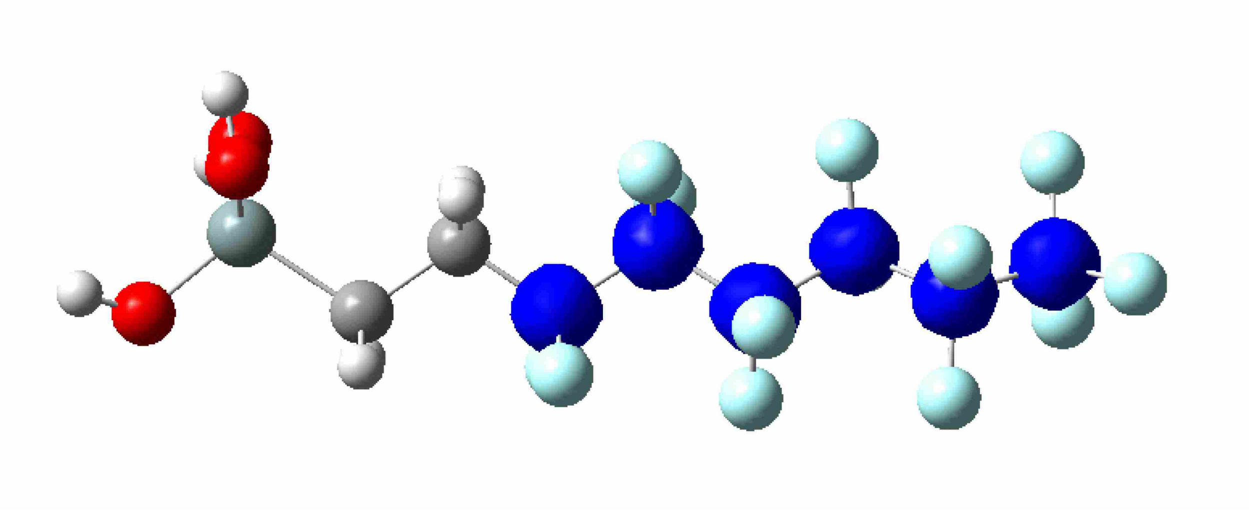

Figure 3-6 Image of the S orbitals mapped onto the 8 carbon perfluorosilane. Each orbital has a corresponding HF energy associated with it. The difference in these energies is calculated in accordance with Koopman's theorem.

3.8 Acknowledgments

This work was funded by Moxtek. We want to also acknowledge Dr. Anubhav Diwan for his assistance in making samples for analysis.

3.9 References

1. Gnanappa, A. K.; O'Murchu, C.; Slattery, O.; Peters, F.; O'Hara, T.; Aszalós-Kiss, B.; Tofail, S. A., Improved aging performance of vapor phase deposited hydrophobic self-assembled monolayers. *Applied Surface Science* **2011,** *257* (9), 4331-4338.
2. Ferraria, A. M.; da Silva, J. D. L.; do Rego, A. M. B., XPS studies of directly fluorinated HDPE: problems and solutions. *Polymer* **2003,** *44* (23), 7241-7249.
3. Zhang, F.-Y.; Advani, S. G.; Prasad, A. K.; Boggs, M. E.; Sullivan, S. P.; Beebe Jr, T. P., Quantitative characterization of catalyst layer degradation in PEM fuel cells by X-ray photoelectron spectroscopy. *Electrochimica Acta* **2009,** *54* (16), 4025-4030.
4. Touhara, H.; Okino, F., Property control of carbon materials by fluorination. *Carbon* **2000,** *38* (2), 241-267.
5. Pujari, S. P.; Spruijt, E.; Cohen Stuart, M. A.; van Rijn, C. J.; Paulusse, J. M.; Zuilhof, H., Ultralow adhesion and friction of fluoro-hydro alkyne-derived self-assembled monolayers on H-terminated Si (111). *Langmuir* **2012,** *28* (51), 17690-17700.
6. de Boer, M. P.; Knapp, J. A.; Michalske, T. A.; Srinivasan, U.; Maboudian, R., Adhesion hysteresis of silane coated microcantilevers. *Acta Materialia* **2000,** *48* (18-19), 4531-4541.
7. Mayer, T. M.; de Boer, M. P.; Shinn, N. D.; Clews, P. J.; Michalske, T. A., Chemical vapor deposition of fluoroalkylsilane monolayer films for adhesion control in microelectromechanical systems. *Journal of Vacuum Science & Technology B: Microelectronics and Nanometer Structures Processing, Measurement, and Phenomena* **2000,** *18* (5), 2433-2440.
8. Liu, S.; Liu, X.; Latthe, S. S.; Gao, L.; An, S.; Yoon, S. S.; Liu, B.; Xing, R., Self-cleaning transparent superhydrophobic coatings through simple sol–gel processing of fluoroalkylsilane. *Applied Surface Science* **2015,** *351*, 897-903.
9. Diwan, A.; Jensen, D. S.; Gupta, V.; Johnson, B. I.; Evans, D.; Telford, C.; Linford, M. R., Superhydrophobic Surfaces with Very Low Hysteresis Prepared by Aggregation of Silica Nanoparticles During In Situ Urea-Formaldehyde Polymerization. *Journal of nanoscience and nanotechnology* **2015,** *15* (12), 10022-10036.
10. Ashurst, W. R.; Carraro, C.; Maboudian, R.; Frey, W., Wafer level anti-stiction coatings for MEMS. *Sensors and Actuators A: Physical* **2003,** *104* (3), 213-221.
11. Jensen, D. S.; Kanyal, S. S.; Madaan, N.; Hancock, J. M.; Dadson, A. E.; Vail, M. A.; Vanfleet, R.; Shutthanandan, V.; Zhu, Z.; Engelhard, M. H., Multi-instrument characterization of the surfaces and materials in microfabricated, carbon nanotube-templated thin layer chromatography plates. An analogy to 'The Blind Men and the Elephant'. *Surface and Interface Analysis* **2013,** *45* (8), 1273-1282.
12. Wu, L.; Cai, L.; Liu, A.; Wang, W.; Yuan, Y.; Li, Z., Self-assembled monolayers of perfluoroalkylsilane on plasma-hydroxylated silicon substrates. *Applied Surface Science* **2015,** *349*, 683-694.
13. Cushman, C. V.; Brüner, P.; Zakel, J.; Major, G. H.; Lunt, B. M.; Smith, N. J.; Grehl, T.; Linford, M. R., Low energy ion scattering (LEIS). A practical introduction to its theory, instrumentation, and applications. *Analytical Methods* **2016,** *8* (17), 3419-3439.
14. Clarke, S. M.; Friščić, T.; Jones, W.; Mandal, A.; Sun, C.; Parker, J. E., Observation of a two-dimensional halogen-bonded cocrystal at sub-monolayer coverage using synchrotron X-ray diffraction. *Chemical Communications* **2011,** *47* (9), 2526-2528.

15. Sunde, M.; Serpell, L. C.; Bartlam, M.; Fraser, P. E.; Pepys, M. B.; Blake, C. C., Common core structure of amyloid fibrils by synchrotron X-ray diffraction. *Journal of molecular biology* **1997,** *273* (3), 729-739.

16. Lee, M. V.; Lee, J. R.; Brehmer, D. E.; Linford, M. R.; Willey, T. M., Unanticipated C□C Bonds in Covalent Monolayers on Silicon Revealed by NEXAFS. *Langmuir* **2009,** *26* (3), 1512-1515.

17. Baer, D. R.; Artyushkova, K.; Richard Brundle, C.; Castle, J. E.; Engelhard, M. H.; Gaskell, K. J.; Grant, J. T.; Haasch, R. T.; Linford, M. R.; Powell, C. J., Practical guides for x-ray photoelectron spectroscopy: First steps in planning, conducting, and reporting XPS measurements. *Journal of Vacuum Science & Technology A: Vacuum, Surfaces, and Films* **2019,** *37* (3), 031401.

18. Fulghum, J. E., Recent developments in high energy and spatial resolution analysis of polymers by XPS. *Journal of electron spectroscopy and related phenomena* **1999,** *100* (1-3), 331-355.

19. Roberts, A.; Engelberg, D.; Liu, Y.; Thompson, G. E.; Alexander, M. R., Imaging XPS investigation of the lateral distribution of copper inclusions at the abraded surface of 2024T3 aluminium alloy and adsorption of decyl phosphonic acid. *Surface and Interface Analysis: An International Journal devoted to the development and application of techniques for the analysis of surfaces, interfaces and thin films* **2002,** *33* (8), 697-703.

20. Tougaard, S., Improved XPS analysis by visual inspection of the survey spectrum. *Surface and Interface Analysis* **2018,** *50* (6), 657-666.

21. Gupta, V.; Ganegoda, H.; Engelhard, M. H.; Terry, J.; Linford, M. R., Assigning oxidation states to organic compounds via predictions from X-ray photoelectron spectroscopy: a discussion of approaches and recommended improvements. *Journal of Chemical Education* **2013,** *91* (2), 232-238.

22. Jain, V.; Biesinger, M. C.; Linford, M. R., The Gaussian-Lorentzian Sum, Product, and Convolution (Voigt) functions in the context of peak fitting X-ray photoelectron spectroscopy (XPS) narrow scans. *Applied Surface Science* **2018,** *447*, 548-553.

23. Singh, B.; Hesse, R.; Linford, M. R., Good practices for XPS (and other types of) peak fitting. *Vac Technol Coating* **2015,** *12*, 25-31.

24. Singh, B.; Diwan, A.; Jain, V.; Herrera-Gomez, A.; Terry, J.; Linford, M. R., Uniqueness plots: A simple graphical tool for identifying poor peak fits in X-ray photoelectron spectroscopy. *Applied Surface Science* **2016,** *387*, 155-162.

25. Cumpson, P. J.; Seah, M. P., Elastic scattering corrections in AES and XPS. II. Estimating attenuation lengths and conditions required for their valid use in overlayer/substrate experiments. **1997,** *25* (6), 430-446.

26. Giesbers, M.; Marcelis, A. T.; Zuilhof, H., Simulation of XPS C1s spectra of organic monolayers by quantum chemical methods. *Langmuir* **2013,** *29* (15), 4782-4788.

27. Hehre, W. J., Ab initio molecular orbital theory. *Accounts of Chemical Research* **1976,** *9* (11), 399-406.

28. Yang, X.; Rees, R. J.; Conway, W.; Puxty, G.; Yang, Q.; Winkler, D. A., Computational modeling and simulation of CO2 capture by aqueous amines. *Chemical reviews* **2017,** *117* (14), 9524-9593.

29. Tardio, S.; Cumpson, P. J., Practical estimation of XPS binding energies using widely available quantum chemistry software. *Surface and Interface Analysis* **2018,** *50* (1), 5-12.

30. Tompkins, H.; Irene, E. A., *Handbook of ellipsometry*. William Andrew: 2005.

31. Guan, F.; Chen, M.; Yang, W.; Wang, J.; Zhang, R.; Yang, S.; Xue, Q., Fabrication of patterned polyaniline microstructure through microcontact printing and electrochemistry. *Applied surface science* **2004,** *230* (1-4), 131-137.

32. Frisch, M. J. T., G. W.; Schlegel, H. B.; Scuseria, G. E.; Robb, M. A.; Cheeseman, J. R.; Scalmani, G.; Barone, V.; Mennucci, B.; Petersson, G. A.; Nakatsuji, H.; Caricato, M.; Li, X.; Hratchian, H. P.; Izmaylov, A. F.; Bloino, J.; Zheng, G.; Sonnenberg, J. L.; Hada, M.; Ehara, M.; Toyota, K.; Fukuda, R.; Hasegawa, J.; Ishida, M.; Nakajima, T.; Honda, Y.; Kitao, O.; Nakai, H.; Vreven, T.; Montgomery, J. A.; Peralta, J. E.; Ogliaro, F.; Bearpark, M.; Heyd, J. J.; Brothers, E.; Kudin, K. N.; Staroverov, V. N.; Kobayashi, R.; Normand, J.; Raghavachari, K.; Rendell, A.; Burant, J. C.; Iyengar, S. S.; Tomasi, J.; Cossi, M.; Rega, N.; Millam, J. M.; Klene, M.; Knox, J. E.; Cross, J. B.; Bakken, V.; Adamo, C.; Jaramillo, J.; Gomperts, R.; Stratmann, R. E.; Yazyev, O.; Austin, A. J.; Cammi, R.; Pomelli, C.; Ochterski, J. W.; Martin, R. L.; Morokuma, K.; Zakrzewski, V. G.; Voth, G. A.; Salvador, P.; Dannenberg, J. J.; Dapprich, S.; Daniels, A. D.; Farkas; Foresman, J. B.; Ortiz, J. V.; Cioslowski, J.; Fox, D. J., *Gaussian 09*, Revision B.01.; Wallingford CT: 2009.

33. Johs, B.; Woollam, J. A.; Herzinger, C. M.; Hilfiker, J. N.; Synowicki, R. A.; Bungay, C. L. In *Overview of variable-angle spectroscopic ellipsometry (VASE): II. Advanced applications*, Optical Metrology: A Critical Review, International Society for Optics and Photonics: 1999; p 1029404.

34. Hilfiker, J. N.; Singh, N.; Tiwald, T.; Convey, D.; Smith, S. M.; Baker, J. H.; Tompkins, H. G., Survey of methods to characterize thin absorbing films with spectroscopic ellipsometry. *Thin Solid Films* **2008,** *516* (22), 7979-7989.

35. Woollam, J. A.; Johs, B. D.; Herzinger, C. M.; Hilfiker, J. N.; Synowicki, R. A.; Bungay, C. L. In *Overview of variable-angle spectroscopic ellipsometry (VASE): I. Basic theory and typical applications*, Optical Metrology: A Critical Review, International Society for Optics and Photonics: 1999; p 1029402.

36. Khorasani, M.; Mirzadeh, H.; Kermani, Z., Wettability of porous polydimethylsiloxane surface: morphology study. *Applied Surface Science* **2005,** *242* (3-4), 339-345.

37. Boscher, N. D.; Vaché, V.; Carminati, P.; Grysan, P.; Choquet, P., A simple and scalable approach towards the preparation of superhydrophobic surfaces–importance of the surface roughness skewness. *Journal of Materials Chemistry A* **2014,** *2* (16), 5744-5750.

38. Zuo, J.; Keil, P.; Valtiner, M.; Thissen, P.; Grundmeier, G., Deposition of Ag nanoparticles on fluoroalkylsilane self-assembled monolayers with varying chain length. *Surface Science* **2008,** *602* (24), 3750-3759.

39. Shah, D.; Patel, D. I.; Roychowdhury, T.; Rayner, G. B.; O'Toole, N.; Baer, D. R.; Linford, M. R., Tutorial on interpreting x-ray photoelectron spectroscopy survey spectra: Questions and answers on spectra from the atomic layer deposition of Al2O3 on silicon. *Journal of Vacuum Science & Technology B, Nanotechnology and Microelectronics: Materials, Processing, Measurement, and Phenomena* **2018,** *36* (6), 062902.

40. Hozumi, A.; Ushiyama, K.; Sugimura, H.; Takai, O., Fluoroalkylsilane monolayers formed by chemical vapor surface modification on hydroxylated oxide surfaces. *Langmuir* **1999,** *15* (22), 7600-7604.

41. Han, L. M.; Timmons, R. B.; Lee, W. W., Pulsed plasma polymerization of an aromatic perfluorocarbon monomer: Formation of low dielectric constant, high thermal stability films. *Journal of Vacuum Science & Technology B: Microelectronics and Nanometer Structures Processing, Measurement, and Phenomena* **2000,** *18* (2), 799-804.

42. Penna, A.; Careri, M.; Spencer, N. D.; Rossi, A., Effects of tailored surface chemistry on desorption electrospray ionization mass spectrometry: a surface-analytical study by XPS and AFM. *Journal of the American Society for Mass Spectrometry* **2015,** *26* (8), 1311-1319.

43. Nansé, G.; Papirer, E.; Fioux, P.; Moguet, F.; Tressaud, A., Fluorination of carbon blacks: an X-ray photoelectron spectroscopy study: I. A literature review of XPS studies of fluorinated carbons. XPS investigation of some reference compounds. *Carbon* **1997,** *35* (2), 175-194.

44. Youssef, A.; Pabon, M.; Severac, R.; Gilbert, R. G., The effect of copolymer composition on the surface properties of perfluoroalkylethyl acrylates. *Journal of applied polymer science* **2009,** *114* (6), 4020-4029.

45. Sakai, Y.; Tazawa, S.; Bratescu, M.-A.; Suda, Y.; Sugawra, H. In *Application of perfluorocarbon liquids for aC: F film production on electrodes by plasma enhanced chemical vapor deposition*, IEEE International Conference on Dielectric Liquids, 2005. ICDL 2005., IEEE: 2005; pp 421-424.

46. Laffineur, F.; Auguste, D.; Plumier, F.; Pirlot, C.; Hevesi, L.; Delhalle, J.; Mekhalif, Z., Comparison between CH3 (CH2) 15SH and CF3 (CF2) 3 (CH2) 11SH monolayers on electrodeposited silver. *Langmuir* **2004,** *20* (8), 3240-3245.

47. Tsibouklis, J.; Graham, P.; Eaton, P. J.; Smith, J. R.; Nevell, T. G.; Smart, J. D.; Ewen, R. J., Poly (perfluoroalkyl methacrylate) film structures: surface organization phenomena, surface energy determinations, and force of adhesion measurements. *Macromolecules* **2000,** *33* (22), 8460-8465.

48. Jain, V.; Wheeler, J. J.; Ess, D. H.; Linford, M. R., Poly(γ-Benzyl L-Glutamate) (PBLG), by Near-Ambient Pressure XPS. *Surface Science Spectra* **2019,** *Submitted.*

CHAPTER 4: Optical Constants of SiO_2 from 196 – 1688 nm (0.735 - 6.33 eV) from 20, 40, and 60 nm Films of Reactively Sputtered SiO_2 on Eagle XG® Glass by Spectroscopic Ellipsometry

4.1 Statement of Attribution

This document was originally published as Johnson, B. I., et al. (2017). "Optical constants of SiO2 from 196 to 1688 nm (0.735–6.33 eV) from 20, 40, and 60 nm films of reactively sputtered SiO2 on Eagle XG® glass by spectroscopic ellipsometry." Surface Science Spectra **24**(2): 026002.

4.2 Abstract

Three thicknesses of reactively sputtered SiO_2, nominally 20, 40, and 60 nm, deposited on Eagle XG® (EXG), an important display glass, were analyzed by spectroscopic ellipsometry (SE). Reflection ellipsometry data from the samples were analyzed from 196 nm to 1688 nm at angles of 55° to 60°, inclusive, in 1° increments. These angles were chosen because they bracket the Brewster angles of both EXG glass and the SiO_2. The backsides of two sets of samples were roughened to suppress backside reflections from the substrates. One set was roughened by sand blasting and the other with a hand-held rotary tool with a stone attachment. These two sets of samples yielded nine data sets collected from nine different samples (three for each nominal thickness of SiO_2), each at six different angles of incidence. The optical constants for each thickness of SiO_2 (for both sets) was determined and contrasted to previously reported values. A set of constants was also obtained for all the films (the material in general) via a multi-sample analysis (MSA). The optical constants of the SiO_2 films were modeled using two poles with transparency assumed over the entire spectral range (a Sellmeier model). A Bruggeman effective

medium approximation (BEMA) roughness layer was included in the model, which assumed 50/50 volume fractions of the modeled SiO_2 optical constants and void. The fit did not substantially improve when an interface layer between the Eagle XG® and the sputtered film was included, so it was omitted. Three sets of previously reported optical constants for the substrate over two wavelength ranges were considered in the modeling. The thin SiO_2 films analyzed herein have very similar optical properties to those of their EXG substrate this is a challenging analytical problem involving a transparent film on a transparent substrate. Accordingly, analysis of multiple samples, an MSA that included multiple film thicknesses analyzed at multiple angles, and an exploration of multiple modeling approaches helped ensure that the optical constants reported herein are accurate and the modeling robust. These measures helped avoid correlation between the optical constants, the layer thicknesses, and the thicknesses of the BEMA layers. Atomic force microscopy (AFM) roughness measurements were made on the SiO_2 films and compared to the roughness values obtained by spectroscopic ellipsometry. In summary, we provide the optical constants and some accompanying physical characterization of sputtered 20 – 60 nm SiO_2 films from 196 – 1688 nm on Eagle XG glass through an analysis that is challenging due to the similarities of the optical functions of the film and the substrate.

4.3 Introduction

Silicon dioxide (and silicon) are extremely important inorganic thin film materials. As such, they have been extensively studied and characterized in various states.[1-10] They have numerous applications, including in energy storage, microelectronics, semiconductor devices, multilayer optical coatings and microelectromechanical systems (MEMS).[11-15] The surface of SiO_2 can be modified using a variety of reagents, including silanes.[16-19] This allows it to be tailored for specific applications, such as enhanced adhesion, superhydrophobicity (if the surface is appropriately rough), self-cleaning, chemical sensing, and chemical separations.[20-23] Silica can be deposited through a variety of methods, including plasma enhanced chemical vapor deposition (PECVD),[24-25] low pressure chemical vapor deposition (LPCVD),[26] e-beam evaporation,[27] atomic layer deposition (ALD),[28-31] sol-gel deposition,[32-33] and sputtering.[30, 34-36] SiO_2 films are also routinely prepared on silicon wafers via thermal oxidation.[37-39] And while each of these methods deposits silicon dioxide, the optical and mechanical properties of these films may vary somewhat depending on the deposition method used. For example, in one study,[40] presumably undertaken at 632.8 nm, the refractive index for reactively sputtered SiO_2 on glass varied from 1.453 – 1.460. In another, which was performed at 632.8 nm, [41] PECVD of SiO_2 resulted in a refractive index of 1.461 – 1.489. Variations in film properties may also result from inhomogeneities in material density, morphology, and stoichiometry as a function of depth and/or lateral position on a surface.[42] Stress can play a role in distorting the amorphous network, which can change the optical properties of the film and/or substrate, sometimes inducing birefringence. Impurities in the sputter target and/or from the chamber may influence the optical properties of the films as well. Other factors that influence thin film properties include deposition temperature, deposition rate, the chemical environment during deposition, and the energy with which deposited particles impinge on a substrate. Because of these variations, it is important to have optical constants specific to the deposition method for characterization of similar films and/or as a starting point for modeling.

In this study, SE was used to characterize reactively sputtered SiO_2 films with nominal thicknesses of 20, 40 and 60 nm deposited using a proprietary method on Eagle XG® glass substrates. (Figure 4-1) We previously reported the optical constants of Eagle XG® from 230 – 1688 nm,[43] and from 196 – 1688 nm,[44] where three sets of optical constants were obtained with these approaches. The uncoated backsides of the Eagle XG® substrates were mechanically roughened by sand blasting to suppress unwanted (incoherent) reflections.[45-46] Samples were air plasma cleaned in a Harrick PDC-32G plasma cleaner (1 min, 18 W) immediately prior to ellipsometric analysis to remove organic contamination that would interfere with the measurement. Measurements, and subsequent modeling, were in reflection mode from 196 nm to 1688 nm. Ellipsometric data were obtained from 55° to 60° in 1° increments and the reflection at each angle was measured for 10 s. These angles bracket the Brewster angle of the glass substrate and the SiO_2 films. Samples were evaluated individually and via an MSA in which data from samples with different film thicknesses were fit simultaneously.[47] In the MSA, the optical constants of the sputtered SiO_2 films were taken to be the same between samples. Data from nine samples (three of each nominal thickness) were simultaneously fit in the MSA. Refractive indices were modeled using two poles (Sellmeier model). These poles are unbroadened oscillators and have an impact on the refractive index, but not the extinction coefficient, of a material. The films were assumed to be transparent over the entire wavelength range considered. As such, no oscillators were included to model absorbing features. The goodness of fit we achieved, as evidenced by low mean square error (MSE) values, suggests that this approach is reasonable. The overall model also included a Bruggeman effective medium approximation (BEMA) roughness layer, consisting of 50% volume fractions of SiO_2 and void.[48] BEMA layers are often used to model interfaces by assuming that the optical constants of the interface, e.g., roughness layer, consist of a mixture of the optical constants of the materials on either side of it. In one model, the thickness of this roughness layer was set to the value obtained by atomic force microscopy (AFM). We also considered an interface layer between the sputtered film and the substrate. It did not significantly improve the fit so it was omitted, i.e., we maintained as much simplicity as possible in the modeling.

There are several approaches for modeling the optical constants of transparent materials. The simplest would be to assume no dispersion at all, i.e., n constant.[49] A somewhat more sophisticated approach is the Cauchy dispersion relationship (see Equation 1).

$$(1) \qquad n(\lambda) = A + \frac{B}{\lambda^2} + \frac{C}{\lambda^4}$$

This relationship works well for a wide variety of transparent materials. However, it does not have a strong physical basis, it is an empirical model, and it only applies over a limited spectral range. Another disadvantage to using the Cauchy model is that it predicts an asymptotically constant index of refraction at longer wavelengths. Real materials have IR absorptions and exhibit a decrease in refractive index at longer wavelengths.

Curve fitting tools such as point-by-point and spline fits are other useful methods for obtaining optical constants. However, point-by-point fitting is not generally Kramers-Kronig (K-K) consistent, often giving abrupt changes in n and k as the fit responds to noise in the measurement, which is unphysical. Under a limited set of circumstances, spline fitting can produce K-K consistent results.[50] However, the positions of the spline nodes must be fit at regular energy intervals. Accordingly, spline fit tables generally have more fit parameters than dispersion relationships and oscillator models.

The pole-pole (Sellmeier) model (vide infra) has a theoretical basis and describes the optical constants of materials over their full transparent wavelength range. Indeed, the pole-pole model is a simple approach that gives K-K consistent results over a material's entire transparent range using only 3 – 4 fit parameters. Unlike the Cauchy model, the pole-pole model can account for decreasing n at longer wavelengths. Accordingly, we modeled the optical constants of SiO_2 with a pole-pole model. One advantage of using this (and other) dispersion relationships is that they can be easily adapted to films with slightly different optical constants by making small adjustments to the model. Clearly this is not possible for optical constants obtained using point-by-point or spline fits.

Our analysis revealed that our sputtered SiO_2 layer has almost exactly the same optical constants as the thermal oxide (SiO_2) reported by Herzinger and coworkers.[5] For example, Herzinger reported n = 1.4655 at 546.1 nm.[5] By comparison, indices of refraction for other forms of SiO_2 have been reported around this wavelength as 1.55-1.56 for quartz, and 1.74 for native oxide.[51]

4.4 Experimental

SiO_2 films were reactively sputtered on Eagle XG® substrates (0.5 mm thick) in an atmosphere containing oxygen and had nominal thicknesses of 20, 40, and 60 nm. The backsides of the substrates were roughened to a matte finish by sand blasting, which effectively gave the substrates an infinite thickness. The fronts of the samples were masked off during this process to protect them from particulate contamination, i.e., they were placed face down in a watch glass and taped to the watch glass along their edges. After sand blasting, the exposed parts of the samples were exhaustively washed with methanol. Immediately prior to analysis, adventitious hydrocarbon was removed from the sample/analysis surfaces with an air plasma (Harrick Plasma Cleaner (PDC-32G), 1 min, 18 W). SE was performed with a variable angle spectroscopic ellipsometer (M-2000D, J.A. Woollam, Lincoln, ME, USA, wavelength range: ca. 190-1688 nm). Data were acquired at the following measurement Angle(s) of incidence: 55°, 56°, 57°, 58°, 59°, 60° and subsequently modelled using the CompleteEASE software from the J.A. Woollam Company. The bottom layer was the substrate, which consisted of Eagle XG® glass. The second layer was a BEMA interface layer between the substrate and the sputtered SiO_2. The next layer was the SiO_2 film, which was modeled using a pole-pole approach (Sellmeier). The final layer was a BEMA roughness layer consisting of 50% volume fractions of SiO_2 (same optical constants as the SiO_2 film) and void. [43,44, 53-54] During modelling, little to no change occurred in the MSE when the BEMA interfacial layer between the substrate and SiO_2 was removed. Accordingly, it was excluded from the model. Table 4-1 below shows the methods used to model the sputtered SiO_2.

4.5 Results and Discussion

Refractive indices/dispersion relationships for SiO_2 were obtained by an MSA of all the

Table 4-1 Approaches used to model films of sputtered SiO2 on Eagle XG®.

Approach Number	Substrate	SiO_2 Layer		BEMA Layer	MSE
	Optical Constants Used	Model Used	Wavelength Range	Thickness	
1	Tauc-Lorentz, 1 Gaussian, and 2 poles as reported by Cushman et al.[43] Model based on reflection and transmission data from 500 µm thick EXG.	Sellmeier (pole-pole)	230-1688 nm	Floated	1.127
2	Sellmeier, as reported by Cushman et al.[44] Model based on reflection data only.	Sellmeier (pole-pole)	196-1688 nm	Floated	0.992
3	Tauc-Lorentz, 3 Gaussians, and 1 pole as reported by Cushman et al.[44] Model based on reflection and transmission data from 100 and 200 µm thick EXG. Amplitudes of the Tauc-Lorentz, 3 Gaussians, and pole floated.	Sellmeier (pole-pole)	196-1688 nm	Floated	1.804
4	Same as Approach 3	Sellmeier (pole-pole)	196-1688 nm	Fixed to AFM Values	3.918

samples (see Figure 4-2) using the four different approaches listed in Table 4-1. Figure 4-2 shows three sets of optical constants that are very close together. These were obtained with SiO_2 and BEMA thickness layers that were allowed to vary (float). Clearly the optical constants of the substrate used here have a rather minor influence on the optical constants obtained for the SiO_2 layers. For example, Approach 2 consisted exclusively of a Sellmeier model for the substrate, while Approach 3 accounted for absorptions in it. The outlying dispersion relationship for SiO_2 in Figure 4-1 was obtained via Approach 4 by fixing the thickness of the BEMA roughness layer to the value obtained by AFM. The average percent differences between these sets of optical constants are given in Table 4-2, where the percent difference at each wavelength was calculated using Equation 2:

$$(2)\ Percent\ Difference_{A,B} = \frac{100}{i} \times \sum_i \left(\frac{|n_{A,i} - n_{B,i}|}{Average(n_{A,i}, n_{B,i})} \right).$$

Table 4-2 Percent differences between the optical constants presented in Figure 2 obtained by the approaches in Table 4-1.

Approaches compared	**1-2**	**1-3**	**2-3**	**3-4**
% Average Percent Difference in Optical Constants	0.03%	0.08%	0.09%	0.89%
Standard Deviation	0.02%	0.04%	0.02%	0.24%

Here, $n_{A,i}$ and $n_{B,i}$ are the refractive indices obtained by two given approaches, e.g., A and B, at a specific wavelength, i. As expected, Table 4-2 shows that Approaches 1 – 3 give essentially the same results, while those from Approach 4 differ from the others. The AFM and SE roughnesses obtained for the films are somewhat different (Tables 4-3 and 4-4), which probably accounts for the less adequate fit obtained by Approach 4. These differences in roughness may be explained by the fact that density gradients have been reported in sputtered thin films.[55-58] That is, AFM is a physical measurement,[59-62] whereas SE has the ability to penetrate into areas that an AFM tip cannot go. Thus, if the lower levels of a film are more compact, differences between AFM and ellipsometry roughness values would not be unexpected. However, perhaps a better explanation for these phenomena is to invoke the observation that while ellipsometric and AFM roughnesses for a given material are generally fairly similar, it is also common for them to differ somewhat from each other.[63] Ultimately, because of its lower MSE, Approach 2 was selected to obtain the optical constants of the material. The fit parameters obtained by fitting Approaches 1 - 4 in Table 4-1 are shown in Table 4-3. Here, in all cases, the ellipsometric thicknesses of the SiO_2 films are reasonably close to the nominal thickness values. Also in Table 4-3, the results from Approaches 1 – 3 are in reasonably good agreement, while those from Approach 4 may differ somewhat, e.g., note the A_{UV} Pole Amp. values as well as the thicknesses of the 40 and 60 nm films.

The dispersion relationships obtained from the MSA correspond to average sets of optical constants for the 20 nm, 40 nm and 60 nm SiO_2 films, where the use of an MSA removes possible correlation between the roughness and thickness fit parameters. Correlation between thickness and roughness was apparent when the data from the 20 nm samples were fit alone, as the analysis yielded negative roughness values. However, the individual analyses of the 40 and 60 nm films gave reasonable (non-negative) roughness values, presumably because the films are becoming thick enough to begin to introduce an interference pattern into the data, which increases the amount of information it holds as a function of angle. Accordingly, to further explore whether the MSA approach provided any benefit, subsets of the spectra were analyzed using MSAs for each group of the different film thickness, i.e., groups of the 20 nm, 40 nm, or 60 nm data. Here, the roughness values for the 20 nm SiO_2 films were fixed to the values obtained for them from the MSA analysis of all of the films. The subsets of the samples were analyzed by MSA using Approaches 1 – 3 in Table 4-1. These results were then compared to those from the comprehensive MSA analysis (see Figure 4-3). The results from Approach 1 (Figure 4-3a) showed very good agreement between the 20 nm, 60 nm, and comprehensive MSA analyses, and reasonable agreement between all the analyses (the 40 nm analysis differed somewhat from the others). The results from Approaches 2 (Figure 4-3b) and 3 (Figure 4-3c) showed better agreement between the results for the individual

Table 4-3 Sellmeier parameters, film thicknesses, film roughnesses, and MSE values for the four fitting approaches in Table 4-1 from an MSA analysis of all the samples.

	Approach 1		**Approach 2**		**Approach 3**		**Approach 4**	
Parameter	**Value**	**Error**	**Value**	**Error**	**Value**	**Error**	**Value**	**Error**
A_{UV} Pole Amp.	211.39	± 0.25	202.13	± 0.12	200.85	± 0.20	159.82	± 0.23
E_{UV} Pole En.	13.728 eV	± 0.074 eV	13.447 eV	± 0.0034 eV	13.383 eV	± 0.0060 eV	12.177 eV	± 0.0074 eV
A_{IR} Pole Amp.	0.0194	± 0.00014	0.0159	± 0.0001	0.0160	± 0.0002	0.0177	± 0.0005
Thickness #1 (20 nm)	17.12 nm	±0.036 nm	17.2 nm	±0.023 nm	18.38 nm	±0.038 nm	18.66 nm	±0.060 nm
Thickness #4 (20 nm)	17.76 nm	±0.035 nm	17.59 nm	±0.023 nm	18.74 nm	±0.037 nm	19.29 nm	±0.060 nm
Thickness #7 (20 nm)	18.03 nm	±0.034 nm	17.71 nm	±0.022 nm	18.84 nm	±0.037 nm	18.89 nm	±0.060 nm
Thickness #2 (40 nm)	37.85 nm	±0.024 nm	38.06 nm	±0.017 nm	38.3 nm	±0.030 nm	34.65 nm	±0.056 nm
Thickness #5 (40 nm)	36.14 nm	±0.024 nm	36.14 nm	±0.017 nm	36.44 nm	±0.030 nm	33.26 nm	±0.057 nm
Thickness #8 (40 nm)	35.67 nm	±0.024 nm	35.68 nm	±0.017 nm	35.99 nm	±0.030 nm	32.89 nm	±0.057 nm
Thickness #3 (60 nm)	59.74 nm	±0.034 nm	60.01 nm	±0.020 nm	59.9 nm	±0.034 nm	52.18 nm	±0.054 nm
Thickness #6 (60 nm)	60.45 nm	±0.034 nm	60.51 nm	±0.020 nm	60.39 nm	±0.034 nm	52.66 nm	±0.054 nm
Thickness #9 (60 nm)	60.53 nm	±0.034 nm	60.46 nm	±0.020 nm	60.35 nm	±0.034 nm	52.6 nm	±0.054 nm
Roughness #1 (20 nm)	2.26 nm	±0.012 nm	2.34 nm	±0.008 nm	1.88 nm	±0.013 nm	0.53 nm	Fixed
Roughness #4 (20 nm)	2.41 nm	±0.012 nm	2.58 nm	±0.008 nm	2.14 nm	±0.013 nm	0.53 nm	Fixed
Roughness #7 (20 nm)	1.99 nm	±0.011 nm	2.21 nm	±0.008 nm	1.77 nm	±0.013 nm	0.53 nm	Fixed
Roughness #2 (40 nm)	3.19 nm	±0.009 nm	3.22 nm	±0.006 nm	3.05 nm	±0.012 nm	0.46 nm	Fixed
Roughness #5 (40 nm)	2.82 nm	±0.008 nm	2.89 nm	±0.006 nm	2.71 nm	±0.011 nm	0.46 nm	Fixed
Roughness #8 (40 nm)	2.45 nm	±0.008 nm	2.49 nm	±0.006 nm	2.31 nm	±0.011 nm	0.46 nm	Fixed
Roughness #3 (60 nm)	3.82 nm	±0.012 nm	3.98 nm	±0.007 nm	3.84 nm	±0.013 nm	0.17 nm	Fixed
Roughness #6 (60 nm)	3.99 nm	±0.013 nm	4.11 nm	±0.007 nm	3.98 nm	±0.013 nm	0.17 nm	Fixed
Roughness #9 (60 nm)	4.16 nm	±0.013 nm	4.24 nm	±0.007 nm	4.11 nm	±0.013 nm	0.17 nm	Fixed
MSE	**1.127**		**0.992**		**1.804**		**3.918**	

Table 4-4 Roughnesses obtained by AFM of ca. 20, 40, and 60 nm SiO_2 films on Eagle XG®. R_a is the average roughness and R_q is the root mean square (RMS) roughness.

Sample name	Spot 1 (Å)	Spot 2 (Å)	Spot 3 (Å)	Average Roughness (Å)
Blank	R_a: 1.2, R_q: 1.5	R_a: 1.7, R_q: 2.5	R_a: 2.0, R_q: 2.8	R_a: 1.6, R_q: 2.3
20 nm	R_a: 4.4, R_q: 5.5	R_a: 2.8, R_q: 3.9	R_a: 5.4, R_q: 6.5	R_a: 4.2, R_q: 5.3
40 nm	R_a: 2.9, R_q: 4.0	R_a: 3.7, R_q: 4.8	R_a: 3.7, R_q: 5.0	R_a: 3.4, R_q: 4.6
60 nm	R_a: 1.7, R_q: 2.3	R_a: 0.1, R_q: 0.9	R_a: 1.4, R_q: 1.9	R_a: 1.1, R_q: 1.7

Table 4-5 Sellmeier parameters, film thicknesses, film roughnesses, and MSE values for an MSA of the 20 nm spectra. Roughness values were fixed to those obtained with a comprehensive MSA using Approach 2 from Table 4-1.

20 nm Spectra with Roughness fixed to MSA Values

PARAMETER	VALUE		ERROR
MSE	0.869		
UV Pole Amp.	214.13	eV ±	0.283
UV Pole En.	13.804	±	0.008
IR Pole Amp.	0.017	±	0
Roughness (1) (nm)	2.34	nm ±	0.008
Roughness (2) (nm)	2.58	nm ±	0.008
Roughness (3) (nm)	2.21	nm ±	0.008
Thickness # 1 (1) (nm)	17.15	nm ±	0.022
Thickness # 1 (2) (nm)	17.54	nm ±	0.022
Thickness # 1 (3) (nm)	17.66	nm ±	0.022

Max difference between results from the comprehensive MSA and the MSA of the three 20 nm spectra using Approach 2 from Table 1.	Wavelength value at max difference (nm)
0.27%	196.01

Table 4-6 Sellmeier parameters, film thicknesses, film roughnesses, and MSE values for an MSA of the 40 nm spectra. Roughness values were fixed to those obtained with a comprehensive MSA using Approach 2 from Table 4-1.

40 nm

PARAMETER	VALUE		ERROR
MSE	0.951		
UV Pole Amp.	208.988	eV ±	0.726
UV Pole En.	13.6	±	0.018
IR Pole Amp.	0.017	±	0
Roughness (3) (nm)	3.86	nm ±	0.045
Roughness (6) (nm)	3.48	nm ±	0.042
Roughness (9) (nm)	3.08	nm ±	0.041
Thickness # 1 (3) (nm)	39.64	nm ±	0.119
Thickness # 1 (6) (nm)	37.63	nm ±	0.109
Thickness # 1 (9) (nm)	37.17	nm ±	0.108

Max difference between results from the comprehensive MSA and the MSA of the three 20 nm spectra using Approach 2 from Table 1.	Wavelength value at max difference (nm)
0.27%	855.84

Table 4-7 Sellmeier parameters, film thicknesses, film roughnesses, and MSE values for an MSA of the 60 nm spectra. Roughness values were fixed to those obtained with a comprehensive MSA using Approach 2 from Table 4-1.

60 nm			
PARAMETER	**VALUE**		**ERROR**
MSE	1.007		
UV Pole Amp.	220.958	eV ±	0.745
UV Pole En.	14.006	±	0.022
IR Pole Amp.	0.018	±	0
Roughness (1) (nm)	4.48	nm ±	0.019
Roughness (2) (nm)	4.61	nm ±	0.019
Roughness (3) (nm)	4.74	nm ±	0.019
Thickness # 1 (1) (nm)	61.42	nm ±	0.052
Thickness # 1 (2) (nm)	61.87	nm ±	0.052
Thickness # 1 (3) (nm)	61.81	nm ±	0.052

Max difference between results from the comprehensive MSA and the MSA of the three 20 nm spectra using Approach 2 from Table 1.	**Wavelength value at max difference (nm)**
0.42%	196.01

samples and the comprehensive analysis. Based on the results in Figures 4-2 and 4-3, and considering the MSE values in Table 4-1, we report and recommend as optical constants for reactively sputtered 20 – 60 nm SiO_2 films the optical constants derived from the comprehensive MSA by Approach 2. We offer without proof the statement that the validity of these optical constants probably extends to some degree outside of this thickness range. To further confirm this model and the optical constants obtained from it, we compared optical constants obtained via the comprehensive MSA from Approach 2 to those obtained from each set of thicknesses (see Tables 4-5 – 4-7). Here, the maximum difference between any value of n in the comprehensive MSA analysis and any value of n in the 20, 40, or 60 nm analysis was 0.27% at 196.01 nm, 0.27% at 855.94 nm, and 0.42% at 196.01 nm, respectively. Additionally, as previously noted (see Table 4-

2), the percent differences between the three best approaches in the comprehensive MSA analyses varied from 0.03% - 0.09%. These rather small differences suggest that the optical constants reported herein are reasonable for sputtered SiO_2. In addition, we created uniqueness plots for these different analyses with different variables from the fits. All of these plots showed uniqueness, indicating that the parameters used in them are not strongly correlated. Finally, as an aid to the interested reader, Figures 4-4 – 4-6 show the raw data for the SiO_2 samples in N, C, and S format, Tables 4-5 – 4-7 give the results of the MSA subset analyses of the 20, 40, and 60 nm films, and Tables 4-8 and 4-9 show comparisons of the indices of refraction of SiO_2 obtained using Approaches 1 – 4 via the comprehensive MSA at specific wavelengths and energies, respectively.

Table 4-8 Comparison of the optical constants for SiO_2 at specific wavelengths obtained using a comprehensive MSA analysis via Approach 2 in Table 4-1.

Wavelength (nm)	Optical Constant (n)			
	Approach 1	Approach 2	Approach 3	Approach 4
197.6	-	1.558	1.561	1.571
232.546	1.523	1.525	1.527	1.527
389.982	1.478	1.477	1.479	1.468
499.725	1.468	1.468	1.469	1.457
699.652	1.461	1.46	1.462	1.448
1649.916	1.446	1.447	1.448	1.432

Table 4-9 Comparison of the optical constants for SiO_2 at specific energies obtained using a comprehensive MSA analysis via Approach 2 in Table 4-1.

Energy (eV)	Optical Constant (n)			
	Approach 1	Approach 2	Approach 3	Approach 4
6.275	-	1.558	1.561	1.571
5.332	1.523	1.525	1.527	1.527
3.18	1.478	1.477	1.479	1.468
2.481	1.468	1.468	1.469	1.457
1.772	1.461	1.46	1.461	1.448
0.752	1.446	1.447	1.448	1.432

4.6 Conclusion

The analyses of three sets of transparent ultra-thin films deposited on transparent substrates were performed to a high degree of confidence and accuracy using SE. This was accomplished using multiple techniques, including proper backside roughening, an MSA, a variable angle analysis, and the use of pre-determined EXG glass optical constants. This example of transparent thin film analysis on a transparent substrate illustrates the degree of sophisticated analyses that can be performed by SE on ultra-thin films that would otherwise be very challenging.

4.7 Figures

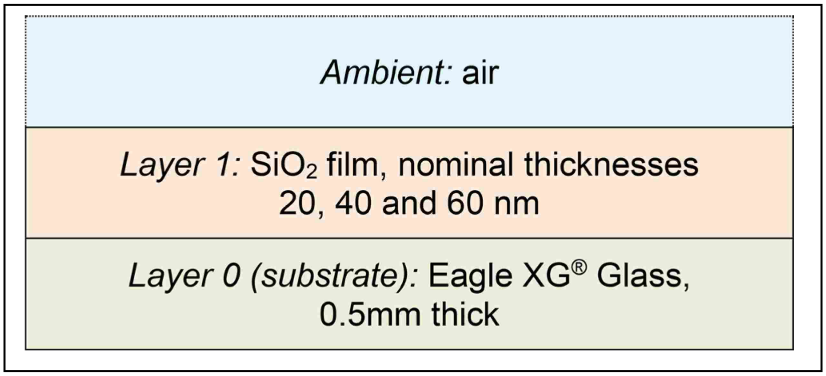

Figure 4-1 Depiction of specimen layers used for data analyses.

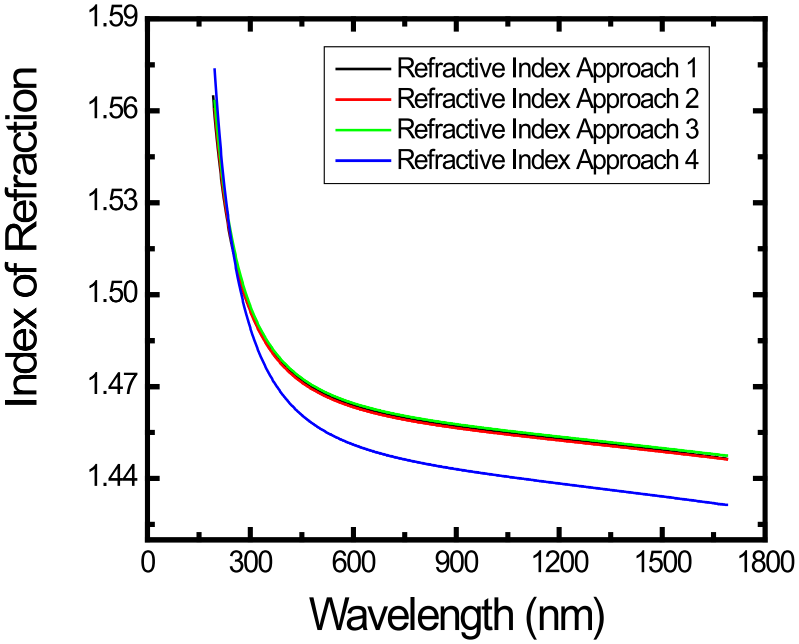

Figure 4-2 Refractive indices for sputtered SiO2 obtained through a multi-sample analysis of nine films of SiO2 with nominal thicknesses of 20, 40, and 60 nm on Eagle XG® using the four approaches described in Table 4-1.

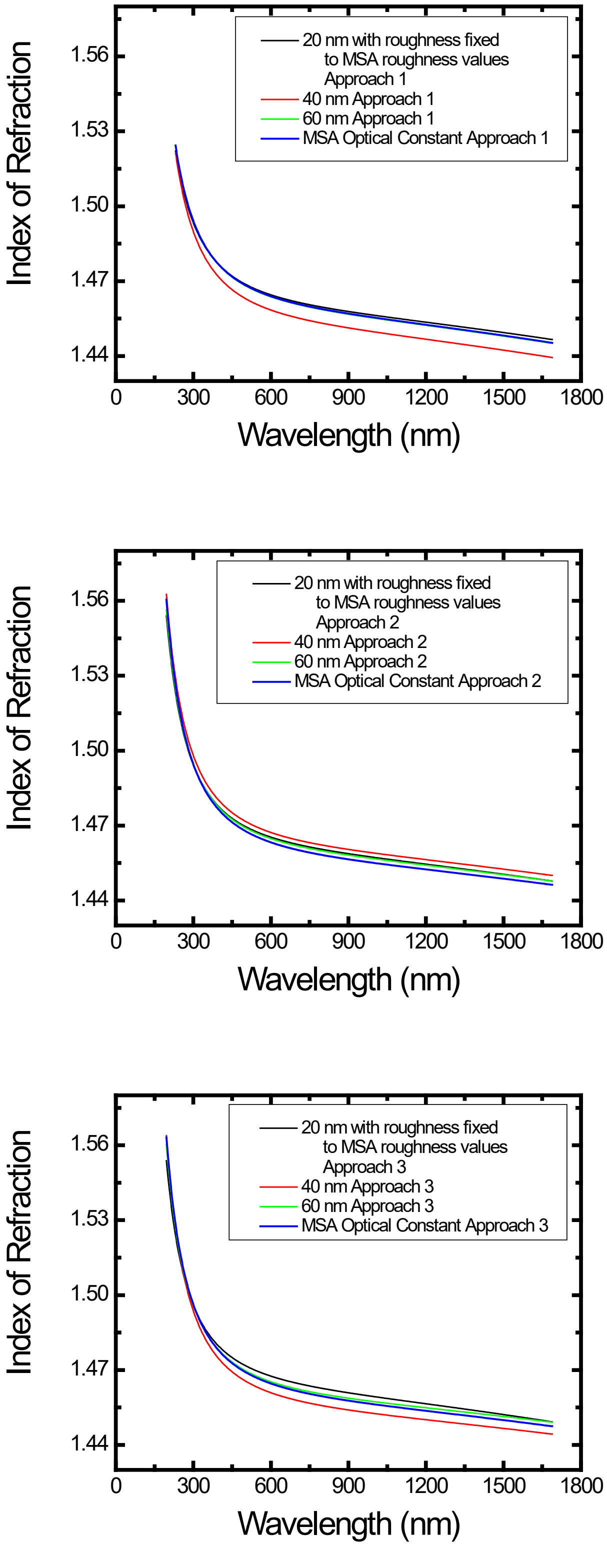

Figure 4-3 Refractive indices of SiO2 obtained via both subset and comprehensive MSAs of 20, 40, and 60 nm films and all the films together using Approaches 1-3 in Table 4-1.

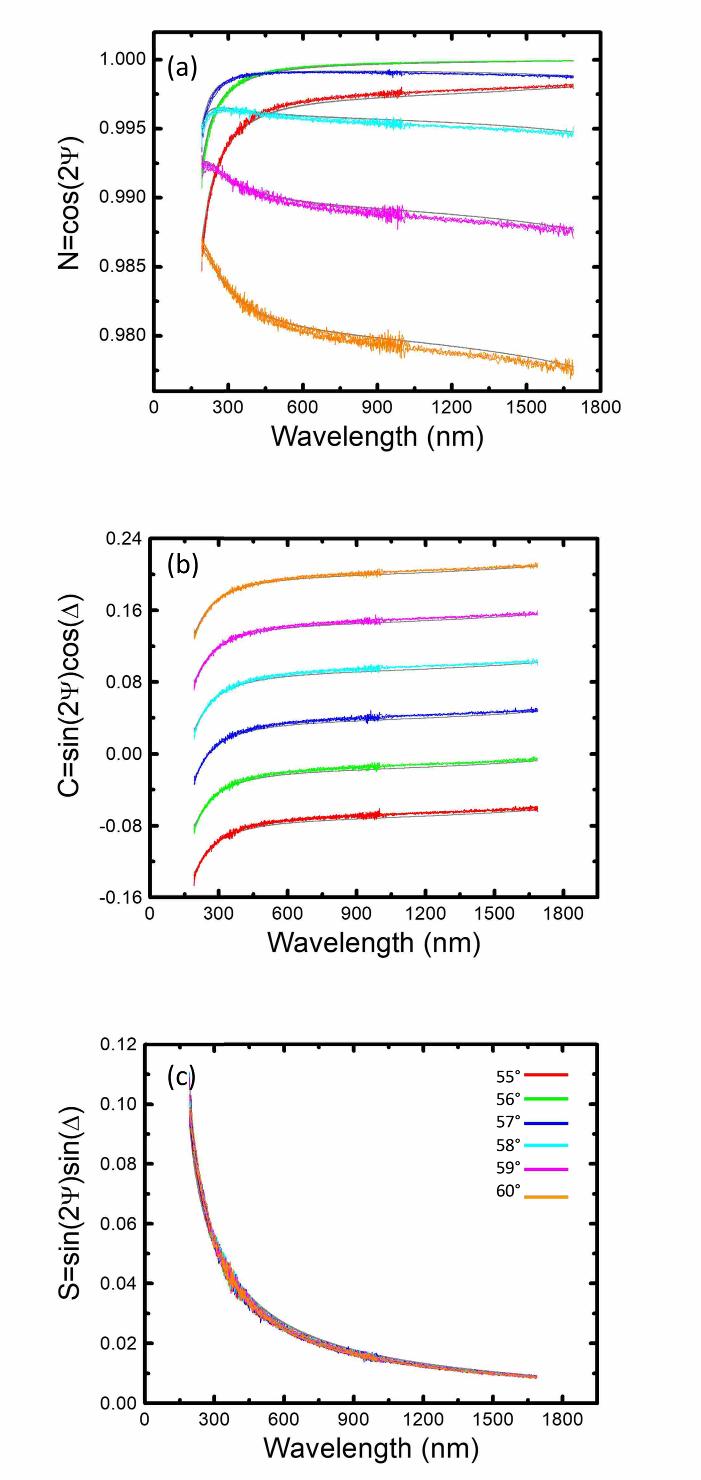

Figure 4-4 Raw ellipsometric data for 20 nm sputtered SiO2 films. (a) N, (b) C, and (c) S. Measurements were taken at six different angles of incidence (55°, 56°, 57°, 58°, 59°, 60°) on three different samples.

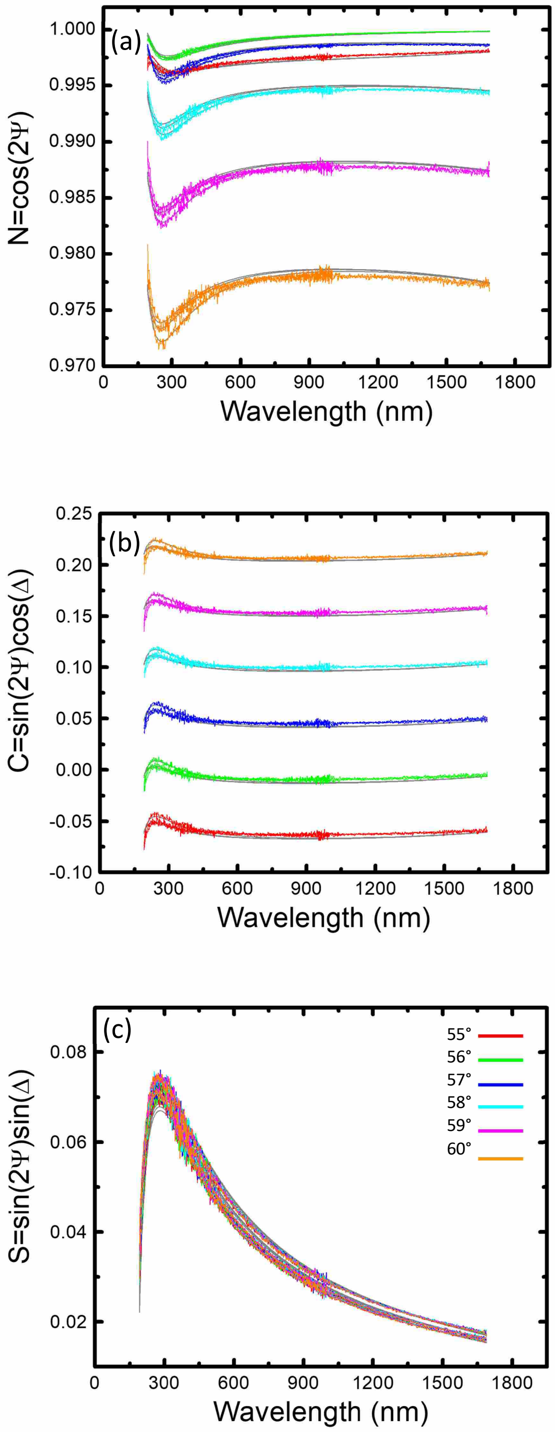

Figure 4-5 Raw ellipsometric data for 40 nm sputtered SiO2 film. (a) N, (b) C, and (c) S. Measurements were taken at six different angles (55°, 56°, 57°, 58°, 59°, 60°) on three different 40 nm samples.

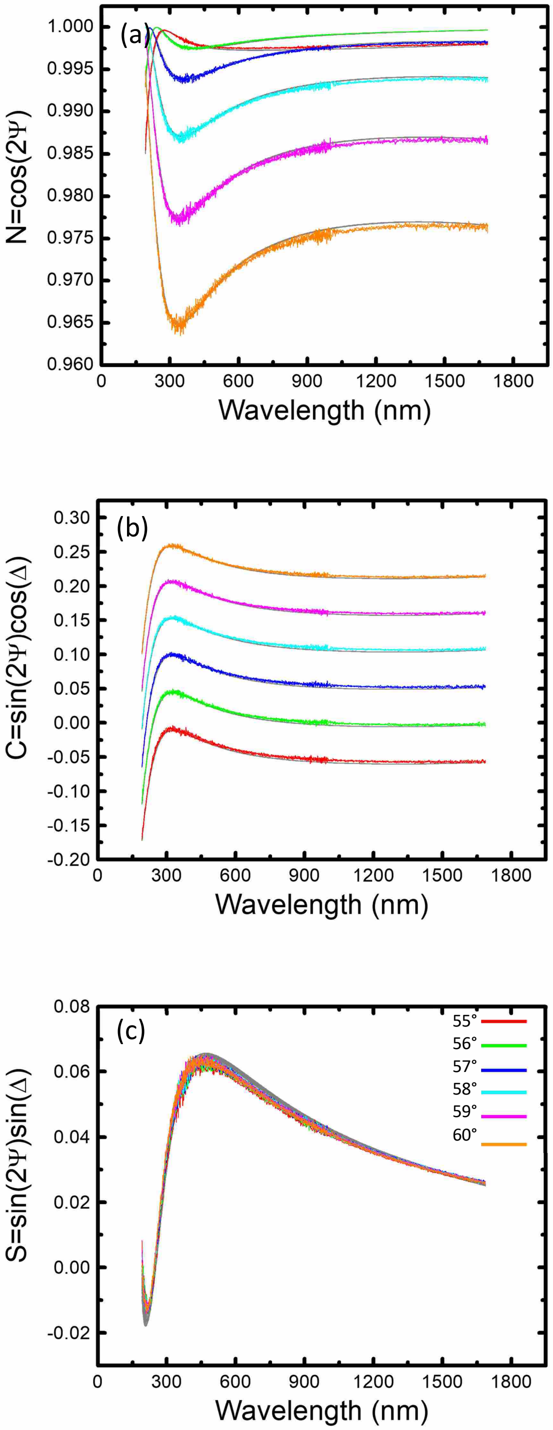

Figure 4-6 Raw ellipsometric data for 60 nm sputtered SiO2 films. (a) N, (b) C, and (c) S. Measurements were taken at six different angles of incidence (55°, 56°, 57°, 58°, 59°, 60°) on three different samples.

4.8 Acknowledgements

This work was supported and funded by Moxtek Inc. in Orem Utah. A special acknowledgement also goes to Anubhav Diwan of Moxtek for supplying these samples.

4.9 References

1. Kitamura, R.; Pilon, L.; Jonasz, M. Optical constants of silica glass from extreme ultraviolet to far infrared at near room temperature. *Applied Optics* **2007,** *46* (33), 8118-8133.
2. Kanyal, S. S.; Jensen, D. S.; Zhu, Z.; Linford, M. R. Silicon (100)/SiO_2 by ToF-SIMS. *Surface Science Spectra* **2015,** *22* (2), 1-6.
3. Jensen, D. S.; Kanyal, S. S.; Madaan, N.; Vail, M. A.; Dadson, A. E.; Engelhard, M. H.; Linford, M. R. Silicon (100)/SiO_2 by XPS. *Surface Science Spectra* **2013,** *20* (1), 36-42.
4. Tan, G. L.; Lemon, M. F.; French, R. H. Optical properties and London dispersion forces of amorphous silica determined by vacuum ultraviolet spectroscopy and spectroscopic ellipsometry. *Journal of the American Ceramic Society* **2003,** *86* (11), 1885-1892.
5. Herzinger, C.; Johs, B.; McGahan, W.; Woollam, J.; Paulson, W. Ellipsometric determination of optical constants for silicon and thermally grown silicon dioxide via a multi-sample, multi-wavelength, multi-angle investigation. *Journal of Applied Physics* **1998,** *83* (6), 3323-3336.
6. Jensen, D. S.; Kanyal, S. S.; Madaan, N.; Hancock, J. M.; Dadson, A. E.; Vail, M. A.; Vanfleet, R.; Shutthanandan, V.; Zhu, Z.; Engelhard, M. H. Multi-instrument characterization of the surfaces and materials in microfabricated, carbon nanotube-templated thin layer chromatography plates. An analogy to 'The Blind Men and the Elephant'. *Surface and Interface Analysis* **2013,** *45* (8), 1273-1282.
7. Lee, M. V.; Guo, D.; Linford, M. R.; Zuilhof, H. Molecular Modeling of Alkyl Monolayers on the Si (100)− 2× 1 Surface. *Langmuir* **2004,** *20* (21), 9108-9113.
8. Linford, M. R.; Fenter, P.; Eisenberger, P. M.; Chidsey, C. E. Alkyl monolayers on silicon prepared from 1-alkenes and hydrogen-terminated silicon. *Journal of the American Chemical Society* **1995,** *117* (11), 3145-3155.
9. Singh, B.; Diwan, A.; Jain, V.; Herrera-Gomez, A.; Terry, J.; Linford, M. R. Uniqueness plots: A simple graphical tool for identifying poor peak fits in X-ray photoelectron spectroscopy. *Appl. Surf. Sci.* **2016,** *387*, 155-162.
10. Yang, L.; Lua, Y.-Y.; Lee, M. V.; Linford, M. R. Chemomechanical functionalization and patterning of silicon. *Accounts of Chemical Research* **2005,** *38* (12), 933-942.
11. Sadigov, A.; Ahmadov, F.; Ahmadov, G.; Ariffin, A.; Khorev, S.; Sadygov, Z.; Suleymanov, S.; Zerrouk, F.; Madatov, R. A new detector concept for silicon photomultipliers. *Nuclear Instruments and Methods in Physics Research Section A: Accelerators, Spectrometers, Detectors and Associated Equipment* **2016,** *824*, 135-136.
12. Liao, S.; Zong, X.; Seger, B.; Pedersen, T.; Yao, T.; Ding, C.; Shi, J.; Chen, J.; Li, C. Integrating a dual-silicon photoelectrochemical cell into a redox flow battery for unassisted photocharging. *Nature Communications* **2016,** *7*.
13. Faggin, F. The MOS silicon gate technology and the first microprocessors. *Nuovo Cimento Rivista Serie* **2015,** *38*, 575-621.
14. Sinha, G.; Yadav, R. K. Optimization of multilayer antireflection coating for visible spectrum on silicon substrate for solar cell application. *Journal of Optical Technology* **2015,** *82* (12), 827-830.
15. Wang, W.; Chen, J. P.; Zivkovic, A. S.; Tanguy, Q. A. A.; Xie, H. K. A Compact Fourier Transform Spectrometer on a Silicon Optical Bench With an Electrothermal MEMS Mirror. *J. Microelectromech. Syst.* **2016,** *25* (2), 347-355.

16. Johnson, B. I.; Cushman, C. V.; Lunt, B. M.; Kaykhaii, M.; Linford, M. R. An Introduction to Silanes, their Chemical Vapor Deposition onto Si/SiO_2, and Characterization of the Resulting Monolayers. *Vacuum Technology & Coating* **2016**.

17. Quast, A. D.; Zhang, F.; Linford, M. R.; Patterson, J. E. Back-Surface Gold Mirrors for Vibrationally Resonant Sum-Frequency (VR-SFG) Spectroscopy Using 3-Mercaptopropyltrimethoxysilane as an Adhesion Promoter. *Applied Spectroscopy* **2011,** *65* (6), 634-641.

18. Husseini, G. A.; Peacock, J.; Sathyapalan, A.; Zilch, L. W.; Asplund, M. C.; Sevy, E. T.; Linford, M. R. Alkyl monolayers on silica surfaces prepared using neat, heated dimethylmonochlorosilanes with low vapor pressures. *Langmuir* **2003,** *19* (12), 5169-5171.

19. Lee, M. V.; Nelson, K. A.; Hutchins, L.; Becerril, H. A.; Cosby, S. T.; Blood, J. C.; Wheeler, D. R.; Davis, R. C.; Woolley, A. T.; Harb, J. N. Nanografting of silanes on silicon dioxide with applications to DNA localization and copper electroless deposition. *Chem. Mat.* **2007,** *19* (21), 5052-5054.

20. Ali, A. M.; Harraz, F. A.; Ismail, A. A.; Al-Sayari, S. A.; Algarni, H.; Al-Sehemi, A. G. Synthesis of amorphous ZnO-SiO_2 nanocomposite with enhanced chemical sensing properties. *Thin Solid Films* **2016,** *605*, 277-282.

21. Steinegger, P.; Asai, M.; Dressler, R.; Eichler, R.; Kaneya, Y.; Mitsuka, A.; Nagame, Y.; Piguet, D.; Sato, T. K.; Schadel, M.; Takeda, S.; Toyoshima, A.; Tsukada, K.; Turler, A.; Vascon, A. Vacuum Chromatography of TI on SiO_2 at the Single-Atom Level. *J. Phys. Chem. C* **2016,** *120* (13), 7122-7132.

22. Zhao, Y.; Xu, Z.; Wang, X.; Lin, T. Photoreactive azido-containing silica nanoparticle/polycation multilayers: durable superhydrophobic coating on cotton fabrics. *Langmuir* **2012,** *28* (15), 6328-6335.

23. Yi-Qin, J.; Yu-Gang, J.; Hua-Song, L.; Li-Shuan, W.; Dan-Dan, L.; Cheng-Hui, J.; Rong-Wei, F.; De-Ying, C. Optical Constants of SiO_2 Films Deposited on Si Substrates. *Chinese Physics Letters* **2014,** *31* (4), 046401.

24. Jung, H.; Kim, W.-H.; Oh, I.-K.; Lee, C.-W.; Lansalot-Matras, C.; Lee, S. J.; Myoung, J.-M.; Kim, H. Growth characteristics and electrical properties of SiO_2 thin films prepared using plasma-enhanced atomic layer deposition and chemical vapor deposition with an aminosilane precursor. *Journal of Materials Science* **2016,** *51* (11), 5082-5091.

25. Amirzada, M. R.; Tatzel, A.; Viereck, V.; Hillmer, H. Surface roughness analysis of SiO_2 for PECVD, PVD and IBD on different substrates. *Appl. Nanosci.* **2016,** *6* (2), 215-222.

26. Son, J.; Efremov, A.; Chun, I.; Yeom, G. Y.; Kwon, K. H. On the LPCVD-Formed SiO_2 Etching Mechanism in CF_4/Ar/O_2 Inductively Coupled Plasmas: Effects of Gas Mixing Ratios and Gas Pressure. *Plasma Chem. Plasma Process.* **2014,** *34* (2), 239-257.

27. Wang, C.; Cho, S. J.; Kim, N. Y. Comparison of SiO_2-based double passivation scheme by e-beam evaporation and PECVD for surface passivation and gate oxide in AlGaN/GaN HEMTs. *Microelectron. Eng.* **2013,** *109*, 24-27.

28. Fang, G.; Xu, L.; Ma, J.; Li, A. Theoretical Understanding of the Reaction Mechanism of SiO_2 Atomic Layer Deposition. *Chem. Mat.* **2016,** *28* (5), 1247-1255.

29. Choi, H.; Uhm, H. S.; Kwon, G. C.; Cho, B.; Yoo, J. Plasma Enhanced Atomic Layer Deposition of SiO_2 Using Space-Divided Plasma System. *Sci. Adv. Mater.* **2016,** *8* (4), 872-877.

30. Jung, H.; Kim, W. H.; Oh, I. K.; Lee, C. W.; Lansalot-Matras, C.; Lee, S. J.; Myoung, J. M.; Lee, H. B. R.; Kim, H. Growth characteristics and electrical properties of SiO_2 thin films

prepared using plasma-enhanced atomic layer deposition and chemical vapor deposition with an aminosilane precursor. *Journal of Materials Science* **2016,** *51* (11), 5082-5091.

31. Pfeiffer, K.; Shestaeva, S.; Bingel, A.; Munzert, P.; Ghazaryan, L.; van Helvoirt, C.; Kessels, W. M.; Sanli, U. T.; Grévent, C.; Schütz, G. Comparative study of ALD SiO_2 thin films for optical applications. *Optical Materials Express* **2016,** *6* (2), 660-670.

32. Kesmez, Ö.; Çamurlu, H. E.; Burunkaya, E.; Arpaç, E. Sol–gel preparation and characterization of anti-reflective and self-cleaning SiO_2–TiO_2 double-layer nanometric films. *Solar Energy Materials and Solar Cells* **2009,** *93* (10), 1833-1839.

33. Hinczewski, D. S.; Hinczewski, M.; Tepehan, F.; Tepehan, G. Optical filters from SiO_2 and TiO_2 multi-layers using sol–gel spin coating method. *Solar Energy Materials and Solar Cells* **2005,** *87* (1), 181-196.

34. Fu, S. W.; Chen, H. J.; Wu, H. T.; Shih, C. F. Effect of SiO_2 layers on electroluminescence from Si nanocrystal/SiO_2 superlattices prepared using argon ion beam assisted sputtering. *Vacuum* **2016,** *126*, 59-62.

35. Kim, J. K.; Jeong, S. H.; Oh, S. A.; Moon, S. J.; Imura, K.; Okada, T.; Noguchi, T.; Yun, E. J.; Bae, B. S. Electrical Characteristics of a-IGZO TFTs With SiO_2 Gate Insulator Prepared by RF Sputtering. *J. Disp. Technol.* **2016,** *12* (3), 5.

36. Ikuno, T.; Ogawa, S.; Suzuki, N.; Ito, T.; Sugimoto, N.; Takeda, Y.; Motohiro, T.; Higuchi, K. Resonant tunneling properties of SiO_2/polycrystalline Si/SiO_2 multilayers fabricated by radio-frequency magnetron sputtering. *Journal of Applied Physics* **2015,** *118* (10), 5.

37. Nagata, K.; Ogura, A.; Hirosawa, I.; Suwa, T.; Teramoto, A.; Hattori, T.; Ohmi, T. Structural Analyses of Thin SiO_2 Films Formed by Thermal Oxidation of Atomically Flat Si Surface by Using Synchrotron Radiation X-Ray Characterization. *ECS J. Solid State Sci. Technol.* **2015,** *4* (8), N96-N98.

38. Kageshima, H.; Uematsu, M.; Shiraishi, K. Theory of thermal Si oxide growth rate taking into account interfacial Si emission effects. *Microelectron. Eng.* **2001,** *59* (1-4), 301-309.

39. Tatsumura, K.; Watanabe, T.; Yamasaki, D.; Shimura, T.; Umeno, M.; Ohdomari, I. Large-scale atomistic modeling of thermally grown SiO_2 on Si(111) substrate. *Japanese Journal of Applied Physics Part 1-Regular Papers Brief Communications & Review Papers* **2004,** *43* (2), 492-497.

40. Wu, W.-F.; Chiou, B.-S. Optical and mechanical properties of reactively sputtered silicon dioxide films. *Semiconductor Science and Technology* **1996,** *11* (9), 1317.

41. Jeong, S.-H.; Kim, J.-K.; Kim, B.-S.; Shim, S.-H.; Lee, B.-T. Characterization of SiO_2 and TiO_2 films prepared using rf magnetron sputtering and their application to anti-reflection coating. *Vacuum* **2004,** *76* (4), 507-515.

42. Groner, M.; Fabreguette, F.; Elam, J.; George, S. Low-temperature Al_2O_3 atomic layer deposition. *Chem. Mat.* **2004,** *16* (4), 639-645.

43. Cushman, C. V.; Sturgell, B. A.; Martin, A. C.; Lunt, B. M.; Smith, N. J.; Linford, M. R. Eagle XG® glass, optical constants from 230 to 1690 nm (0.73-5.39 eV) by spectroscopic ellipsometry. *Surface Science Spectra* **2016,** *23* (1), 55-60.

44. Cushman, C. V.; Sturgell, B. A.; Martin, A. C.; Lunt, B. M.; Smith, N. J.; Linford, M. R. Eagle XG® glass, optical constants from 196 to 1690 nm (0.73-5.39 eV) by spectroscopic ellipsometry. *Submitted to Surface Science Spectra* **2016**.

45. Synowicki, R. Suppression of backside reflections from transparent substrates. *Physica Status Solidi (c)* **2008,** *5* (5), 1085-1088.

46. Tompkins, H.; Tiwald, T. In *Spectroscopic Ellipsometry Analysis of Optical Coatings on Transparent Substrates*, Proceedings of the Annual Technical Conference-Society of Vacuum Coaters, 2007; p 354.

47. Hilfiker, J. N.; Singh, N.; Tiwald, T.; Convey, D.; Smith, S. M.; Baker, J. H.; Tompkins, H. G. Survey of methods to characterize thin absorbing films with Spectroscopic Ellipsometry. *Thin Solid Films* **2008,** *516* (22), 7979-7989.

48. Benzarti, Z.; Khelifi, M.; Halidou, I.; El Jani, B. Study of Surface and Interface Roughness of GaN-Based Films Using Spectral Reflectance Measurements. *Journal of Electronic Materials* **2015,** *44* (10), 3243-3252.

49. Akagawa, M.; Fujiwara, H. Optical characterization of textured SnO_2: F layers using spectroscopic ellipsometry. *Journal of Applied Physics* **2012,** *112* (8), 083507.

50. Johs, B.; Hale, J. S. Dielectric function representation by B-splines. *Physica Status Solidi (a)* **2008,** *205* (4), 715-719.

51. J.A, W. CompleteEASE® software package

52. Cushman, C. V. Z., J.; Sturgell, B. A.; Major, G. I.; Lunt, B. M.; Brüner, P.; Grehl, T.; Smith, N. J.; Linford, M. R. Time-of-Flight Secondary Ion Mass Spectrometry of Wet and Dry Chemically Treated Display Glass Surfaces *Journal of the American Ceramic Society.* **2017,** *Manuscript accepted.*

53. Jellison, G.; Sales, B. Determination of the optical functions of transparent glasses by using spectroscopic ellipsometry. *Applied Optics* **1991,** *30* (30), 4310-4315.

54. Synowicki, R. A.; Johs, B. D.; Martin, A. C. Optical properties of soda-lime float glass from spectroscopic ellipsometry. *Thin Solid Films* **2011,** *519* (9), 2907-2913.

55. Synowicki, R. Spectroscopic ellipsometry characterization of indium tin oxide film microstructure and optical constants. *Thin Solid Films* **1998,** *313*, 394-397.

56. El Rhaleb, H.; Benamar, E.; Rami, M.; Roger, J.; Hakam, A.; Ennaoui, A. Spectroscopic ellipsometry studies of index profile of indium tin oxide films prepared by spray pyrolysis. *Appl. Surf. Sci.* **2002,** *201* (1), 138-145.

57. Jung, Y. S. A spectroscopic ellipsometry study on the variation of the optical constants of tin-doped indium oxide thin films during crystallization. *Solid State Communications* **2004,** *129* (8), 491-495.

58. Lohner, T.; Kumar, K. J.; Petrik, P.; Subrahmanyam, A.; Bársony, I. Optical analysis of room temperature magnetron sputtered ITO films by reflectometry and spectroscopic ellipsometry. *Journal of Materials Research* **2014,** *29* (14), 1528-1536.

59. Tranchida, D.; Piccarolo, S.; Deblieck, R. Some experimental issues of AFM tip blind estimation: the effect of noise and resolution. *Measurement Science and Technology* **2006,** *17* (10), 2630.

60. Zenhausern, F.; Adrian, M.; Emch, R.; Taborelli, M.; Jobin, M.; Descouts, P. Scanning force microscopy and cryo-electron microscopy of tobacco mosaic virus as a test specimen. *Ultramicroscopy* **1992,** *42*, 1168-1172.

61. Fang, S.; Chen, W.; Yamanaka, T.; Helms, C. Comparison of Si surface roughness measured by atomic force microscopy and ellipsometry. *Applied Physics Letters* **1996,** *68* (20), 2837-2839.

62. Bustamante, C.; Vesenka, J.; Tang, C. L.; Rees, W.; Guthold, M.; Keller, R. Circular DNA molecules imaged in air by scanning force microscopy. *Biochemistry* **1992,** *31* (1), 22-26.

63. Dahal, L. R.; Sainju, D.; Podraza, N.; Marsillac, S.; Collins, R. Real time spectroscopic ellipsometry of Ag/ZnO and Al/ZnO interfaces for back-reflectors in thin film Si: H photovoltaics. *Thin Solid Films* **2011,** *519* (9), 2682-2687.
64. Tiwald, T. Sellmeier Dispersion. *J.A. Woollam Co., Inc. Annual Newsletter* **January, 2009,** (10), 8-9.

CHAPTER 5: Conclusion

5.1 Key Findings from Each Chapter

The means by which surfaces and interfaces interact with each other and their environments plays a crucial role in today's technology and drives future research in this area.[100] Indeed, surface modification and characterization have advanced to the point that they now occur routinely at the nanometer scale and even down to the molecular level.[100] In this dissertation, I prepared three different ultra-thin films under controlled environments and addressed subsequent analytical challenges. Ultimately, I was able to apply and develop various analytical methods for thin film characterization, gaining insight into these materials and their potential interactions with their environments.

In Chapter 2, I present the real time (dynamic) SE and XPS characterization of MgF_2 -coated aluminum thin films. Analyses of these optical stacks showed that both optical and chemical changes took place in the aluminum films beneath ultrathin films of magnesium fluoride. I found here that the aluminum films oxidize over time, but that this oxidation is retarded by increasingly thick MgF_2 overlayers. The XPS data for this study were collected from seven different samples over a period of 3 – 10 months. The oxidation of aluminum was confirmed by increases in the O 1s signal and the chemically shifted (Al^{3+}) Al 2p and Al 2s signals. A model for oxide growth, which included a correction for the thickness of the MgF_2 layer, was based on the relative areas of the Al^{3+} and metallic Al peaks. This analysis showed that oxidation increased linearly with the logarithm of time as in the following empirical formula: oxide thickness= k*ln (t) +b. This logarithmic model fits the data somewhat better than the Cabrerra-Mott (CM) model, which has been applied to monitor thin oxide films.

SE was also able to detect time-dependent changes in the optical stacks. These measurements were collected immediately after the stacks were deposited and then again after several hours and even months. In the SE data analysis, it became clear that the optical constants of the ultrathin metal (aluminum) films depended strongly on their deposition conditions and thickness so they needed to be individually fit. The optical constants of the Al films were initially estimated via an MSA of similar stacks. Two different models were then employed to work up the Al_2O_3 thickness vs. time data generated from the dynamic SE analyses. While the second of these models gave more physically reasonably results, both made nearly identical predictions about the rate of Al oxidation beneath the MgF_2 coatings. The oxidation changes I observed were similar to those found by XPS – they followed the simple logarithmic model more closely than the Cabrerra-Mott model. It was important in these analyses to know the thickness of the MgF_2 layer as accurately as possible. It was, however, challenging to determine the optical function of MgF_2 on Al_2O_3 because of the similarity of their optical functions. Ultimately, I was able to develop an iterative method for determining the MgF_2 layer thicknesses by XPS using standards of known thicknesses. I also found that MgF_2 deposited on heated substrates results in denser films. Although this had been suspected for some time, to the best of my knowledge, no one has ever verified this fact.

My work in Chapter 3 focused on the CF_2/CF_3 C 1s narrow scan envelopes of four fluorosilane adsorbates: $CF_3(CH_2)_2SiCl_3$, $CF_3(CF_2)_3(CH_2)_2SiCl_3$, $CF_3(CF_2)_5(CH_2)_2SiCl_3$, and $CF_3(CF_2)_7(CH_2)_2SiCl_3$. This work was done to address the issue of finding the correct CF_2/CF_3 area ratios (m_{CF_2/CF_3}) from X-ray photoelectron spectroscopy (XPS) C 1s narrow scans of materials containing $–CH_2CH_2(CF_2)_nCF_3$, n = 0, 1, 2, …, moieties. Here, the quality of the modeling was assessed based on the m_{CF_2/CF_3} slope values being close to unity, the y-intercept values of these lines approaching zero, and the standard deviations of the residuals of the fits. I started this analysis with the simplest possible model (two unconstrained peaks). I then obtained additional information for this modeling by determining the expected widths of the CF_2 and CF_3 peaks from standards and by performing ab initio calculations via Koopman's approximation on the silane adsorbates. Ultimately, two semiempirical models, which were based on both Literature precedent and the ab initio calculations, produced the best results.

Chapter 4 describes an SE study of reactively sputtered SiO_2 films, nominally 20, 40, and 60 nm thick, deposited on Eagle XG® (EXG), an important display glass. This analysis relied on multiple experimental and computational considerations, including proper backside roughening (two methods for doing this were considered), an MSA, data collection at different angles of incidence, and the use of pre-determined EXG glass optical constants. The combination of these efforts yielded a set of high quality optical constants for sputtered SiO_2. In other words, this work illustrates that appropriate experimental and modeling efforts can allow meaningful information to be extracted from SE analyses of transparent thin films on transparent substrates.

Appendix 1: Appropriate Back Side Roughening Is a Key for Spectroscopic Ellipsometry Analysis of Transparent Materials

A1.1 Statement of Attribution

This article was originally published as Johnson, B. I., et al. (2018). Appropriate Backside Roughening is Key for Good Spectroscopic Ellipsometry Analysis of Transparent Materials. Vacuum Technology & Coating. **19:** 26-30.

A1.2 Introduction

Proper sample preparation often plays a key role in surface analysis. For example, X-ray photoelectron spectroscopy (XPS) and time-of-flight secondary ion mass spectrometry (ToF-SIMS) probe less than 10 nm into a material – it doesn't take much contamination to completely obscure any signal coming from a surface with these techniques.[1] Spectroscopic ellipsometry (SE) is also exquisitely sensitive to sample preparation and contamination. As a rather crude demonstration of this sensitivity, we recently showed the results of pressing a thumb into a silicon wafer, i.e., we left a thumbprint on the surface. This perturbation led to substantial changes in the SE measurement.[2] In this article we'll talk about surface/material preparation for SE of transparent samples. In particular, we'll deal in a practical way with the issue of backside reflection from transparent samples. These reflections are incoherent (lacking a phase relationship) with the reflected light and can degrade the quality of a measurement.

A1.3 Discussion

When compared to XPS and ToF-SIMS, SE has some real advantages. Some examples of these advantages are: (i) SE analyses can usually be done quickly in the open air, (ii) the instruments are often about an order of magnitude cheaper than XPS and ToF-SIMS systems, and (iii) the penetration depth of the technique can be hundreds of nanometers or more for samples that absorb little or no light. With regards to this last advantage, you would be unable to analyze a moderately thick optical stack/multilayer by XPS or ToF-SIMS without depth profiling, but such types of analyses are routinely done with SE. Also note that SE measurements do not require external references or calibrations. However, like XPS and ToF-SIMS, SE data analysis can take a considerable amount of time – you may be able to acquire data from a new sample in a few minutes, but the analysis of the data can take days or weeks.

SE uses light of a known polarization state to probe surfaces and materials.[3] This light will have both p- and s-polarized components, i.e., electric field components that are in and out of the plane of incidence, respectively (see Figure A1.1). SE determines the intensity ratio and phase difference of the p- and s-polarized components of the light after it reflects from a surface of interest. Of course this means that the sample of interest must be at least moderately flat. The information obtained by SE can be expressed as:

$$\rho = tan(\Psi)e^{i\Delta} \tag{1}$$

Thus, the two key parameters measured in SE are ψ and Δ, which provide information about the amplitude ratio and phase difference of the p and s components of the light, respectively. Structural/morphological information about samples is generally obtained from SE by modeling. That is, one creates a model that represents a physical system, which may consist of a substrate layer, multiple layers that represent thin films, as well as roughness, interface, and gradient layers. The optical constants of the layers and substrate may or not be known prior to the modeling. The standard equations of light and optics, e.g., Fresnel's equations and Snell's law, are used to calculate the theoretical values of ψ and Δ for the model and these values are compared to those determined experimentally. Parameters in the model, e.g., film thicknesses, roughnesses, or optical constants, can then be varied to minimize the error between the experimentally and theoretically determined values of ψ and Δ.

Glass is an incredibly important material. It is a building material; it is used to create external and internal windows in buildings. It is made into vessels that store food and beverages, and also into vessels for cooking and science – most of the organic chemistry ever performed has been done in glass. Fiber optics are made of glass, and they have revolutionized our ability to communicate. Display glasses are the basic substrates onto which the electronics of many consumer devices are created, e.g., the electronics in our cell phones are generally microfabricated on these surfaces, and in general there is another piece of glass at the top of your cell phone. Glass is even important because of its ability to trap nuclear waste products. Clearly glass plays an incredibly important role in modern technology. In addition, glass matters for geology (there are natural glasses like obsidian that have been useful to man for millennia), and in archeology (people have been making and manipulating functional and decorative glass objects for a very long time). It is easy to see why the study and characterization of glasses is important at both the academic and industrial levels.

SE is an important analytical technique for the characterization of glasses it is an extremely sensitive tool that is highly dependent on film and material composition.[4-6] Therefore, it is essential that sample preparation for SE be performed with care. Since glass is transparent, light from an ellipsometer will reflect off of its top and bottom surfaces, as shown in Figure A1.2. Though it could be argued that this would be advantageous because the light reflecting off of the back of the sample will pass through/probe the entire sample, as noted above, the light reflecting from the bottom surface is generally incoherent with the light reflecting off of the top of the sample. Note, however, that a very powerful way of studying a transparent material by ellipsometry is to perform reflection and transmission measurements on it and to combine the two into a single model. The transmission measurement will be more sensitive to absorptions in the glass than the reflection data. Thus, the backside-reflected light is a hindrance to the measurement and modeling, and it would be ideal if it could be eliminated or suppressed. It should come then as no surprise that people have considered a variety of methods to deal with this light in their studies of glass. These include the use of index coupling (IC) agents, such as light oils, that are placed onto the backside of the glass which is subsequently put onto an absorbing surface, e.g., an anodized aluminum surface.[7-8] We have, for example, used cedar oil in our lab for this purpose. (As a minor side benefit here, cedar oil smells good.) An index matching fluid allows the light that reaches the backside of the glass substrate to continue into the oil until it reaches an absorbing surface, which eliminates it. Another method employs translucent Scotch™ tape on the backside of the glass substrate.[7, 9-10] The polymer in the tape's adhesive similarly acts as an index matching material, and the tape itself scatters the light. Yet another option, is to use a thick sample, which will physically separate the reflections off of the sample, i.e., the reflected light from the top surface can be directed into the detector at the exclusion of the beam of light from the lower surface. The final method we will talk about here is backside roughening. In backside roughening we physically roughen the backside of the glass. This resulting roughened surface scatters the light incident on it.[6-8] Although it is a destructive method, it is effective for glass measurements by SE. (It should go without saying here that if you want to combine transmission and reflection measurements in your model, you should do the transmission measurements before you roughen one of the surfaces.) The question we ask here is, how good or smooth does the roughening need to be for an acceptable and reproducible signal to be produced? It could be argued that because the light is being dispersed and removed from the field of optical view to the detector that the smoothness and quality of a roughened backside would not make a large difference in the data being received at the detector. We now compare and discuss the SE results obtained from roughening the backside of a glass sample in two different ways: using a hand-held Dremel® tool and by sandblasting. As we will show, sandblasting produces a higher quality, more uniform matte finish, which appears to be superior for removing backside reflections in SE measurements. These results are a byproduct of a multi-sample analysis we did of 20, 40, and 60 nm sputtered films of SiO_2 on Eagle XG® glass.[6]. By 'multi-sample analysis we mean that all the data were fit together in the model.

In our study, we first used a hand-held Dremel® tool with a stone bit (Figure A1.3) to roughen the backsides of each of the samples, as shown in Figure A1.4. After they were analyzed by SE, Different sets of optical constants were then derived for the samples using different multi-sample analyses, i.e., different groupings of the samples. The assumption a priori was that each set of optical constants should be fairly close to the others. The results were not as good as we would have hoped for – notice the scatter in the results in Figure A1.5. Accordingly, another set of samples with nominally identical sputtered SiO_2 films on them were prepared by sandblasting their backsides. While even simple pieces of laboratory equipment often cost thousands of dollars, we obtained our sandblaster for only about $200 from a local hardware store (see Figure A1.6). To prepare the samples for sandblasting, they were taped face down to a watch glass (see Figure A1.7). Here, the tape only touched the edges of the glass sample, but the tape made a seal between the glass slide and the watch glass so that only one side of the sample would be affected. This set up is illustrated in Figure A1.8. Using this approach, nine samples were roughened in about a quarter of the time as compared to roughing nine samples with the Dremel®. The result of this sandblasting is seen in Figure A1.9. It is clear that the sandblasting has created a uniform frosted finish over the glass. When the optical constants for the samples were determined and compared, the difference between them was significantly less than what had been found with the Dremel® (see Figure A1.10). This improved sample preparation gave us much more confidence in the final optical constants we determined for this important material. In summary, data quality can often be directly related to sample preparation.

A1.4 Conclusion

In this work we showed the importance of proper sample preparation for material characterization, and in particular the importance of proper backside roughening for transparent substrates measured in SE. We compared the indices of refraction from two sets of samples, each with identical surface preparations and substrates. By visual inspection, it was clear that the glass surface with a higher quality of backside roughening yielded more precise and accurate results. The optical constants were obtained with greater confidence as a direct result of the superior backside roughening.

A1.5 Figures

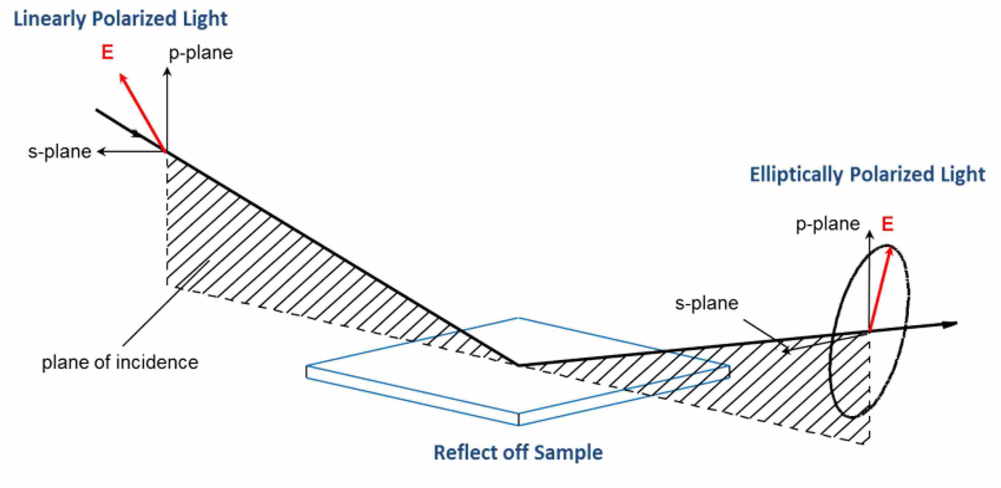

Figure A0-1 Visual representation of Elliptically polarized light Used from – this figure is from: the JA Woollam web sitesitehttps://www.jawoollam.com/resources/ellipsometry-tutorial/what-is-ellipsometry

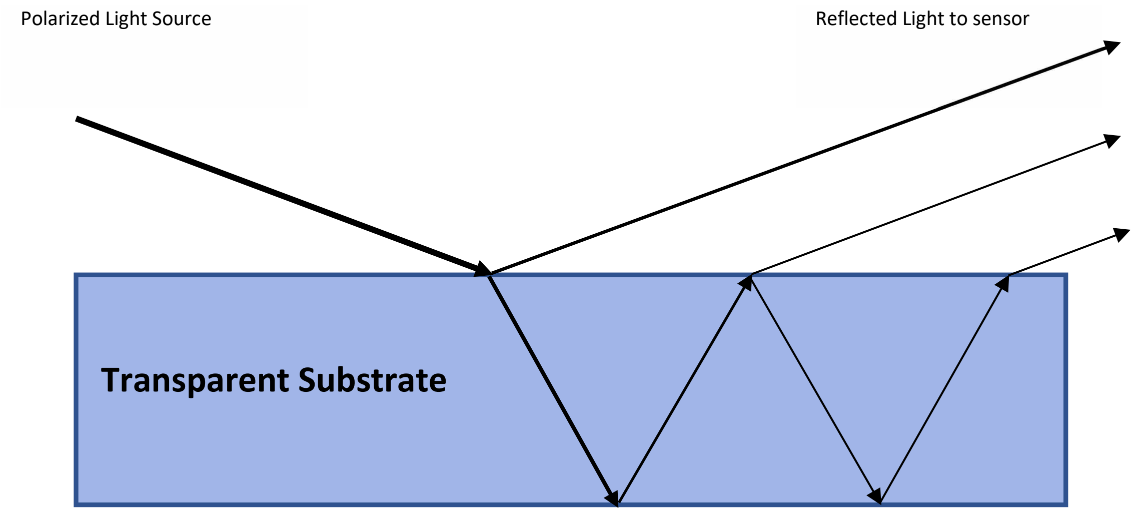

Figure A0-2 Visual depiction of backside reflection from transparent substrate

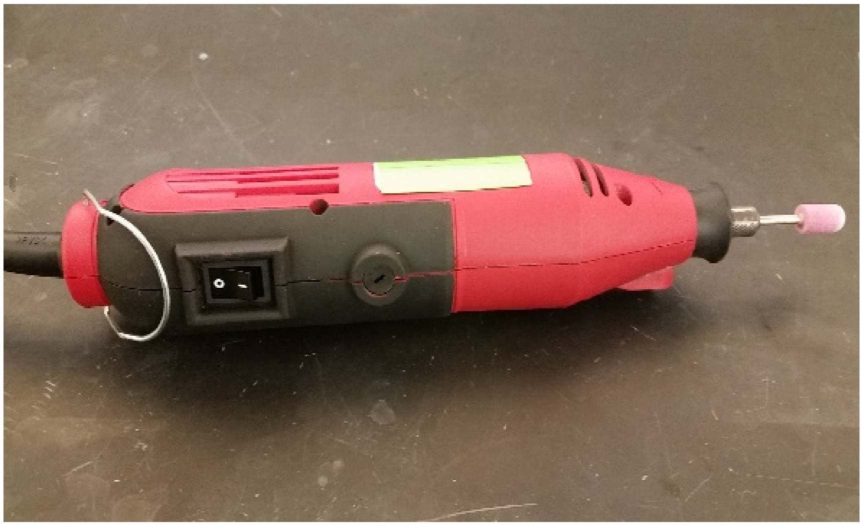

Figure A0-3 Dremmel tool used to roughen backsides of EXG™

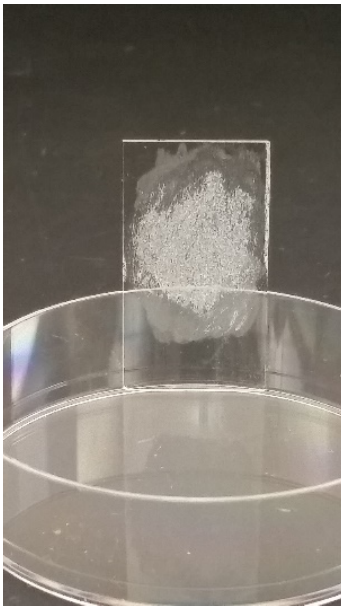

Figure A0-4 EXG™ slide roughened by hand-held tool

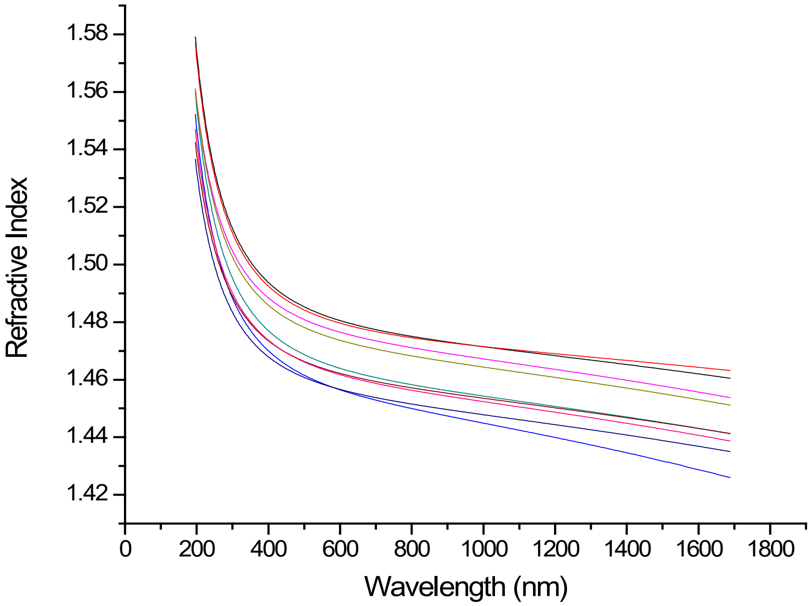

Figure A0-5 Refractive Index for dremmel roughened glass substrate

Figure A0-6 Sandblaster used for roughening of glass substrate

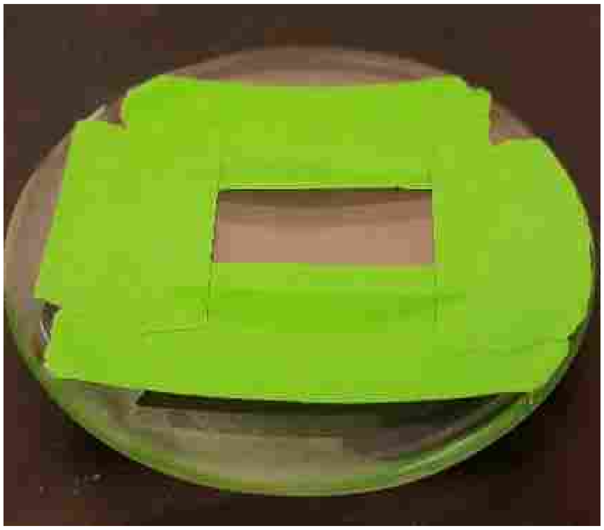

Figure A0-7 Set-up for roughening of glass substrate by sandblaster

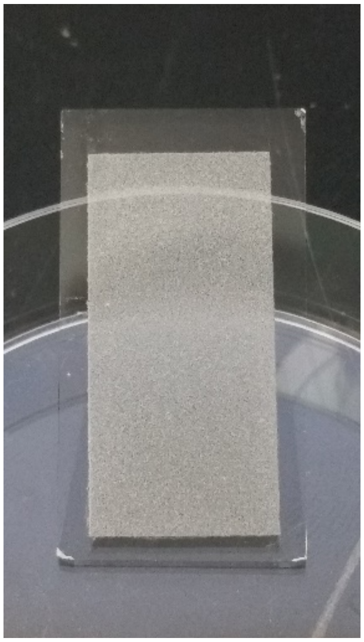

Figure A0-8 Set-up for roughening of glass substrate by sandblaster

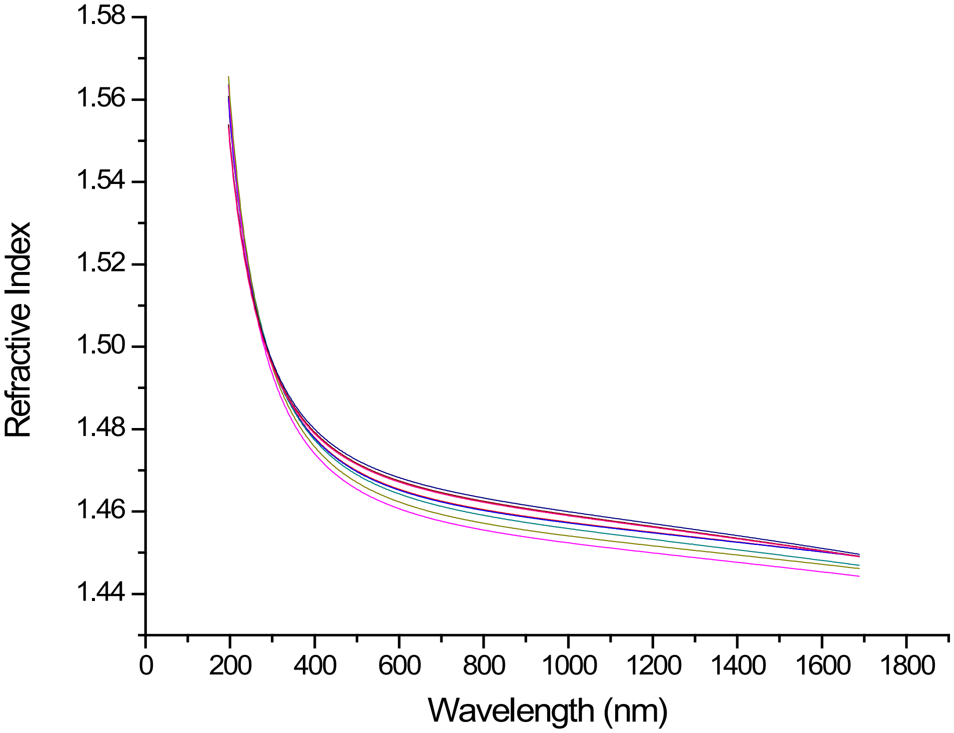

Figure A0-9 Refractive Index for sandblaster roughened glass substrate

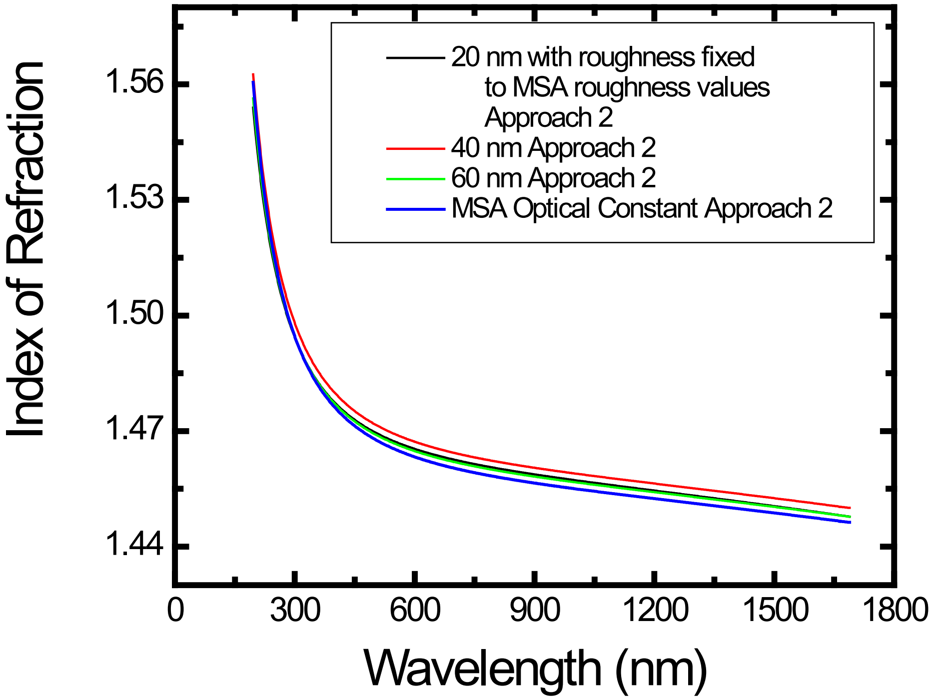

Figure A0-10 Refractive indices of SiO2 obtained via comprehensive MSAs of 20, 40, and 60 nm films. Figure obtained from Reference 5

A1.6 References

1. Chatterjee, S.; Singh, B.; Diwan, A.; Lee, Z. R.; Engelhard, M. H.; Terry, J.; Tolley, H. D.; Gallagher, N. B.; Linford, M. R., A perspective on two chemometrics tools: PCA and MCR, and introduction of a new one: Pattern recognition entropy (PRE), as applied to XPS and ToF-SIMS depth profiles of organic and inorganic materials. *Applied Surface Science* **2018,** *433*, 994-1017.
2. Bagley, J. D.; Tolley, D. H.; Linford, M. R., Reevaluating the Conventional Approach for Analyzing Spectroscopic Ellipsometry Psi/Delta vs. Time Data. Additional Statistical Rigor May Often Be Appropriate.
3. Fujiwara, H., *Spectroscopic ellipsometry: principles and applications*. John Wiley & Sons: 2007.
4. Cushman, C. V.; Sturgell, B. A.; Martin, A. C.; Lunt, B. M.; Smith, N. J.; Linford, M. R., Eagle XG® glass, optical constants from 230 to 1690 nm (0.73-5.39 eV) by spectroscopic ellipsometry. *Surface Science Spectra* **2016,** *23* (1), 55-60.
5. Cushman, C. V.; Johnson, B. I.; Martin, A.; Lunt, B. M.; Smith, N. J.; Linford, M. R., Eagle XG® glass: Optical constants from 196 to 1688 nm (0.735–6.33 eV) by spectroscopic ellipsometry. *Surface Science Spectra* **2017,** *24* (2), 026001.
6. Johnson, B. I.; Cushman, C. V.; Rowley, J.; Lunt, B. M.; Smith, N. J.; Martin, A.; Linford, M. R., Optical constants of SiO2 from 196 to 1688 nm (0.735–6.33 eV) from 20, 40, and 60 nm films of reactively sputtered SiO2 on Eagle XG® glass by spectroscopic ellipsometry. *Surface Science Spectra* **2017,** *24* (2), 026002.
7. Synowicki, R., Suppression of backside reflections from transparent substrates. *physica status solidi (c)* **2008,** *5* (5), 1085-1088.
8. Hayton, D.; Jenkins, T., On the frustration of back-surface reflection from transparent substrates in ellipsometry. *Measurement Science and Technology* **2003,** *15* (2), N17.
9. Funke, S.; Miller, B.; Parzinger, E.; Thiesen, P.; Holleitner, A.; Wurstbauer, U., Imaging spectroscopic ellipsometry of MoS2. *Journal of Physics: Condensed Matter* **2016,** *28* (38), 385301.
10. Kageyama, S.; Akagawa, M.; Fujiwara, H., Ellipsometry characterization of a-Si: H layers for thin-film solar cells. *Journal of Non-Crystalline Solids* **2012,** *358* (17), 2257-2259.

Appendix 2: Development of a Small Dry Box for Transferring Silanes for CVD. (It's Better to Make Good Measurements on Well-Prepared Samples than to Study Samples of Questionable Quality.)

A2.1 Statement of Attribution

This article was originally published as Johnson, B. I., et al. (September 2018). "It's Better to Make Good Measurements on Well-Prepared Samples than to Study Samples of Questionable Quality. Development of a Small Dry Box for Transferring Chemicals (Silanes) for CVD" Vacuum Technology & Coating. **19:** 26-31.

A2.2 Introduction

Surface characterization represents a commitment of resources. It takes time to make measurements, and it takes time to analyze and understand the results. Given the opportunity, one is generally better off producing higher quality samples and analyzing them than the opposite. With this in mind, it is prudent to ensure that the materials that are used for surface modifications are high quality, maintained, and properly prepared.

A2.3 Discussion

A2.3.1 Silanes and Their Deposition

We have a chemical vapor deposition (CVD) oven from Yield Engineering Systems (see Figure 1) that we use to modify surfaces with silanes. Silanes have the name they do because they are chemical derivatives of silane, SiH_4. That is, they are molecules in which one or more of the hydrogens on SiH_4 has been replaced by another chemical moiety. In some cases, the new groups on the silanes react with SiOH groups (silanols) on silica. As a result, silanes have been used for many years to treat and chemically modify silica and other related materials. Some of the most common silanol-reactive groups on silanes are the methoxy, ethoxy, chloro, and dimethylamino groups, which are written chemically as: $-OCH_3$ (-OMe), $-OCH_2CH_3$ (-OEt), -Cl, and $–N(CH_3)_2$, respectively, where the methyl (CH_3) and ethyl (CH_2CH_3) groups in organic chemistry can be conveniently abbreviated 'Me' and 'Et', as they are here. The reactions of these silanes with a surface silanol, which we represent as '$Si_{surf}OH$' is as follows:

(i) $Si_{surf}OH + MeOSiRR'R'' \rightarrow Si_{surf}OSiRR'R'' + MeOH$

(ii) $Si_{surf}OH + EtOSiRR'R'' \rightarrow Si_{surf}OSiRR'R'' + EtOH$

(iii) $Si_{surf}OH + ClSiRR'R'' \rightarrow Si_{surf}OSiRR'R'' + HCl$

(iv) $Si_{surf}OH + (CH_3)_2NSiRR'R'' \rightarrow Si_{surf}OSiRR'R'' + (CH_3)_2NH$

Here are a few clarifying notes for these reactions: (i) we have represented the three other groups on the silane molecules here as generic R groups – they could be any groups that are chemically reasonable, and the use of R, R' and R'' indicates that the three R groups may be the same or different, (ii) the silanes we have shown so far are monofunctional – they only have one silanol-reactive group, (iii) we are ultimately forming an Si-O-Si (siloxane) covalent bond here, i.e., we are tethering the silane to the surface through this linkage, and (iii) you can make silanes with two (bifunctional), three (trifunctional), and four (tetrafunctional) silanol-reactive groups on them.

Unfortunately, silanes that react with silanols also react with water – there is a clear chemical similarity between a silanol group (SiOH) and water (H_2O). This means that silanol-reactive silanes are water sensitive reagents and that exposing them to water changes them. For example, the reactive groups on the monofunctional silanes we've been considering can react in the presence of water to make a dimer, as follows:

(i) $H_2O + 2\ MeOSiRR'R'' \rightarrow R''R'RSiOSiRR'R'' + 2\ MeOH$

(ii) $H_2O + 2\ EtOSiRR'R'' \rightarrow R''R'RSiOSiRR'R'' + 2\ EtOH$

(iii) $H_2O + 2\ ClSiRR'R'' \rightarrow R''R'RSiOSiRR'R'' + 2\ HCl$

(iv) $H_2O + 2\ (CH_3)_2NSiRR'R'' \rightarrow R''R'RSiOSiRR'R'' + 2\ (CH_3)_2NH$

This dimer will not react with silanes – its silanol-reactive groups are gone. Accordingly, you shouldn't expect that exposing a surface to a wet silane (a silane that has been exposed to some amount of water) will give the same results as exposing it to a dry one. Thus, if you use a wet monofunctional silane thinking it is a dry one, you expose your surface to a lower concentration of your reagent than you had planned to. This lower concentration will translate into a lower reaction rate. It also represents a waste of material.

Things are arguably worse when you work with difunctional, trifunctional, or tetrafunctional silanes. When exposed to water, all of them can polymerize. The difunctional silane can make a linear polymer, and the trifunctional and tetrafunctional silanes can make network (crosslinked) polymers (see Figure 2). These reactions can be done in a controlled fashion in the presence of some water to make desired materials, e.g., to deposit very thin films of polymerized silanes on surfaces. However, when it comes to the reagents themselves, exposure to water can render them useless for their intended reactions.

Traditionally, the primary method of depositing silanes on surfaces has been by immersing them in a liquid solution of the reagent. This approach can be effective. However, it has some pitfalls and inherent difficulties that one should be aware of. First, it often uses a lot of organic solvent – both in the solution of the silane and to rinse the surfaces that are thus prepared. Obviously, there are health, safety, and disposal issues associated with using organic solvents. Second, in many cases the deposition solutions contain defined quantities of water, and we have seen that water reacts with silanes. Accordingly, one is often doing a deposition here with a 'moving target', i.e., a solution that is changing over the course of the deposition. A consequence of this second point is that depositions with trifunctional and tetrafunctional silanes can be hard to control – they can give messy results if they are not properly done.

The more modern way of depositing silanes on surfaces is by chemical vapor deposition.[1-3] This will generally be done in a vacuum oven into which the vaporized silane is injected. In general, the neat (pure) silane is used so no organic solvents are necessary. Thus, the silane is not polymerizing in a liquid around the substrate while it is depositing. The hydration state of the surface (the amount of water on it) can be controlled by these ovens. Overall, CVD of silanes can be very reproducible – it generally offers more control than can be obtained in the corresponding liquid phase depositions. For these reasons, CVD of silanes is used in clean rooms and for other commercial deposition of these reagents. Perhaps its only major downside is the cost of the equipment and its maintenance.

A2.3.2 Characterization of Silane Thin Films

Silane thin films can be characterized with a variety of different techniques. Here is a list of some of those that are used.

- X-ray photoelectron spectroscopy (XPS) has been widely used for this purpose. XPS is a surface characterization technique that probes 5-10 nm in materials. It delivers the elemental compositions and oxidation states of the elements in thin films.[4] XPS will probably be most helpful in the analysis of silane films if the silane contains a unique atom – an atom that isn't carbon or silicon (XPS can't 'see' hydrogen). For example, if we deposit 3-aminopropyltriethoxysilane (see Figure 3) on the native oxide of silicon, the silane brings nitrogen with it, which should not have been present on the original surface and will provide solid evidence for this deposition.[2] However, XPS is performed under vacuum, and the sample loading, transfer, and pump down can take a little while – it can take and hour or two to get XPS data from a surface. Near ambient pressure XPS (NAP-XPS) often allows this data to be collected much more quickly because it is performed under a very modest and quickly reachable vacuum of ca. 10 Torr.[5] In many cases, XPS analyses are non-destructive.

- Time-of-flight secondary ionization mass spectrometry (ToF-SIMS) is another vacuum analytical method that delivers chemical information about materials.[6] It is generally sensitive to the upper few monolayers of a material – it is even more surface sensitive than XPS. It is a form of surface mass spectrometry that can deliver a great deal of chemically specific information about a surface. For example, it has been widely used to identify and study polymers on surfaces. In general, ToF-SIMS analyses can be acquired more quickly than XPS analyses, which makes it a better tool for analyzing large numbers of samples. ToF-SIMS depth profiling can be performed to give layer-by-layer characterization of surfaces. While static (surface) ToF-SIMS only probes a small fraction of a surface, it must be considered to be at least somewhat destructive – it is based on the ejection (sputtering) of material from surfaces.
- Spectroscopic Ellipsometry (SE). SE is a non-destructive method. It is widely used to obtain film thickness and their optical functions, although for fundamental reasons it will

not generally be possible to obtain the optical functions of ultrathin (< 10 nm) silane films.[7] An estimate of these functions will often need to be used. SE is one of the most used methods in our lab. It is quick, easily performed under ambient conditions, and for simple analyses like an ultrathin silane film on a silicon wafer it yields immediate results. It is helpful in SE to begin an analysis with a reasonable estimate of the nature and thickness of the film one is analyzing.

- Water contact angle goniometry (WCA) is another important surface characterization method. It is also very rapid and convenient – it is generally performed in an open laboratory with relatively inexpensive equipment. In WCA, a surface is probed with a droplet of a liquid, which is often water. The degree to which the droplet wets the surface or beads up on it is quantified by the angle the drop makes with the surface. Contact angle measurements of a surface made before and after a deposition can provide direct evidence for that deposition. Different materials have different, known contact angles, so a comparison of the contact angles from a surface to literature values can be helpful. Contact angles can be useful for assessing surface cleanliness. For example, after cleaning in piranha solution (a caustic and toxic mixture of concentration sulfuric acid and ca. 30% hydrogen peroxide), a silicon wafer will be wet by water (have a very low contact angle – less than 10 - 15°). After the same clean wafer has sat out in a lab for a week and gathered hydrocarbons from its surroundings, it will have a higher water contact angle.

A2.3.3 Development of a Dry Box for Transferring Silanes

Disclaimer. While the authors have found that the modified sandblasting equipment described herein works well for transferring silanes, it makes no guarantee that this box or the *modifications to it will work other laboratories or for any other purposes. The reader is advised to consult the health and safety professionals at their organization for advice on making and using such a device.*

Our CVD system uses vials with septa that are filled with silanes (See Figure 4) for injection of these reagents. Two needles are inserted into these vials. One of them is used to draw the silane into the CVD system, and the other provides a positive pressure of an inert gas; without the positive pressure of gas, removal of the silane will create a negative pressure in the vial, which will draw in air. Of course the air contains water vapor, so preventing it from coming in contact with the silane is important.

This leads us to our next point, which is: how do we get the silane into the vial in the first place? First, however, it should be noted that there are a few silanes that come in bottles with septa on them. However, in most cases, the silanes needs to be transferred/loaded into a vial by the user.

One option is to use a glove box. However, not every laboratory has a glove box, so there is the initial expense of purchasing one, after which it must be maintained. We have used a glove box that is in another lab in our building to transfer our silanes, but it seemed advantageous to have our own system. However, we didn’t want to pay for a large glove box that would only be used on occasion.

So we took a different approach. We had recently purchased a bench-top sand blasting system for about $200 from a local hardware store for the purpose of frosting the backsides of the transparent substrates we use for spectroscopic ellipsometry. It occurred to us that the sealed chamber with gloves going into it might also make a good, dry box for transferring our silanes from the bottles they came in into vials. Unlike most glove boxes, this box is relatively small – it has a small footprint on the bench.

The sandblasting box we used is shown in Figure 4. The foot pedal shown in the front view of the device is used to inject air (in our case inert gas) into the box, which allows both hands to perform in-box manipulations. The lower picture shows the inside of the box. It is certainly not as big as a glove box – you wouldn't do a chemical reaction in it. However, it is certainly large enough to do a simple chemical transfer.

Some repurposing of the commercial sandblasting box was necessary so that it could be used for silane transfer – it underwent a few minor modifications that took about an afternoon. First, the filter and a small plastic plug used to prevent sandblasting media from leaking out of the bottom of the unit were removed and the resulting holes were stopped-up with rubber stoppers. There were also three small holes left by the screw hardware that held the filter in place; these holes also had to be covered. This was easily done using small bolts and Teflon®/PDMS washers. These modifications are shown in **Figure 5.**

In addition to these changes, the solid nozzle assembly inside the unit was removed and the hose feeding this unit was moved below the grate into the bottom area of the sandblaster box. As this hose was the inlet for the compressed air, it worked as the inlet for the N_2 gas for purging. The exhaust vent for the sandblasting box had a hose line attached to it that connected the unit to the exhaust hood. This attaching line was also fitted with a rubber stopper with a hole with a one-way check valve to ensure no backflow from the exhaust entered back into the sandblasting box. Finally, the air inlet for the sandblaster box was valved in with an N_2 line as shown in Figure 6. At this point, the sandblasting box had become a transfer box.

A2.3.4 Mathematical Analysis of the Box

Our next task was to figure out how long to purge the box to remove the air in it. Obviously, we didn’t think it would be worth the time to do a high-level, detailed analysis of the flow and mixing of gases in the box. However, it did seem reasonable to apply some basic theory to the problem to have an estimate for the time we should wait for the box to purge before loading a vial. Accordingly, we used the basic theory of mixing that is taught in most elementary differential equations courses.

These equations rely on a knowledge of the internal volume of the box. Because of its irregular shape, determining its value was not an entirely trivial task. In particular, the bottom (basin) of the transfer box has an odd shape. Its volume was measured by simply filling it with water and weighing the water. The remainder of the box could then be theoretically broken down into simpler geometric shapes, which allowed their volumes to be determined. These calculations and measurements gave us an internal void volume for the box of 25.9 L.

We next needed to know the flow rate of N_2 into the box. For this task we purchased and used a simple ACR Acrylic Flow Meter from Dakota Instruments. With this ball type gas flow-rate meter, we were able to measure the flow rates in and out of the transfer box.

In our case we used a stainless steel N_2 gas ball float flow rate meter that measured from 5 to 45 L/min as presented in Figure 7. However, while assessing the inlet flow rate for our transfer box, the flow rate meter was not able to directly measure this as the inlet flow rate exceeded the capacity of our meter. To compensate for this limitation and assess our inlet flow rate, the inlet pressure was reduced and flow rate was graphed as a function of inlet pressure. To these ends, a linear graph was created and a line equation of $1.2x+0.6$ (Equation 1) was fit onto the points as shown in Figure 8. With our operating pressure of 90 psig, we were able to assess an inlet flow rate of 108.6 L/min calculated from Equation 1. In addition to an inlet flow rate, we also measured the outlet flow rate. With the outlet flow rate measurements, there was no need to perform any types of extrapolation or adjust our nominal pressure setting as the outlet flow rate proved to be the bottle neck in the N_2 flow within the transfer box with a maximum flow rate of 25.96 L/min. The exit flow rate did not exceed the limitations of the gas flow-rate meter. As such, the flow rate that we used for our mixing problem was indeed the 25.96 L/min flow rate.

The final step in our procedure development was the integration of both the volume of the transfer box and the controlling flow-rate for our N_2 gas in the unit. With these two factors we were able to calculate when the transfer box was at equilibrium with the N_2 gas flow and how much percentage of N_2 was present in relation to the air in the transfer box. To do this we used a simple first-order differential equation with a mixing in a vat model. We also made a couple of assumptions: there was an even mixing occurring during the introduction of N_2, and because the inlet flow-rate was so high, an equilibrium flow-rate (not to be confused with equilibrium mixing) was achieved almost instantaneously. We also assumed that the entire volume of the transfer box will have all of the air/N_2 mixing while N_2 was introduced, and as such we used the entire volume of the transfer box as the volume of what would be the "liquid" as is used in a mixing in a vat model and as such, the volume of the transfer box will always be the same. To start, we introduced N_2 gas (100%) with a flow rate of 25.96 L/min into the transfer box and at the same time it was exiting at some concentration as a function of time. This is represented in Equation 2 below:

Equation 2: $\frac{dN}{dt} = 25.96\ \frac{L}{min} \times 100\%(concentration) - 25.96 \frac{L}{min} \times \frac{N(L)}{25.892\ L}$

This equation can be simplified as follows:

Equation 3: $\frac{dN}{dt} = \frac{672 - 25.96}{25.892} \rightarrow \frac{dN}{672 - 25.96} = \frac{dt}{25.892}$ which we then integrate for the following equation:

Equation 4: $\frac{ln|672-25.96N|}{-25.96} = \frac{t}{25.892} + c_1$ and with some mathematical manipulation we can come to here:

$$ln|672 - 25.96N| = \frac{-25.96t}{25.892} - 25.96c_1$$

$$ln|672 - 25.96N| = -1.0023t + c_2 \quad where: \; -25.96c_1 = c_2$$

Through exponentiation, we come up with the following equation:

Equation 5: $|672 - 25.96N| = e^{-1.0023t+c_2}$ Now assigning $c_{3=}e^{c_2}$, equation 5 can be simplified to:

Equation 6: $|672 - 25.96N| = c_3e^{-1.0023t}$ Which can be broken further down to :

$672 - 25.96N = \pm c_3e^{-1.0023t}$ and if we use the plus sign for all values of $c_3 < \frac{672}{25.96}$ and the minus sign for all values of $c_3 > \frac{672}{25.96}$, we come up with an equation of:

Equation 7: $672 - 25.96N = c_4e^{-1.0023t}$ where c_4 can be any variable $+, -,$ or 0. Moreover, if we assign $c = -{}^{c_4}/_{25.96}$ and perform one more mathematical manipulation we have:

Equation 8: $N(t) = \frac{672}{25.96} + ce^{-1.0023t}$

In an analysis of equation 8, we see that if either c is 0, we can see that the $ce^{-1.0023t}$portion of equation 8 falls to 0 and as such an equilibrium volume of N_2 gas in the chamber reaches a volume of $\frac{672}{25.96}$ or 25.889. In addition to this, by re-substituting $-{}^{c_4}/_{25.96}$ into the place of c, we can plainly see that $\frac{-c_4e^{-1.0023t}}{25.96}$ will fall to 0 very quickly for just about any constant c with any time greater than 0 due to the large denominator stemming from the multiplication of 25.96 by $e^{1.0023t}$. With these analyses in hand, we were able to assess that an equilibrium volume of 25.889 Liters of N_2 (99.7% N_2 by volume) in the transfer box can be reached in any time greater than 2 minutes. This analysis along with mathematical method has given us confidence that our transfer box was more than adequate for handling air sensitive materials in the small quantities that we use.

A2.4 Conclusion

With this simple apparatus, many air sensitive, high quality thin-film coating precursors were successfully synthesized. Though there are many other apparatuses on the market that facilitate this type of work, this system was only a fraction of the price and proved very convenient for our purposes.

A2.5 Figures

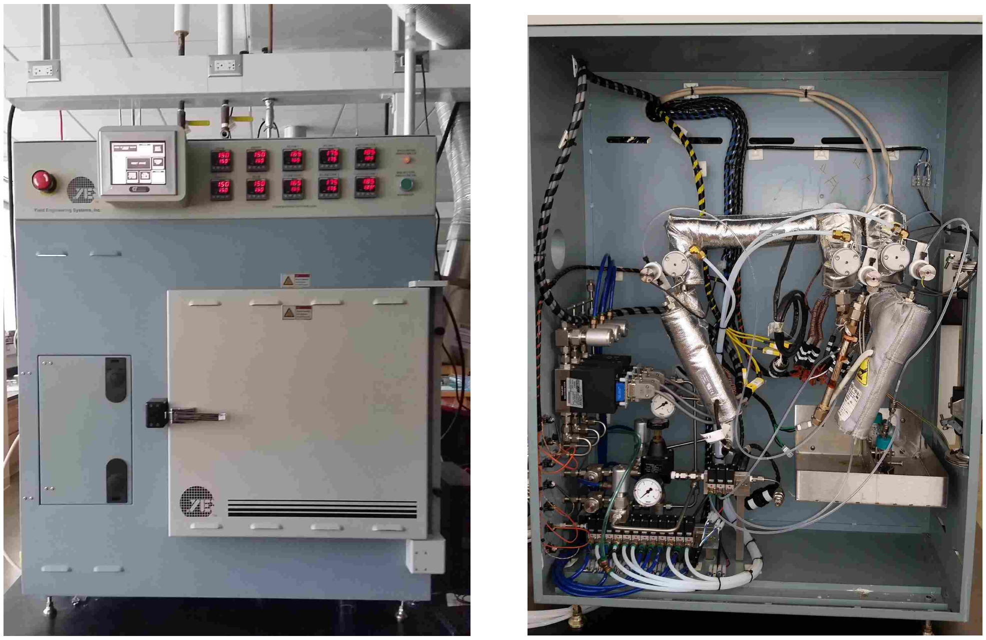

FigureA0-1 Yield Engineering Systems (YES) 1224p Oven

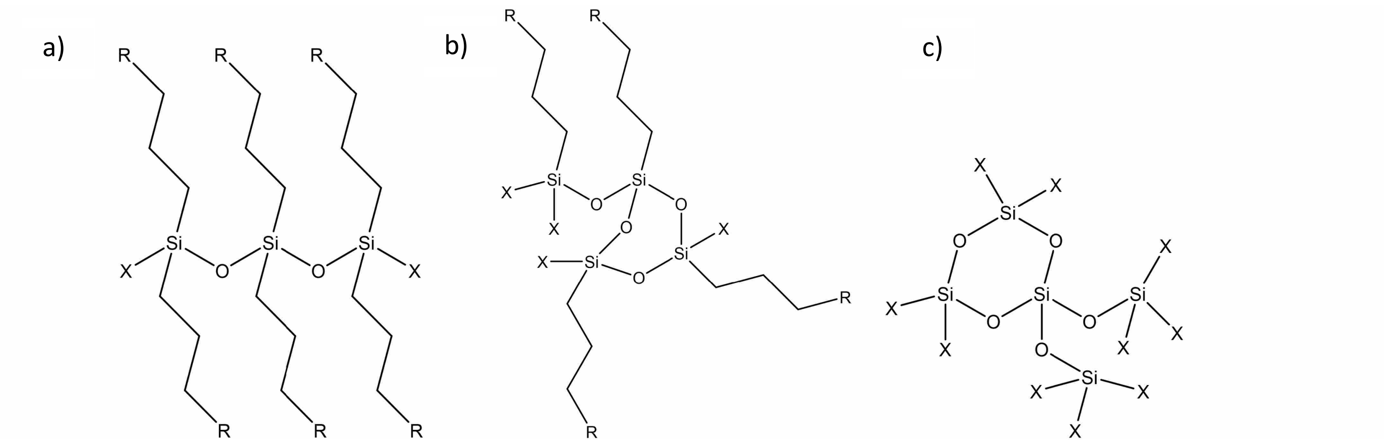

Figure A0-2 Examples of polymerized silanes. (a) Three difunctional silanes, (b) three trifunctional silanes, and (c) four tetrafunctional silanes after reaction

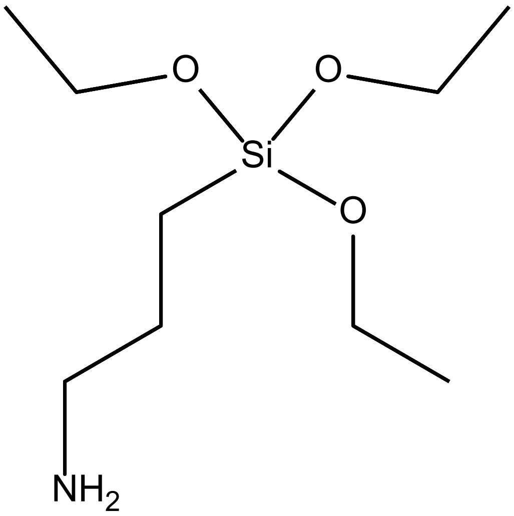

Figure A0-3 3-aminopropyltriethoxysilane

Figure A0-4 Septum precursor vial in YES 1224P CVD Oven

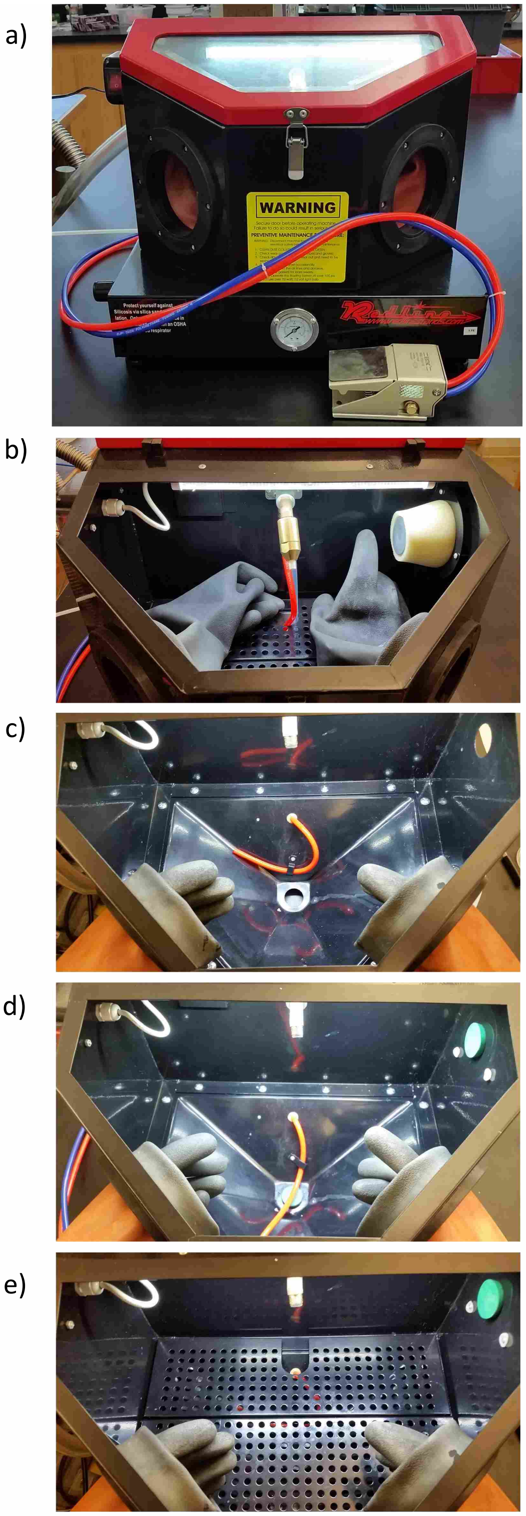

Figure A0-5 a) and b) Redline RE22 Benchtop Abrasive Sand Blasting Cabinet as received c) Removal of filter, bottom plug and nozzle assembly d) Addition of stoppers and screws to seal transfer box
e) Placement of bottom plates in transfer box

Figure A0-6 N_2 gas and exhaust connections for transfer box

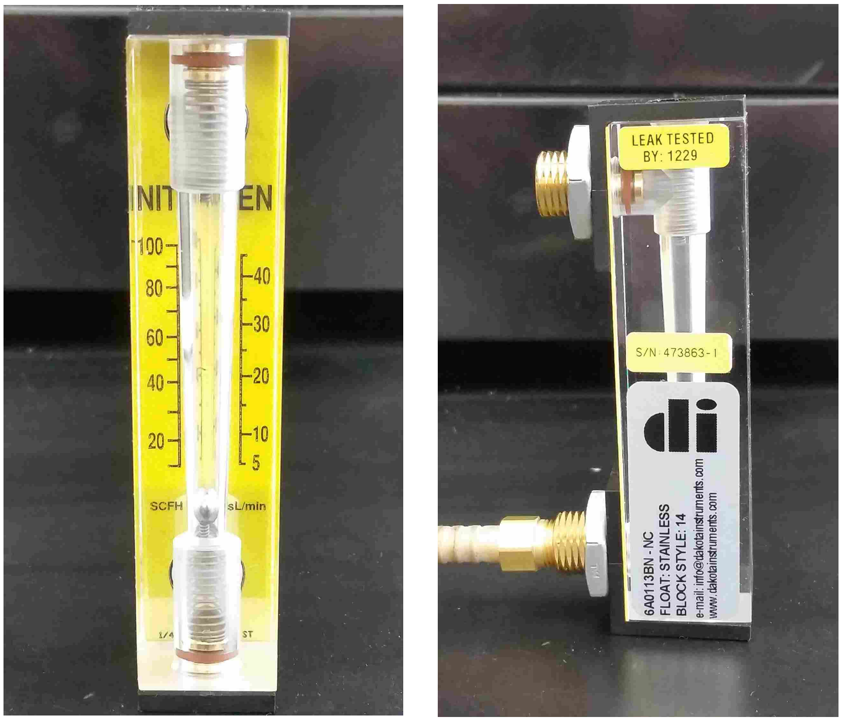

Figure A0-7 Stainless steel ball float flow rate meter used to assess transfer box flow rate

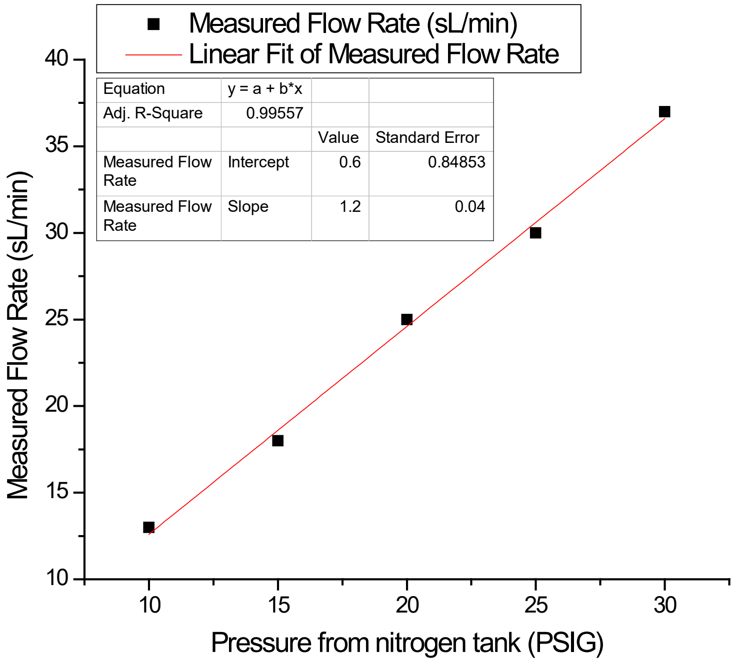

Equation	y = a + b*x		
Adj. R-Square	0.99557		
		Value	Standard Error
Measured Flow Rate	Intercept	0.6	0.84853
Measured Flow Rate	Slope	1.2	0.04

Figure A0-8 Extrapolation curves for N_2 gas inlet flow rate measurement in transfer box

A2.6 References

1. Johnson, B. I.; Cushman, C. V.; Lunt, B. M.; Kaykhaii, M.; Linford, M. R., An Introduction to Silanes, their Chemical Vapor Deposition onto Si/SiO_2, and Characterization of the Resulting Monolayers. *Vacuum Technology & Coating* **2016**.
2. Zhang, F.; Sautter, K.; Larsen, A. M.; Findley, D. A.; Davis, R. C.; Samha, H.; Linford, M. R., Chemical vapor deposition of three aminosilanes on silicon dioxide: surface characterization, stability, effects of silane concentration, and cyanine dye adsorption. *Langmuir* **2010,** *26* (18), 14648-14654.
3. Gupta, V.; Madaan, N.; Jensen, D. S.; Kunzler, S. C.; Linford, M. R., Hydrogen plasma treatment of silicon dioxide for improved silane deposition. *Langmuir* **2013,** *29* (11), 3604-3609.
4. Gupta, V.; Ganegoda, H.; Engelhard, M. H.; Terry, J.; Linford, M. R., Assigning oxidation states to organic compounds via predictions from X-ray photoelectron spectroscopy: a discussion of approaches and recommended improvements. *Journal of Chemical Education* **2013,** *91* (2), 232-238.
5. Cushman, C. V.; Dahlquist, C. T.; Dietrich, P.; Bahr, S.; Thiben, A.; Schaff, O.; Banerjee, J.; Smith, N. J.; Linford, M. R., Trends in Advanced XPS Instrumentation. 5. Near-Ambient Pressure XPS. *Vacuum Technology & Coating* **2017**.
6. Spool, A. M., *The Practice of TOF-SIMS: Time of Flight Secondary Ion Mass Spectrometry*. Momentum Press: 2016.
7. Tompkins, H. G.; Hilfiker, J. N., *Spectroscopic Ellipsometry: Practical Application to Thin Film Characterization*. Momentum Press: 2015.

Appendix 3: Oxidation of Aluminum Protected by Wide Band Gap MgF_2 Layers as Followed by X-ray Photoelectron Spectroscopy

A3.1 Statement of Attribution

This document was originally published as Johnson, B. I.; Avval, T. G.; Hodges, G.; Membreno, K.; Carver, V.; Allred, D. D.; Linford, M. R., Oxidation of Aluminum Protected by Wide Band Gap MgF2 Layers as Followed by X-ray Photoelectron Spectroscopy. In *TechCon 2019 62nd Annual SVC Technical Conference*, Long Beach Convention Center, Ca, 2019.

A3.2 Abstract

Aluminum enjoys broad band reflectivity and is widely used as an astronomical reflector. However, it oxides rapidly, and this oxide absorbs very short wavelength light, which limits the performance of aluminum mirrors. Accordingly, thin transparent layers, such as films of MgF_2, are used to protect aluminum. In this study, we present an X-ray photoelectron spectroscopy (XPS) study of the chemical changes in MgF_2 - protected aluminum that take place as it oxidizes (is exposed to the air). XPS reveals the rate of Al oxidation for different MgF_2 thicknesses as determined from measurements obtained from 5 min to 8 months of air exposure. The degree of Al oxidation depends on the MgF_2 over layer thickness.

A3.3 Introduction

Aluminum has unique properties and numerous applications[1-3]. It is generally considered to be an easy metal to work with. It has a relatively low melting point, it is ductile yet strong enough to be used in structural applications, it is lightweight, it can be alloyed, and it is unmatched in its ability to reflect light over a wide energy range[4]. A drawback to aluminum is that its surface oxidizes quickly. Of course, a small amount of oxide is not a limitation for most of aluminum's applications. However, aluminum oxide, even when only a few nanometers thick, absorbs short wavelength light, which significantly limits aluminum's ability to act as a space mirror and collect light over the widest possible wavelength range[5-9]. Because of the importance of aluminum and aluminum oxide, these materials have previously been studied by various experimental and theoretical methods, including X-ray photoelectron spectroscopy (XPS)[10-15].

A general strategy for preventing aluminum from oxidizing while preserving its optical properties is to coat it with a wide band gap material[16-19]. These types of barrier layers, e.g., MgF_2 and other inorganic salts, have been used for decades to protect aluminum reflectors, including those in the Hubble space telescope[5, 20-24]. Indeed, aluminum is currently being proposed as the primary reflector for future space missions such as the LUVOIR project, which will be the flagship NASA space observatory for the 2020s and 2030s. However, in spite of the importance of protecting aluminum mirrors, we are not aware of any systematic XPS analysis of MgF_2 - protected aluminum mirrors. Here we present such a study. We show that XPS can be used to follow aluminum oxidation under MgF_2 layers of varying thickness, and that its oxidation rate depends on the thickness of the MgF_2 over it, i.e., thicker MgF_2 films result in slower Al oxidation. This document follows our recent, related conference proceedings on the spectroscopic ellipsometry (SE) analysis of the oxidation of MgF_2 - protected aluminum[25].

A3.4 Experimental

A3.4.1 Instrumentation

XPS was performed with a Surface Science SSX-100 instrument (maintained by Service Physics, Bend, OR, USA) with a hemispherical analyzer. The instrument employs monochromatic Al Kα X-rays. Survey scans were collected with an X-ray spot size of 800 x 800 μm^2, an instrument resolution of ‘4’, a nominal pass energy of 150 eV, 6 passes/scan, and a step size of 1 eV[23, 24]. High resolution (narrow) scans were collected over the Al 2s region, centered at a binding energy of 120 eV, with an energy window of 40 eV, and a step size of 0.0625 eV. The number of scans ranged between 15 and 35, and the spot size was 800 x 800 μm^2 with an instrument resolution of ‘3’ (nominal pass energy of 100 eV). Area ratios were calculated using the CasaXPS modelling/fitting software (Casa Software Ltd., Version 2.3.18PR1.0). SE (M-2000D, J.A. Woollam, Lincoln, NE, USA, wavelength range: ca. 190-1688 nm, CompleteEASE data analysis software) was used to measure the thicknesses of model/calibration MgF_2 layers on previously characterized silicon substrates. Data were acquired at 75°. Modeling was performed with the optical functions in the instrument software for MgF_2 (MgF_2E (Sellmeier)) and Si/SiO_2 (Si_JAW and SIO2_JAW, respectively).

A3.4.2 Deposition of Al and MgF_2

Four sets of aluminum films were deposited using a Denton (Morristown, NJ) DV-502 A thermal evaporator. This evaporator uses two independent resistance-heated sources for depositions and a rotating stage to ensure even depositions. An Inficon (Bad Ragaz, Switzerland) quartz-crystal monitor (QCM) in the chamber made in situ thickness measurements so that the system could automatically close a shutter assembly to end depositions. The thickness values from the QCM (previously calibrated) were used in this study for the MgF_2 thicknesses. For each sample preparation, a 1” piece of aluminum wire was placed into a tungsten resistance heater coil and a molybdenum boat was filled with ca. 15 g of MgF_2. Prior to deposition, the system was pumped to a base pressure of 4×10^{-6} torr and the Al was deposited at a rate of 35 Å/sec to achieve a thickness of 150 Å. The MgF_2 was then immediately deposited onto the Al at a rate of 3 Å/sec.

The time for both depositions was 35 – 45 s. Immediately following the depositions of Al and MgF_2, the chamber was vented with $N_2(g)$, which took 1.5 – 2 min. The samples were then removed and rushed to the SE and XPS instruments for analysis. Samples were timed from chamber removal to the beginning of SE or XPS analysis. Each sample was divided into multiple pieces: one piece for SE analysis and the others for XPS.

A3.5 Results and Discussion

A3.5.1 XPS Analysis

XPS is a surface sensitive technique that probes the upper 5 – 10 nm of materials. It yields elemental compositions and oxidation states[20]. XPS Al 2s narrow scans of MgF_2 – protected Al (see Figure A3-1) were modeled by peak fitting, which is often essential in XPS data analysis because the natural line widths in XPS are often comparable to the chemical shifts for the elements[26].

To study the oxidation rate of Al as a function of MgF_2 thickness, we examined the Al 2s signal at ca. 118 eV. The Al 2s and 2p peaks are the most intense signals from Al. We chose the Al 2s region for simplicity, i.e., so that we would not need to consider spin-orbit splitting, which should be accounted for in Al 2p peak analysis. For the peak fitting, two types of pseudo Voigt synthetic line shapes were considered: Gaussian-Lorentzian product (GLP) and Gaussian-Lorentzian sum (GLS) functions[22]. Ultimately, we used GLS line shapes because they fitted our data better than the GLP functions. As expected, the lower energy component in the Al 2s narrow scans attributable to the unoxidized (metallic) Al film exhibited greater Lorentzian character and was narrower than the peak that accounted for the oxide in the material – we attribute the greater width (FWHM) of the oxide signal to disorder in the oxide and phonon broadening[27]. To obtain the best fits to the narrow scans, we varied the Lorentzian character of both fit components to minimize the standard deviation of the residuals (STDRes) to the fit. This analysis (see Figure A3-2) yielded best values of the Lorentizian character/fraction in the GLS line shapes of 50% and 0% for the Al and Al_2O_3 fit components, respectively. These values were used in the remainder of this study.

XPS spectra of MgF_2 - covered Al layers were acquired as a function of time. For example, Figure A3-3 shows representative Al 2s narrow scans taken at three air exposure times.

Table A3-1 Average FWHM values, peak energy (BE) differences, and ratios of FWHM values for the Al and Al_2O_3 fit components in the Al 2s narrow scans considered in this study.

MgF_2 Thickness (nm)	**Average FWHM Al 2s Peak**	**Average FWHM Al_2O_3 2s Peak**	**Average BE Difference Al-Al_2O_3 2s Peaks**	**Average FWHM Ratio Al_2O_3 /Al 2s Peaks**
1.82	1.76 ± 0.14	2.96 ± 0.14	2.49 ± 0.10	1.68 ± 0.09
2.20	1.68 ± 0.06	2.82 ± 0.08	2.59 ± 0.08	1.68 ± 0.08
2.30	1.74 ± 0.04	2.99 ± 0.08	2.46 ± 0.04	1.72 ± 0.06
3.08	1.71 ± 0.04	3.15 ± 0.22	2.75 ± 0.24	1.84 ± 0.16
Average	**1.72 ± 0.07**	**2.98 ± 0.13**	**2.57 ± 0.12**	**1.73 ± 0.09**

Oxidation of the Al layer is clearly taking place here, as evidenced by the steady increase in the Al_2O_3 to Al area ratio. In spite of the fact that neither the separation nor the full width at half maximum (FWHM) values for the Al and Al_2O_3 fit components were constrained in any of these fits, the average FWHM values for the Al and Al_2O_3 fit components across the fits were very similar: 1.72 ± 0.07 eV and 2.98 ± 0.13 eV, respectively, which is consistent with these peak envelopes being well described by the two proposed components. These FWHM values are within 10% of respective literature values for γ-Al_2O_3, and within 15% for Al metal[26-29]. In addition, the energy difference between the Al_2O_3 and Al fit components was quite constant: 2.57 ± 0.12 eV, as was the ratio between them (see Table A3-1). These results suggest that our model for analyzing the Al 2s peak envelope was reasonable.

Figure A3-4 shows the Al_2O_3/Al fit component ratios from MgF_2 - protected samples exposed to the air for between 5 min and 8 months. Reasonable linear fits to the data are obtained by relating the Al_2O_3/Al area ratio to the logarithm of time, as follows:

(1) $Al_2O_3/Al = m \ln t + b$

where m and b are the slope and intercept of this line. It is significant that (i) both the Al_2O_3/Al ratios and m values (slopes) are smallest for the thickest over layers of MgF_2, which confirms their ability to slow aluminum oxidation, and (ii) oxidation appears to continue over the entire exposure of the samples to the air. To further emphasize the decrease in oxidation with increasing over layer thickness, the m values (slopes) for the lines in Figure A3-4 are plotted in Figure A3-5 as functions of MgF_2 thickness.

A3.6 Conclusion

The effects of MgF_2 thickness on the oxidation rate of aluminum was determined by XPS. The raw data showed that as the MgF_2 thickness increased, the oxidation rate of aluminum decreased. Good fits to the Al 2s narrow scans were obtained with relatively few constraints. The Gaussian-Lorentzian sum functions used to model the Al_2O_3 and Al peaks in the Al 2s narrow scans had 0% and 50% Lorentzian character, respectively. Plots of the Al_2O_3/Al ratios as a function air exposure time showed that oxidation increased in a logarithmic fashion that depended on the thickness of the MgF_2 over layer.

A3.7 Acknowledgments

The authors gratefully thank and acknowledge the Utah NASA Space Grant Consortium for funding this work, and also SVC for a travel award to BIJ to attend the SVC conference in Long Beach, CA in 2019.

A3.8 Figures

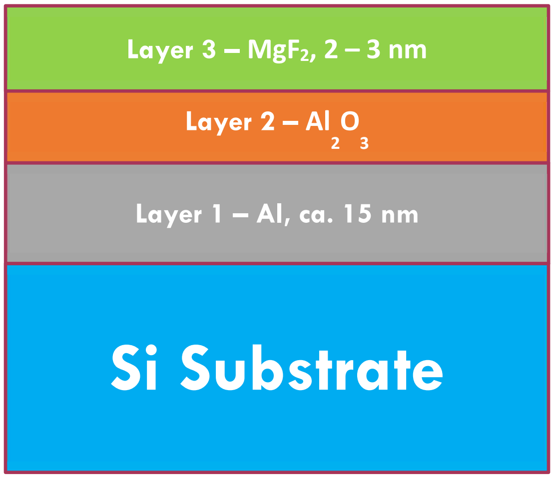

Figure A3-1 Model of the stack deposited and analyzed in this study (not to scale).

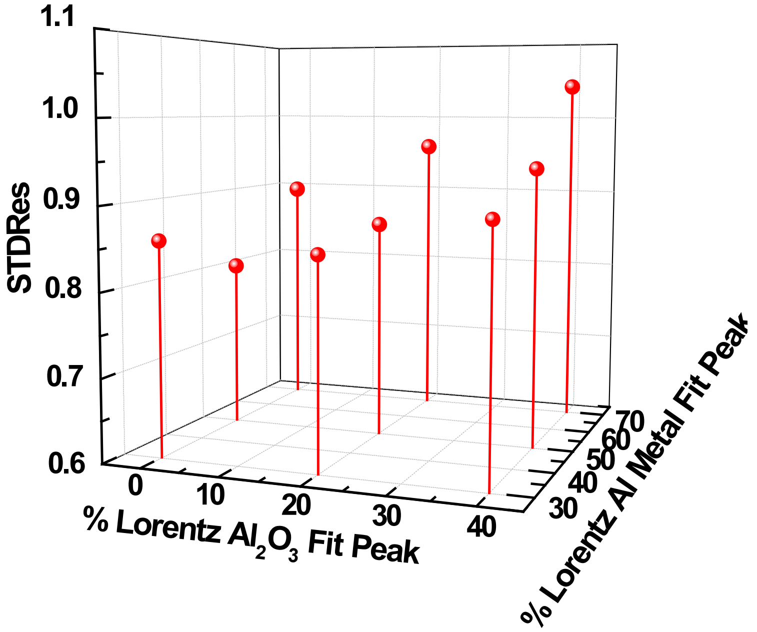

Figure A3-2 The standard deviation of the residuals (STDRes) for fits of the Al 2s XPS narrow scans as a function of the Lorentzian character in the Al_2O_3 (oxide) and Al (metal) fit components. These values are the averages of fits to 27 narrow scans.

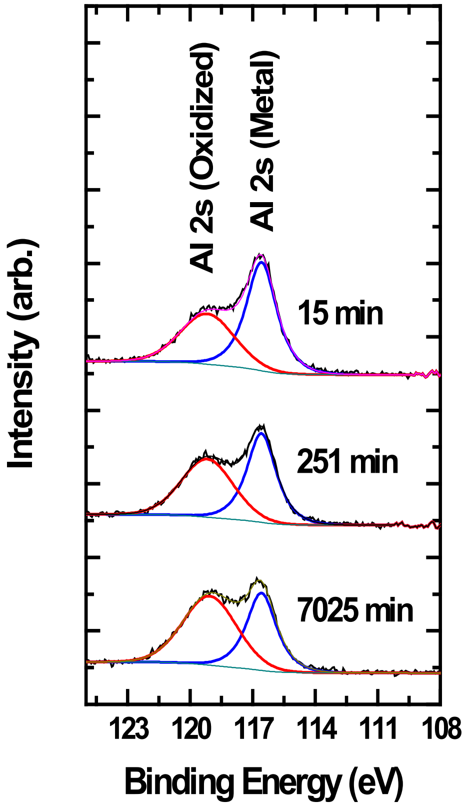

Figure A3-3 Representative Al 2s narrow scans from MgF_2 – coated Al as a function of air exposure time.

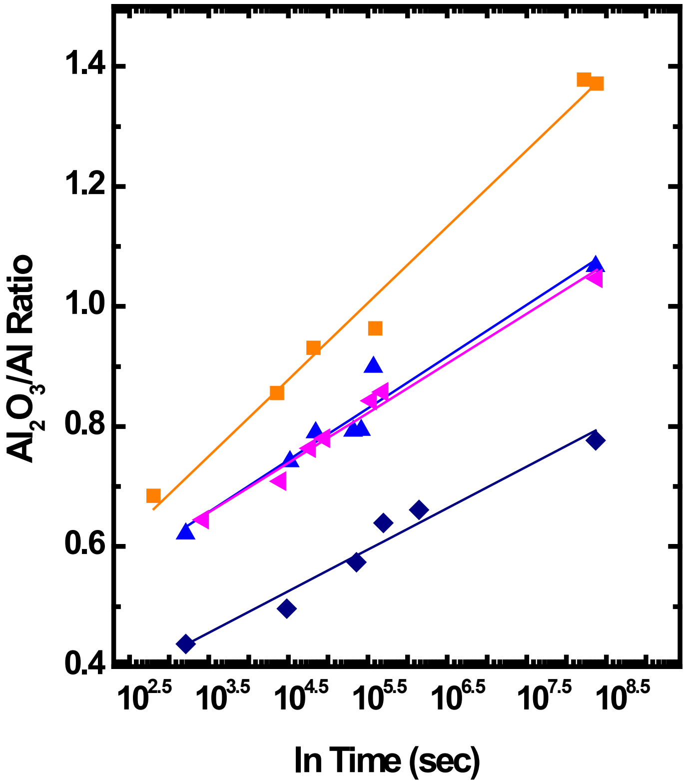

Figure A3-4 XPS Al_2O_3/Al ratios as a function of air exposure time as fit to the following lines:

■ 1.82 nm MgF_2: y=0.0637 ln(x)+0.305
▲ 2.20 nm MgF_2:y=0.0414 ln(x)+0.367
◀ 2.30 nm MgF_2: y=0.0431 ln(x)+0.356
◆ 3.08 nm MgF_2: y=0.0346 ln(x)+0.214

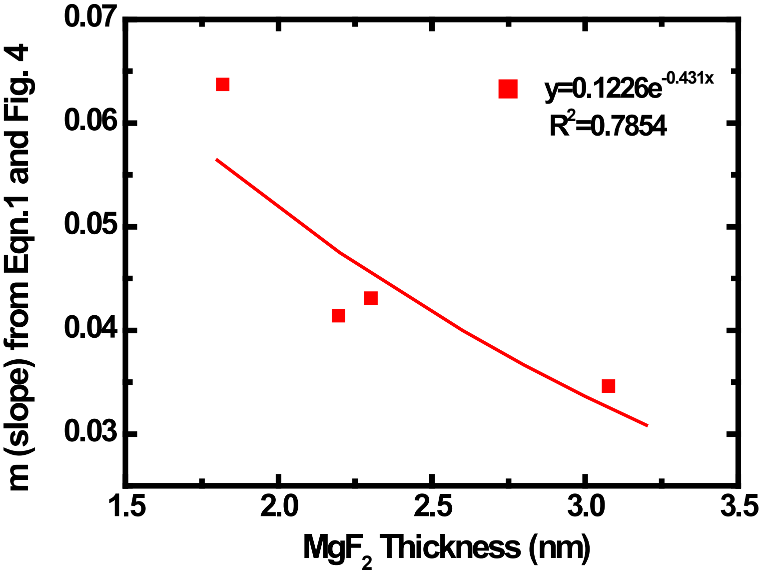

Figure A3-5 Values of m determined from Equation 1 and Figure A3-4. In large measure, the fit to these values here should be considered a guide to the eye.

A3.9 References

1. Bertram, M.; Martchek, K. J.; Rombach, G., Material flow analysis in the aluminum industry. *Journal of Industrial Ecology* **2009,** *13* (5), 650-654.

2. Das, S.; Yin, W., Trends in the global aluminum fabrication industry. *JOM* **2007,** *59* (2), 83-87.

3. Skillingberg, M.; Green, J., Aluminum applications in the rail industry. *LIGHT METAL AGE-CHICAGO-* **2007,** *65* (5), 8.

4. Hass, G.; Tousey, R., Reflecting coatings for the extreme ultraviolet. *JOSA* **1959,** *49* (6), 593-602.

5. Bridou, F.; Cuniot-Ponsard, M.; Desvignes, J.-M.; Maksimovic, I.; Lemaire, P. In *VUV mirrors for the (80-120 nm) spectral range*, Advances in Optical Thin Films, International Society for Optics and Photonics: 2004; pp 627-637.

6. Brune, H.; Wintterlin, J.; Behm, R.; Ertl, G., Surface migration of ‘‘hot’’adatoms in the course of dissociative chemisorption of oxygen on Al (111). *Physical review letters* **1992,** *68* (5), 624.

7. Do, T.; McIntyre, N.; Harshman, R.; Lundy, M.; Splinter, S., Application of parallel factor analysis and x-ray photoelectron spectroscopy to the initial stages in oxidation of aluminium. I. The Al 2p photoelectron line. *Surface and interface analysis* **1999,** *27* (7), 618-628.

8. Trost, J.; Brune, H.; Wintterlin, J.; Behm, R.; Ertl, G., Interaction of oxygen with Al (111) at elevated temperatures. *The Journal of chemical physics* **1998,** *108* (4), 1740-1747.

9. Zhukovskii, Y. F.; Jacobs, P.; Causá, M., On the mechanism of the interaction between oxygen and close-packed single-crystal aluminum surfaces. *Journal of Physics and Chemistry of Solids* **2003,** *64* (8), 1317-1331.

10. Do, T.; Splinter, S.; Chen, C.; McIntyre, N., The oxidation kinetics of Mg and Al surfaces studied by AES and XPS. *Surface Science* **1997,** *387* (1-3), 192-198.

11. Fernández-Perea, M.; Larruquert, J. I.; Aznárez, J. A.; Pons, A.; Méndez, J. A., Vacuum ultraviolet coatings of Al protected with MgF 2 prepared both by ion-beam sputtering and by evaporation. *Applied optics* **2007,** *46* (22), 4871-4878.

12. Lazić, I.; Thijsse, B. J., An improved molecular dynamics potential for the Al–O system. *Computational Materials Science* **2012,** *53* (1), 483-492.

13. Madaan, N.; Kanyal, S. S.; Jensen, D. S.; Vail, M. A.; Dadson, A. E.; Engelhard, M. H.; Samha, H.; Linford, M. R., Al2O3 e-Beam Evaporated onto Silicon (100)/SiO2, by XPS. *Surface Science Spectra* **2013,** *20* (1), 43-48.

14. S. Kanyal, S.; Jensen, D. S.; Zhu, Z.; Linford, M. R., Al2O3 e-beam evaporated onto silicon (100)/SiO2 by ToF-SIMS. *Surface Science Spectra* **2015,** *22* (2), 7-13.

15. Sherwood, P. M., Curve fitting in surface analysis and the effect of background inclusion in the fitting process. *Journal of Vacuum Science & Technology A: Vacuum, Surfaces, and Films* **1996,** *14* (3), 1424-1432.

16. De Marcos, L. V. R.; Larruquert, J. I.; Méndez, J. A.; Gutiérrez-Luna, N.; Espinosa-Yáñez, L.; Honrado-Benítez, C.; Chavero-Royán, J.; Perea-Abarca, B., Optimization of MgF 2-deposition temperature for far UV Al mirrors. *Optics express* **2018,** *26* (7), 9363-9372.

17. Fateh, B.; Brooks, G. A.; Rhamdhani, M.; Taylor, J.; Davis, J.; Lowe, M., Study of Early Stage Interaction of Oxygen with Al; Methods, Challenges and Difficulties. In *Light Metals 2011*, Springer: 2011; pp 725-730.

18. Lousada, C. M.; Korzhavyi, P. A., First stages of oxide growth on Al (1 1 0) and core-level shifts from density functional theory calculations. *Applied Surface Science* **2018,** *441*, 174-186.
19. Wilbrandt, S.; Stenzel, O.; Nakamura, H.; Wulff-Molder, D.; Duparré, A.; Kaiser, N., Protected and enhanced aluminum mirrors for the VUV. *Applied optics* **2014,** *53* (4), A125-A130.
20. Gupta, V.; Ganegoda, H.; Engelhard, M. H.; Terry, J.; Linford, M. R., Assigning oxidation states to organic compounds via predictions from X-ray photoelectron spectroscopy: a discussion of approaches and recommended improvements. *Journal of Chemical Education* **2013,** *91* (2), 232-238.
21. Hass, G., Filmed surfaces for reflecting optics. *JOSA* **1955,** *45* (11), 945-952.
22. Jain, V.; Biesinger, M. C.; Linford, M. R., The Gaussian-Lorentzian Sum, Product, and Convolution (Voigt) functions in the context of peak fitting X-ray photoelectron spectroscopy (XPS) narrow scans. *Applied Surface Science* **2018,** *447*, 548-553.
23. Shah, D.; Patel, D. I.; Roychowdhury, T.; Rayner, G. B.; O'Toole, N.; Baer, D. R.; Linford, M. R., Tutorial on interpreting x-ray photoelectron spectroscopy survey spectra: Questions and answers on spectra from the atomic layer deposition of Al2O3 on silicon. *Journal of Vacuum Science & Technology B, Nanotechnology and Microelectronics: Materials, Processing, Measurement, and Phenomena* **2018,** *36* (6), 062902.
24. Tougaard, S., Improved XPS analysis by visual inspection of the survey spectrum. *Surface and Interface Analysis* **2018,** *50* (6), 657-666.
25. Johnson, B. I.; Gholian Avval, T.; Hodges, G.; Membreno, K.; Allred, D. D.; Linford, M. R. In *Real-Time Monitoring of Aluminum Oxidation Through Wide Band Gap MgF2 Layers for Protection of Space Mirrors*, 2019 25th Annual Fellowship Symposium, Brigham Young University, Utah NASA Space Grant Consortium: Brigham Young University, 2019.
26. Wyatt, D. M.; Gray, R. C.; Carver, J. C.; Hercules, D. M.; Masters, L. W., Studies of Polymeric Bond Failure on Aluminum Surfaces by X-ray Photoelectron Spectroscopy (ESCA). *Applied Spectroscopy* **1974,** *28* (5), 439-445.
27. Rotole, J. A.; Sherwood, P. M., Gamma-alumina (γ-Al2O3) by XPS. *Surface Science Spectra* **1998,** *5* (1), 18-24.
28. Strohmeier, B. R., Gamma-Alumina (γ-Al2O3) by XPS. *Surface Science Spectra* **1994,** *3* (2), 135-140.
29. Rotole, J. A.; Sherwood, P. M., Corrundum (α-Al2O3) by XPS. *Surface Science Spectra* **1998,** *5* (1), 11-17.

Appendix 4: Real-Time Monitoring of Aluminum Oxidation Through Wide Band-Gap MgF_2 Layers for Protection of Space Mirrors

A4.1 Statement of Attribution

This document was originally published as Johnson, B. I.; Gholian Avval, T.; Hodges, G.; Membreno, K.; Allred, D. D.; Linford, M. R. In *Real-Time Monitoring of Aluminum Oxidation Through Wide Band Gap MgF2 Layers for Protection of Space Mirrors*, 2019 25th Annual Fellowship Symposium, Brigham Young University, Utah NASA Space Grant Consortium: Brigham Young University, 2019.

A4.2 Abstract

Because of its extraordinary and broad reflectivity, aluminum is the only logical candidate for advanced space mirrors that operate deep into the UV. However, aluminum oxidizes rapidly in the air, and even a small amount of oxide (as little as a nanometer) can have a noticeable, detrimental impact on its reflectivity at short wavelengths. Thin films of wide band gap materials like MgF_2 have previously been used to protect aluminum surfaces. Here we report the first real-time, spectroscopic ellipsometry (SE) study of aluminum oxidation as a function of MgF_2 over layer thickness, which ranged from 0 – 6 nm. SE data analysis was performed vis-à-vis a multilayer optical model that included a thick silicon nitride layer. The optical constants for evaporated aluminum were initially determined using a multi-sample analysis (MSA) of SE data from MgF_2 protected and bare Al surfaces. Two models were then considered for analyzing the real-time data obtained from Al/MgF_2 stacks. The first used the optical constants of aluminum obtained in the MSA with two adjustable parameters: the thicknesses of the aluminum and aluminum oxide layers. The thicknesses obtained from this model showed the expected trends (increasing Al_2O_3 layer

thickness and decreasing Al layer thickness with time), but some of the Al_2O_3 thicknesses were unphysical (negative). Because the optical constants of very thin metals films depend strongly on their structures and deposition conditions, a second, more advanced model was employed that fit the optical constants for Al, and also the Al and Al_2O_3 thicknesses, for each data set. In particular, the Al and Al_2O_3 thicknesses and optical constants of Al were determined in an MSA for each of 50 evenly spaced analyses in each four-hour dynamic run performed. The resulting optical constants for Al were then fixed for that sample and the thicknesses of the Al and Al_2O_3 layers were determined. While the first and second models yielded similar Al and Al_2O_3 thickness vs. time trends, the film thicknesses obtained in this manner were more physically reasonable. Thicker MgF_2 layers slow the oxidation rate of aluminum. The oxidation of aluminum was also followed and confirmed by X-ray photoelectron spectroscopy (XPS). The results from this work should prove useful in protecting space mirrors prior to launch.

A4.3 Introduction

Aluminum is a plentiful, inexpensive metal with a myriad of applications.[1-3] One of these is as a reflector for astronomical observation. Indeed, aluminum is the best-suited reflective coating for space mirrors because of its unmatched ability to reflect over a wide energy range, including into the deep UV.[4, 5] However, a significant challenge in working with aluminum is the speed with which its surface oxidizes in the air.[5-7] The resulting oxide absorbs short wavelength light, which limits aluminum's performance.[5, 8] To overcome this deficiency, wide band gap, protective coatings, e.g., MgF_2, have been deposited onto aluminum mirrors.[9, 10] This approach was taken with the Hubble space telescope. That is, the goal of depositing thin, fluoride-based, inorganic layers onto aluminum mirrors is to create a robust layer that prevents (or limits) oxidation of aluminum prior to launch while allowing adequate reflection at lower wavelengths.[4, 5, 9, 11] In order to maintain satisfactory reflectance at shorter wavelengths, inorganic fluoride barrier layers can only be ca. 3 nm thick, which still allows significant oxygen leakage. Accordingly, a number of studies have focused on developing robust, transparent passivation layers for aluminum.[5, 11]

For this study, we prepared and studied 0 – 6 nm protective coatings of MgF_2 on Al using real-time/dynamic spectroscopic ellipsometry (SE). Both the Al and MgF_2 were deposited by thermal evaporation. The resulting optical stacks were analyzed in real-time with scans taken repeatedly over four hours. The optical constants of extremely thin metal films can vary greatly depending on thickness, morphology, and deposition conditions. Accordingly, the optical constants of aluminum evaporated with our deposition system of the approximate thickness used in our study were obtained from a multi-sample analysis (MSA) of aluminum films coated with thick MgF_2 layers and bare, but oxide-coated, aluminum. A relatively simple model with two parameters (the thicknesses of the aluminum and aluminum oxide layers) was then applied to the dynamic data (scans repeatedly taken over four hours) obtained from each sample. The trends (rates of oxidation of aluminum) obtained in this study were reasonable. As expected, thicker MgF_2 films led to slower oxidation of the underlying aluminum. However, some of the thicknesses of the Al_2O_3 films in this modeling were unphysical – they were negative. Accordingly, a second model was applied to the data in which the parameters that governed the aluminum optical constants were varied along with the thicknesses of the aluminum and alumina layers. This model gave much more satisfactory results. Oxidation of aluminum was also confirmed and followed by X-ray photoelectron spectroscopy (XPS).

A4.4 Experimental

A4.4.1 Deposition of Al and MgF_2

Thin films of aluminum were deposited with a Denton DV-502 A thermal evaporator. This tool employs two independent resistance-heated sources and a rotating stage. The film thickness was measured and controlled in situ during the deposition using an Inficon quartz crystal monitor (QCM). For depositions, a piece of high purity aluminum wire, 1" long, was placed into a standard tungsten resistance heater coil, and ca. 15 g of MgF_2 was placed into a molybdenum boat. After the evaporator reached a base pressure of 4×10^{-6} Torr, the Al heater was turned on to achieve a deposition rate of 35 Å/sec. After 150 Å of Al was deposited, the QCM automatically closed the shutter between the deposition source and the substrate, and MgF_2 was immediately deposited at a rate of 3 Å/sec. The overall deposition of both Al and MgF_2 took 35 – 45 seconds. The substrate was not heated for these depositions – the sample was nominally at room temperature. Directly following the depositions of Al and MgF_2, the chamber was vented with N_2 gas, which took 1.5 – 2.0 minutes. The samples were then removed and rushed to the SE and XPS instruments for measurement. These transfers took approximately 5 min. The time from sample removal from the chamber to analysis was recorded.

A4.4.2 Instrumentation

SE was performed with a variable angle spectroscopic ellipsometer (M-2000D, J.A. Woollam Company, Lincoln, ME, USA, wavelength range: ca. 190-1688 nm). Series of time-dependent SE measurements were obtained using the 'in situ' mode of the instrument, which allowed the ellipsometer to acquire SE data from a sample every 2.3 s over a period of 4 h. Data were acquired at 75° and subsequently modelled using the CompleteEASE® SE instrument analysis software. The model in Figure A4-1, which shows the types of stacks prepared and studied in this work, employed optical constants that were obtained as follows. The 'Si Substrate' layer was modeled with the optical constants for silicon in the instrument software, and 'Layer 1 – SiO_2' and 'Layer 3 – SiO_2' were modeled with the optical constants for silicon native oxide in the instrument software. The optical constants for 'Layer 2 – Si_3N_3' were obtained by reformulating/reparameterizing the optical constants for silicon nitride in the instrument software as a Tauc-Lorentz and a Gaussian oscillator. The optical constants for 'Layer 4 – Al' were obtained from a multi-sample analysis as described below. The 'Layer 5 – Al_2O_3' and 'Layer 6 – MgF_2' layers were modeled with the optical constants for these materials in the instrument software. XPS was performed using an SSX-100 instrument with a hemispherical analyzer (maintained by Service Physics, Bend, OR, USA). The instrument employed monochromatic Al Kα X-rays and had a take-off angle of 35°. Survey scans were obtained with a spot size of 800 x 800 μm^2 with a resolution of 4 (nominal pass energy of 150 eV). Each survey spectrum is the average of 6 scans (passes) with a step size of 1 eV. High-resolution scans of the Al 2s peak were centered at 120 eV with a window width of 40 eV and a step size of 0.0625 eV. The spot size was again 800 x 800 μm^2, the resolution was 4 (nominal pass energy of 150 eV), and 20 scans were averaged to obtain each spectrum. Peak fitting was performed with CasaXPS (Casa Software Ltd., Version 2.3.18PR1.0).

A4.5 Results and Discussion

In spectroscopic ellipsometry (SE), light of a known polarization state is directed onto a surface, and changes in that polarization are detected. Through creation of models and adjustment of the parameters in them, SE can be used to determine a variety of material properties including film thicknesses, surface roughness, and optical constants of materials. However, due to the complexity of the optical stack in the present work (see Figure A4-1), the thicknesses of the MgF_2 and Al_2O_3 layers, as determined by SE, appeared to be correlated. Accordingly, the thickness of the MgF_2 layer in each optical stack was determined separately by XPS, which was then fixed to this value in the subsequent SE modeling. The following procedure describes how these measurements and calculations were performed.

1. Different thicknesses of MgF_2, which covered the range of thicknesses of interest in this study, were deposited onto shards of native oxide-terminated silicon (Si/SiO_2). Prior to these depositions, the thicknesses of the native oxide layers were determined by SE using the optical constants for native oxide and crystalline silicon in the instrument software.
2. The thicknesses of the MgF_2 thin films were determined by SE using the optical constants of MgF_2 in the instrument software with the thicknesses of the SiO_2 layers fixed to those obtained for each shard prior to the MgF_2 depositions.
3. These same samples ($Si/SiO_2/MgF_2$) were then analyzed by XPS, and the areas of the Mg 2s and Si 2p peaks (all chemical states) were determined using CasaXPS. These areas were then inserted into Equation 1 [12, 13]

$$\ln\frac{(I_O/s_O)}{(I_S/s_S)} - \left[\left(\frac{E_O}{E_S}\right)^{0.75} - \frac{1}{2}\right]\frac{t}{\lambda_O\cos\theta} - \ln 2 = \ln sinh\left(\frac{t}{\lambda_O\cos\theta}\right) \qquad (1)$$

Here, I_o and s_o are the intensity and sensitivity factor respectively of the MgF_2 layer, and I_s and s_s are the intensity and sensitivity factor of the substrate (Si). These sensitivity factors

(s_o and s_s) were obtained from CasaXPS. E_o and E_s are the binding energies of the Mg 2s and Si 2p signals, respectively, and λ_o is the attenuation length of the Mg 2s photoelectrons in MgF_2. With this information, the value of λ_o was the only unknown in Equation 1. The value of λ_o was then adjusted until the two sides of Equation 1 were equal. This approach was taken with four thicknesses of MgF_2 that yielded four λ_o values, as follows: (1.6 nm MgF_2, λ_o: 6.1 nm), (2.1 nm MgF_2, λ_o: 5.3 nm), (3.3 nm MgF_2, λ_o: 4.6 nm), and (5.1 nm MgF_2, λ_o: 4.2 nm). This limited set of data suggests that as the MgF_2 film thickness increases, the attenuation length through it decreases. This would be consisted with the deposition of an increasingly dense film of MgF_2 as its thickness increases, i.e., the defects in the film may be increasingly filled in as it becomes thicker. Because most of the MgF_2 thicknesses used in this study were more than 2 nm thick, a λ_o value of 4.5 nm was chosen for this work.

4. With a value of λ_o for Mg 2s photoelectrons in MgF_2, Equation 1 was used again, but this time to solve (iteratively again) for the thickness of a MgF_2 layer. In this case, the substrate was considered to be aluminum, i.e., the entire Al 2p peak area (all chemical states) was employed. That is, XPS was performed on each optical stack to obtain the intensities of the Mg 2s and Al 2p peaks that were needed for Equation 1.
5. The results obtained from this method were within about 5% of the values predicted during each deposition by the QCM, where the QCM had previously been calibrated with MgF_2 thicknesses obtained from this material on native oxide-terminated silicon shards.

Overall, this approach should account for any run-to-run variation in the deposition of the MgF_2. The optical constants of thin metal films depend strongly on their structure and deposition conditions.[14, 15] Thus, it was necessary to determine the optical constants of the Al films produced with our evaporation system, i.e., while those in the instrument software might an appropriate starting point, it is unlikely they would be suitable for our modeling. The determination of the optical constants of aluminum was done using an MSA with (i) three Al films (nominally 15 nm thick) that were covered with thick films of MgF_2 (nominally 25 nm thick) and (ii) one bare aluminum surface (nominally 15 nm thick). These layers were deposited onto silicon nitride ($Si/SiO_2/Si_3N_4/SiO_2$) substrates (the nominal thicknesses of the Si_3N_4 layers in these stacks was 300 nm). The bare aluminum film was expected to have some oxide on it, i.e., it was modeled as an aluminum layer beneath an Al_2O_3 layer. For this modeling, the optical constants of Al_2O_3 from the instrument software were used. Because of the thicknesses of the MgF_2 layers here, it was assumed that they had no aluminum oxide under them. Note that the MgF_2 thickness could be determined directly by SE here because no Al_2O_3 was present. The starting point for the optical constants of Al in these analyses was the “Al (Lorentz).mat” model in our instrument software, which contains seven Lorentzian oscillators. To determine the optical constants for our evaporated aluminum, the amplitudes and breadths, but not the positions, of these Lorentzians were allowed to vary one at a time. In this analysis, the amplitude of one of the Lorentzians went to zero so it was omitted. Prior to the deposition of Al and MgF_2, the thicknesses of the layers in the substrate (from the ‘Si Substrate’ through ‘Layer 3 – SiO_2’ layer) had been measured, modeled, determined, and then fixed.

To study the MgF_2 passivation of aluminum, Al (nominal thickness of 15 nm) and then MgF_2 (different thicknesses) were deposited onto fully characterized $Si/SiO_2/Si_3N_4/SiO_2$ substrates. These $Si/SiO_2/Si_3N_4/SiO_2/Al/MgF_2$ stacks were then removed from the evaporation chamber, which ‘started the clock’ for the sample. As quickly as possible, each sample was moved to the ellipsometer, and a four-hour run was commenced that repeatedly collected SE data from the sample. The stack was then analyzed by XPS to determine the thickness of its MgF_2 layer. Two models were finally used to analyze each four-hour set of SE data.

Table A4-1 Results from the two models used to analyze the dynamic sets of SE data generated in this study.

MgF_2 Thickness	Model 1 MSE	Model 2 MSE
0.000 nm	1.200	0.315
1.726 nm	0.754	0.410
2.096 nm	15.491	1.385
2.847 nm	3.275	2.930
3.550 nm	300.000	7.623
3.554 nm	1.234	0.370
4.322 nm	0.754	0.315
4.544 nm	16.961	3.515
5.358 nm	0.833	0.252
5.974 nm	33.685	5.813
Samples w/neg. Al2O3 Thicknesses	6 of 9	2 of 10
Samples that could not be fit	1	0

The first SE model (Model 1) was based on (i) previous characterization of the $Si/SiO_2/Si_3N_4/SiO_2$ substrates with all layer thicknesses and optical constants fixed, (ii) the optical constants that had been generated for a ca. 15 nm Al film in the four-sample MSA described above, (iii) the optical constants of Al_2O_3 that were in the instrument software, and (iv) the thickness of MgF_2 that had been determined by XPS and the optical constants of MgF_2 from the instrument software. Thus, there were only two unknowns in Model 1, which were the thicknesses of the Al and Al_2O_3 films (see again Figure A4-1). This model was applied to each set of dynamic data collected in each four-hour analysis from 10 samples with different MgF_2 thicknesses.

Table A4-1 presents the mean squared error (MSE) value of the fits obtained with Model 1 for each of these samples. It is clear here that some of the data sets are well fit (lower MSE values), while others are poorly fit (higher MSE values). Table A4-1 also reports that with Model

1, one of the samples could not be fit (the one with an MSE of 300), and 6 of the remaining 9 samples showed at least some Al_2O_3 thicknesses that were negative, which is obviously unphysical. Indeed, Figure A4-2 shows representative results from Model 1 for two samples with different MgF_2 thicknesses that gave positive and negative thicknesses for the Al_2O_3 layer.

In spite of the fact that Model 1 predicted negative Al_2O_3 thicknesses for a significant fraction of the samples, all of the Al_2O_3 and Al thicknesses for the samples that could be fit showed the same trends, which were increasing Al_2O_3 thicknesses and decreasing Al thicknesses. In particular, it was found that the plots of the Al_2O_3 thicknesses vs. time for the different samples were approximately straight lines, and that they could be reasonably fit to equation of the form:

$$(2) \qquad t_{Al2O3} = k \ln t + b$$

where t_{Al2O3} is the thickness of the Al_2O_3 film, t is time, k represents the rate of oxidation of the sample, and b is the y-intercept of the line. Figure A4-3 shows the values of k that were thus obtained as a function of the MgF_2 thickness in the samples. It is clear that k decreases as the thickness of the MgF_2 over layer increases, which is the expected behavior for this system.

The negative thicknesses for Al_2O_3 predicted by Model 1 are somewhat disconcerting. We reasoned that perhaps this model was giving unphysical results for this layer because we were requiring the same optical constants for Al to be applied to all the stacks – we previously noted that optical constants for extremely thin metal films are *not* constant. Accordingly, a second SE model/approach (Model 2) was developed in which the optical constants of Al were determined/allowed to vary for each sample (the amplitudes and breadths, but not the center energies, of all the Lorentzians varied). The thicknesses of the Al and Al_2O_3 layers also varied in this model. The lower MSE values for Model 2 (see Table A4-1) suggested that this approach more closely represented each material. In other words, the improved MSE values support the idea that the Al optical constants vary between the samples. Two other indications that Model 2 is an improved representation of our materials are that all of the samples could be fit with Model 2, and only 2 of the 10 samples showed negative Al_2O_3 thicknesses. Plots of Al_2O_3 thickness vs. the log of time were again found to be quite linear and were fit with Equation 2. The resulting k values are plotted in Figure A4-3. It is significant that they are nearly identical to those obtained with Model 1. That is, these results suggest that the decrease in k observed with increasing MgF_2 thickness is not an artifact of either measurement.

A4.6 Conclusions

We have shown real time (dynamic) SE analysis of ten MgF_2 - coated aluminum thin films. The MgF_2 thicknesses were determined by a combination of XPS and SE. The optical constants of the Al films were initially estimated via an MSA of similar materials. Two different models were employed to work up the Al_2O_3 thickness vs. time data generated from the dynamic SE analyses. While the second model gave more physically reasonably results, both made nearly identical predictions of the rate constants for Al oxidation beneath MgF_2 coatings.

A4.7 Figures

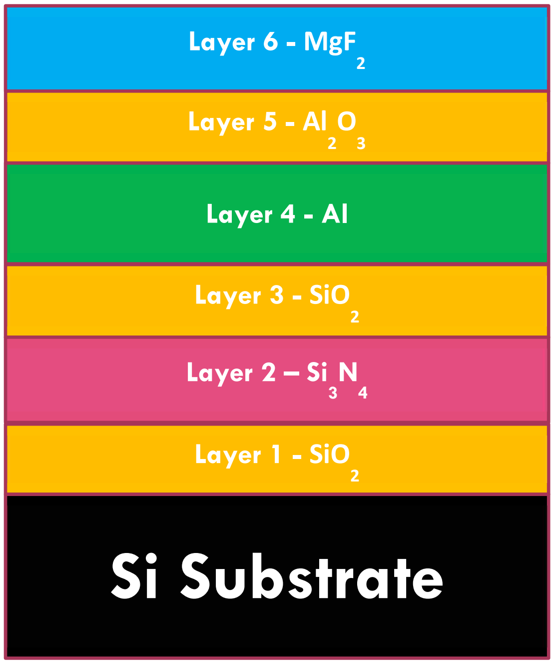

Figure A4-1 Representation of the optical stacks prepared and analyzed in this work. The bottom layers up through Layer 3 represent the Si/Si_3N_4 substrate. Layers 4 and 6 represent the Al and Mg deposited on the substrate. Layer 5 represents the oxidized Al that forms on the Al layer.

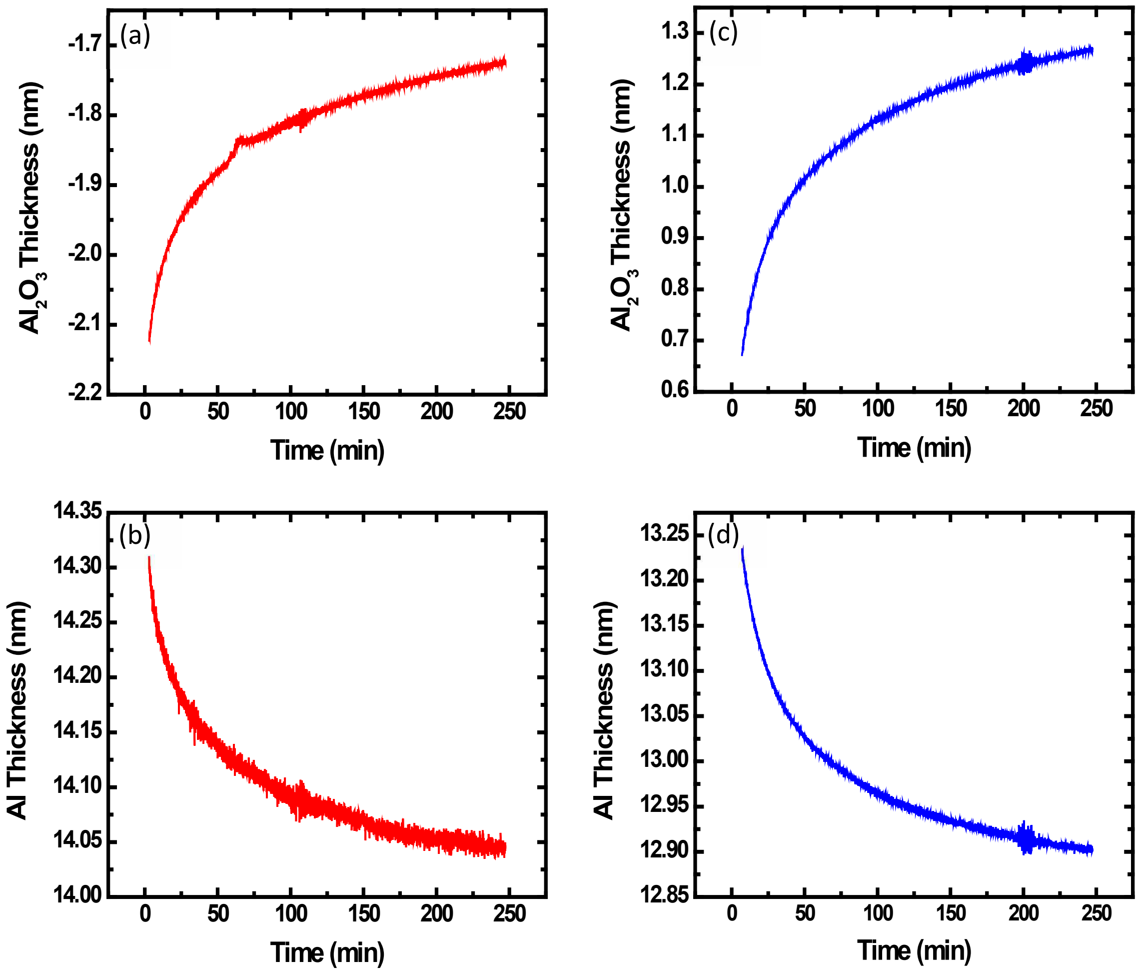

Figure A4-2 Thicknesses of Al_2O_3 and Al determined by Model 1 from two representative samples that showed negative (a) and positive (c) Al_2O_3 thicknesses. Also shown are the Al thicknesses obtained as a function of time for these surfaces.

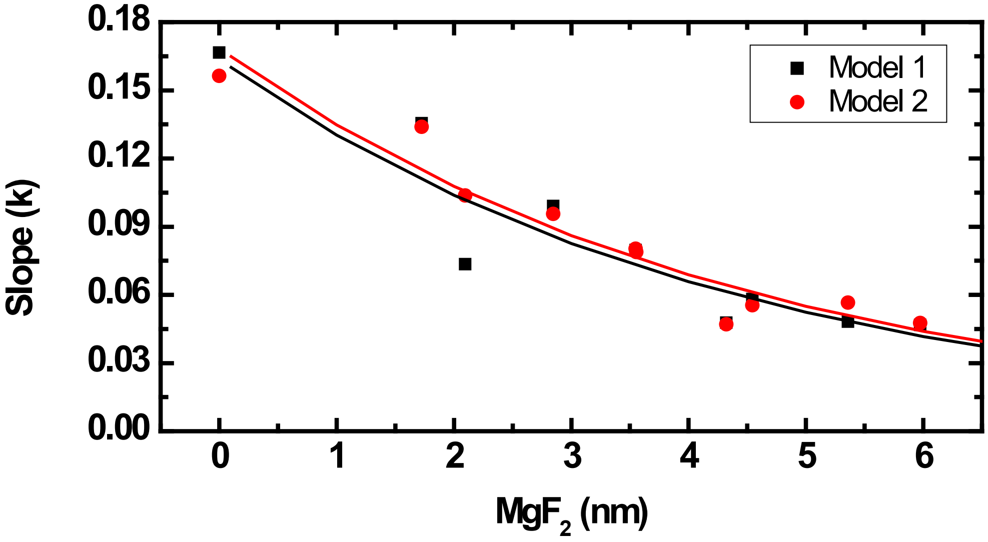

Figure A4-3 Values of k determined from Equation 1 from data generated from Models 1 and 2 employed in this study

A4.8 Future Work/Publication

A more complete treatment of these and other results is being written. It will include XPS analysis showing oxidation of aluminum vs. time and more advanced SE modeling.

A4.9 Acknowledgments

The authors gratefully thank and acknowledge the Utah NASA Space Grant Consortium for funding this work.

A4.10 References

1. Skillingberg, M.; Green, J. J. L. M. A.-C.-. Aluminum applications in the rail industry. **2007,** *65* (5), 8.

2. Bertram, M.; Martchek, K. J.; Rombach, G. J. J. o. I. E., Material flow analysis in the aluminum industry. **2009,** *13* (5), 650-654.

3. Das, S.; Yin, W. J. J., Trends in the global aluminum fabrication industry. **2007,** *59* (2), 83-87.

4. Hass, G.; Tousey, R. J. J., Reflecting coatings for the extreme ultraviolet. **1959,** *49* (6), 593-602.

5. Bridou, F.; Cuniot-Ponsard, M.; Desvignes, J.-M.; Maksimovic, I.; Lemaire, P. In *VUV mirrors for the (80-120 nm) spectral range*, Advances in Optical Thin Films, International Society for Optics and Photonics: 2004; pp 627-637.

6. Trost, J.; Brune, H.; Wintterlin, J.; Behm, R.; Ertl, G. J. T. J. o. c. p., Interaction of oxygen with Al (111) at elevated temperatures. **1998,** *108* (4), 1740-1747.

7. Brune, H.; Wintterlin, J.; Behm, R.; Ertl, G. J. P. r. l., Surface migration of ''hot''adatoms in the course of dissociative chemisorption of oxygen on Al (111). **1992,** *68* (5), 624.

8. Zhukovskii, Y. F.; Jacobs, P.; Causá, M. J. J. o. P.; Solids, C. o., On the mechanism of the interaction between oxygen and close-packed single-crystal aluminum surfaces. **2003,** *64* (8), 1317-1331.

9. Fernández-Perea, M.; Larruquert, J. I.; Aznárez, J. A.; Pons, A.; Méndez, J. A. J. A. o., Vacuum ultraviolet coatings of Al protected with MgF 2 prepared both by ion-beam sputtering and by evaporation. **2007,** *46* (22), 4871-4878.

10. Wilbrandt, S.; Stenzel, O.; Nakamura, H.; Wulff-Molder, D.; Duparré, A.; Kaiser, N. J. A. o., Protected and enhanced aluminum mirrors for the VUV. **2014,** *53* (4), A125-A130.

11. De Marcos, L. V. R.; Larruquert, J. I.; Méndez, J. A.; Gutiérrez-Luna, N.; Espinosa-Yáñez, L.; Honrado-Benítez, C.; Chavero-Royán, J.; Perea-Abarca, B. J. O. e., Optimization of MgF 2-deposition temperature for far UV Al mirrors. **2018,** *26* (7), 9363-9372.

12. Cumpson, P. J. J. S.; development, I. A. A. I. J. d. t. t.; application of techniques for the analysis of surfaces, i.; films, t., The Thickogram: a method for easy film thickness measurement in XPS. **2000,** *29* (6), 403-406.

13. Cumpson, P. J.; Seah, M. P. J. S.; development, I. A. A. I. J. d. t. t.; application of techniques for the analysis of surfaces, i.; films, t., Elastic scattering corrections in AES and XPS. II. Estimating attenuation lengths and conditions required for their valid use in overlayer/substrate experiments. **1997,** *25* (6), 430-446.

14. Girtan, M.; Rusu, G.; Rusu, G. J. M. S.; B, E., The influence of preparation conditions on the electrical and optical properties of oxidized indium thin films. **2000,** *76* (2), 156-160.

15. Martin, P. J. J. o. m. s., Ion-based methods for optical thin film deposition. **1986,** *21* (1), 1-25.